Developing functionalised artificial magnetosomes as theranostic agents for cancer nanomedicine

By:

Christopher Legge

A thesis submitted in partial fulfilment of the requirements for the degree of
Doctor of Philosophy

The University of Sheffield
Faculty of Science
Department of Chemistry

March 2021

ABSTRACT

Nanomedicine is a rapidly developing field which utilises the unique properties of nanomaterials for the treatment and diagnosis of disease. Current nanomedicines are predominantly used for the delivery of drugs and other treatments, and the majority of these are liposome based. Although they have been shown to be able to deliver treatments directly to the cell there are disadvantages such as the high cost of synthesis and difficulty in storage. The development of newer nanomaterials, including polymersomes, allow for the formation of nanomedicines that are biologically safe and have the ability to be functionalised.

Magnetic nanoparticles (MNPs) offer unique properties for nanomedicine. Their magnetism allows them to not only be magnetically targeted to the site of interest but also the ability to generate heat when exposed to alternating magnetic fields, allowing for a targeted method of hyperthermia treatment.

Here I show that MNPs can be synthesised with sufficient magnetic properties to generate heat at therapeutically relevant temperatures of over 45 °C with a specific absorbance ratio of 49.82 ± 3.412 W/g. These particles are coated with a biocompatible coating that enables the functionalisation of the MNPs. These particles were synthesised at two clinically relevant sizes to compare their suitability for use. These were 21.9 ± 3.2 nm and 42.12 ± 12.66 nm and produced using a coprecipitation reaction with a forward and reverse addition of iron salt solution.

The synthesised particles were well tolerated by two breast cancer cells lines at concentrations up to 200 µg/ml and internalised at concentrations from 5 – 200 µg/ml, this internalisation was observed to be a concentration dependant effect with higher concentrations showing a greater amount of internalisation. Internalisation was measured over a 24-hour period and there was seen to be no time dependent factor in the internalisation of these particles.

The use of hyperthermia in the treatment of cancer has been well established.[1] Here I show that hyperthermia is not only capable of inducing thermoablation and coagulative necrosis of cancers of tumours, but that mild hyperthermia can sensitise cells to poly ADP ribose (PARP) inhibitors through the degradation of Breast Cancer Gene 2 (BRCA2) protein. Although a single treatment was sufficient for BRCA2 degradation it was seen that multiple treatments were required for effective treatment with hyperthermia and combined PARP inhibition.

Although the synthesised MNPs showed great promise in hyperthermia treatment, they are not true bio-mimics of magnetosomes, I have developed a method of synthesis of iron oxide within a pre-formed polymersome. The advantage of this method is that it allows the predetermination of the vesicle size and the composition by altering the ratio of polymer chains and the functional groups. The presence of acidic residues on the inner membrane was seen to dramatically affect the formation of iron oxides within the inner lumen of the polymersomes. By altering the concentration of the iron salt solution as well as the size of the lumen core, the size of the formed iron oxide nano particle was altered.

TABLE OF CONTENTS

LIST OF FIGURES

LIST OF TABLES

LIST OF ABBREVIATIONS

AMF	Alternating magnetic field
APTES	3-Aminopropyl) tetraoxysilane
ATM	Ataxia-telangiectasia mutated
ATRP	Atomic transfer reversible polymerisation
AuNP	Gold nanoparticle
BBB	Blood brain barrier
BER	Base excision repair
bNHEJ	Back up non homologous end joining
BRCA2	Breast cancer susceptibility gene 2
BSA	Bovine serum albumin
CADB	4-cyanopentanoic acid dithiobenzanoate
cNHEJ	Classical non homologous end joining
CNS	Central nervous system
CTA	Chain transfer agent
DAPI	4',6-diamidine-2'-phenylindole dihydrochloride
ddH$_2$O	Double distilled water
DLS	Dynamic light scattering
DMEM	Dulbecco's modified eagles medium
DMSO	Dimethyl sulphoxide
DSB	Double stranded break
ECL	Enhanced chemiluminescence
EDTA	Ethylenediaminetetraacetic acid
EM	Electron microscopy
FACS	Fluorescent activated cell sorting
FCS	Foetal calf serum
FSC	Forwards scatter
FTIR	Fourier transform infrared spectroscopy
HBOC	Hereditary breast and ovarian cancer
H$_c$	Coercivity
HT	Hyperthermia treatment
ICP-OES	Inductively coupled plasma optical emission spectrometry
IHT	Incubator hyperthermia treatment
ILP	Intrinsic loss parameter

IMS	Industrial methylated spirit
IONP	Iron oxide nanoparticle
IR	Infrared
MHT	Magnetic hyperthermia treatment
MMR	Mismatched repair
MNP	Magnetic nanoparticle
M_r	Remnant magnetisation
MRI	Magnetic resonance imaging
M_s	Magnetic saturation
MTB	Magnetotactic bacteria
NEAA	Non-essential amino acids
NHEJ	Non homologous end joining
NP	Nanoparticle
OMM	Outer mitochondrial membrane
PBD	Polybutadiene
PBD-PEO	Poly(butadiene-b-ethylene oxide)
PBS	Phosphate buffered saline
PDI	Polydispersity index
PEG	Polyethylene glycol
PEO	Polyethylene oxide
PET	Positron emission tomography
PHPMA	hydrophobic 2-hydroxypropyl methacrylate
PI	Propidium iodide
PISA	Polymer induced self-assembly
PMPC	Poly(2-methacryloyloxyethyl phosphorylcholine)
PMSF	Phenylmethanesulfonyl fluoride
RAFT	Reversible addition fragmentation chain transfer polymerisation
RFA	Radiofrequency thermal ablation
RITC	Rhodamine B Isothiocynate
ROS	Reactive oxygen species
RPA	Replicating protein A
RRTCP	Reverse room temperature co-precipitation
RTCP	Room temperature co-precipitation reaction
SAED	Small area electron diffraction
SAR	Specific absorbance ratio

SAXS	Small angle x-ray scattering
SERS	Surface enhanced raman spectroscopy
SPIONs	Superparamagnetic iron oxide nanoparticles
SPM	Superparamagnetic
SSB	Single stranded break
SSC	Side scatter
ssDNA	Single stranded DNA
TBS	Tris buffered saline
TEM	Transmission electron microscopy
TEOS	Tetraethyl orthosilicate
TNFα	Tumour necrosis factor alpha
UV	Ultraviolet
VSM	Vibrating sample magnetometry
XRD	X-ray diffraction

BIBLIOGRAPHY

Bain J, Legge C.J., Beattie D.L., Sahota A., Dirks C., Lovett J.R and Staniland S.S. *A biomimetic magnetosome: formation of iron oxide within carboxylic acid terminated polymersomes.* Nanoscale, 2019, 11(24): p. 11617 – 11625. DOI: https://doi.org/10.1039/c9nr00498j

Taher Z, Legge C, Winder N, Lysyganicz P, Rawlings A, Bryant H, Muthana M and Staniland S. *Magnetosomes and Magnetosome Mimics: Preparation, Cancer Cell Uptake and Functionalization for Future Cancer Therapies.* Pharmaceutics, 2021, 13(3): p.367. DOI: https://doi.org/10.3390/pharmaceutics13030367

Author Declarations and Contributions

Except where specific references have been made to other sources the work. This thesis is the original work of the author and has not been submitted wholly or in part for another degree.

Chapter 3: All ICP-OES data was collected by Neil Bramall and Heather Grievson at The University of Sheffield. VSM data was collected in collaboration with Nicola Morley at The University of Sheffield. All XRD data was collected by Craig Robertson at The University of Sheffield.

Chapter 4: Flow cytometry data was collected in collaboration with Natalie Winder at The University of Sheffield.

Chapter 5: Data in this chapter was collected with the help of Annie Sohota (MChem) at The University of Sheffield who assisted with PDB-PEO and 70:30 RAFT polymer work. Annie carried out work under my supervision and direction as part of her final year project. Polymer synthesis and characterisation was performed in collaboration with Deborah Beattie in The Armes Group at The University of Sheffield.

ACKNOWLEDGEMENTS

CHAPTER ONE: INTRODUCTION

1 INTRODUCTION

Cancer affected nearly 2 out of every 100 people worldwide in 2018 with 9.6 million deaths.[2] Cancer is a genetic disorder that is caused either by genetic (hereditary) or epigenetic factors which cause the malignant transformation of healthy cell into cancerous cells. Although there have been major advances in the development of cancer therapies there are still some major difficulties. This is in part is due to the heterogenous nature of tumours with different molecular features which make them difficult to treat with targeted therapies as well the development of drug resistance. An example of this is the ATP cassette binding protein ABCG2 which is found in breast cancer cells which causes the efflux of cytotoxic drugs from the cell cytoplasm. The development of new treatments to overcome the limitations of current ones is crucial to develop therapies that will continue to be effective. Hyperthermia (HT) has is known to increase the effectiveness of anti-cancer therapies, but current hyperthermia methods can be largely invasive as well as inefficient. Nanomedicine is a rapidly growing field that has shown promise in the development of treatments for cancer.

1.1 PHYSICAL EFFECTS OF HYPERTHERMIA TREATMENT ON TUMOUR TISSUES

At temperatures between 60 – 100°C (thermoablative temperatures) coagulative necrosis occurs which causes the denaturation of proteins leading to instant cell death.[3] Above these temperatures carbonisation of the cells occurs which can have a negative effect on treatment. Dissemination of tumour cells can occur due to an increase in the interstitial pressure, as well as heat damage not dissipating due to insulation of the treatment area via the carbonised cells.[4] Temperatures of 42 – 45°C can cause irreversible cellular damage to tumours, treatment times of 1 hour leads to the inactivation of proteins which leads to eventual cell death. However, this is a delayed response that can be measured 24 hours post treatment.[5,6] Tumour vasculature is also noticeably affected during HT at temperatures exceeding that of mild hyperthermia treatment, at these temperatures only a slight increase in blood flow is often observed.[7] When temperatures reach the therapeutic range a noticeable effect on the tumour microvasculature occurs. At treatments temperatures of up to 45 °C there is an irreversible reduction of blood flow to the tumour due to tumour vascular damage.[8] At thermoablative temperatures the tumour microvasculature is irreversibly destroyed similar to other tissues that are exposed to thermoablative temperatures.[8]

1.1.1 SUBCELLULAR EFFECTS ON HYPERTHERMIA TREATMENTS

Thermoablative temperatures (≥ 60 °C) cause instantaneous cell death in tumours, whereas temperatures up to 47 °C cause cell functionality and morphological changes. Membrane integrity is affected by the application of HT an increase in membrane fluidity is observed

and membrane irregularities. This leads to actin and microtubule dysfunction leading to a loss of facilitated diffusion across the cell membrane.[9] This results in the accumulation of metabolites within the cell causing eventual cell death, although the effect on membrane integrity can lead to cell death this is not believed to be the main cause of hyperthermia based cell death.[8,10,11]

Mitochondria are one of the main organelles that are damaged in HT. Mitochondrial dysfunction is a known effect of hyperthermia exposure and the effects appear very soon after HT is initiated. The loss of mitochondrial function is seen to correlate well with the loss of cell viability.[12] The effects of increased permeability on membranes causes proton leaking across the inner membrane of the mitochondria and impaired oxidative phosphorylation.[13] HT in therapeutic regions can lead to further mitochondrial damage with a reduction in ATP synthesis and mitochondrial swelling. Apoptotic factors from mitochondria are released due to Bcl-2 homology 3 proteins causing translocation of Bax proteins from the outer mitochondrial membrane (OMM), this causes the release of cytochrome C into the cytoplasm.[13,14]

The loss of mitochondrial function and the halt in oxidative respiration can cause an increase in super oxide anion levels (O_2^-). This increase in O_2^- causes an increase in oxidative stress and this coupled with the increase in mitochondrial Ca^{2+} levels causes the opening of the mitochondria permeability transport pore, this is the cause of OMM swelling and can lead to the rupture of the OMM releasing cytochrome c into the cytoplasm.[14,15]

Hyperthermia also effects the synthesis and replication of DNA, the mechanism of how this happens is not believed to be attributed to a single repair pathway but may be caused by affecting multiple repair mechanisms. Direct damage of DNA by hyperthermia is believed to cause DNA breaks and chromosomal aberrations through the denaturing of proteins and interfering in DNA replication.[16,17] HT at therapeutically relevant temperatures is known to induce phosphorylation of histone H2AX (γH2AX) in a similar manner to ionising radiation which is an indicator of DSBs.[18] This formation of γH2AX foci was seen to be dependent on ataxia-telangiectasia mutated (ATM) protein kinase, which is an indicator of DNA damage. However, it has been found that even though hyperthermia induces γH2AX foci at 43 °C (equivalent to a 2 Gy dose of ionising radiation) it does not induce the same number of DSBs but substantially lower (≈4-9 DSBs as opposed to 70 − 80 DSB).[18,19] Hyperthermia induced γH2AX foci formation has been shown to not be associated with a process of thermal sensitivity. As the intensity of foci between cells, with differing levels of thermal sensitivity, was found to be similar to the wild types cells and the resolution of the induced foci was not

affected by thermal sensitivity.[18] Furthermore it has been observed that there is a lack of 53BP1 and SMC1 induction and no co-localisation of 53BP1 with γH2AX is observed, as is present in γH2AX foci induced in IR treated cells.[19] These results suggest that HT does not induce DSBs in DNA but the formation may be due to alteration in the chromatin structure. This could explain why a plateau was observed in the formation of γH2AX foci with a limited number of sites for chromatin modification, this supports the evidence that foci formation is due to chromatin alterations and not DSBs.[19] It is apparent that HT does effect cell cycle and can influence cell cycle progression in response.

1.1.2 CELL CYCLE EFFECTS OF HYPERTHERMIA TREATMENT

The cell cycle is the process through which cells replicate via mitosis. The cell cycle is broken down into stages which are G1(interphase), S(interphase), G2(interphase) and M(mitotic phase) (**Error! Reference source not found.**). During G1 phase the cell accumulates the material for chromosomal DNA and proteins associated with this. During S phase DNA begins to replicate to produce identical pairs of sister chromatids. The centrosomes also duplicate which gives rise to the production of mitotic spindles. During the G2 phase the cell undergoes rapid growth and the synthesis of required proteins as well as dismantling of the cytoskeleton to provide resources which will be required in the mitotic phase of the cell cycle. The mitotic phase is the process in which the duplicated chromosomes are arranged into two separate daughter cells.
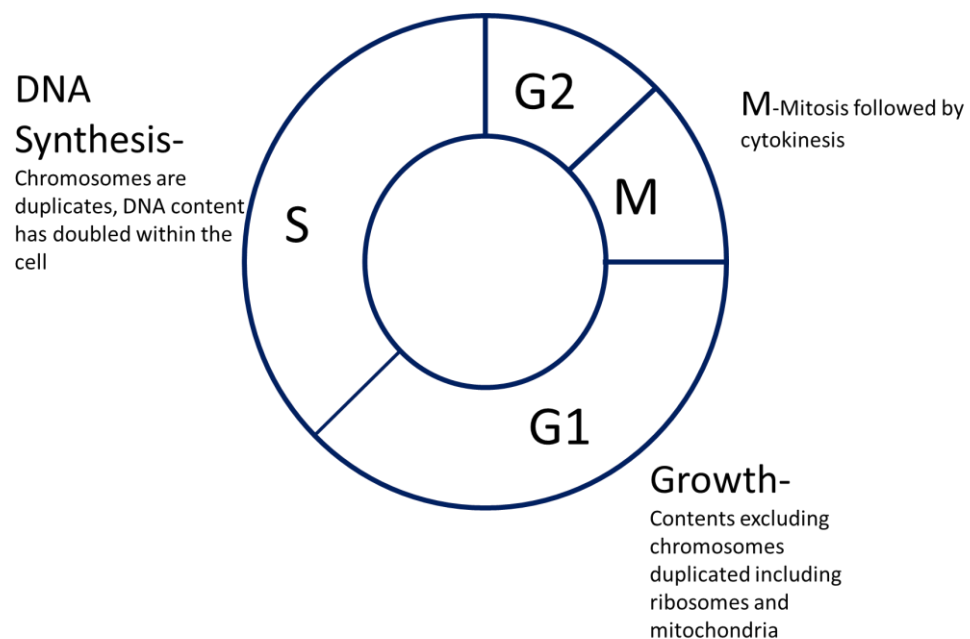
Figure 1.1.1 – Overview of the cell cycle phases involved in mitosis.

DNA damage in cells causes the initiation of cell cycle check points, these check points are managed by two kinases ataxia-telangiectasia mutated (ATM) and Rad3 related (ATR). ATM

is activated in response to DSBs by MRN mostly in the G1 phase of the cell cycle. Whereas ATR is recruited to the presence of SSB at stalled replication forks in S phase. These kinases are recruited to the site of DNA damage along with other repair factors, this in turn recruits repair proteins to the site of the damaged chromatin which causes the activation of cell cycle checkpoints. These checkpoints are controlled by factors including CHk1, CHK2, P53, CDC25a, WEE1 along with other factors.

Although there has been no direct link with mild hyperthermia causing DNA damage, cells do respond to HT and this is dependent on the phase of the cell cycle. When in G1 phase cells do not show DNA damage after HT treatment indicating no sensitivity to HT. Cells in S and M phase showed increased sensitivity to HT, with cells in S phase typically showing an increase in chromosomal aberrations at temperatures of 42.5 °C and above. Cells in S phase are typically 3 times more sensitive to HT than cells in G1 phase.[20,21] HT can slow down cell cycle progression through S phase and initiate cell cycle arrest when long term chronic HT is initiated.[22] This S phase arrest can lead to the accumulation of cyclin B1 within the cell leading to the activation of M phase kinase, eventually leading to cell death.[18] The lesions formed during S phase caused by HT have been seen to be completely reversible, if HT conditions are removed and DNA replication can be delayed for long enough (2 – 6 hours). This is the length of time required for repair directly affected by the level of severity of the lesions.[18,23]

Hyperthermia also causes G2/M arrest due to the suppression of Ku80 as well as the activation of ATR and Chk1 by heat stress of over 42.5 °C.[24] ATR is responsible for the phosphorylation of Chk1 during heat stress independent of ATM activity. This is because heat stress is known to induce SSBs as well as inhibiting DNA replication, which is expected to produce stalled replication forks which may result in the observed ATR activity.[25] p53 is a transcription factor and is activated in response to cell stress this activation of p53 causes further activation of genes that control cell responses.[26] Temperatures of 41 °C cause the unfolding of large regions of p53 which may inhibit their ability to interact with Mdm2 which is responsible for maintaining the normal low levels of p53.[24,26] The loss of interaction of p53 with Mdm2 can lead to the accumulation of p53, resulting in cell cycle arrest and will only enter mitosis if the cell conditions allow this (removal of excess p53).[26] ATM-Chk2 signalling under hyperthermia conditions is believed to be caused by the presence of ROS and not the presence of DNA DSBs, As ROS have been seen to act directly on the inactive ATM Dimer as it causes the formation of a disulfide bond between the monomers. This happen independent of the MRN complex which is crucial for its recruitment to the site of DSBs, This is because MRN is translocated my the nucleus to the cytoplasm in response to

4

hyperthermia. [27] This activity of ATR-Chk1 and ATM Chk2 activation and subsequent cell cycle arrest is believed to be a protective measure to stop the formation of broken chromosomes and subsequent cell death.

1.1.3 HYPERTHERMIA EFFECTS ON DNA REPAIR PATHWAYS

1.1.3.1 Excision Repair Pathways

The base excision repair (BER) is responsible for the majority of all DNA repair including DNA lesions caused by oxidised base, abastic sites as well as SSBs. The repair of these DNA lesions is completed by a relatively small number of proteins including DNA glycosylases, AP endonucleases, DNA polymerase and DNA ligases.[24,28] BER is initiated by the removal of damaged bases by DNA glycosylases, this generates an AP site which is then removed by the AP endonucleases. DNA polymerase then repairs this gap by recruiting the correct nucleotide and the DNA ligase seals the gap.[24,28] Nucleotide excision repair (NER) is the mechanism for the removal of large DNA lesions which can cause helix disorders which include cyclobutene-primidine dimers.[29,30] DNA mismatched repair (MMR) is active during the S phase of the cell cycle when DNA is undergoing replication and is responsible for repairing DNA mismatches that occur during replication.[31]

BER has been identified as being affected by moderate HT, with increased levels of DNA damage and inhibition of base excision observed after IR treatment at temperatures between $43 - 45\ °C$.[32,33] The increased DNA damage was only observed in the IR treated cells and not when hyperthermia was applied alone. Possible causes of this increased DNA damage are the inhibition of BER by hyperthermia that leads to the conversion of the damaged bases being converted to DSB as they are unable to be repaired. BER inhibition by hyperthermia was confirmed to be affected by hyperthermia at least to a moderate extent, due to the proteasome mediated degradation of 8-oxoguanine DNA glycosylase which can induce increased sensitisation to both chemotherapies and IR therapies.[34]

1.1.3.2 Non homologous End Joining.

Non homologous end joining (NHEJ) is one of the main mammalian DNA repair pathways for repairing DSBs and is active throughout the cell cycle. The majority of DNA DSB have non compatible DNA overhangs, this is either due to the bases not being compatible or alteration of the overhangs by chemical modification.[35] In NHEJ these overhangs are resected through exonuclease or endonuclease activity which creates short compatible regions for DNA joining.[35] Two methods of NHEJ have been discerned, these are classical NHEJ (cNHEJ) and back up NHEJ (bNHEJ).[35,36] These pathways use distinctly different sets of proteins for repair of the DSBs, cNHEJ which is the predominant repair pathway for DSB in G0,G1 and G2 uses

Ku heterodimer, DNA-PK, 53BP1 and XRCC4/Ligase IV.[24,35,36] The Ku heterodimer is one of the factors that binds initially to the DSB site and becomes a scaffold for the other nucleases and ligases to bind to for DNA break repair, DNA-PK forms a complex with the Artemis nuclease which processes the ends before ligation which is under taken by XRCC4/Ligase IV. [24,35,36] The bNHEJ uses many repair proteins that are involved in the repair of SSBs as well as many proteins that are involved in homologous recombination (HR).[36] Although both of these repair pathways are believed to be error prone due to the alteration of the DNA ends cNHEJ is believed to be more accurate than bNHEJ. As bNHEJ is known to be a source of major genomic instability and chromosome translocation it is important to have a repair mechanism for repairing DSB when the main pathways fail.[24,36] The effects of hyperthermia on NHEJ are that DNA-PKcs have been shown to be heat sensitive to temperatures of 44 °C for 15 mins, although there are conflicting results that NHEJ is upregulated during HT.[37] These conflicting results suggest that the effect of HT on NHEJ may be more temperature dependent than other pathways as well as cell line dependent.[38]

1.1.3.3 Hyperthermia Effects on Homologous Recombination

Homologous recombination (HR) is known to be affected by HT, temperatures greater than 41 °C cause the temporary degradation of BRCA2 through proteasomal mediated degradation as it is targeted by proteasomes for break down and recycling of the amino acid structure and subsequent of recruitment of Rad51 to the site of the DSB.[39] At temperatures greater than 42.5 °C Rad51 is unable to be recruited to the site of stalled replication forks leading to the collapse of these replication forks. The increase in sensitivity does not result in increased senescence in cells that were treated through hyperthermia alone. Degradation of BRCA2 reduces the cells capacity for HR, and makes them sensitive to Parp inhibitors in animal models.[24] This approach could provide a useful treatment option in multiple cancer therapies, due to the low side effects.[35,37] It was also observed that ligase IV is upregulated in response to HT when BRCA2 is down regulated which suggests that NHEJ is recruited to perform more DSB in the absence of HR.[38] This loss of BRCA2 and Rad51 recruitment to the site of DSBs is similar to *BRCA2* mutated cancers which are susceptible to treatment with PARP inhibitors. With this loss of BRCA2 that is induced by mild HT in cells that do not possess a *BRAC2* mutation it is possible that PARP sensitivity may be conferred allowing for the treatment of these cancers with a targeted drug therapy that is known to have improved patient quality of life in comparison to standard therapies.[40,41]

1.1.4 BREAST CANCER SUSCEPTIBILITY GENE AND HOMOLOGOUS RECOMBINATION

Breast cancer susceptibility gene 2 (*BRCA2)* plays an important role in tumour suppression. The BRCA2 protein is responsible for the localisation of recombinant proteins to the site of

single strand over hangs, in double stranded breaks to initiate DSB repair within cells. Mutations in this gene are a major risk factor for breast and ovarian cancer, with the lifetime risk for ovarian cancer being 20 % greater and 80 % greater for breast cancer.[42] Inheritance of mutations is through an autosomal dominant manner, and inheritance of one copy of the gene along with an epigenetic mutation on the other, is termed hereditary breast and ovarian cancer (HBOC) syndrome.[43] This is associated with earlier onset of disease, as well as multiple primary tumours.[44] A mutation in *BRCA2* is also associated with male breast and prostate cancer.[44]

BRCA2 encodes for the BRCA2 protein, which is 3,418 amino acids in length.[45] It contains eight 40 amino acid motifs,[46] and forms nuclear foci during the S phase of replication. BRCA2 plays an important role in HR, which is a DNA DSB repair mechanism that is responsible for repairing broken or damaged DNA. The use of HR allows for accurate, error free, repair of the damaged DNA sequence through the use of the sister chromatid. This ensures damaged DNA is repaired without mistakes.[45]

The HR pathway is not the only DSB repair pathway. Non-homologous end joining is an alternative repair pathway but does not produce such error free repair as in HR. This is due to the formation of blunt ends by removing the single stranded overhangs present on DSB. It is also unable to respond to damage in DNA replication forks.[47]

The HR takes place during the S/G2 phases of cell cycle replication and can be separated into three separate stages; the presynaptic stage, the synaptic stage, and the post-synaptic phase.[45,48]

During the presynaptic phase of HR, the 5' 3' DNA ends are resected, to produce 3' single stranded DNA (ssDNA) overhangs. These are then bound by replicating protein A (RPA) with a high affinity. RPA inhibits the binding of Rad51 a recombinase protein to the ssDNA, as well as strand invasion activity. However, this is overcome by the Rad51 cofactor Rad52, which facilitates binding to the ssDNA by removing RPA as well as recruiting more RAD51 proteins to the presynaptic filament.[48–50] (Figure 1.1.2). Although RPA inhibits the binding of Rad51, it is responsible for stimulating recombination by preventing the formation of secondary structures along the DNA.[48,49] RAD51 contains two DNA binding sites, which both provide a function for HR. The first binding site is responsible for binding ssDNA in the initiation of HR, the second DNA binding site is responsible for initiating homology probing.[51]

Once bound to ssDNA, Rad51 causes the extension and stretching of the invading presynaptic filament strand into the sister chromatid.[47,52] This is assisted by the binding of cofactor Rad54, which activates strand invasion into the homologous DNA sequence and binding to

the pairing site (Figure 1.1.2).[53,54] The invading strand uses the template strand from the sister chromatid to synthesise template DNA with the 3' end of the invading strand acting as a primer for the synthesis of the DNA16. This is called D loop formation. During the homology search, there is no contact between the target DNA and the recombination enzymes, so interaction between the target DNA and the nucleoprotein filament is completely dependent on areas of sequence homology. This enables a reduction of the amount of non-specific binding in sequences that are not homologous to the desired target sequence. It has been suggested that Rad54 aids the search for homologous sequences in the target DNA strand, and once located, the formation of paranemic joints can occur to help with the alignment of the homologous DNA strand.[54,55]
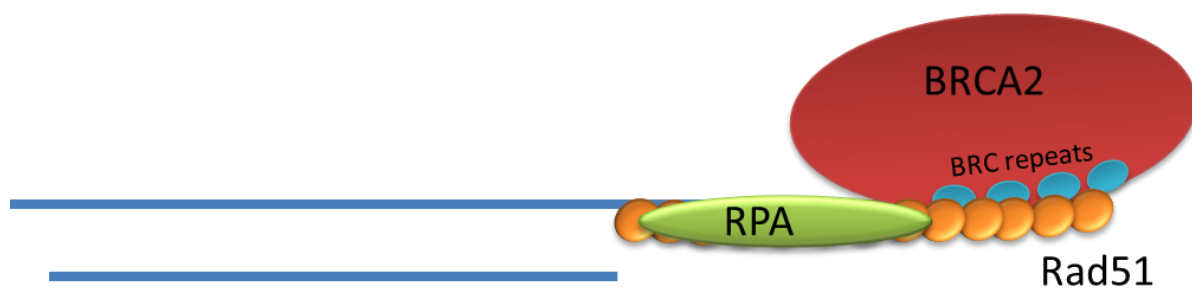
Figure 1.1.2 – Schematic of BRCA2 recruitment of RAD51 in the repair of double stranded breaks.

Once the strand has been synthesised, reattachment to the original strand occurs through two mechanisms: either a second invasion event or annealing to the displaced strand resulting in crossover or non-crossover products.[56,57]

BRCA2 plays an important role, as it binds to Rad51 at the *brc* motifs, which are encoded onto exon 11 of the *BRCA2* gene.[58] The 8 brc repeats are a repetitive sequence of 30 amino acids,[59] and are responsible for the binding BRCA2 to the single strand overhangs on the DSBs as well as the nuclear localisation of Rad51 (Figure 1.1.2) Rad51 is generally produced during the S phase of replication during HR.[52] When BRCA2 is not present, Rad51 is localised to the cytoplasm instead of the nucleus, suggesting a role for BRCA2 in Rad51 transport.[60] BRCA2 is able to bind up to six RAD51 proteins on each BRCA2 protein.[57] Brc 5, brc 6, brc 7 and brc 8 are responsible for binding the Rad51 to ssDNA after stable binding of BRCA2 to Rad51.[61] The brc motifs BRC3 and BRC4 are responsible for the binding to RAD51 and DNA filaments, and stabilisation of RAD51, with brc3 interacting at the N terminus.[62] There is another possible mechanism of BRCA2 RAD51 interaction. BRCA2 may put RAD51 into an activated state so that it is able to be recruited into a repair complex. This allows it to be localised to the site of a DSB for repair. This has been theorised to be important to prevent unwanted formation of RAD51 complexes on double stranded DNA and may supress the

formation of RAD51 ssDNA complexes to the ssDNA present during DNA replication.[60] (Figure 1.1.3).

Brc4 has been shown, along with brc1, brc2 and brc3, to help stabilise DNA filaments by inhibiting the DNA dependent ATPase activity of Rad5.[61,62] Brc repeats have been shown to maintain the nucleoprotein filament in an active state, so it is ready for strand exchange. [59] The brc repeats brc5, brc6, brc7 and bc8 could be responsible for bidirectional growth, which allows both the homology search and strand invasion of the HR pathway.[61] These brc motifs may also assist in the assembly of Rad51 filaments.[61,62] MRE11, which is responsible for the end processing in HR and NHEJ by producing 5'-3' re-sectioned ends for HR, can also cause the degradation of stalled replication forks.[59,63] BRCA2 protects the stalled replication forks by preventing nucleolytic lesions forming.[59,63]

BRCA2 also regulates the interactions between Rad51 and DNA.[64] This prevents interactions that may inhibit HR, providing evidence for BRCA2 as a regulator for HR, as it is responsible for the binding of Rad51 to single stranded DNA.[59,60,65]The brc repeats have proven to be responsible for BRCA2 preferential targeting of single stranded DNA over double stranded DNA, by slowing the recruitment of Rad51 to double stranded DNA.[57]

Mutations in BRCA2 can have a detrimental effect on cell survival. A single point mutation within a brc motif, as well as truncations in the brc region, can lead to an increased risk of cancer.[59] This is due to less efficient binding and nucleation of RAD51 to the site of DNA, which requires the functionality of all brc motifs within BRCA2.[62] Truncations and loss of brc repeats were shown to cause an increased sensitivity to sources of DNA damage, as well preventing the localisation of Rad51 to the site of DNA damage.[59] Mutations within the region of the 8 brc repeats can lead to loss of expression of the protein through nonsense messenger RNA decay. Within the BRCA2 mutation there are breast cancer and ovarian cancer regions, with 33 breast cancer regions identified in BRCA2, which are generally located within the oligonucleotide binding fold domains. Increased breast and ovarian cancer risk are associated with nonsense messenger RNA decay within brc repeats.[66]
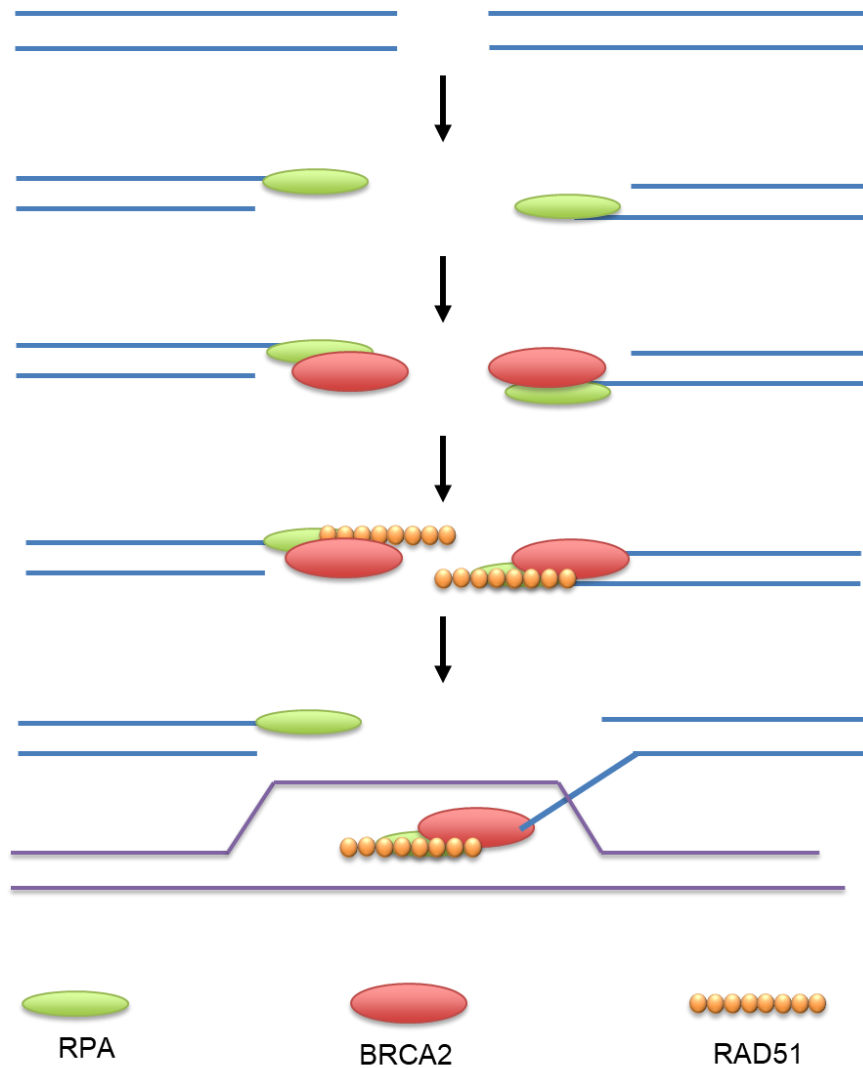
Figure 1.1.3 – The binding of BRCA2 and RAD52 over hangs in homologous recombination during the pre-synaptic and synaptic phase.

1.1.5   PARP INHIBITION

SSB within DNA can form due to oxidative stress, reactive oxygen species, or abortive cellular activity.[67] Roughly 10^4 SSBs occur daily in every cell.[68] PARP 1, the most abundant enzyme of the parp family, is a DNA repair enzyme, responsible for the repair of SSB.[69,70] PARP 1 has three main domains responsible for repair in SSB; a DNA binding domain, an auto modification domain, and a c terminal domain.[69] The DNA binding domain has three zinc fingers, which bind to DNA breaks and activate the Parp 1 protein.[69]

Once bound to the DNA, PARP 1 recruits repair proteins to assist SSB repair and through the conversion of NAD+ into ADP ribose.[70] As well as playing a major role in SSB repair, PARP 1 is upregulated in HR deficient cell lines, and may play a major role in the restarting of stalled replication forks.

Parp inhibitors are responsible for inhibiting the action of PARP 1 to cause the development of DSB, in BRCA2 deficient cells this leads to the specific targeting of these cells for

programmed cell death whilst healthy cells are able to repair these formed DSB through HR. PARP inhibitors act to trap PARP, as well as PARP intermediates, onto the break lesion. This allows the enzyme inhibitor complex to inhibit DNA repair transcription and replication. These have been shown to be increasingly more lethal than inactivation of PARP 1.[71] The protection of the replication forks is recognised as a possible method of synthetic lethality caused by the use of PARP 1 inhibitors, although parp inhibitors cause a delay in the repair of SSB as well as progress for S to G2/M phase, there is no increase in the number of SSB detected in treated cells. This suggests that the lethality of PARP inhibitors is not caused by an increase in SSB, or an increase in DSBs, as an increase in these is not detected after PARP inhibition or knock down through short interfering RNA.[68,70,72] These would normally be repaired through HR mediators, as well as protection of the stalled replication forks from degradation proteins which cause degradation.

In BRCA2 deficient cells, targeting of PARP 1 facilitates the killing of tumour cells through a synthetic lethality process, as the loss of functional BRCA2 prevents the cells' ability to perform HR, and the inhibition of PARP 1 causes the loss of the ability to repair SSBs. Synthetic lethality is when the loss of two genes causes programmed cell death, but loss of the genes individually does not.[70,73]

Inhibition of PARP 1 leads to the collapse of replication forks in SSB repair, due to the conversion of SSB to DSB after treatment with PARP inhibitors. This collapse causes the homologous recombination pathway to be recruited to repair the breaks.[68] Due to BRCA2 negative cancer cell lines being deficient in HR, Inhibition of PARP1 results in a decreased survival of treated cells.[68] This allows the specific targeting of BRCA2 tumours with Parp 1 inhibitors, as it creates a synthetically lethal response only in the cells that are deficient in BRCA2. Inhibition of PARP does not cause any adverse effects in mice and only mild side effects have been detected due to the high selectivity of PARP inhibitors.[71]

1.2 HYPERTHERMIA TREATMENT OF CANCERS

Cancer cells are known to exhibit increased sensitivity to hyperthermia treatment (HT) and are irreversibly damaged at temperatures lower than those seen in non-cancerous cells.[74] This is due to the physical and metabolic differences between cancerous and non-cancerous cells. Cancerous cells have a low efficiency of ATP production which reduces the amount of ATP that is available for maintaining membrane stability with a reduction in the membrane potential due to reduced potassium and sodium transport. The loss of potassium transport means the cell cannot regulate its pH.[75] Along with this membrane permeability which effects the transport of magnesium, calcium, and water into and out of the cells of is altered and its inability to regulate pH cancerous cells. As well as an impairment in potassium and sodium transport the membrane of the cell can also differ in their lipid and sterol content. Hyperthermia treatment in cancer therapy generally involves the heating of the tumour above 39 °C, however there is a broad temperature range with temperatures greater than 60 °C relating to thermoablative treatments and temperatures between 39 – 42 °C relating to mild hyperthermia. The cellular response to HT varies depending upon the temperatures induced.

1.2.1 CURRENT METHODS OF HYPERTHERMIA TREATMENT
1.2.1.1 High Frequency Thermoablation

Radiofrequency thermal ablation (RFA) is a non-surgical minimally invasive method that is widely used to treat tumours in kidney, breast, bone, and lung. These use needle probes to induce lesions within the tumours to induce thermal ablation, although these needles only induce lesions 1.6 cm in diameter.[76] The probes are directed to the site of the tumour under ultrasound, computed tomography or magnetic resonance guidance.[11] The RFA generates hyperthermia by an alternating electrical current (200 – 1200 kHz) generating an alternating electrical field within the tumour tissue, this causes increased friction and agitation in the ions within the tumour tissue due to the difference in the resistance of the tumour tissue and the needle.[77]
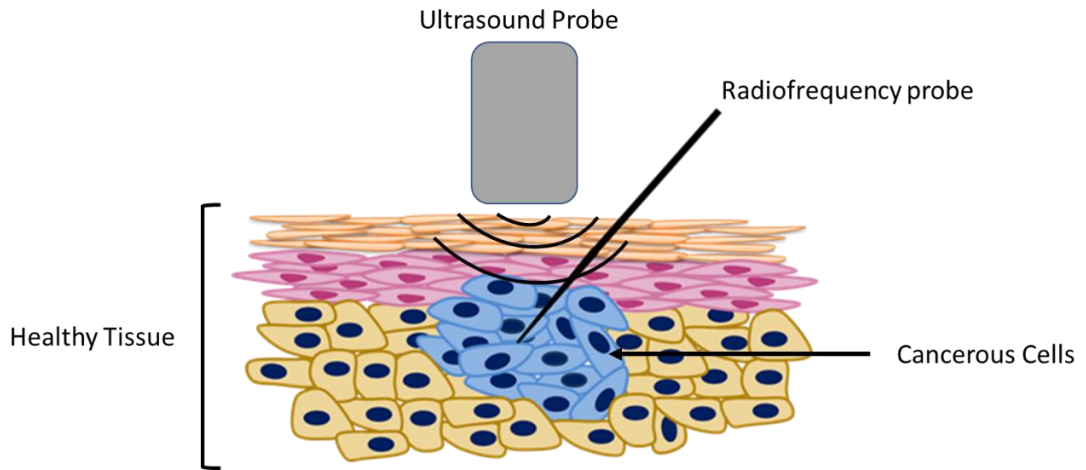
Figure 1.2.1 – Radiofrequency thermal ablation

1.2.1 CONTINUOUS HYPERTHERMIC PERITONEAL PERFUSION.

Continuous hyperthermic peritoneal perfusion is used to treat cancers within the abdominal cavity this includes liver, ovarian, stomach and colorectal cancers in which a warmed fluid is administered to the abdominal cavity, this is usually performed in the presence of chemotherapeutic agents (Figure 1.2.2).[78]
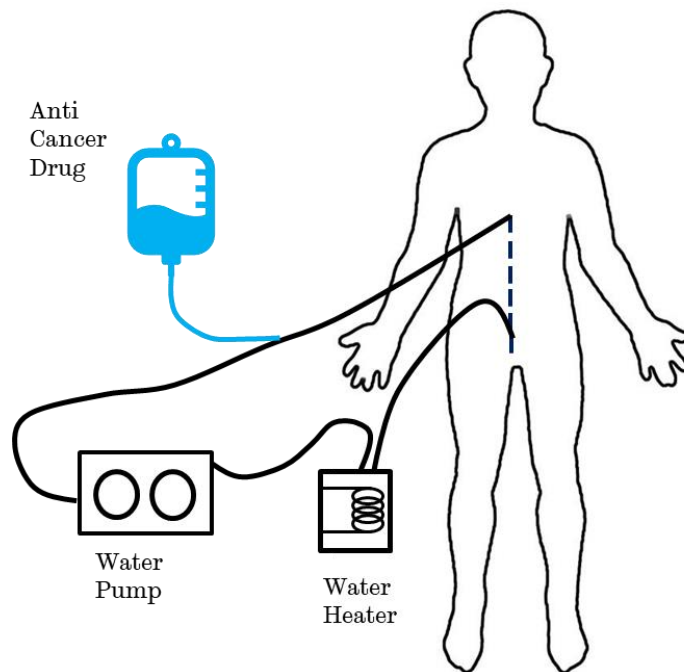
Figure 1.2.2 – Continuous hyperthermia peritoneal perfusion

13

1.3 NANOMEDICINE

Nanomedicine is the application of nanotechnology for medicinal purposes is an increasingly expanding area of medicine with nanoparticles (NPs) having been successfully used in a number of treatments.[79] Nanomedicine is defined as "the use of nanoscale materials for the diagnosis, monitoring, control, prevention, and treatment of disease".[80] Nanomedicine utilises the unique properties that nanoscale materials possess when compared with large scale materials, nanomedicines utilise NPs. The size definition of NPs can vary greatly as there is no officially adopted status for what classes as a nanomaterial. Nanoscale materials can be defined as being sub-micron in size, having one dimension that is less than 100 nm which is the definition the European chemical agency defined a NP as, although the National Nanotechnology Initiative (NNI) defined nanoparticles as having a diameter ranging from 1 to 100 nm.[81–83] This lack of definition can lead to confusion regarding nanomaterials and their uses. NPs have gained attention in the medical field due to the small size and large surface area, with their small size allowing for intracellular uptake as well as their ability to be used as contrast agents for the imaging of diseases due to their unique nanoscale properties.[84]

The majority of NPs are used as imaging agents for the diagnosis of disease, this is due to the unique properties that these nanomaterials possess but a major developing field of nanomedicine is their use as delivery vectors for treatments.[83,85] The benefit of this is that drugs can be administered at a reduced dose with increased effectiveness, hopefully reducing the level of side effects that is experienced by the patient. As well as reducing the drug load, nanomaterials can help drugs to reach impermeable regions that are selective in their transport such as the blood brain barrier (BBB) which protects the brain and central nervous system (CNS). Use of nanomaterials for encapsulation of drugs and therapies provides further protection to the treatment as without this protective layer the therapy would be degraded and rendered useless following administration. An example of this is mRNA vaccines as they require a delivery vessel due to their high instability in physiological conditions due to the presence of ribonuclease.

The use of nanomaterials for treatment is not only limited to drug delivery, the intrinsic properties of certain materials also lead them to be useful for both diagnostic and therapeutic benefits.[83,86]

1.4 TYPES OF NANOPARTICLES

NPs used in nanomedicine can be classified as organic, inorganic or carbon based depending on the material they are made from. The type of material chosen can affect the properties of the NP and it is an important consideration when designing NPs for a particular treatment.

Table 1.4.1 – Nanoparticles used in nanomedicines grouped by chemical characteristics.

Organic	Inorganic	Carbon
Liposomes	Gold	Nanotubes
Niosomes	Quantum dot	
Polymersome	Magnetosome	
	Magnetite NPs	

1.4.1 ORGANIC NANOPARTICLES

Organic NPs possess a multitude of advantages for nanomedicines and have been developed for drug delivery as well as immunoassays. A major advantage of organic NPs is that they can overcome some of the chronic nanotoxicity that is observed with inorganic NPs.[87] The majority of organic NPs are synthesised using one of two methods, either a bottom up or top down approach.[88] Bottom up synthesis involves assembling molecules into NPs, self-assembly is a common method of NP bottom up synthesis. Whereas top down synthesis involves breaking down of bulk molecules into nanoscale materials, this can be performed via electro-spraying, homogenisation and milling as well as other techniques.[88]

1.4.1.1 Liposomes

Liposomes are the most common and most thoroughly investigated nanocarriers that have been produced.[89] Liposomes are composed of small bilayer vesicles made up of phospholipids with the nonpolar hydrophobic regions orientated towards the centre of the membrane and the hydrophilic, this produces a closed structure with an aqueous core that is ideally suited for drug delivery or the transport of small molecules.[90,91] The structure of liposomes can be altered to form both unlayered and multi layered lamella. The rigidity of the membrane can be altered, using longer saturated hydrocarbon chains can increase the membrane rigidity whereas the use of shorter or unsaturated hydrocarbon chains produces membranes that are more flexible and disordered.[88,91] The main advantage of liposomes is the low toxicity they induce, the ability to encapsulate both hydrophilic and hydrophobic compounds and their biodegradability allowing them to be used with little concern for accumulation within organs.[88,90]

Due to the nature of uneven blood distribution around the body with higher blood flow to different regions which may not be where the therapeutic target is the majority of drugs have low therapeutic indexes which means they require a larger dose of drug to produce a therapeutic effect which increases the risk of adverse effects. Liposomal drug carriers have been shown to increase the therapeutic index of drugs and this is due to their ability to easily cross cell membranes as certain drug compounds cannot easily do due to their chemical

structure. This reduces the amount of treatment that is required to reach the threshold dose for a therapy to be effective.[90,92] Liposome production can be broken down in to two main categories mechanical dispersion and solvent dispersion. Mechanical dispersion can be further broken down with different methods used to produce either unilamella or multi-lamella vesicles. Sonication (tip or bath) is the most extensively used method in the production of small unilamella lipid vesicles from multi lamella vesicles. However, this method can produce a mixed solution of both single and multi-lamella vesicles and pollution of the solution with titanium from the sonicator probe can occur. Cell extrusion has shown to be a more beneficial method of liposome synthesis and vesicles are extruded through a membrane with a fixed pore size to produce small unilamella vesicles. This reduces the damage to the membrane proteins and increases the entrapment time for molecules within the liposome.

Solvent dispersion uses lipids in a solvent solution to form liposomes, either through the evaporation of the solvent or mixing of the solvent with a buffer to cause liposome formation. These methods produce heterogeneous populations with a large size population distribution.

Although liposomes have great potential as a drug and therapeutic delivery agent, they still suffer from some major drawbacks: the high cost of liposome production due expensive precursor materials and additional costs involved in vesicle clean-up to remove solvents and other contaminants. Additionally, low solubility and short half-life mean that liposomes do not last long in solution and are not easily stored.

1.4.1.2 Niosomes

Non-ionic surfactant vesicles (niosomes) are a newer class of NP that were initially developed and utilised by the cosmetics industry. They are formed of non-ionic surfactants (SPANs TWEENs and BRIJ) and lipid compounds which produce a closed structure with a bilayer membrane when exposed to aqueous media and the induction of an external energy source (heating or mechanical).[93,94] The structure of the membrane orders the hydrophobic parts of the membrane way from the aqueous solution with the hydrophilic heads in contact with the aqueous medium (Figure 1.4.1). Niosomes differ from liposomes as they generally only have a single hydrophobic tail.
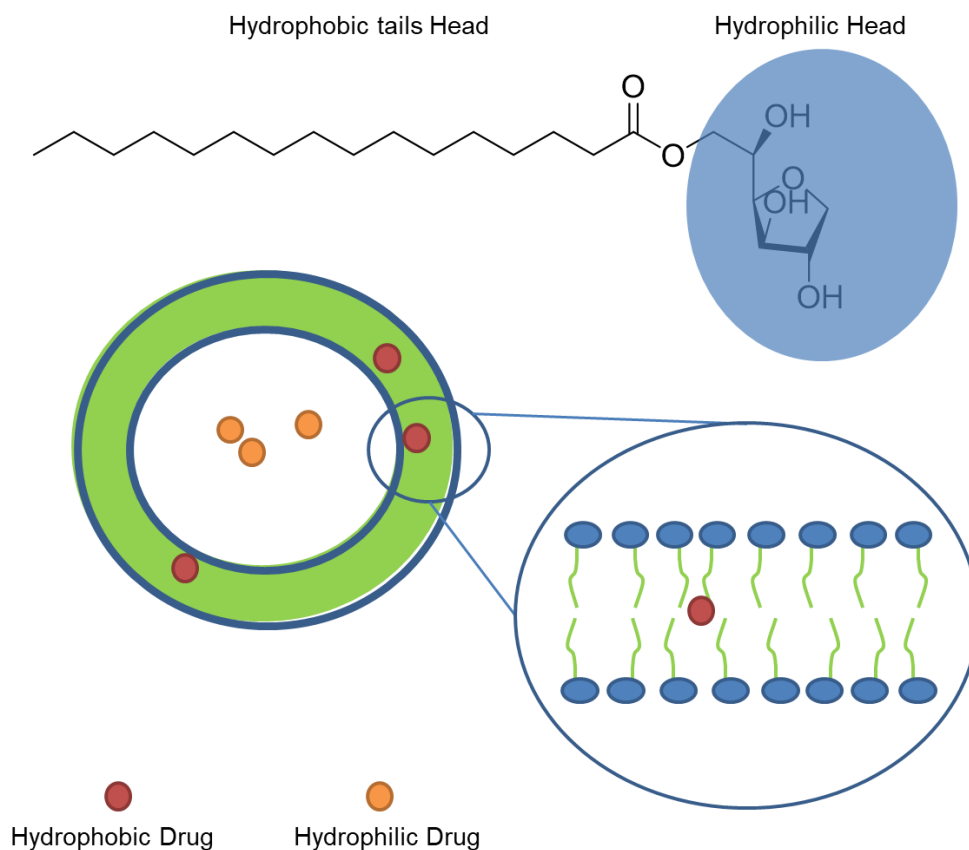
Figure 1.4.1 – Niosome structure and the encapsulation of hydrophilic (inner core) and hydrophobic drugs (within the membrane).

Similarly to liposomes niosomes can be classified into small unilamella vesicles, large unilamella vesicles, and multi-lamella vesicles.[95,96] Niosomes offer major advantages as they can deliver both hydrophobic and hydrophilic drug molecules. Hydrophobic drugs are entrapped within the bilayer and hydrophilic drugs are encapsulated within the core of the vesicle (Figure 1.4.1). Amphiphilic drugs span the hydrophilic core and lipophilic tails.[93] Niosomes possess many of the same benefits as liposomes including biocompatibility and biodegradability as well as improving the therapeutic index of drug treatments. Niosomes also offer many advantages over liposomes including reduced cost in both production and storage compared to liposomes and they offer improved stability due to the presence of non-ionic surfactants.

Although there are many benefits to niosomes there are still some drawbacks including that toxicity has not been as well studied, other nanocarriers and alterations of different surfactants can alter the toxicity of the niosomes. Similarly, to liposomes the instability of niosomes in aqueous solutions can cause their shelf life to suffer and the difficulty in the sterilisation of niosomes due to their incompatibility for heat sterilisation.[94,97]

1.4.1.3 Polymersomes

Amphiphilic block co-polymers are macromolecules contain blocks of chemically distinct monomers, polymers that contain two distinct monomers are known as di-block co-polymers and polymers that contain three different monomers are tri-block co-polymers (ABA) (Figure 1.4.2). Di-block co-polymers (AB) that contain hydrophobic and hydrophilic blocks of polymer form amphiphilic structures which can be vesicles nanoparticles and rods. Block co-polymers are mainly synthesised using living polymerisation as this allows the addition of the different polymer blocks through the addition of monomers as there is no chain termination in these reactions. Reversible addition-fragmentation chain transfer polymerisation (RAFT) enables the control of the polymer molecular weight as well as the dispersity of each block through the use of a chain transfer agent (CTA).[98] The morphology of RAFT polymersomes is affected by the length of the hydrophobic block so controlling this length is imperative for controlling the morphology. The use of a RAFT polymerisation allows for polymerisation with a high tolerance for functional groups and wide temperature range during synthesis.[98,99] Atomic transfer reversible polymerisation (ATRP) is a polymerisation technique that results in a narrow size distribution of the formed polymer because of equal propagation of the polymer chains. ATRP forms polymer chains by forming carbon bonds between vinyl polymers through the use of a metal halide catalyst. Similarly, to RAFT synthesis ATRP has a high tolerance for functional groups.
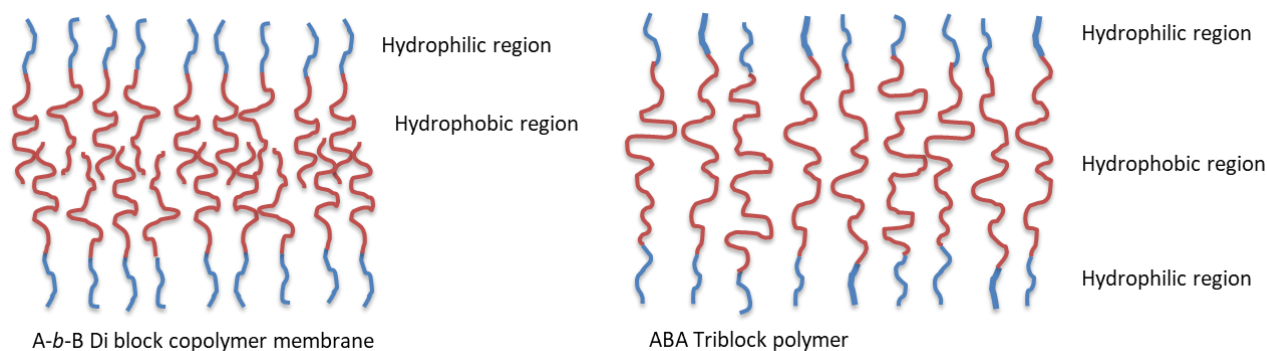
Figure 1.4.2 – Polymer membrane formation for both di-block and tri-block polymers.

AB diblock copolymers are the most prevalent block co polymer. These consist of a hydrophilic and hydrophobic block and these form as the hydrophobic block try to reduce their contact with the aqueous solution, so they aggregate forming the inner portion of the membrane. The hydrophilic blocks form the outer portion of the membrane as well as the inner portion of the membrane. ABA triblock copolymers have two possible confirmations when they form a vesicle structure. The vesicle can form in a similar manner to the AB block copolymer as the hydrophobic region spans the inner portion of the vesicle membrane and

the hydrophilic portions are expressed on the exterior and interior face of the membrane. The other possible formation is that the polymer bends so the that two hydrophilic blocks form on the same exterior or interior portion of the membrane.

1.4.1.3.1   Polymersome Formation

Two methods of polymersome formation are well established, solvent free and solvent displacement. Solvent free methods consist of techniques such as thin film rehydration and polymer induced self-assembly (PISA).

Thin film rehydration involves dissolving the polymer in a solvent onto a flat surface and the solvent evaporated to produce a film on the base of the surface. Upon addition of an aqueous solution there is budding of the film which produces vesicles.[100,101]

Polymer induced self-assembly is a technique the utilises the differences in the different solubilities of the monomer and polymers. Polymerisation of the hydrophobic monomer by the hydrophilic macro-CTA results in an increasing hydrophobicity of this hydrophobic block. This increasing hydrophobicity results in the self-assembly of the polymersome to reduce the interfacial tension of the hydrophobic polymer. Prior to the self-assembly of polymersomes it was found that there was a liquid-liquid phase separation. This phase separation is responsible for determining the size as well as membrane thickness. This technique can produce a variety of polymer morphologies including worms spheroids and vesicles this is dependent on the length of the hydrophilic polymer as well as the degree of polymerisation of the hydrophilic block.[101,102] Low levels of polymerisation result in no self-assembly of the polymersomes, as the level of polymerisation increase this reaches a critical point at which micelles start to form. The formation of vesicle and rod like structures does not occur until the polymer reaches a significantly high level of polymerisation. Control over the morphology of the structure occurs by altering the ratio between the hydrophobic and hydrophilic blocks.

pH as well as temperature are also known to drive the assembly of amphiphilic block co polymers with increasing temperature leading to the deprotonation of the hydrophobic block increasing it hydrophobicity resulting in self-assembly when the pH and temperature reaches a critical point.

Although liposomes membranes are more similar in structure to cell membranes due to having a lipid bilayer, they are noticeably thinner with a thickness of 3 – 5 nm, whereas cell membranes are 8 – 10 nm. This difference is due to the lack of membrane proteins in liposomes which are found within the cell membranes. Polymersomes can be altered to have membrane thickness in the range 5 – 50 nm depending on the parameters chosen (Figure 1.4.3). Both lipid and polymersome vesicles can produce small and large unilamella but

polymersomes offer a more colloidal stable vesicle, has versatility in membrane permeability and molecular loading within the vesicle core and membrane.[103]
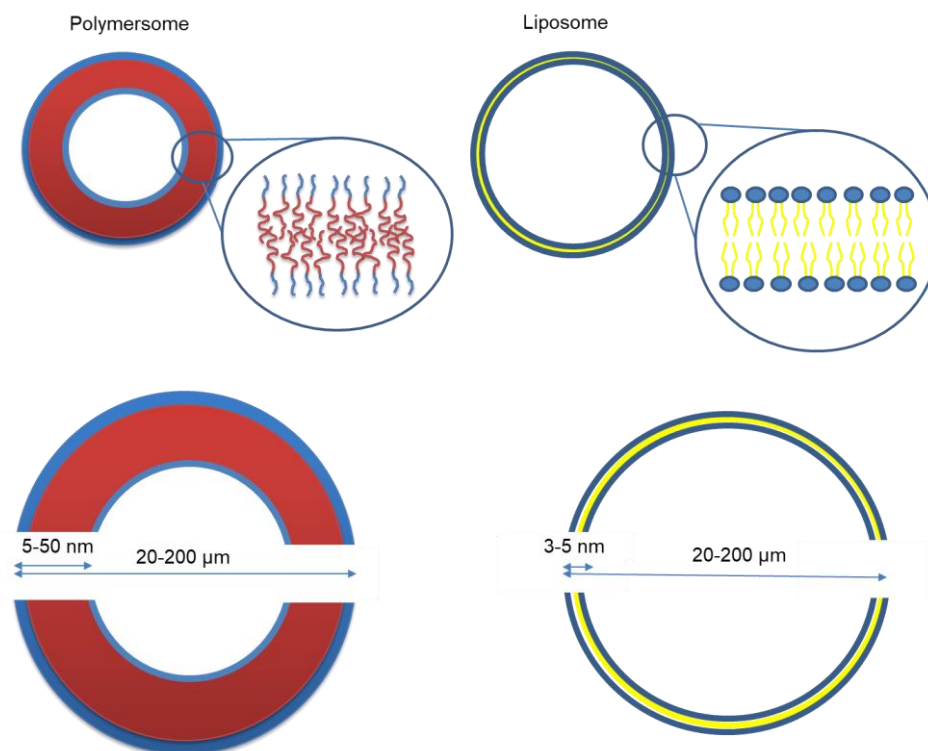
Figure 1.4.3 – Schematic of polymersome and liposomes, showing structural differences and size ranges.

1.4.1.3.2   Formation of Nanoparticles within Vesicles

The formation of NPs within polymersomes allows for the protection and transport of NPs within the polymersome, taking advantage of the properties of the polymersome. The formation of NPs within a polymersome can occur through a number of methods. Encapsulation of nanoparticles by polymersomes can occur during the formation of vesicles. This co-assembly of the polymer and NP and the ratio between the two can determine the final morphology of the vesicle as well as the localisation of NPs within the vesicle.[104] These NPs can be encapsulated within the membrane of the of the vesicle as well as the inner lumen, the presence of high concentration of NPs within the polymer can produce multicavity polymersomes with multiple inner lumens.[104] The formation of nanomaterials within polymersomes has mostly been accomplished within lipid vesicles, these vesicles are used as a container for the formation of nanomaterials.[105] The formation of iron oxide material within liposomes was shown to produce NPs with a range of structures and morphologies that were affected by the shape and dimension of the vesicles that they were synthesised within.[106] This was not limited to just iron oxide nanoparticles, cadmium and copper sulphate nanomaterials have also been synthesised within lipid vesicles. Their size is

controlled via the amount of precursor material present within the inner lumen of the vesicles or by controlling the time at which the reaction is halted. The rate of formation of the NPs is altered by adjusting the pH of the reaction, with a decrease in pH causing an increase in cadmium and copper sulphate formation due to an increase in permeation of sulphide into the vesicle.[107]

These methods allow for the formation or encapsulation of nanomaterials within lipid vesicles and tuning of particle size via controlling the starting material and reaction pH. The use of biomimetic approaches to the synthesis of nanomaterials within vesicles has shown to be able to produce polycrystalline particles within giant vesicles, this is achieved using a slow growth method of synthesis through nanotubes that connect the vesicle to the substrate which allow the transfer of medium within the vesicles.[105] This formation produces larger particles than electrofusion methods, electrofusion is the process of fusing vesicles containing different reactants using an external electric current. The external electric current initiates vesicle fusion of Na_2S and $CdCl_2$ resulting in CdS nanoparticles in the range of 4-8 nm being synthesised.[105]

Although the majority of work on the synthesis of NPs within vesicles has been conducted within lipid based the use of polymer vesicles has shown the ability to form NPs within their centre. Formation of Cu NPs within niosomes was shown to exert an increased level of control on the size and shape of the Cu NPs synthesised, this helped to overcome the difficulties that occur in traditional synthesis of Cu NPs such as formation of large aggregates as well prevention of oxidation.[108] The use of polymersomes as a nanoreactor has shown some promise with Bain *et al* showing the formation of polymersomes with enhanced MRI contrast after formation of iron oxide NPs within them.[109] These iron oxide NPs were seen to form not within the inner lumen of the polymersome but within the polymersome membrane itself. Possibly due to the efflux of the base from the polymersome interacting with the iron salt as they enter the polymersome due to electroporation.

The use of vesicles as nanoreactors has shown great promise in biomimicry for the formation of NPs, it has also shown the ability to influence the size of the formed particle as well as providing protection from oxidation. There is the added benefit of reducing the need for harsh chemicals making it a greener and more environmentally method of synthesis.[105,107–110]

1.4.2   INORGANIC NANOPARTICLES

Inorganic NPs are those that have been made from metal alloys (e.g., Gold, silver) or semiconductor materials (e.g., Iron oxides (see section 1.4.2.3) or carbon nanodots

lanthanide ions) and produce a broad range of properties including optical and magnetic properties as well as local surface plasmon resonance which can produce surface bands in the UV-visible near infrared range which respond to changes in the chemical environment. These properties of inorganic NPs is what makes them unique in terms of nanomedicines.[111] Inorganic NPs can also have fluorescent, near infrared and magnetic saturation capabilities which make them an ideal imaging agent. They can be used in techniques such as magnetic resonance imaging (MRI), positron emission tomography (PET), plasma enhanced fluorescence (PEF) and surface enhanced Raman spectroscopy (SERS). The use of NPs in these techniques offers many benefits over traditional imaging methods, it allows for multiple imaging using the same agent, enabling multi-modal imaging to increase the amount of information obtained.[112,113] Functionalisation of inorganic NPs has shown to improve uptake into cells and allows for the attachment of drugs to NPs, this allows them to be used as not only a diagnostic agent but also a therapeutic agent which has recently been termed "theragnostic agent".[114–116]

1.4.2.1 Gold Nanoparticles

Gold NPs (AuNP) are an attractive NP for nanomedicine as they offer unique optical properties for imagining and also have high biocompatibility and cell internalisation.[113,117,118] AuNPs are capable of size control within the nanoscale range.[119,120] AuNPs offer high drug loading density due to their large surface area for small size, and the ability to attach ligands for improved uptake and distribution. AuNPs are the most highly used in nanomedicine with multiple gold based therapies working their way into clinical trials.[121] Recently Astra Zeneca has developed a Tumour necrosis factor alpha (TNFα) loaded AuNPs in collaboration with Cytimmune that has recently entered phase 1 clinical trials.[122] This popularity is due to the ease of surface functionalisation that enables them to be coated with a variety of compounds with ease including polyethylene glycol, carboxyl groups, DNA, RNA and antibodies.[110,123–128] The ease of chemical conjugation, high biocompatibility and the fact that AuNPs do not accumulate within the liver of *in vivo* models and the ability to avoid phagocytosis via macrophages makes AuNPs an incredibly versatile NP for nanomedicine.[129]

1.4.2.2 Magnetic iron oxide nanoparticles

1.4.2.2.1 Magnetosomes

Bacterial magnetosomes are a type of prokaryotic organelle which consist of a phospholipid membrane which contains a magnetic crystal core. Bacterial magnetosomes are produced by magneto tactic bacteria (MTB) which are a heterogenous group of prokaryotic organisms that form iron oxide NPs within a phospholipid bilayer[130] MTB form these magnetosomes

intracellularly within the bacteria and show alignment to the magnetic poles (magneto taxis).[131] Magnetosomes form in a size range of 35 – 120 nm and are capable of producing a variety of shapes of nanocrystals including cubo-octahedral, rectangular, hexagonal prism and bullet shaped NPs. The vast majority of which are magnetite nanoparticles (Fe_3O_4) but greigite (Fe_3S_4) are also known.[132–134] The magnetic NPs (MNPs) that are produced are within the single domain crystal size, formed in chains along the central axis of the MTB and align the bacteria to magnetic field lines.[130]

The synthesis of MNPs within magnetosomes takes place through a process of biomineralisation. The shape, size, and location of magnetosomes is controlled by proteins found within the membrane of the MTB (Figure 1.4.4). In *Alphaproteobacteria* which are the most characterised MTB these proteins are encoded by a group of genes within the MTB and are found within four conserved gene clusters within a specific region of the MTB chromosome.[135] The four gene operons are: *mms6, mamGFDC, mamAB, and mamXY.*[136] *mms6* encodes for the Mms6 protein which is involved in controlling the size of the magnetite crystal.[137,138] The Mms6 protein is bound to the membrane and the C terminus of the protein interacts with iron ions and iron crystals.[138] The *mamXY* operon encodes for the mamX protein which is responsible for controlling the size and maturation process of the magnetosome.[139] The MamY protein is believed to be responsible for the invagination of the magnetosome membrane during formation and regulation of the vesicle shape.[139,140] The *mamGFDC* encodes for four small proteins MamG, MamF, MamD and MamC that are responsible for helping to controlling the size and maturation of NPs, knock out of *mamGFDC* gene resulted in smaller magnetite NPs.[141,142] The mamGFDC proteins are believed to possibly aid in controlling magnetite size and maturation by controlling the inner conditions of the magnetosomes including the pH, redox conditions or through an well as an anti-inhibitory effect on magnetite crystal growth although the exact method of crystal size control is yet unknown.[142,143] The mamAB operin encodes for17 proteins within magnetosomes (MamA, B, E, H, J, K, L, M, N, O, P, Q, R, S, and U) that are involved across the different stages of magnetosome formation[144] as well as iron transport and crystal nucleation and growth (Figure 1.4.4). MamB, I, L and Q are believed to be responsible for the invagination of the magnetosome membrane, with MamB also being responsible for iron transport (Figure 1.4.4).[145] MamI, and L are believed to be responsible for membrane bending during invagination. Biomineralisation within the magnetosome involves the transport of iron and its nucleation. Along with MamB MamM and MamH are responsible for iron transport in the magnetosome.[146] When the genes controlling these proteins are lost

they result in the formation of no magnetite crystal or a dramatic decrease in the magnetic response. This highlights the importance of iron transport to within the magnetosomes membrane for the formation and growth of magnetite crystals. For crystal size and morphology within magnetosomes Mms6 protein is shown to control the formation of magnetite nanoparticles.[6] It has also been shown to tightly associate with magnetite synthesising highly ordered cubo-octahedral crystals. Whilst the loss of the *mms6* gene results in other iron oxides that are not magnetite forming.[138]

MamL	MamH	MamE
MamQ	MamM	MamO
MamB	MamO	MamN
Mamγ	MamI	MamP
		MamR
		MamS
		MamT
		Mms6
		MmsF
Vesicle formation	Iron uptake and magnetite nucleation	Crystal Maturation
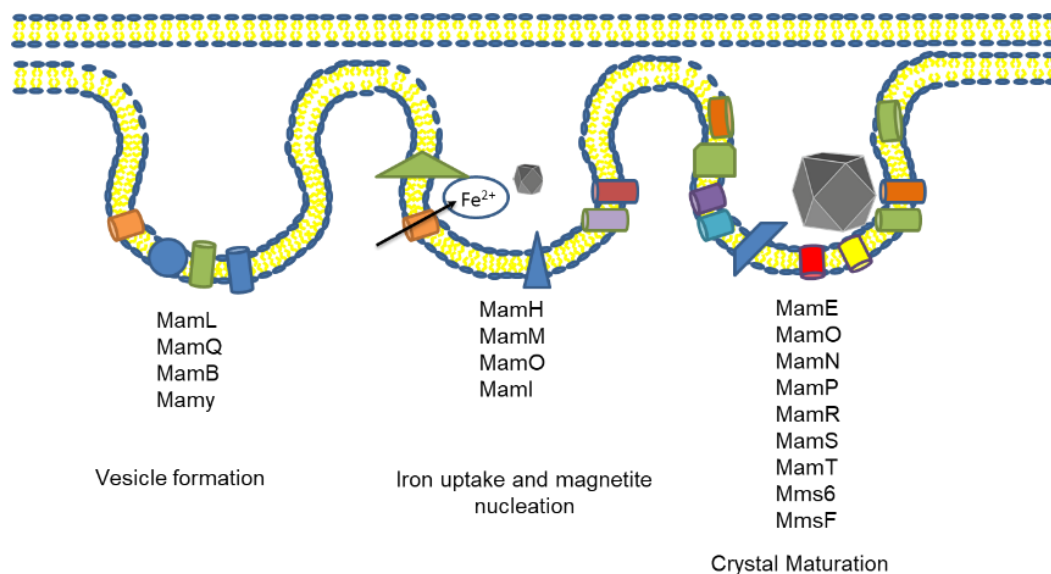
Figure 1.4.4 – Simplified representative diagram of magnetite crystal formation and growth within magnetosomes.

1.4.2.3 Magnetite nanoparticles

Magnetite (Fe_3O_4) is an iron oxide ferrimagnetic material that has previously been used in biomedical applications due to the magnetic properties that it exhibits.[147] The magnetic properties that magnetite exhibits are due to its ferrimagnetic inverse spinel structure 2:1 ratio of Fe^{3+} to Fe^{2+} ions.

The unit cell of magnetite comprises 32 O^{2-} anions, and 24 iron cations (eight Fe^{2+} and sixteen Fe^{3+}) these iron ions are organised in either tetrahedral or octahedral sites within the crystal. Eight tetrahedral and sixteen octahedral positions are occupied in the unit cell, with the general form of the inverse spinel: (B)[AB]O4 where (A) are the tetrahedral sites and [B] octahedral sites. The divalent ferrous cations occupy the octahedral sites(B), with the trivalent ferric cations occupying both tetrahedral(A) and octahedral(B) sites. This arrangement gives magnetite the formula $Fe^{3+}(Fe^{2+}Fe^{3+})O_4$. This distribution of metal ions is driven by the crystal field stabilisation energy. Fe^{2+} in the inverse spinel structure has a higher

stabilisation energy for the octahedral positions than Fe^{3+}, meaning Fe^{3+} will occupy all the tetrahedral sites, and half the octahedral sites. Through the process of super exchange dictated through the bridging oxygen the octahedral and tetrahedral sites have unpaired electrons aligned anti-parallel, so the Fe^{3+} spins will cancel each other out, and the Fe^{2+} electrons align to provide the net overall magnetic moment.[148]

| O^{2-} 32 per unit cell | Octahedral sites $Fe^{3+}/ Fe^{2+} O_h$ 16 per unit cell | Tetrahedral sites Fe^{3+} 8 per unit cell |
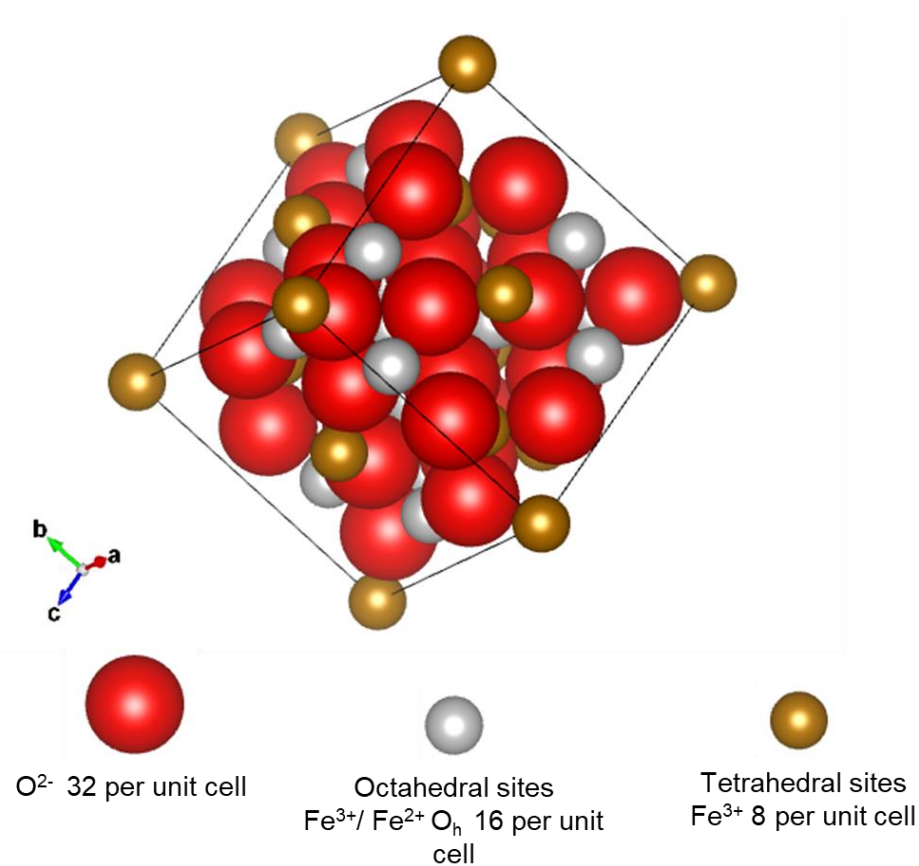
Figure 1.4.5 Unit cell structure of Magnetite showing the Octahedral (silver) and tetrahedral sites (bronze).

1.5   MAGNETIC HYPERTHERMIA

1.5.1   NANOSCALE HEATING OF MAGNETIC NANOPARTICLES

Although MNPs are known to respond to an AMF the ability of MNPs to generate heat within their vicinity has been debated. Rabin (2002) who using a theoretical model stated that there would be less than a 10^{-5} °C increase in temperature between the nanoparticles surface and the bulk media for a particle of 100 nm in diameter.[149] Keblinski (2006) also modelled the ability of MNP heat transfer and stated that there would be no heat rise in the surrounding environment of the particles, this has been disproven with experimental data which showed that MNPs were able to generate sufficient heat within their immediate vicinity.[150] This was tested by the coupling of fluorescent dyes to a polymer surrounding the MNP which reacts to a temperature of 35 °C, upon applying an AMF the bulk temperature was observed to be no hotter than 20 °C whilst the intensity of the fluorescent dye was observed to increase

upon exposure to an AMF.[151] As well as this MNPs were targeted towards the cell surface protein responsible for the influx of calcium ions into the cell. The application of an AMF resulted in an influx of calcium ions to the cell which indicates a minimum temperature of 42 °C had been reached.[152] These results along with others as well *in vitro, in vivo* and clinical data show the that MNPs are capable of sufficient heat transfer from their surface to the surrounding environment although this only occurs within the immediate vicinity of the MNP and these would be effective in a clinical environment.

1.5.2 MAGNETIC HYPERTHERMIA HEATING OF TUMOURS.

Magnetic hyperthermia treatment (MHT) utilises the magnetic properties of MNPs to generate heat to clinically relevant temperatures. Currently magnetic hyperthermia has only been approved for the treatment of glioblastoma brain tumours using MHT (MFH 300F NanoActivator®; MagForce Nanotechnologies AG, Berlin, Germany) this treatment is able to treat target areas of 20 cm.[153,154] NP heating is determined by the specific absorbance ratio (SAR) which is the heating power of the NPs per unit mass of particles (g).[155] This value is dependent on the suspension of the NPs and reported SAR values may not represent the actual heat transferred to a system. The SAR values can be used to determine the power of the MNPs, but this can also be affected by the physical and magnetic properties of MNPs. SAR values are also proportional to the frequency and the strength of the AMF which effects the power both linearly and quadratically respectively.[155] The intrinsic loss parameter (ILP) removes these factors and generates the value of the intrinsic power of the MNPs. This quantifies the amount of energy that can be transferred to a system by MNPs in an AMF, in particles relevant for clinical applications. Neéls relaxation is where the magnetic moment aligns with the magnetic field and Brownian motion is where the particle rotates as a whole and is responsible for generating heat.

Superparamagnetic iron oxide nanoparticles (SPIONs) are single domain so have a constant magnetic moment (Figure 1.5.1). Brownian motion occurs when there is a rotation of the whole particle (Figure 1.5.1) the generation of hyperthermia is through the shear stress in the surrounding material. This occurs when the anisotropy of the particle is high enough to overcome the inertia and the particle rotates.[156] Neéls relaxation occurs if the particle itself remains fixed, but the magnetic moment oscillates (Figure 1.5.1).[156] When there is zero magnetic field, SPIONs magnetic moment will be dictated by the crystalline anisotropy of the particle. When exposed to a magnetic field this can provide sufficient energy to cause the moment to realign with the field from the crystalline anisotropy directed moment.[155,156] The relaxation back to equilibrium causes the release of energy as thermal energy. In an alternating magnetic field, the time constant is shorter than the time taken for the NP

orientation to change, so the NP remains fixed whilst the magnetic moment flips between the parallel and anti-parallel orientation (Figure 1.5.1).[155–157]
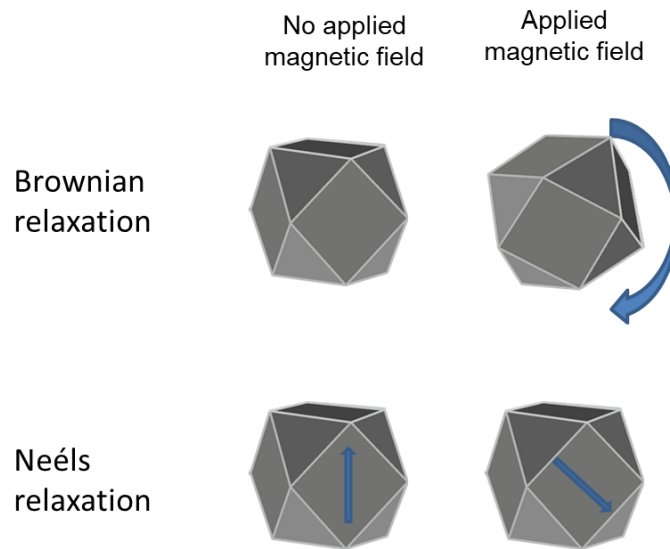
Figure 1.5.1 – Brownian and Neéls relaxation on MNPs when under an applied magnetic field.

Neéls relaxation time can be determined by the equation:

$$\tau_N = \frac{\tau_0}{2}\sqrt{\pi\frac{kT}{KV}e^{\frac{KV}{kT}}}$$

(1.1)

Equation 1.1. Neéls relaxation Where K is the anisotropy and V is the volume of the particle.

The Brownian relaxation time can be calculated as:

$$\tau_{B=\frac{3\eta V_H}{kT}}$$

(1.2)

Equation 1.2. Where V_H is the hydrodynamic volume and ή is the dynamic viscosity of the fluid.

Both Brownian motion and Neéls relaxation occur simultaneously during MHT so the relaxation time of the particles is determined by:

$$\frac{1}{\tau} = \frac{1}{\tau_N} + \frac{1}{\tau_B}$$

(1.3)

Equation 1.3 Particle relaxation time.

Both of these methods generate heat in MHT. MHT has been shown to be able to generate hyperthermia more efficiently than other methods of HT treatment including radio frequency ablation and continuous hyperthermic peritoneal perfusion.[158] MNPs offer the ability to deliver heat to a target site in a minimally invasive manner, act as drug carriers, are able to be directed to a specific site of interest by magnetic fields and so offer many advantages over traditional HT.

1.6   Synthesis of Magnetite Nanoparticles

There are a large number of synthesis methods for the preparation of magnetite NPs including co-precipitation, thermal decomposition, sol-gel and solvothermal. These methods follow a bottom-up approach with the atoms stacking up on top of each other producing crystal planes and further planes stacking on top of the ones already produced. The method of magnetite production can affect the size as well as the shape of the magnetite NP.[159,160]

1.6.1   Co-precipitation of Magnetite Nanoparticles

Co-precipitation of magnetite is one of the most widely used method for the synthesis of magnetite NPs.[161] This method is extensively used due to the ease of synthesis, no precursors complexes are required, reaction takes place at room temperature or slightly elevated temperatures (below 100 °C) and does not require the use of any harmful chemicals.[160,162] The co-precipitation method of synthesis also allows for easy scale up of the reaction to improve reaction yields and is an eco-friendly synthesis.[163] The reaction for magnetite coprecipitation is shown in equation 1.5.

$$2Fe^{3+} + Fe^{2+} \xrightarrow{Base} Fe_3O_4 \tag{1.5}$$

Equation 1.5 Co-precipitation reaction for the synthesis of magnetite.

The synthesis of magnetite by co-precipitation is performed by the addition of a base to dissolved ferrous and ferric iron salts in an aqueous solution in an inert atmosphere. There are two main pathways for co-precipitation of magnetite, the partial oxidation of ferrous hydroxide takes place using different oxidising agents at temperature this produces spherical NPs.[164] The second method requires the hydrolysis of Fe^{2+} and Fe^{3+} iron ions which form in the correct molar ratio of ferrous to ferric irons (2:1) for the inverse spinel structure of magnetite to form.[161]

The size and shape of iron oxides produced by the co-precipitation method can be affected by alterations in any of the parameters for its synthesis, these include the ratio of ferrous to ferric iron salts, the type of iron salt (chloride, sulphate and nitrate), the temperature of the reaction, the base, pH and whether there is a magnetic field present.[165] pH plays a major role in the formation of magnetite, basic conditions are critical for its formation as pHs ranging from 6 – 9 will produce εFe_2O_3 at a 2:1 molar ratio of ferric to ferrous ions, increasing the pH to 9 allows for the formation of magnetite to takes place.[166] This increase in pH also effects the size of the particles formed, with decreasing magnetite diameters observed when synthesised at pH 9.06, 10 and 11 NP crystallite size decreases from 11 – 10 nm down to 7 nm respectively. Decreasing pH was also observed to influence the size distribution of the particles, increasing pH results in a heterogenous distribution with average particle size

decreasing as pH increases with a bimodal distribution.[167] This is supported by other works that showed that increasing pH and ionic strength of the reaction medium decreases the particle size in the order of one magnitude from 15 – 2 nm, all this supports that controlling the reaction pH is important for control of particles size.[168]

The method of pH addition alters the formation of magnetite, most co-precipitation reactions occur with an abrupt change in reaction pH. This is because of the different formation routes in abrupt changes to slow addition methods, in the abrupt addition of iron to a basic solution of ferrihydrite the phase formed consists of mainly of Fe^{3+} and iron hydroxide carbonate plates formed of Fe^{2+}, as the reaction progressed these plates decrease and eventually disappear and the ferrihydrite phase grew producing NPs of $Fe_3O_4/\gamma-Fe_2O_3$. This indicates that the iron hydroxide carbonate plates were used to supply the growth of the ferrihydrite phases into MNPs.[169]

The ratio of iron salts to sodium hydroxide is an important factor that has a more dramatic effect on particle size than stirring rate, reaction time and temperature. A stoichiometric ratio of ion salt to hydroxide produced particles of a larger size than an excess concentration of either hydroxide or iron chloride salts.[170]

Although co-precipitation can produce size-controlled NPs using a green, quick, inexpensive, and easily scalable method, there are a few drawbacks to this method. This includes the tendency to agglomerate because of their small size and high surface energy and the production of heterogenous populations.[159]

1.6.2 Thermal Decomposition

Thermal decomposition synthesis of magnetite produces NPs from organometallic precursors, this produces particles with a narrow size distribution and high crystallinity. However, high temperatures are required during synthesis (300, 700 and 900 °C).[159,171] Synthesis of NPs through this method involve the initial formation of a precursor which is most often an iron oleate complex, this breaks down at 250 °C and this change in temperature is known to effect particle size with increasing reaction temperature resulting in increased particle size.[172] The addition of oleic acid surfactant can also effect formation by delaying growth of the particles, this occurs by competing with oxygen and iron for binding resulting in slow growth and produces particles that are larger in size, monodisperse and single crystalline.[159,172] Iron pentacarbonyl and iron oxyhydroxide are also similarly used for thermal decomposition synthesis.[172]

The synthesis of magnetite via thermal decomposition requires the reaction to take place in an inert atmosphere, this contradicts the idea that oxygen is required for magnetite

formation. Recent work has shown that during thermal decomposition a wüstite intermediate stage is formed and upon exposure to oxygen after the reaction the wüstite intermediate phase is oxidised into magnetite.[171,173]

The formation of a layer of non-magnetic material is observed in the synthesis of magnetite NP using thermal decomposition, this 'dead layer' or phase impurity is seen surrounding the MNPs and is approximately a thickness of a unit cell after synthesis. The formation of this dead layer can effect magnetic performance of the particle reducing the coercivity (H_c).[171,172] Although surface modification can improve the magnetic properties with molecular oxygen improving the magnetic diameter.[172]

Disadvantages of thermal decomposition is the requirement to use high temperatures, expensive precursor materials and toxic solvents used during synthesis. The synthesised NPs are only soluble in solvents which means that biological applications are limited.[174]

1.6.3 SOL-GEL SYNTHESIS OF MAGNETIC NANOPARTICLES

Sol-gel synthesis of MNPs is similar to thermal decomposition as it involves the use of precursor complexes and high temperatures, to synthesise MNPs the precursors which are mostly metal alkoxides undergo hydrolysis and condensation.[159,175] Although it does not require as expensive and highly toxic materials as thermal decomposition.[175] However, there is more difficulty in the production of magnetite as using iron (II) chloride as a precursor produces magnetite at 300 °C but at 350 °C hematite is produced. Ferric nitrate and ethylene glycol are used as precursors and synthesis is carried out at temperatures of 200 – 400 °C, this results in particles that can be size tuned by altering the reaction temperature, higher temperatures result in larger diameter particles.[175] The presence of oxygen can alter the iron oxide formed with γFe_2O_3 and αFe_2O_3.[175]

1.7 MAGNETIC PROPERTIES OF MAGNETITE

Magnetism is the response of a material to an external magnetic field.[176] The magnetic properties are determined by the location of the electron and structure of the material. Diamagnetic materials have no net magnetic moment in the absence of an applied field, this is due to all electrons being paired up. Whereas in paramagnetic materials, at least one electron is unpaired, and the atom has an overall net spin. In the absence of an external magnetic field the spins are randomly orientated leading to no magnetic moment. Whereas when an external magnetic field is applied the electrons dipoles realign with the magnetic field.[176]

Atomic structures that are ordered give rise to materials with bulk magnetism with long-range ordering and remnant magnetism are observed in the absence of an external field.

Ferromagnetic materials have all atomic magnetic moments aligned in parallel; this causes remnant magnetism when the external field is removed. Antiferromagnetic materials are made of paramagnetic atoms where the magnetic dipoles are aligned in antiparallel, thus of equal magnitude but opposite in direction, this results in a net magnetic moment that is zero. Ferrimagnetic materials have a difference in the magnitude of the atomic moments and they are aligned anti-parallel to each other so the moments do not cancel and an overall net magnetisation is observed (Figure 1.7.1).[148,177] Magnetite is a ferrimagnetic material, in magnetite the two iron ions have different oxidation states (Fe^{2+} and Fe^{3+}) resulting in magnetite having a faced centre cubic spinel structure (Figure 1.4.5) with 32 O^{2-}, 16 Fe^{3+} and 8 Fe^{2+}. The ferrous ions occupy half the octahedral sites, and the ferric ions occupy the remaining octahedral and tetrahedral sites. The two cations in the octahedral layer are close enough that this enables electrons to 'hop' between the overlapping d orbitals of the ions.[178]
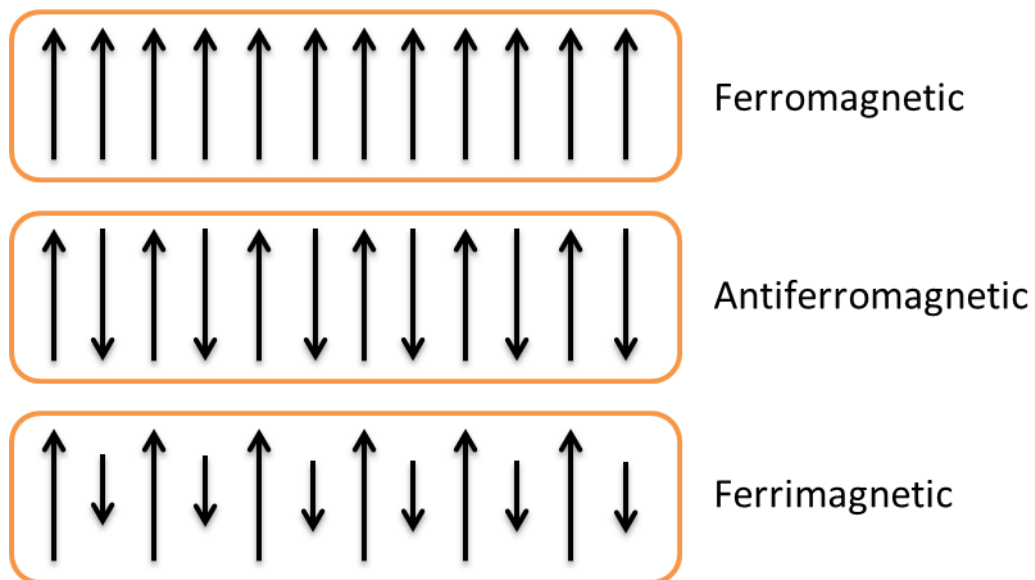
Figure 1.7.1 – Magnetic dipoles of different magnetic materials.

When magnetic particles reach a sufficient large size, domain walls start to form. This is due to the energy favourability of producing a domain wall. A domain wall is a region between different magnetic domains. Magnetic domains form to reduce the magnetostatic energy of the particle and this increases the magnetic anisotropy of the particle.[148,177] An example is in ferrimagnetic magnetite particles that are spherical in morphology, these have a maximum critical domain size of 100 nm.[148] Under the critical size (≤ 100 nm) this produces particles that are single domain. When particles reach a sufficiently small size, they will become superparamagnetic in nature (Figure 1.7.2). This means that they will only exhibit magnetic properties when an external magnetic field is applied.

When particles transition from single domain to multidomain particles an alteration in coercivity (Hc) can be observed. As particle size increases Hc increases until it meets the transition size and a decrease in coercivity is observed, this is due to the formation of multiple crystal domains.[179]
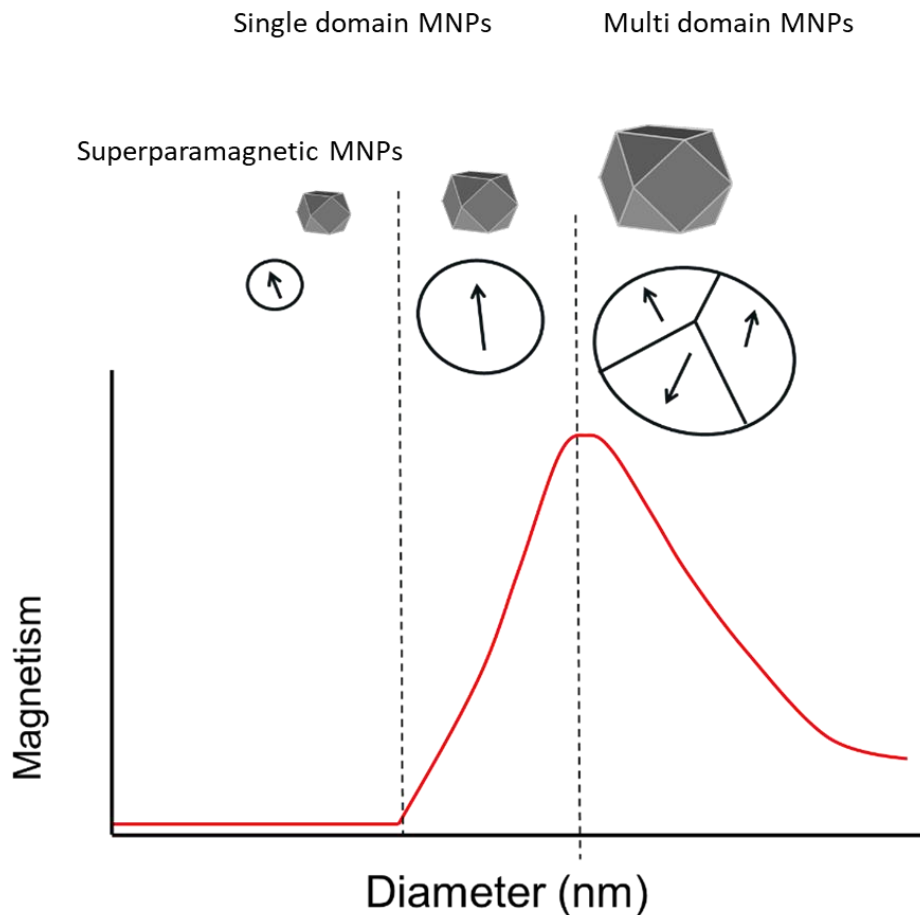
Figure 1.7.2 – The effect of nanoparticle size on coercivity (Hc) and the formation of domain walls.

1.8 BIOMIMICRY AND SYNTHESIS OF IRON OXIDES WITHIN LIPOSOMES AND POLYMERSOMES

Magnetosomes possess many advantages in the synthesis of MNPs due to the presence of multiple proteins to control nucleation, growth, shape, and iron transport within the membrane. This allows for the synthesis of biocompatible coated MNPs that have uniform shape and size to be synthesised in an easily scalable green way without the use of solvents and high temperatures. They also possess many advantages for use in biomedical applications due to improved magnetic characteristics that they have in comparison to synthetically produced MNPs.[180] These advantages are offset by some of the disadvantages that magnetosome synthesis has, namely the slow growth and low yields of MTB and inefficient production of MNPs even in improved fermentation reactions. The ability to mimic the benefits of magnetosomes (controlled nucleation and growth) in a system that can

produce high yields in much shorter times would prove highly beneficial for biomedical applications. Currently the biomimicry of magnetosomes has been investigated in both liposomes and polymersomes, both of which mimic the phospholipid bilayer present in magnetosomes.[106,109] The use of polymersomes as a magnetosome mimic have been investigated by *Bain et al* who showed that electroporation can be used to cause iron ion influx into the polymersome although the iron ions did not enter the lumen and nucleated within the polymer.[109]

Mimicry of the growth of iron oxides within a liposome membrane showed that precipitates formed within a liposome membrane differed in structure and morphology to those produce in aqueous solution, with the size and shape of the produce iron oxide being influenced by the vesicle characteristics.[106] Although this shows that it is possible to synthesise iron oxide NPs within a liposome there is less control of the shape and size of the produced particles compared to magnetosomes. This is due to the vast array of proteins present in magnetosomes to control synthesis that are not present in a simple liposome vesicle.

The addition of identified magnetosome proteins to the synthesis of magnetite NPs has shown to improve the synthesis of MNPs improving both the shape and size control, but isolation, purification and scale up make using these proteins as a standard addition to reactions a costly and time consuming process.[137,181] Although the use of these membrane bound proteins is not feasible, mimicry of the effects of these proteins is possible. Mms6 is has multiple carboxylic acid motifs within the C terminus which creates a negative surface charge for binding of both ferric and ferrous iron ions for nucleation of magnetite within the core of magnetosomes.[144] This mimicry of magnetosomes and subsequent synthesis of iron oxides within the vesicle show that it is possible to mimic the effect of magnetosomes, although NPs were not produced with the same level of control. As a single uniform magnetite nanoparticle was not produced within each vesicle but many smaller particles were synthesised indicating further control was required.

1.9   CONCLUSION AND PROJECT OUTLINE

In this chapter the effects of different levels of hyperthermia on cancerous cells and how this treatment effects both the physiological and cellular features of a tumour have been discussed. In particular it has been shown how HT can affect the mechanisms of DNA repair, most notably HR which is responsible for error free repair of double stranded breaks. Hyperthermia results in the degradation of the BRCA2 protein which mimics *BRCA2* mutated cancers. These cancers are susceptible to treatment with PARP inhibitors. PARP inhibitors show an advantage over traditional therapies including chemotherapy and radiotherapy as

they result in a better quality of life for the patient. A limitation of PARP inhibitors is that they can only be used in *BRCA2* mutated cancers. The use of mild HT may allow the use of PARP inhibitors in cancer that do not have *BRCA2* mutations, although there is very little evidence showing that hyperthermia has induced PARP sensitivity, and this requires further investigation. Current HT treatment methods can be invasive and difficult to treat deep tumours. The use of nanomedicine for the treatment of cancers has become an increasing area of interest, in particular MNPs as they can generate heat when exposed to an alternating magnetic field. Although the ability of MNPs to generate heat depends largely on its physical and chemical properties. Adjustment of these properties is vital for their use in biomedical applications and developing MNPs that are sufficiently small in size, so that they do not cause blockages within blood vessels but have sufficient ability to generate heat is vital. Magnetosomes have been observed to show superior magnetic properties over synthetically produced MNPs due to the presence of proteins which control the size, shape, and crystal properties of the MNP. Although magnetosomes show superior magnetic properties to MNPs, they do suffer from many caveats including their slow growth time and low yields as well as this they can also induce an immune response when used a nanomedicine. The use of artificial magnetosomes can overcome these caveats as these can be synthesised rapidly and inexpensively, physical, and chemical properties can be tuned to suit their intended application. However, it has yet to be shown that magnetite nanoparticles can be synthesised within the polymersome lumen with which shows sufficient magnetic properties for their use in magnetic hyperthermia.

Therefore, the work completed in this thesis focuses on the synthesis of MNPs that are suitable for biomedical applications with polydispersity and physicochemical properties suitable for high internalisation and low nanotoxicity achieved through alterations to certain physical characteristics. The identified MNPs that are suitable for biomedical applications will be introduced into breast cancer cell lines to observe how they interact with cells and the effect they have on them. Further investigation of the effect of HT on the sensitivity of non *BRCA2* mutated cells will be undertaken to observe if HT can induce PARP sensitivity and if MHT is able to induce similar effects for PARP therapy, so as to be suitable for the improved treatment of cancers. Artificial magnetosomes will developed to improve their physiochemical structures for the synthesis of MNPs within the lumen, with the addition of carboxylic acid groups to the membrane to improve the control over the synthesis of MNPs with the optimisation of iron ions.

1.10 Summary of Chapters

In this study and subsequent chapters, the ideas introduced in this chapter are developed with the aim of inducing MHT within cells that enables the treatment of cancers with PARP inhibitors, and that suitable artificial magnetosomes are capable of being synthesised and developed to mimic the biomineralization of magnetite in magnetosomes. In chapter 2 all the methods used throughout the study are outlined. Chapter 3 investigates how the alteration of physiochemical properties of MNPs can greatly affect their potential as a biomedicine by effecting the surface properties as well as their behaviour. Chapter 4 looks at how cells respond to treatment with the suitably identified MNPs and how they are distributed within the cell. Chapter 5 investigates how hyperthermia effects breast cancer cells in relation to BRCA2 and how they respond to combined therapies. Chapter 6 investigates how polymersomes can be used as an artificial magnetosome and their suitability to form MNPs within them. The effect alteration of electroporation conditions, different iron salts and concentrations and alteration of carboxylic acid content of the polymersome is studied to identify how this effects MNP formation and growth.

CHAPTER TWO: MATERIALS AND METHODS

2 MATERIALS AND METHODS

2.1 MATERIALS

2.1.1 CHEMICALS

Table 2.1.1 – List of chemicals used and their suppliers.

Chemical	Supplier
Acetone	Fisher Scientific
Amersham enhanced chemiluminescence (ECL) western blotting reagent	GE Life Sciences
Ammonium Hydroxide 28-30%	Sigma Aldrich
(3-Aminopropyl) tetraoxysilane (APTES)	Sigma Aldrich
Bovine serum albumin (BSA)	Sigma Aldrich
4',6-Diamidine-2'-phenylindole dihydrochloride	Vector Laboratories
Dimethyl sulphoxide (DMSO)	Fischer Scientific
Ethanol	VWR
Ethanol	Fisher Scientific
Ethylenediaminetetraacetic acid (EDTA)	Sigma Aldrich
Ferric sulphate	Sigma Aldrich
Ferrous Sulphate Heptahydrate	Sigma Aldrich
Hydrochloric acid	Sigma Aldrich
Industrial methylated spirit (IMS)	Fisher Scientific
Methanol	Fisher Scientific
Methylene Blue	Sigma Aldrich
Nitric Acid	Fisher Scientific
Phenylmethanesulfonyl fluoride (PMSF)	Sigma Aldrich
Phosphate Buffered Saline	Sigma Aldrich
Propidium iodide (PI)	Sigma Aldrich
Protease inhibitor	Sigma Aldrich
Rhodamine B Isothiocynate (RITC)	Sigma Aldrich
Sodium Hydroxide	Sigma Aldrich
Tetra Ethyl Orthosilicate	Sigma Aldrich
Tris Base	Fisher Scientific
Triton X-100	Sigma
Tween 20	Acros Organics
Universal x-ray developer	Champion Protochemistry
Universal x-ray fixer	Champion Protochemistry

2.1.2 CELL LINES

Table 2.1.2 – List of cell lines used along with a description and their supplier.

Cell Line	Supplier	Description
4T1	ATCC	Mouse mammary gland breast cancer
TS1	ATCC	Mouse B cell myeloma
MCF7	ATCC	Human epithelial mammary gland breast
MDA-MB-231	ATCC	Human epithelial mammary gland Breast

2.2 SYNTHESIS OF MAGNETITE NANOPARTICLES

2.2.1 CO-PRECIPITATION OF MAGNETITE NANOPARTICLES

Room temperature co-precipitation was used to prepare magnetite nanoparticles. Where the 1:2 ratio of mixture ferric and ferrous salts in alkali solution of NaOH to raise the pH under nitrogen gas supplied to degassed the solution to prevent oxidation of ferrous to ferric.[182] Fe_3O_4 nanoparticles were synthesized via alkaline precipitation. The reaction process for the formation of MNPs is:

$$Fe^{2+} + 2Fe^{3+} + 8OH^- \rightarrow Fe_3O_4 + 4H_2O \qquad 2.1$$
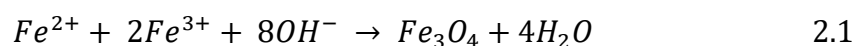
Magnetic nanoparticles were synthesised using a reverse room temperature co-precipitation (RRTCP) with Ferric sulphate ($Fe_2(SO_4)_3$) (Fe^{III}) and ferrous sulphate heptahydrate ($FeSO_4$) (Fe^{II}) were dissolved in 8 ml of nitrogen sparged Milli Q ultra-pure water to yield a concentration of 46.5765 mM for the ferric sulphate and 113.5616 mM for the ferrous sulphate hydrate. This dissolved iron salt solution was added at a rate of 50 µl/min into a 20 ml solution of 0.2 M sodium hydroxide. The reaction was kept under a nitrogen atmosphere for the duration and stirred at 400 rpm with a 1 cm stirrer bar.

The room temperature co-precipitation reaction (RTCP) was performed with Ferric sulphate ($Fe_2(SO_4)_3$) (Fe^{III}) and ferrous sulphate heptahydrate ($FeSO_4$) (Fe^{II}) were dissolved in 20 ml of nitrogen sparged Milli Q ultra-pure water to yield a concentration of 18.6306 mM for the ferric sulphate and 45.4246 mM for the ferrous sulphate hydrate. 8 ml of 0.5 M sodium hydroxide was added at a rate of 50 µl a minute into the 20 ml solution of iron to produce a final concentration of 0.2 M sodium hydroxide. The reaction was kept under a nitrogen atmosphere for the duration and stirred at 400 rpm with a 1 cm stirrer bar.

2.2.2 PURIFICATION OF MAGNETIC NANOPARTICLES

The magnetite particles were removed from the reaction vessel, magnetically separated, and washed with Milli Q ultrapure water until a neutral pH was obtained (determined by pH

indicator paper). The magnetic nanoparticles were dried using a vacuum oven (40 °C) and weighed.

2.3   SURFACE MODIFICATION OF MAGNETIC NANOPARTICLES

2.3.1   SILICA COATING OF MAGNETIC NANOPARTICLES

3.6 mg/ml of magnetic nanoparticles was dispersed in ethanol and sonicated for 15 minutes in a sonic bath to fully disperse the particles. 6 ml of MilliQ ultrapure water and 3 ml of ammonium hydroxide (28 – 30 %) were added to the magnetic nanoparticle solution at room temperature, followed by the addition of 0.4 ml of tetraethyl orthosilicate (TEOS) under stirring for 5 hours. The magnetic nanoparticle solution was magnetically collected, washed using ethanol and Milli Q ultrapure water, and dried via a vacuum oven (40 °C).

2.3.2   SURFACE FUNCTIONALISATION OF MAGNETIC NANOPARTICLES

10 mg of silica coated magnetic nanoparticles were added to 50 ml of toluene (99.9 %) and sonicated for 15 minutes so as to fully disperse the magnetic nanoparticles. 2 ml of ammonium hydroxide (28 – 30 %) and 200 µl of (3-Aminopropyl) tetraoxysilane (APTES) were added under constant stirring for 1 hour at room temperature. Magnetic nanoparticles were collected, washed initially in toluene then subsequently in MilliQ ultrapure water and dried in a vacuum oven (40 °C) and weighed.

2.3.3   RHODAMINE B ISOTHYOCYNATE DOPING OF SILICA MAGNETIC NANOPARTICLES

Rhodamine B isothiocyanate (RITC) was coupled with (3-Aminopropyl)triethoxysilane (APTES) to produce a fluorescently labelled silica RITC-APTES. 10 mg of RITC was reacted with 44 µL of APTES (molar ratio of RITC:APTES = 1:10) in 0.75 mL of ethanol for 2 days in under constant agitation in dark conditions. After coupling the RITC-APTES stock solution was kept at a constant temperature of 4 °C until use. 50 µl of the coupled RITC-APTES was added to the reaction described in section 2.3.2 after 10 minutes. And the reaction was left to stir for a further 50 minutes.

2.4   CHARACTERISATION OF MAGNETIC NANOPARTICLES

2.4.1   X-RAY DIFFRACTION (XRD)

X-ray powder diffraction use the constructive interference of monochromated X-rays within the crystal lattice which generates a peak in intensity. The crystal lattice spacing (*d*) is related to the to the scattering angle (θ) by Bragg's law.

$$n\lambda = 2d\sin\theta \qquad\qquad 2.2$$

Where n is the order and λ is the wavelength of the incident ray. The intensity peaks that are caused by constructive interference are produced at the 2θ angle, this can be converted to the *d* spacings and compared to known crystallography standards to determine the crystal species that has been produced.

Samples that were produced in coprecipitation reactions were dried under vacuum and loaded into a glass capillary tube before XRD was performed using a Bruker Advanced (Bruker Corporation Billerica, Massachusetts, USA) at the University of Sheffield Centre for Chemical Instrumentation and Analytical Services. X-rays were generated at 40 KeV with a Cu source (λ = 1.54056 Å), with x-ray intensities collected between 2θ = 20° and 80° at 0.05° intervals. The intensity of the diffraction rings was analysed using Graph Pad Prism.

2.4.1.1 XRD Size Analysis from Scherrer Equation

The crystalline size of nanoparticles was determined using the Debye-Scherrer equation to this allows determination of the sub-micron crystallite size.

$$D = \frac{k\lambda}{\beta cos\theta}$$ 2.3

Where D is the crystalline size, k is the shape factor (which here was the shape factor for a sphere = 0.89), λ is the wavelength of the electron source (1.54056 Å), β is the width of the diffraction peak at half the maximum intensity and θ is the Braggs angle.

2.4.2 TRANSMISSION ELECTRON MICROSCOPY (TEM)

TEM uses a focused beam of electrons (100 – 400 KeV) that travel through a high vacuum column and are focused upon a sample by an electromagnetic field and lenses. TEM relies on the incidence electrons being scattered from the image and a shadow image is detected on a phosphor screen or a charged coupled device. The density of the material being determined by the darkness of the image. Crystalline structures can be analysed by electron diffraction with positive interference leads to discreet electron spots that can be matched to the d spacing of the material.
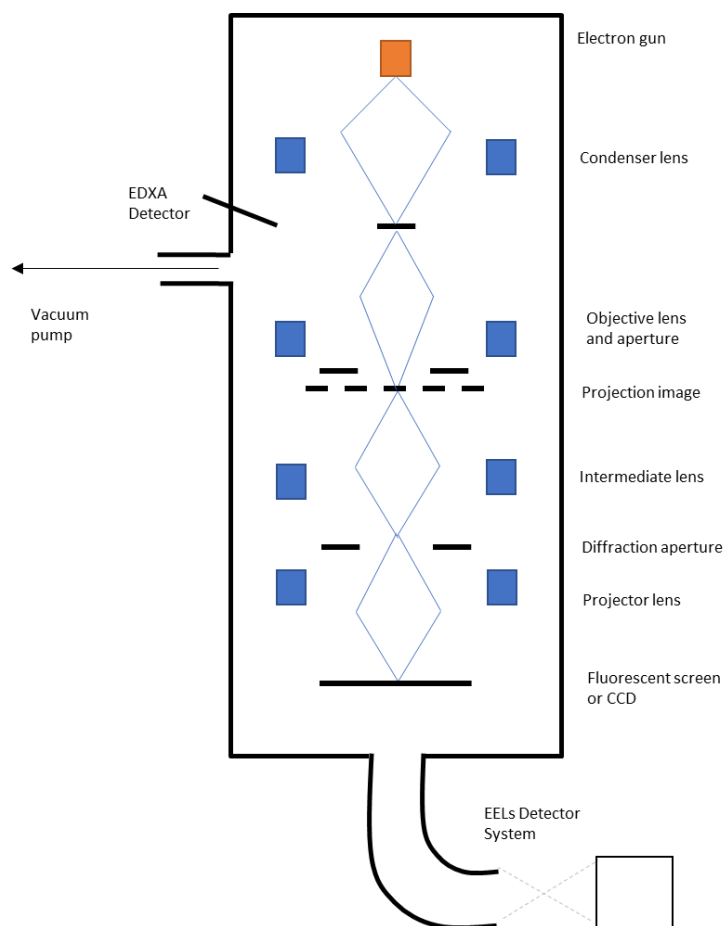
Figure 2.4.1 – Transmission Electron Microscopy schematic (adapted from figure 2.8 in Kelsall et al (2005)).[183]

TEM analysis was performed using a FEI Technai G2 Spirit TEM (FEI 14 company, Hillsboro, Oregon, USA) at the Electron Microscopy Unit, Department of Biomedical Science, University of Sheffield. 10 μl of magnetic nanoparticles was dispersed on to a carbon coated copper electron microscopy grid (S162-3, Agar). After 1 minute the excess liquid was blotted away with filter paper and the grid was dried using a vacuum line. Images were processed with Gatan Digital Micrograph software.

2.4.3.1 TEM Staining

Staining was performed on samples with low electron density that would not show great contrast under electron microscopy. The use of staining provides increased contrast due to the heavy metal salts present in the staining solution. Staining is performed on samples prepared as described in 2.3.2 and then the addition of the high contrast stain (2 % uranyl acetate or 0.075 % uranyl formate) is applied for 30 seconds, washed and dried using a vacuum line.

Grain Size Analysis

Sizing of TEM images was performed on ImageJ analysis software with the longest axis being measured. Approximately 100 samples were measured per sample and this data was fitted with a Gaussian distribution in GraphPad Prism.

2.4.3 FOURIER TRANSFORMED INFRARED SPECTROSCOPY (FTIR)

Fourier Transformed Infrared spectroscopy (FTIR) measures how much of infrared radiation is passed through a sample (transmittance) or absorbed by the sample (absorbance). The resulting information that is detected by the FTIR analyser represents the molecular profile of the sample which can be decoded (Fourier transformed) into a representative spectrum.
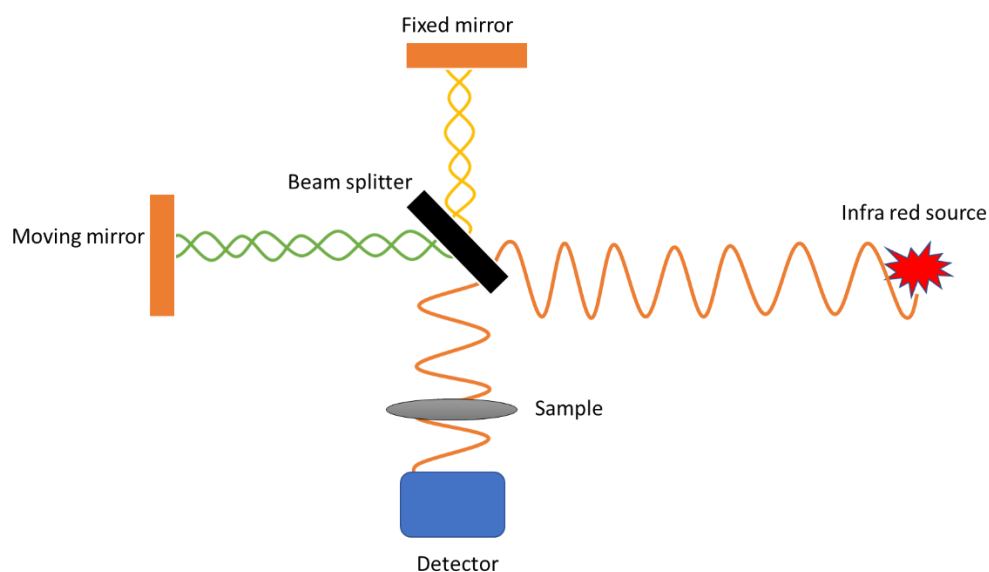
Figure 2.4.2 – Schematic showing FTIR detector.

150 mg Potassium bromide (KBr) was heated to a minimum of 100 ° C before being ground with 1 % w/w of the sample to be measured. Once ground the sample was pressed into a KBr disc under 9 tonnes of pressure. The absorbance of the sample was measured from 400 – 4000 cm^{-1} on a Spectrum II (Perkins Elmer, Waltham, Massachusetts, USA) Infrared Spectrometer.

2.4.4 HYDRODYNAMIC SIZING BY DYNAMIC LIGHT SCATTERING (DLS)

Hydrodynamic sizing measures the size of particles in suspension. A laser light source is shot through the sample and fluctuations in scattering intensity are measured. These fluctuations are due to Brownian motion of the particle in solution and the resultant information can be used to determine the hydrodynamic size by applying the scattering autocorrection. Large particles cause more scattering than small particles which is related to the diffusion co-efficient.

Measurements of MNPs were performed at 0.01 mg/ml using a Malvern Zetasizer NanoZS equipped with a 4mW He-Ne laser (λ = 633 nm) and an avalanche photodiode detector. Samples were sonicated and dispersed in disposable cuvettes and measured at 25 °C. The mean size number was measured over 3 consecutive runs comprising ten measurements per run. Polymersome samples were measured on 0.1 % w/v aqueous dispersions and the Stokes-Einstein equation was used to calculate the intensity average hydrodynamic size of the particles.

2.4.5 ZETA POTENTIAL

Zeta potential measures the electrokinetic energy in a colloid. Measurement of the electrical potential energy is measured at the interfacial double layer at the slipping plane.[184] Nanoparticles have a net surface charge and this attracts a concentration of ions of the opposite surface charge near to the nanoparticle surface.[185] Zeta potential measurements are made when a sample is placed between two electrodes and when a voltage is applied to the electrodes the particles will migrate towards the electrode that has an opposite charge to the slipping plane of the particle. The speed at which the particles move towards the electrode is measured by the scattering of light, this is proportional to the speed of the particles. The particles speed is measured across a range of voltages and the zeta potential is calculated from these readings.
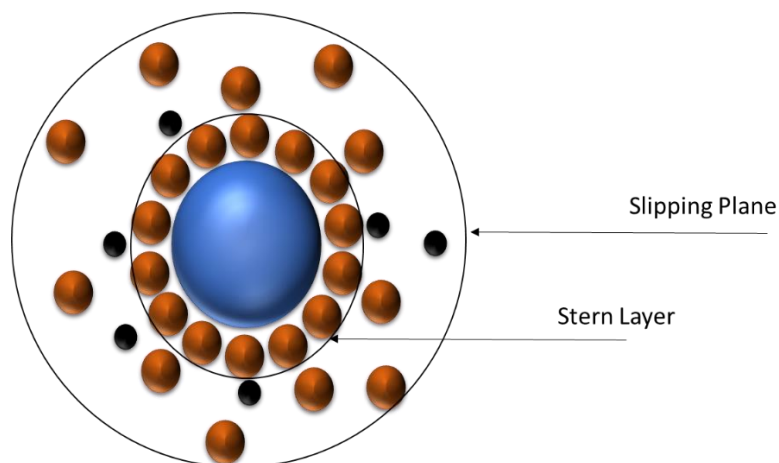
Figure 2.4.3 – Schematic of negatively charge particle and the stern layer and the slipping plane.

For MNP samples 0.01 mg/ml were suspended in water or cell culture medium and the zeta potential measured in a disposable cuvette using a Malvern Zetasizer NanoZS at 25 °C. 100 measurements were recorded for each sample.

Polymersome samples were measured in a 0.1 wt% solution dispersed in potassium chloride (1mM) and the pH was adjusted manually using 0.01, 0.05 or 0.1 M sodium hydroxide.

2.4.6 INDUCTIVELY COUPLED PLASMA OPTICAL EMISSION SPECTROSCOPY (ICP-OES)

Inductively coupled plasma optical emission spectroscopy is used to determine the mass of Fe in the samples. ICP-OES uses an argon plasma which contain argon ions. The argon plasma is produced when argon gas is passed through a plasma torch with electrons, these electrons are accelerated, and they collide with the argon atoms which results in further electrons being released and the formation of argon ions. Elements are introduced into the plasma in the form of atoms which become ionised. These atoms or ions within the plasma become excited which results in electrons jumping from a lower energy level to a higher level. When these excited atoms or ions undergo relaxation, they revert back to their original state and photons are emitted. These photons have a characteristic wavelength which matches to the respective element. These are compared to a standard so a calibration curve can be made and the concentration of the element in the samples determined.[186]

Samples were prepared by dissolving in aqua regia (4:1 molar ratio $HCl:HNO_3$) followed by dilution with MilliQ ultrapure water. Samples were analysed using a Spectro-Ciros-Vision ICP-OES spectrometer. All ICP-OES data was collected by Neil Bramall and Heather Grievson at the University of Sheffield.

2.4.7 VIBRATING SAMPLE MAGNETOMETRY (VSM)

Vibrating sample magnetometry (VSM) works on the principle of Faraday's Law of magnetic induction which states that a change in the magnetic environment of a coil of wire will result in the induction of a voltage within the coil.[187] VSM measures the magnetic moment of the entire sample. During measurement, the sample is constantly vibrated at a fixed frequency between two pickup coils within electromagnets (Figure 2.4.4). The changing magnetic flux that is detected in the pickup coils is proportional to the magnetic moment and causes induction of an AC voltage in the pickup coils. This voltage is fed to an amplifier which records the magnetic moment of the sample.[188]
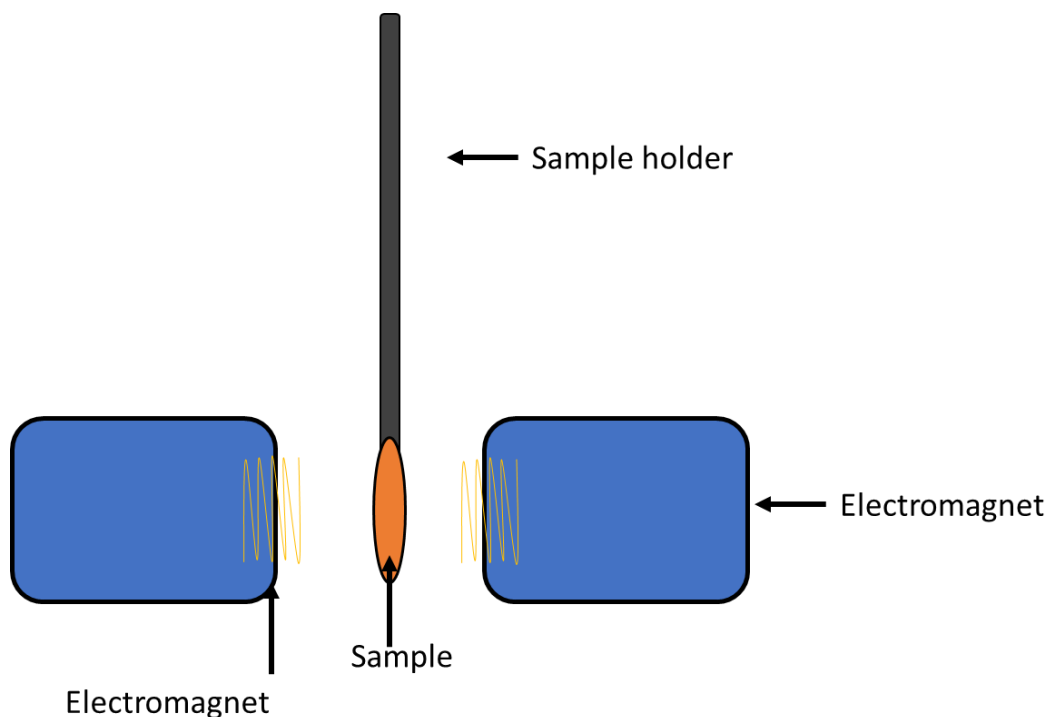
Figure 2.4.4 – Schematic representing vibrating sample magnetometry.

VSM was used to determine the magnetic properties of synthesised MNPs. NP samples were dried in a vacuum oven (1 hour at 40 °C) before being weighed into a gelatine capsule. The gelatine capsule was mounted on the end of a carbon fibre rod and loaded into the VSM (Quantum Design's MPMS 3) and the sample offset corrected. The samples were vibrated at 12.9 Hz and the magnetic response was measured over a range of -10 000 Oe to 10 000 Oe at 300 K. This produced a magnetic hysteresis loop at a constant temperature. From the hysteresis loop that was generated the coercivity (Hc), magnetic saturation (Ms) and remnant magnetisation (M_r) could be determined.

2.4.8 FLUORESCENT MEASUREMENT OF MNPS

A fluorometer measures the fluorescence that is emitted when electrons of a fluorescent object are excited by a specific wavelength of light and emit a lower energy (longer) wavelength of light. The sample is exposed to a light source with a filter to define a group of excitation wavelengths. The light emitted from the sample is passed through another filter which removes the excitation wavelengths but also allows emission wavelengths to pass through to a detector.

Samples were prepared at 1 mg/ml before sonication and dispersion in a quartz cuvette in MilliQ ultrapure water. Samples were exposed to an excitation wavelength of 400 – 580 nm and the emission recorded from 400 – 580 nm.

2.4.9 DETERMINATION OF HYPERTHERMIA PROPERTIES OF MNPS

When exposed to an alternating magnetic field magnetic materials generate heat, this heat is generated by hysteresis loss, Neéls relaxation or Brownian motion. The heating ability of MNPs is quantified by the SAR of the particles, this is the measure of the amount of power that the particles can deliver per unit mass and is an extrinsic parameter measured on the response of heating.[156] The calculation of SAR is shown in equation 2.4:

$$SAR = \left(\frac{C}{M^{fe}}\right)\left(\frac{\Delta T}{\Delta t}\right) \qquad 2.4$$

Where C is the specific heat capacity of the material. M^{fe} is the mass of magnetic material. ΔT is the change in temperature and Δt is the change in time. The intrinsic loss parameter (ILP) of the materials was determined by the equation:

$$ILP = \frac{SAR}{fH^2} \qquad 2.5$$

Were f is the frequency of the applied alternating magnetic field and H^2 is the field strength. Samples were prepared by weighing and dispersing in MilliQ ultrapure water into an Eppendorf. The sample was placed into the centre of the AMF field generator 9 turn coil (Magnetherm, Nanotherics) and the frequency of the alternating field was set at 173.7 kHz with the applied voltage of 15.1 V and the A200 capacitor. The change in temperature was measured by a fibreoptic probe inserted into the centre of the sample. The calculation of SAR and ILP were determined by the heating curve recorded.[155]

2.5 SYNTHESIS OF POLYMERSOMES

2.5.1 SYNTHESIS OF POLY(BUTADIENE-B-ETHYLENE OXIDE) PBD-PEO POLYMERSOMES

Poly(butadiene-b-ethylene oxide) (PBD-PEO) polymersomes were synthesised in an adapted procedure reported by the group.[109] Three different methods of polymer vesicle preparation were prepared by the dissolution of PBD_{2500}-PEO_{1300} (Polymer Source Inc, Canada) 10 mg were dissolved in 1 ml of chloroform. The polymer solution was dried in a vacuum oven (40 °C) to produce a thin film. The film was rehydrated in 1 ml of NaOH (10 mM) to encapsulate base within the polymersome.

2.5.1.1 Vesicle Size Control

2.5.1.2 Stirring

The PBD-PEO polymers were stirred at 200 rpm for 24 hours at room temperature.

2.5.1.3 Tip Sonication

Tip sonication produces good size control in comparison to stirring due to the high frequency and the controlled amplitude. Sonication (Vibracell, Sonics) is applied for 30 minutes at an amplitude of 75 % using a 3 mm narrow sonication tip.

2.5.1.4 Extrusion

Extrusion of the polymersomes is expected to produce the tightest size control of the particles due to the consistent pore size. Extrusion breaks down larger polymersomes which re-assemble into smaller polymersomes. The size of the formed polymersomes is dictated by the pore size of the filter is. Extruded samples were passed through a filter and a membrane with a 100 nm pore size that was pre-soaked in 10 mM NaOH. The polymer was passed through the membrane 15 times.

2.5.2 Synthesis of Poly(2-(methacryloyloxy)ethyl phosphorylcholine)-poly(2-hydroxypropyl methacrylate) / poly(ethylene glycol)-poly(2-hydroxypropyl methacrylate) (PEG-PHPMA/PMPC-PHPMA) Raft Polymersomes

All precursor material for the synthesis of RAFT polymersomes was prepared by Deborah Beattie in the Armes group (University of Sheffield).

2.5.3 Synthesis of [0.7 PEG$_{113}$ + 0.3 PMPC$_{28}$] − PHPMA$_{400}$ Diblock Copolymer nanoparticles via RAFT Aqueous Dispersion Polymerisation

A (0.7 PEG$_{113}$ + 0.3 PMPC$_{28}$)-PHPMA$_{400}$ vesicle at 20 % w/w solids was produced by poly(2-methacryloyloxyethylphosphorylcholine) (PMPC$_{28}$) macro-CTA (51.6 mg, 6.0 µmol), hydroxypropylmethacrylate (HPMA) monomer (1.1627 g, 8.1 mmol; target DP = 400) and poly(ethylene glycol) (PEG$_{113}$) macro-CTA (74.5 mg, 140 × µmol), 2-2,2'-Azobis[2-(2-imidazolin-2-yl)propane] dihydrochloride (VA-044) initiator (22 mg, 6.7 µmol; CTA/initiator molar ratio = 3) were dissolved in 5.1294 g of water and the pH was adjusted to 6.78 using NaOH (0.1 M). The solution was sealed and degassed under nitrogen for 30 minutes at room temperature before being immersed in an oil bath at 50 °C and stirred at 500 rpm for 4 hours. The reaction was quenched by exposure to air and cooled to room temperature.

2.5.4 Synthesis of [x PEG$_{113}$ + (1 - x) PMPC$_{28}$] − PHPMA$_{400}$ Diblock Copolymer nanoparticles via RAFT Aqueous Dispersion Polymerisation.

A (0.60 PEG$_{113}$ + 0.40 PMPC$_{28}$) − PHPMA$_{400}$ vesicles at 10 % w/w solid were synthesised by the PEG$_{112}$ macro-CTA (30.0 mg, 6.0 µmol), PMPC$_{28}$ macro-CTA (32.0 mg, 4.0 µmol), HPMA monomer (536 mg, 3.70 mmol) and VA-044 initiator (1.00 mg, 3.1 µmol, macro-CTA/VA-044 = 3.0) being dissolved in 5.392 g of deionised water in a glass vial. The pH of the solution was adjusted to 6.8 by the addition of 0.1 M NaOH. The subsequent solution was degassed via nitrogen sparging for 30 minutes in an ice bath prior to be being lace in a 50 °C oil bath for 4 hours under constant stirring. The polymerisation of was quenched by exposure to air whilst the solution cooled down to room temperature.

The different molar fractions of PEG in the polymersomes were produced by altering the molar fraction of the PEG$_{133}$ to either 1 or 0.8 producing [x PEG$_{113}$ + (1 - x) PMPC$_{28}$] − PHPMA$_{400}$ nanoparticles were prepared at 10% w/w.

2.5.5 SYNTHESIS OF PMPC 28 -PHPMA 450 DIBLOCK COPOLYMER VESICLES VIA RAFT AQUEOUS DISPERSION POLYMERISATION OF HPMA

PMPC$_{28}$ macro-CTA (80.0 mg, 9.3 μmol), HPMA monomer (600 mg, 4.2 mmol) and VA-044 initiator (1.0 mg, 3.1 μmol, macro-CTA/VA-044 = 3.0) were dissolved in 2.0418 g of deionised water in a glass vial to produce a 25 % w/w solution. The subsequent solution was degassed via nitrogen sparging for 30 minutes in an ice bath prior to be being lace in a 50 °C oil bath for 4 hours under constant stirring. The polymerisation of was quenched by exposure to air whilst the solution cooled down to room temperature.

2.5.6 BASE ENCAPSULATION INTO RAFT POLYMERSOMES

To encapsulate base within the polymersomes 2.5 ml of polymersomes was incubated within 2.5 ml of NaOH (10 mM) for 24 hours to allow for the NaOH to permeate the core of the polymersomes.

2.6 EXCESS BASE REMOVAL FROM POLYMERSOMES

The removal of excess base from the solution surrounding the polymersomes was vital to prevent the formation of iron oxides around the outer membrane of the polymersomes. Polymersomes were ran through a PD-10 (GE health care) size exclusion column replace the outside base with PBS buffer.

2.7 ELECTROPORATION OF POLYMERSOMES

Electroporation causes permeation of membranes by the application of a voltage across the membrane. Polymersomes were electroporate to allow transportation of the iron salts across the membrane to the basic core of the polymersomes. Electroporation was performed on a Biorad Multipulser at 1000 V with the average pulse length of 2.4 ms, 10 pulses were applied to each sample.

2.7.1 PBD-PEO POLYMERSOMES

PBD-PEO polymers with a basic core (0.5 ml, 1 mg/ml) were added to 0.5 ml of 10 mM or 200 mM of a 1:2 Fe(II): Fe(III) salt solution prior to electroporation. Post electroporation samples were left over night to allow for precipitation. Samples were centrifuged at 7000 rpm for 10 minutes (Genfuge 24D Microcentrifuge, Progen Scientific).

2.7.2 RAFT POLYMERSOMES

(0.7 PEG$_{113}$ + 0.3 PMPC$_{28}$)-PHPMA$_{400}$ Raft polymersomes with a basic core (200 μl) were added to concentrations of iron (1:1 v/v ratio) of 10 mM 1:2 Fe(II):Fe(III), 10 mM Fe(II), 50 mM Fe(II), 100 mM Fe(II) and 200 mM Fe(II). [xPEG$_{113}$ + (1 - x) PMPC$_{28}$] − PHPMA$_{400}$ and PMPC$_{28}$-PHPMA$_{450}$ polymersomes (200 μl) were added to concentrations of iron (1:1 v/v

ratio) of 10 mM Fe(II), 50 mM Fe(II), 100 mM Fe(II). The resulting solutions were electroporated in ice cooled cuvettes. Samples were allowed to precipitate overnight before clean-up.

2.8 EXCESS IRON REMOVAL FROM POLYMERSOMES

Excess iron that had not been incorporated into the polymersome were removed using a PD-10 size exclusion column. The polymersomes were transferred into a PBS buffer after removal of excess iron from the solution.

2.9 INVITRO CELL CULTURE EXPERIMENTS

2.9.1 CELL CULTURE REAGENTS

2.9.1.1 Foetal Calf Serum (FCS)

Virus, endotoxin, and mycoplasma free FCS was supplied by Seralab and stored at -20 °C prior to use.

2.9.1.2 Cell Culture Medium

All cells were cultured in Dulbecco's modified eagles' medium (DMEM) containing 4.5 g/L glucose with L-glutamine (MCF7 and MDA-MB-231). Cell culture medium (Lonza) was stored at 4 °C prior to use. Cell culture medium was supplemented with 10 % FCS serum and 1x non-essential amino acids (NEAA) (Lonza).

2.9.1.3 Trypsin and versine/EDTA

TrysinEDTA (0.5 g/l Trypsin, 0.2 g/L versine EDTA) was supplied by Lonza and stored at -20 °C prior to use.

2.9.1.4 Sterile Phosphate Buffered Saline

PBS was produced by dissolving 1 PBS tablet per 100 ml of double distilled H_2O (ddH_2O) and sterilised by autoclave and stored at room temperature.

2.9.1.5 Tris-buffered Saline (TBS)

TBS (10x) was produced by dissolving Tris Base (24.2 g, 200 mM) and NaCl (80 9, 1.4 M) in 900 ml of ddH_2O. pH was adjusted to 7.6 using HCl (0.5 M) and the final volume adjusted to 1 L using ddH_2O. A 1x solution of TBS was produced by diluting the 10x solution with ddH_2O. 10x and 1x solution was stored at room temperature.

2.9.1.6 1 M Tris pH 6.8 and 8.0

Tris (1 M) was produced by dissolving Tris Base (121.1 g) in 900 ml of ddH_2O. The pH was adjusted to 6.8 or 8.0 by the addition of HCl (5 M). The final volume was adjusted to 1 L with ddH_2O. Tris was stored at room temperature.

2.9.1.7 5x RIPA Lysis Buffer

5x RIPA lysis buffer (100 ml) was produced by the addition of 25 ml of Tris (1 M, pH 8.0, 250 mM) to 15 ml of NaCl (5 M, 750 mM), 5 ml of 10% SDS (0.5 %), 5 ml of NP-40 (5 %), 2,5 g of sodium deoxycholate (2.5 %) and ddH$_2$O. 5x RIPA lysis buffer was stored at room temperature.

2.9.1.8 5x SDS Sample Buffer

5x SDS sample buffer (100 ml) was produced by the addition of 25 ml of Tris (1 M, pH 6.8) (250 mM), 10 g of SDS (10 %), 50 ml of glycerol (50 %), 5 ml of β-mercaptoethanol (5 %), 20 mg of bromophenol blue (0.02 %) and ddH$_2$O. 5x SDS buffer was stored at room temperature,

2.9.1.9 Bolt Running Buffer

Bolt running buffer was prepared from 20x Bolt MES SDS running buffer. 50 ml of 20x bolt MES SDS buffer was added to 950 ml of ddH$_2$O to produce a 1x solution. 20x and 1x Bolt MES SDS running buffer was stored at room temperature.

2.9.1.10 Bolt Transfer Buffer

A 1x Bolt transfer buffer was produced from a 20x Bolt transfer buffer. 50 ml of 20x Bolt transfer buffer was added to 850 ml of ddH$_2$O, 100 ml of methanol and 1 ml of antioxidant. 1x and 20x Bolt transfer buffer were stored at room temperature.

2.9.1.11 Irradiation

Irradiation of cell was performed in a 3.7 L irradiator cannister and delivered directly to cells either in a 6 well plate or a 33 mm^3 dish using a CIB/IBL 437 CS-137 irradiator.

2.9.1.12 Antibodies

2.9.1.12.1 Primary antibodies

Table 2.9.1 – Primary antibodies used along with their host animal, manufacturer, and application. Where WB = western blot and IF = immunofluorescence.

Antibody	Host Animal	Manufacturer (CAT number)	Application (Dilution)
B-tubulin	Mouse	Sigma-Aldrich (T8328)	WB (1: 10 000)
BRCA2	Mouse	Milli Pore (OP95-100µg)	WB (1: 500)
γH2AX	Rabbit	Cell Signaling Technology	IF (1: 1000)
RAD51	Rabbit	Santa Cruz (H92, SC-8349)	IF (1:1000)

2.9.1.12.2 Secondary Antibodies

Table 2.9.2 – Secondary antibodies used along with their host animal, manufacturer, and application. Where WB = western blot and IF = immunofluorescence.

Antibody	Host Animal	Manufacturer (CAT number)	Application (Dilution)
Anti-mouse IgG horse radish peroxidase (HRP)	Horse	Cell signalling technology (7076)	WB (1immn:2000)
Anti-rabbit Alexa 594	Goat	Life Technologies (A11012)	IF (1:1000)
Anti-rabbit Alexa 488	Mouse	Life Technologies (A11017)	IF (1:1000)
Dapi	-	Sigma Aldrich (10236276001)	IF (1:1000)
Phalloidin 488	-	Santa Cruz (sc-363791)	IF (1:1000)

2.10 MAMMALIAN CELL CULTURE

2.10.1 CELL PASSAGING

Human and mouse breast cancer cell lines were incubated at 37 °C in a 5 % CO_2 Atmosphere in T25 or T75 flasks. Cells were passaged by the cell culture media being removed and the cells washed twice in 5 ml of PBS. 1 ml of pre warmed trypsin and incubation at 37 °C was used to dislodge cells from the bottom of the flask. Once cell was fully dislodged in trypsin EDTA 9 ml of pre warmed (37 °C) cell culture media was added to the flask to dilute the trypsin. Cells were then seeded to a new flask.

All experiments were performed when the confluency of the cells was at 60-80 % to ensure cells were in the logarithmic growth phase.

2.10.2 FREEZING CELLS

After resuspension in fresh media following trypsinisation cells were centrifuged in a 15 ml falcon tube (1200 rpm) for 3 minutes. The cell pellet was resuspended in cell culture media supplemented with 10 % DMSO at a cell density of $1x10^6$ cells per ml. Cells for freezing were deposited into 1 ml cryovials and stored at -80 °C over night in a Mr Frosty™ container (Thermo Fisher). Short term storage (<1 year) of cells were kept at -80 °C and long-term storage (> 1 year) of cells were stored in liquid nitrogen (-178 °C).

2.10.3 THAWING CELLS

Frozen cells were resuscitated by rapid thawing as 37 °C in a water bath. Cells were transferred from a cryovial to a 15 ml falcon and 9 ml of pre-warmed (37 °C) cell culture media was applied in a dropwise manner. Cells were centrifuged (1200 rpm) for 3 minutes before resuspension in cell culture media and seeding into a T25 cell culture flask.

2.10.4 TREATMENT OF CELLS WITH MNPS

Cells were seeded at the required density before being allowed to adhere for a minimum of 4 hours. cell culture media corresponding to the volume of MNP (1 mg/ml stock concentration) was removed. MNPs at the required concentration was added to each sample.

2.10.4.1 Incubator Hyperthermia Treatment (IHT)

Cells treated by hyperthermia in an incubator were incubated for 1, 2 and 4 hours at 42 °C in a 5 % CO_2 environment.

2.10.4.2 Magnetic Hyperthermia Treatment

Cells were plated and allowed to adhere to the plate for a minimum of 4 hours, at a concentration of cells and MNPs dependent of assay. Samples were exposed to an AMF generator (NanoTherics) with a frequency of 173.7 kHz, voltage of 15.1 V and an A200 capacitor or 520.9 KHz, a voltage of 29.4 and an A88 capacitor. Exposure occurred at room temperature.

2.10.4.3 Olaparib treatment Alone

Cells were plated and allowed to adhere to the plate for a minimum of 4 hours. Cells were treated with concentrations of Olaparib (0.5 µM to 5 µM) as appropriate.

2.10.4.4 Combined Olaparib and Incubator Hyperthermia Treatment (IHT)

Cells were plated and allowed to adhere to the plate for a minimum of 4 hours. Cells were treated with concentrations of Olaparib (0.5 µM to 5 µM) as appropriate and incubated at 42 °C for the appropriate time.

2.10.4.5 Combined Olaparib and Magnetic Hyperthermia (MHT)

Cells were treated with concentrations of Olaparib (0.5 µM to 5 µM) as appropriate, at a concentration of cells and MNPs dependent of assay. Samples were exposed to an AMF generator (NanoTherics) with a frequency 520.9 KHz, a voltage of 29.4 and an A88 capacitor at room temperature.

2.10.5 ALAMAR BLUE CELL VIABILITY ASSAY

Cell viability was measured using the Alamar blue cell viability assay that uses resazurin which is converted to resorufin (a red fluorescent indicator) in metabolically active cells to determine the amount of metabolically active cells.

Cells were seeded into a 96 well plate at a density of 5000 cells per well (200 µl) and allowed to adhere. Cells were treated with concentrations of MNP suspended in cell culture media and incubated for 24, 48, and 72 hours. After incubation 20 µl of Alamar blue reagent was added to each well (10 %) and the cells incubated at 37 °C for a minimum of 2 hours. The

intensity of the fluorescent signal was measured using a fluorescent plate reader at 560/590 nm (ex/em).

2.10.6 CLONOGENIC SURVIVAL ASSAY

Cells were seeded into a 6 well plate at a density of 500 cells per well in 2 ml of cell culture media and allowed to adhere. Cells were treated with concentrations of MNP and left to form colonies for 10 – 14 days, after which culture media was removed and the and stained with methylene blue in methanol (4 g/L). Colonies were defined using a threshold of 50 viable cells and counted. Plating efficiency was calculated as the number of colonies/number of cells plated. Survival fraction was calculated as the plating efficiency of condition/plating efficiency of the untreated control.

2.10.7 FLUORESCENT ACTIVATED CELL SORTING P.I LIVE DEAD SURVIVAL

2.10.7.1 Cell Harvesting

$2x10^5$ cells were seeded per well in a 6 well plate and left to adhere. Cells were treated with concentration of MNPs and incubated for 24 hours. Cells were harvested for FACS analysis by washing twice with PBS and dislodging cells with 0.2 ml of trypsin EDTA. Cells were collected with 1 ml of ice-cold PBS and pooled with media and PBS wash offs. In a 15 ml falcon tube and resuspended in 1 ml of PBS.

2.10.7.2 Propidium iodide (PI) live dead analysis.

Propidium iodide (PI) binds to DNA by intercalating between DNA bases with no sequence preference. PI cannot permeate the membrane of viable cells but when it binds to DNA the fluorescence increases 20-30-fold allowing for the identification of dead cells.

Cells were suspended in a 500 μl solution of PI (0.1 mg/ml) for 15 minutes at room temperature prior to analyse after which cell were kept on ice in dark conditions cells were analysed by flow cytometry on a FACS Calibur (BD Biosicences).

2.10.7.3 Analysis

Cells were plotted with the forwards scatter (FSC) against the side scatter (SSC) and viable cells were gated and cell debris discarded. The FL3 height (FL3-H) histogram were produced, and the population of PI positive cells were gated in the untreated control and applied to the treated samples with the percentage of cell population measured.

2.10.8 FLUORESCENT ACTIVATED CELL SORTING (FACS) CELL CYCLE ANALYSIS PROPRIDIUM IODIDE (PI) STAINING

2.10.8.1 Cell harvesting and PI staining.

$2x10^5$ cells were seeded per well in a 6 well plate and left to adhere. Cells were treated with concentration of MNPs and incubated for 24 hours. Cells were harvested for FACS analysis by washing twice with PBS and dislodging cells with 0.2 ml of trypsin EDTA. Cells were collected with 1 ml of ice-cold PBS and pooled with media and PBS wash offs. In a 15 ml falcon tube and resuspended in 1 ml of PBS before cells were pelleted and washed twice (2000 rpm, 2 minutes) in 1 ml of PBS and transferred to an Eppendorf. Cells were pelleted (2000 rpm, 5 minutes, 4 °C) and the PBS removed. Cells were dispersed in 1 ml of ice-cold methanol and stored at -20 °C for 1 hours, before pelleting (2000 rpm, 5 minutes, 4 °C) and removal of all methanol. The cells were rehydrated in PBS for 1 hour at room temperature and pelleted (2000 rpm, 5 minutes, 4 °C) to remove all the PBS. The pellet was resuspended in 500 µl of PI/RNAse A (18 µg/ml PI, 8 µg/ml RNAse A).in incubated for a minimum of 1.5 hours at 4 °C in dark conditions prior to FACS. Analysis was performed on Facs Calibur (BD Biosciences)

2.10.8.2 Analysis

Cell doublets were excluded by plotting FL3 (PI)-Area against FL3-Width and gating FL3-Width low cells (Figure 2.10.1). A FL3-height (FL3-H) histogram was produced from the gated population. G1 proportion of cells was defined by gating across the base of the first peak in FL3-H plot (~200 FL3-H), G2-M proportion of cells was defined by gating across the base of the second peak in FL3-H plot (~400 FL3-H). Sub G1 population was defined as all signal to the left of the first peak, S phase population was defined as all signal between first and second peaks.
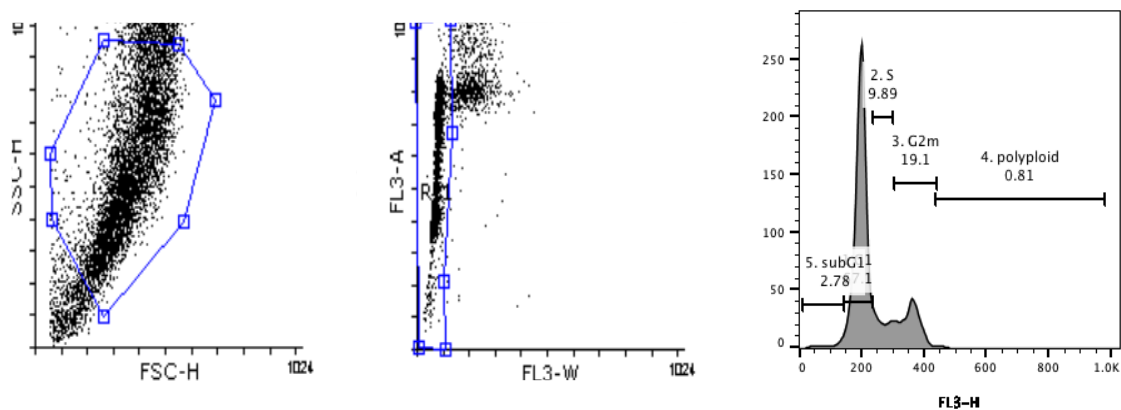
Figure 2.10.1 – FACS gating strategy outline. Cell debris was excluded in the graph on the top right. Cell doublets were excluded in the centre plot. Doublets are visible as the population stained with greater PI width. Single cell population was taken forward for cell cycle analysis. The right plot demonstrates the cell cycle profile with PI height was plotted as a histogram.

2.10.9 ICP-OES ANALYSIS OF INTRACELLULAR IRON.

The uptake of iron within cells was measured using ICP-OES. Cells were seeded at a density of $5x10^4$ cells per well in a 24 well plate. After treatment with appropriate concentrations of MNPs cells were left to incubate (37 °C) for appropriate times. After incubation cells were washed thoroughly five times with PBS to remove an MNPs that had not been internalised. 0.2 ml of trypsin EDTA was added to the cells and incubated at 37 °C until all cells had dislodged from the base of each well. After dislodging, 0.8 ml of PBS was added to each well and the cells transferred to a glass vial. 1 ml of aqua regia (HCl:Nitric acid 3:1 molar ratio) was added to the sample and diluted before being submitted to ICP-OES as described in 2.4.6. ICP-OES results were converted to the total amount of iron within each sample indicating the amount of internalised iron with the sample.

2.10.10   LIGHT MICROSCOPY

2.10.11   PRUSSIAN BLUE STAINING OF INTRACELLULAR IRON.

2.10.11.1   Cell Treatment

$5x10^4$ cells were seeded directly onto the surface of 70% IMS sterilised 22mm x 22mm microscope cover slips in a 24 well plate. Cells were allowed to adhere for 4 hours before the cells were treated with the appropriate concentrations of MNPs and incubated for 24 hours. After which cells media was removed and the cells washed three times with PBS before being fixed with ice cold acetone (200 µl) for 10 minutes at 4 °C. Cells were then treated with 200 µl of a 1:1 solution of potassium ferrocyanide (2%):HCl (1 M) an incubated for 37 °C for 1 hour. After washing cells were mounted onto a microscope slide by inverting onto Shandon immune mount (Thermofisher).

2.10.11.2   Analysis

Images of Prussian blue stained cells were taken using the 60x objective on a Nikon Eclipse. MNP iron internalisation was determined by the dark blue stain within detected within the membrane of cells. Images were processed with NIS elements viewer.

2.10.12   IMMUNOFLUORESCENCE
2.10.12.1   Slide preparation

2.10.12.1.1 Rhodamine B coupled MNP Internalisation Assessment

2.10.12.1.1.1   Cell treatment

5×10^4 cells were seeded directly onto the surface of 70 % IMS sterilised 22 mm x 22 mm microscope cover slips in a 24 well plate. Cells were allowed to adhere for 4 hours before cells were treated with the appropriate amount of RITC-MNPs and incubated for 24 hours. Cell's media was removed after 24 hours, and cells washed twice with 500 µl of TBS and fixed with 200 µl of 4 % paraformaldehyde for 15 minutes at room temperature. Cells were briefly washed once in TBS (200 µl) before washing three times (10 minutes) with 200 µl of TBS 0.2% Tween20 on a rocker at room temperature. 200 µl of TBS 1 % BSA, 0.25 % Triton X containing 1:1000 Phalloidin (Santa Cruz) and Dapi 1 % BSA, 0.25 % Triton X containing 1:1000 for 1 hour in dark conditions. Unbound secondary antibody was removed by washing in 200 µl of TBS 0.2 % Tween 20 for 10 minutes, then twice in 200 µl of TBS (10 minutes). After washing cells were mounted onto a microscope slide by inverting onto Shandon immune mount (Thermofisher).

2.10.12.1.2 γH2AX repair assessment

2.10.12.2   Cell treatment

5×10^4 cells were seeded directly onto the surface of 70 % IMS sterilised 22 mm x 22 mm microscope cover slips in a 24 well plate. Cells were allowed to adhere for 4 hours before the cells were treated with the appropriate amount of MNPs and incubated for 24 hours. Cell's media was removed after 24 hours, and the cells washed a twice with 500 µl of TBS and fixed with 200 µl of 4 % paraformaldehyde for 15 minutes at room temperature. Cells were briefly washed once in TBS (200 µl) before washing three times (10 minutes) with 200 µl of TBS 0.2% Tween20 on a rocker at room temperature. Cells were blocked with 200 µl of TBS 3% BSA for 1 hour at room temperature. Cells were then washed twice (10 minutes) with 200 µl of TBS 0.2 % Tween at room temperature under constant agitation. After washing 100 µl of TBS 0.5 % BSA, 0.25 % Triton X containing a 1:500 dilution of γH2AX (Cell Signalling) primary antibody was added to each well. Cells were incubated with primary antibody overnight at 4 °C in a humidifying chamber. Wells were washed three times (10 minutes) to remove unbound

primary antibody with 200 µl of TBS 0.2 % Tween 20 under constant agitation. 100 µl of TBS 0.5% BSA, 0.25 % Triton X containing 1:500 dilution of Anti-rabbit Alexa 594 (Life Technologies) secondary antibody. Cells were incubated in the secondary antibody in the dark for 1 hours at room temperature. Unbound secondary antibody was removed by washing in 200 µl of TBS 0.2 % Tween 20 for 10 minutes, then twice in 200 µl of TBS (10 minutes). Cells were mounted were mounted onto a microscope slide using Vectorshield hard set mountant 4',6-diamidine-2'-phenylindole dihydrochloride (DAPI) (Vector Laboratories) and the edges of the cover slip sealed with nail varnish. Coverslips were dried for 2 hours at room temperature in the dark before storing at 4 °C prior to use.

2.10.13 RAD51 Foci Formation

2×10^5 cells were seeded directly onto the surface of 70 % IMS sterilised 22 mm x 22 mm microscope cover slips in a 33 mm^3 dishes. Cells were allowed to adhere for 4 hours before the cells were treated with either IR or incubator hyperthermia treatment for 2 hours prior (42 °C) to IR and 4 hours post IR or a sham treatment of the Cells being placed in the IR canister but not irradiated. Media was removed after 4 hours, and the cells washed a twice with 500 µl of TBS and fixed with 500 µl of 4 % paraformaldehyde for 15 minutes at room temperature. Cells were briefly washed once in TBS (200 µl) before washing three times (10 minutes) with 500 µl of TBS 0.2% Tween20 on a rocker at room temperature. Cells were blocked with 500 µl of TBS 3% BSA for 1 hour at room temperature. Cells were then washed twice (10 minutes) with 200 µl of TBS 0.2 % Tween at room temperature under constant agitation. After washing coverslips were inverted onto 100 µl of TBS 0.5 % BSA, 0.25 % Triton X containing a 1:500 dilution of γH2AX (Cell Signalling) primary antibody. Cells were incubated with primary antibody overnight at 4 °C in a humidifying chamber. Coverslips were everted. Wells were washed three times (10 minutes) to remove unbound primary antibody with 500 µl of TBS 0.2 % Tween 20 under constant agitation. Coverslips were then inverted onto 100 µl of TBS 0.5% BSA, 0.25 % Triton X containing 1:500 dilution of Anti-rabbit Alexa 594 (Life Technologies) secondary antibody. Cells were incubated in the secondary antibody in the dark for 1 hours at room temperature. Coverslips were everted and unbound secondary antibody was removed by washing in 500 µl of TBS 0.2 % Tween 20 for 10 minutes, then twice in 500 µl of TBS (10 minutes). Cells were mounted were mounted onto a microscope slide using Vectorshield hard set mountant 4',6-diamidine-2'-phenylindole dihydrochloride (DAPI) (Vector Laboratories) and the edges of the cover slip sealed with nail varnish. Coverslips were dried for 2 hours at room temperature in the dark before storing at 4 °C prior to use.

2.10.14   ANALYSIS

2.10.14.1   Rhodamine B coupled MNP Internalisation Assessment

Images of cells were taken to identify MNP internalisation using a 60x objective Nikon TE200 Inverted Fluorescence and Phase Contrast Microscope. Fluorescent images from separate channels were visualised with NIS. Fluorescent images from separate channels were merged using ImageJ.

2.10.14.2   γH2ax repair assessment

Images for the assessment of cells γH2AX repair were taken with the 60x and 100x objective on a Nikon TE200 Inverted Fluorescence and Phase Contrast Microscope and processed with NIS elements viewer pro. Fluorescent images of different channels were merged using ImageJ. A minimum of 100 cells were counted for condition, counting the number of γH2ax foci per nucleus. Mean foci per cell (nucleus) was then calculated.

2.10.14.3   Rad51 Foci Formation

Images for the assessment of cells RAD51 foci formation were taken with the 60x and 100x objective on a Nikon TE200 Inverted Fluorescence and Phase Contrast Microscope and processed with NIS elements viewer pro. Fluorescent images of different channels were merged using ImageJ. A minimum of 50 cells were counted for condition, counting the number of RAD51 foci per nucleus. Mean foci per cell (nucleus) was then calculated.

2.10.15   INCUBATOR HYPERTHERMIA

Cells were seeded at a density of $2x10^6$ cells per well into a 6 well plate and allowed to adhere for a minimum of 4 hours. cells were incubated in a 42 °C incubator for 1, 2 or 4 hours.

2.11   WESTERN BLOTTING

2.11.1   LYSATE PREPARATION FOR WESTERN BLOT

2.11.1.1 Cell Pre-treatment

Cells were treated with incubator hyperthermia as described in section or by magnetic hyperthermia as described in section.

2.11.1.2 Lysate preparation

Media was removed and the cells were washed twice with 500 µl of PBS and the cells were dislodged with 500 µl of trypsin EDTA. The trypsinised cells were then diluted in 2 ml of cell culture media and collected in to a 15 ml falcon tube. The cells were pelleted at 12000 rom before resuspension in 1 ml of ice-cold PBS and transferred to an Eppendorf (1.5 ml) on ice. Cells were pelleted (1200 rpm) before 100 µl of 1x RIPA buffer (200 µl of 5x RIPA lysis buffer, 10 µl of PMSF (100 mM), 10 µl of SIGMAFAST protease inhibitor). Pelleted was resuspended in the lysis buffer by vortexing every 10 minutes for 30 minutes on ice. Pellets were passed

through a 25 G needle 10 times and centrifuged for 10 minutes at 13400 rpm at 4 °C and the supernatant transferred to a fresh 1.5 ml Eppendorf for western blot analysis.

2.11.1.3 Protein Quantification

Protein concentration in the lysate was performed by using a Bradford assay in a 1.5 ml Eppendorf tube. A standard curve of protein concentrations was made using a BSA of known concentration (Table 2.11.1).

Table 2.11.1 – Production of BSA protein standard curve.

Total Protein (µg)	0.1 mg/ml BSA (µl)	ddH$_2$O (µl)	Biorad Protein Assay Dye Reagent Concentration (µl)
0	0	800	200
1	10	790	200
5	50	750	200
10	100	700	200
15	150	650	200
20	200	600	200

1 µl of each lysate was added to 799 µl of ddH$_2$O and 200 µl of Biorad Protein Assay dye reagent concentrate was added to the lysate and BSA in a 1.5 ml Eppendorf. Lysate and standard were incubated for a minimum of 5 minutes before the optical density (OD) at 55 nm wavelength was measured (Multiskan FC Thermo Scientific). BSA standards ODs were plotted to produce a protein concentration against OD. This Standard curve allowed the quantification of the protein concentration from the OD reading. This allowed quantification of protein added to each lane.

2.11.1.4 Bolt Bis Tris gels

15 µl of lysate sample was loaded per lane. With 45 µg of protein loaded per lane. 10 µl of Hi-Mark high molecular weight protein standard was run in parallel to the sample. Proteins were separated by size for 1.5 hours at 150 Vs in 1x Bolt running buffer.

2.11.1.5 Protein Transfer

Proteins were transferred from the gels to a Protan nitrocellulose membrane transfer membrane. This was achieved by running at 30 V on ice at 4 °C overnight and then at 100 V for 1 hour on ice in a Criterion Blotter (BioRad) in 1x Bolt MES transfer buffer.

2.11.1.6 Membrane Blocking and Probing

Membranes were block in 5% Milk (Marvel) TBS for 1 hour at room temperature. Probing of membranes with primary antibodies in blocking solution was performed overnight at 4 °C on a rocker. Following incubation membranes were washed three times in TBS Tween 20 (0.05%) (10 minutes). Membranes were incubated with secondary antibodies with HRP

labelling diluted in blocking solution. Membranes were washed three times in TBS-Tween 20 (0.05 %) (10 minutes).

2.11.1.7 Enhanced Chemiluminescence (ECL)

ECL detection reagents 1 and 2 (2 ml) (ECL western blotting detection reagent kit, Amersham) were mixed and applied to the membrane for 1 minute at room temperature, before being removed. Membranes were then exposed to X-ray film in a dark room and the chemiluminescent signal was developed (RG universal X-ray developer, RG universal X-ray fixer).

2.12 THERMAL IMAGING OF SAMPLES IN AN ALTERNATING MAGNETIC FIELD

Thermal imaging was observed in samples exposed to an alternating magnetic field at a frequency of 520.9 KHz, Voltage of 29.4 V and a B22 capacitor. Thermal images were obtained with a CAT S62 (Bullitt Group) thermal camera with image processing on FLIR image analysis software.

CHAPTER THREE: SYNTHESIS AND CHARACTERISATION OF MAGNETITE NANOPARTICLES

3 SYNTHESIS AND CHARACTERISATION OF MAGNETITE NANOPARTICLES

3.1 INTRODUCTION

MNPs have a wide range of potential uses in the area of biomedicines such as: delivery vectors,[115,189] diagnostic tools[148] and as a treatment via hyperthermia.[6] The physiological properties of MNPs have an important effect on how they interact at a cellular level, these effects can improve or hinder the performance of the particles.

One of the most important aspects for MNP biomedicines is particle size, as this not only effects their magnetic properties and how they interact with other particles but also how they are distributed and cleared within the body and their interaction with cells.[190] This highlights the importance of size control during the synthesis of MNPs as they require sufficient SAR to induce hyperthermia at feasible concentrations that do not induce high levels of nanotoxicity. Particles that are below a threshold size 20 nm have superparamagnetic properties whereas particles that are too large (>100 nm) can reduce their magnetic properties when multi domains form. Therefore, the synthesis of particles within a 'goldilocks' size range (10 – 100 nm) is essential, particles must be sufficient in size to generate high heating power but not so large that they aggregate heavily.[191]

As well as size, surface properties affect MNP interactions in the body with charge greatly affecting uptake and also the toxicity of MNPs. Positively charged NPs have a marked increase in uptake compared to negatively charged particles although they do show reduced viability and effect the mitochondrial functions of cells, but this is a trade-off that is beneficial for targeted therapies. The use of a protective coating allows for control of the surface and particle size as well as the surface charge which help to improve uptake and biocompatibility.[192,193] It also allows for functionalisation for targeting specific tumour cells as has been previously shown, as well as improve stability in aqueous solutions.[194]

Magnetite shows great potential as a biomedical MNP due to the ability to be synthesised in a small size range of less than 50 nm which are known to internalise more readily that particles that are large than this it also has an active surface that has the ability to be functionalised and has comparatively low toxicity compared to other MNPs.[195,196] Magnetite is also an ideal material for hyperthermia treatment due to its intrinsic magnetic properties. Here the synthesis of MNPs and analysis of their physical and magnetic properties are determined and discussed to understand their suitability for hyperthermia treatment both *in vitro* and *in vivo*.

In this chapter the physical, chemical, and magnetic properties of the synthesised and functionalised MNPs are analysed as well as their surface properties, to determine how this effects their suitability as a nanomedicine.

The aims of this chapter are:

1. To confirm that iron oxide magnetite has been synthesised.

2. To determine the size and size distribution of the particles and the presence of surface coatings as well as the thickness of the coatings.

3. To determine the physiochemical properties of the synthesised MNPs and how the presence of surface coating and functionalisation alters their properties.

4. Measurement of the magnetic properties of the synthesised MNPs and determine how the presence of coatings affect this.

3.2   SYNTHESIS AND COATING OF MNPS

Co-precipitation of magnetite NPs was produced from a mixture of ferrous and ferric iron salts iron sulphate hydrate ($Fe_2(SO_4)_3$) and iron sulphate heptahydrate ($FeSO_4$ xH_2O). This was performed at a 0.5 M concentration; this was chosen as it matched closely to the molar ration of ferrous to ferric ions in magnetite (0.6 M) the choice of the 0.5 M is due to this ratio producing a more homogenous size distribution during synthesis.

For co-precipitation to take place the iron salts must be exposed to basic conditions for nucleation and synthesis to take place. There are many factors that can affect the formation of MNPs with the pH as well as the rate of pH change and temperature. Here a room temperature co-precipitation reaction (RRTCP) was performed with the addition of NaOH base to the mixture valence iron solution under stirring and an inert atmosphere as the presence of oxygen during synthesis results in the formation of maghemite which has poorer magnetic properties than magnetite. To produce MNPs of a different size a reverse room temperature co-precipitation reaction was performed, with the addition of a mixed iron solution to a NaOH basic solution. The addition of the mixed valence iron solution to the basic solution results in a much more abrupt pH change in the RRTCP reaction.

The difference in synthesis methods produced particles which had a markedly different visible size and morphology with the RRTCP producing particles with a range of 11-34 nm whilst the RTCP particles showed a much larger size distribution of 10-65 nm. The RTCP particles produce NPs with a larger diameter as well as reduced consistency in morphology with more obvious amorphous iron on the NP surface. Along with spherical NPs there was a high concentration of needle like iron structure present within the sample (Figure 3.4.2). These needle structures were not observed in the RRTCP as well as a much more defined

morphology. Both the RTCP and the RRTCP MNPs were seen to agglomerate in TEM but this is consistent with the particles synthesised by this method. Agglomeration of MNPs after dispersal was seen to happen at a much faster rate in the RTCP NPs as these dropped out of solution at a rapid rate within a few minutes of dispersal whereas the RRTCP stayed in solution for a much longer period of time.
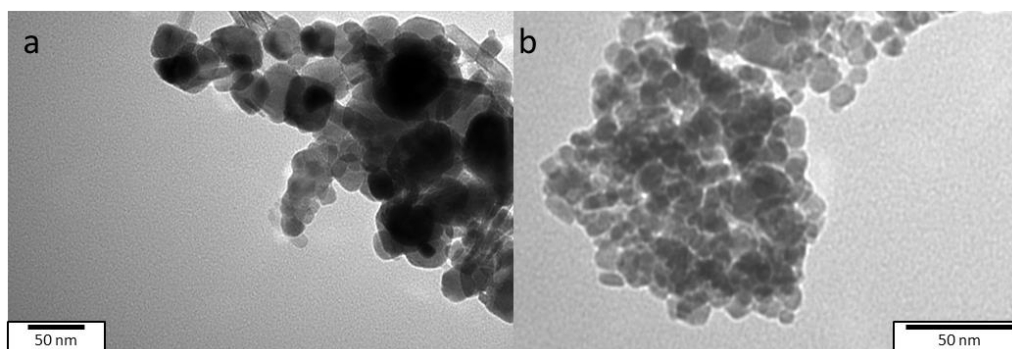
Figure 3.2.1 – TEM of synthesised magnetic nanoparticles. a) Room temperature co-precipitation. b) Reverse room temperature co-precipitation nanoparticles.

By just altering how the iron solution is exposed to base the size of the MNPs has been significantly altered. The slow addition of base in the RTCP caused a much larger diameter of MNP to be produced with the particle size increasing in this reaction even though the end pH would remain the same. Whereas in the RRTCP the addition of the iron solution to a strongly basic solution produced MNPs of a much smaller diameter.

The synthesised MNPs were further modified with a silica (Figure 3.2.2) coating to help to improve the physical characteristics to aid in biocompatibility and distribution. NH_2 Functionalised silica was chosen as this allows further surface modification with drug or targeting moieties is that is required. The presence of the NH_2 groups should also produce a positive surface charge which should improve the uptake on the MNPs within cancers cells as has been readily reported. [192] This was further modified in the RRTCP particles with a RITC-APTES coating to enable fluorescent imaging of the cell as well as further analysis of biodistribution using fluorescent techniques. This was not performed in the RTCP particles as these showed characteristics that were decided to not take forward into cellular experiments.
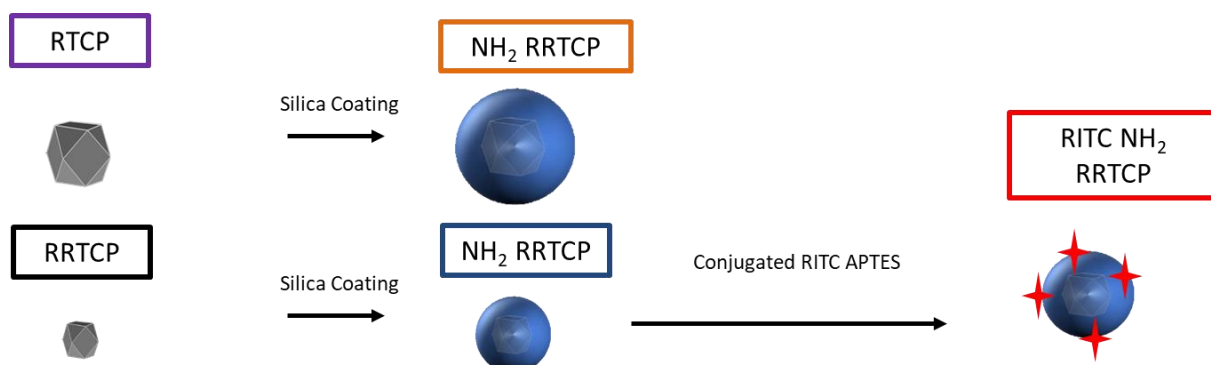
Figure 3.2.2 – Schematic showing the surface modification of MNPs after synthesis with amine functionalised silica and the fluorescent tagging of the RRTCP MNPs with rhodamine B isothiocyanate.

The fluorescent tagging of the NH_2 RRTCP with RITC was accomplished via conjugation to the amine functional groups present on APTES prior to the coating of the preprepared TEOS coated MNPs.
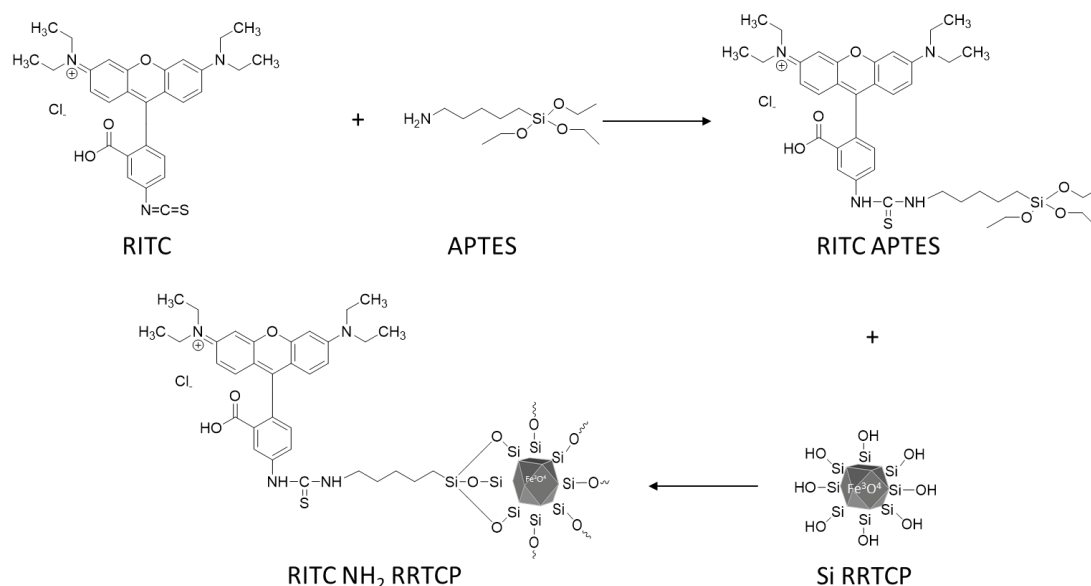
Figure 3.2.3 - Conjugation of RITC to APTES prior to the coating of Si RRTCP with RITC NH_2

3.3   XRD ANALYSIS OF SYNTHESISED MNPS

The crystal structure of the MNPs was determined via XRD to determine what iron oxide has been produced during synthesis. In all the samples that were tested there were six distinct diffraction peaks present in the XRD spectra indicating that the same Iron oxide had been produced in the two synthesis and that further modification did not alter the RRTCP MNP. These spectra produced showed diffraction at 2θ = 30.1°, 35.5°, 43.2°, 53.7°, 57.2° and 62.7°, corresponding to the (220), (311), (400), (422), (511) and (440) planes of magnetite. Presence of these planes indicate that magnetite was formed, but there are small peaks present at (31.8), (60.1), (71.3) and (74.2) these first two peaks correspond to maghemite whereas the third matches closely to the (620) peak of magnetite and the final peak of 430 peak of

heametite. This also showed that in both reaction mechanisms magnetite was produced and that altering this did not affect the iron oxide that was produced. The XRDs of the of the synthesised MNPs showed prominent peaks in the XRD show the highly crystalline nature of the MNPs. The RRTCP and the subsequent surface modified RRTCP MNPs had peaks with a broad diameter than the RTCP peaks which matched the result seen from the TEM imaging, as a broader peak indicates a smaller diameter of MNP. This matches the observed size difference in TEM imaging as RTCP images were seen to have a larger diameter than the RRTCP. Although the coating of the MNPs did not indicate there was no alteration of the MNP during the surface coating and modification. Although there was no alteration in the peak position the NH_2 SiRRTCP (Figure 3.3.1 c) MNPs showed a higher level of noise compared with the other samples, this may be as a result of the low sample volume that used for XRD. This is due to the yield reduction during the surface modification sets. As the MNPs were modified there was only a 10 % yield of sample collected at each stage. This resulted in the final NH_2 SiRRTCP particles being required for biological experiments so there was only a small amount of material available for analysis.
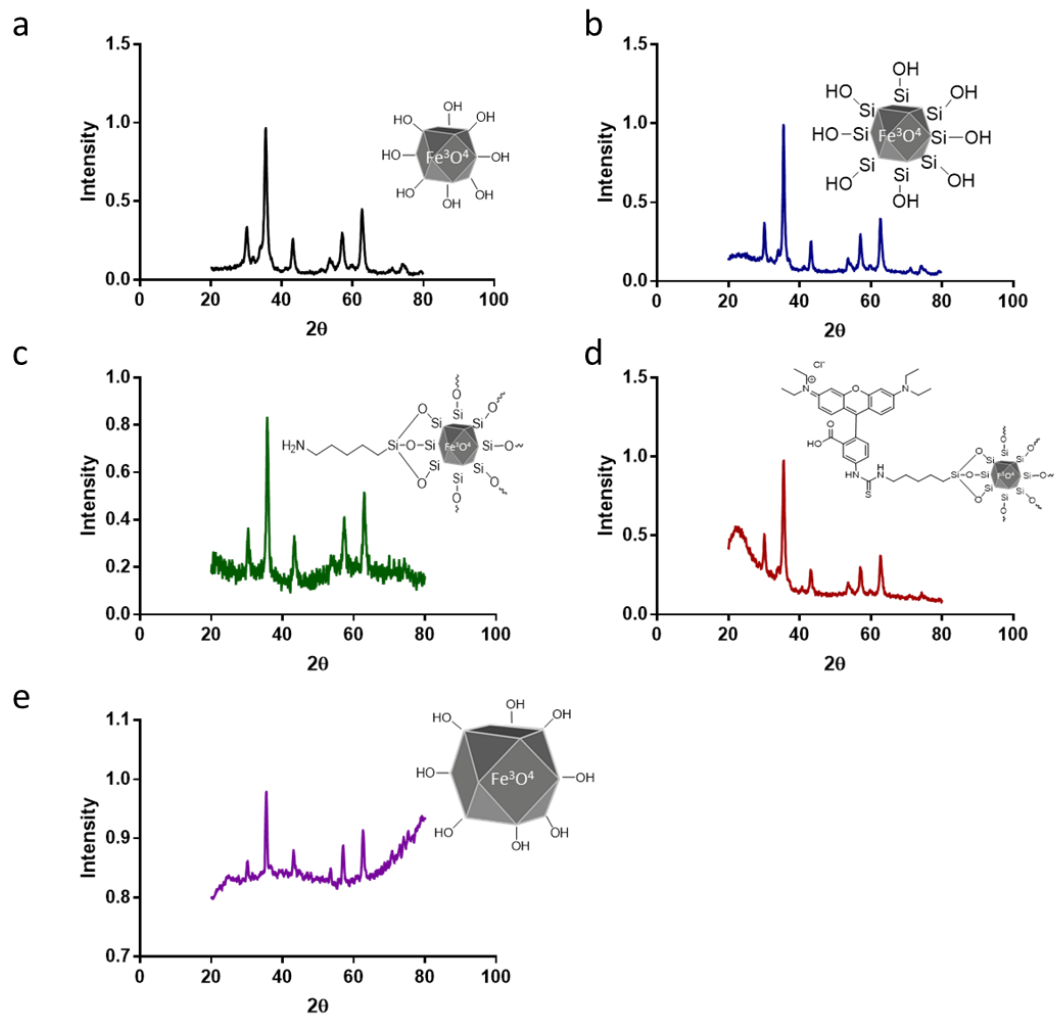
Figure 3.3.1 – XRD Spectra for iron oxide NPs. RRTCP (a) and altered surface coatings: (b) – coating with TEOS, (c) – functionalised TEOS layer with addition of NH2 amine groups and (d) – Rhodamine B fluorescently coupled silica with amine functionalisation (e) RTCP Inserts show chemical structure.

The miller indices of all samples closely matched the expected values for the main diffraction peaks for magnetite which confirms that magnetite has been produced and that this is homogenous solution and there is no other maghemite present as this would result in additional peaks observed or peak splitting.

Table 3.3.1 – Identified 2θ peak positions from each sample and the corresponding miller indices of magnetite. Theoretical 2θ values obtained from the RRUFF project.

Miller Indices	220	311	400	422	511	440
Theoretical Magnetite	30.21	35.58	43.25	53.66	57.20	62.82
RRTCP	30.17	35.56	43.26	53.75	57.07	62.69
SiRRTCP	30.12	35.47	43.33	53.66	57.05	62.76
NH$_2$ SiRRTCP	30.18	35.53	43.22	53.67	57.31	62.89
Rhob SiRRTCP	30.18	35.51	43.07	53.61	57.04	62.79
RTCP	30.1	35.4	43.1	53.6	57.1	62.7

3.4 SIZE ANALYSIS OF SYNTHESISED AND COATED MNPS

Accurate size determination of MNPs remains one of the most important characteristics in synthesis of MNPs as particle size can determine both physical and chemical characteristics. The high surface to volume ratio of MNPs, which is inversely proportional to the diameter of the MNPs, causes a large portion of their atoms to be present on the surface of the MNP and this property means that these materials differ in behaviour to their bulk material counterparts.[177,197] MNP size can directly impact upon saturation magnetisation with a linear correlation as the size of MNPs in single domain particles increases this results in an increase in their magnetic properties with an increase in coercivity as the MNP size increases in single domain particles to a maximum value before the formation of multiple domains takes place.[177,179,198] Magnetic materials are made up of magnetic domains which are typically in the range of 100 nm, bulk materials are made up of multiple domains whilst MNPs are typically smaller than the size of a magnetic domain and have a singular magnetic orientation.[148] Below a threshold size particles can exhibit SPION behaviour with a large magnetic moment that is continually changing direction.[148] MNPs size can affect how they interact within biological systems, with smaller nanoscale particles showing increased uptake and penetration than compared to larger particles. So accurate determination of size is important in understanding how particles may act when used as a therapeutic.

3.4.1 CRYSTALLINE SIZE DETERMINATION

From the diffraction pattern the crystal size of the particle can be determined using the Scherrer equation. The most intense peak was chosen for this calculation which relates to a

2θ value of 35.5°. The crystal size calculated from the diffraction pattern are shown in Table 3.4.1.

Table 3.4.1 – Theoretical particle sized as calculated from the Scherrer equation for all the synthesised and coated particles.

Particle	Scherrer crystal size (nm)
RRTCP	11.9
SiRRTCP	16.9
NH$_2$ SiRRTCP	17.1
Rhob SiRRTCP	15.0
RTCP	27.2

The theoretical crystal size as determined from the Scherrer equation shows that uncoated particles (RRTCP) have a crystal size of 11.9 nm but all the coated MNPs have a larger crystal size. This increase in crystal size can be explained by the effect of the silica coating on the MNPs. As the modification of the surface can protect the surface from further oxidation and protects the inverse spinel structure of the magnetite. The RTCP MNPs showed the largest crystalline size compared with the RRTCP MNPs this was expected due to the larger observed size in the RTCP from TEM. Although the Scherrer equation gives the crystalline size of the iron oxide core, but it makes a number of assumptions, and these can affect the accuracy of the equation including particle size homology as well as the shape of the MNPs. A spherical shape factor of 0.9 was used in the equation for size determination although from TEM analysis this is not the case for the entire population of particles more so in the RTCP MNPs where cubic particle as well as spherical can be observed.

3.4.2 VISUAL SIZE ANALYSIS OF MNPS

TEM analysis of the particles allows for accurate size analysis as well as determination of the shape of MNPs. It also allows for measurement of non-crystalline features of MNPs for both the magnetite crystal and the silica coating that envelops it. Size analysis of the particles was performed by measuring the diameter of a minimum of 100 particles. Figure 3.4.1 (a) shows uncoated magnetite NPs, Figure 3.4.1 (b) and (c) show the silica coated and the RITC coupled magnetite NPs.

Analysis of the coated magnetite MNPs in RRTCP synthesised MNPs show that the silica completely enveloped individual particles producing single crystal coated magnetite MNPs (Figure 3.4.1) which is advantageous as it reduces the size of the particles and produces more uniform particle size distribution. Whereas in the RITC MNPs it appears that multiple RRTCP MNPs have been coated.

Size analysis of magnetite NPs showed that the RRTCP MNPs synthesised had a mean diameter of 8.3 nm (± 1.6) with a distribution range of from 3.9 to 11.6 nm (Figure 3.4.1 c). The size of the MNPs produced indicate that they are single domain, as magnetite NPs are known to be single domain in spheres at size of ~100 nm, but this can vary depending on particle morphology.[179] As the average size of the particle is under 10 nm this puts the particles within the SPM range, it is estimated that particles under 20 nm can be SPM in nature whereas larger particles bulk ferrimagnetic properties.[179,199]
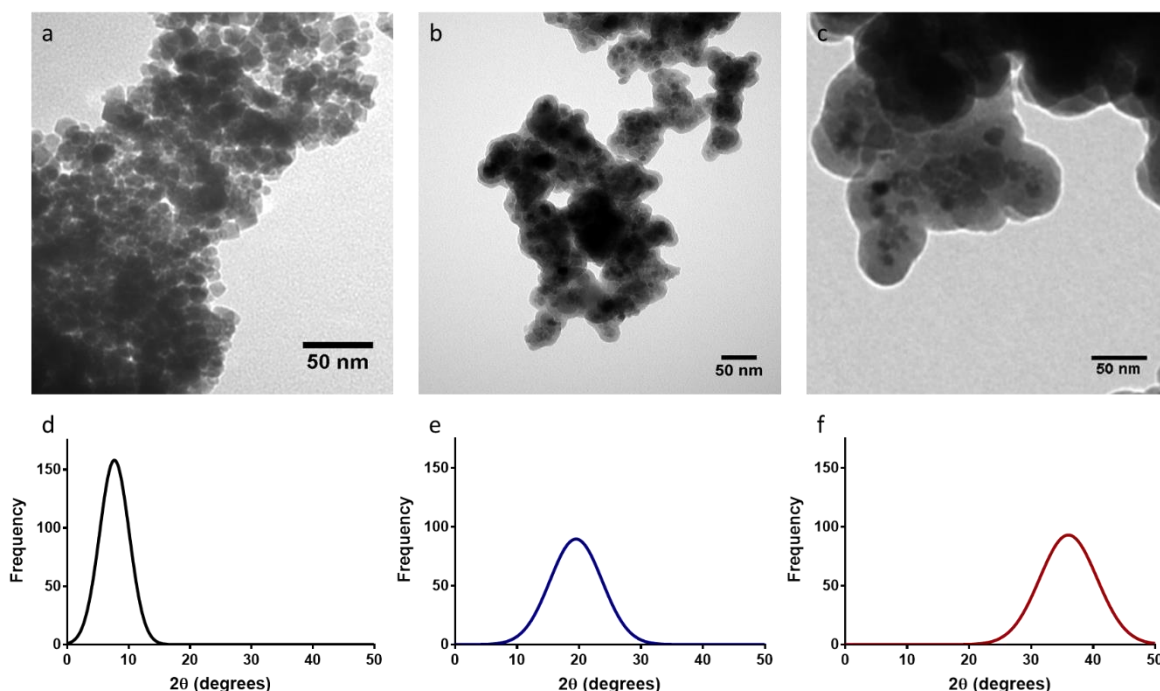
Figure 3.4.1 – Size and morphological analysis of synthesised MNPs. (a-c) TEM imaging of the MNPs (a) RRTCP, (b) NH$_2$ SiRRTCP and (c) RITC NH$_2$ SiRRTCP. Size distribution of MNP diameter (d) RRTCP, (e) NH$_2$ SiRRTCP and (f) RITC NH$_2$ SiRRTCP n=2.

Once coated the MNPs increased in diameter to a mean size of 21.9 (±3.2) nm with a distribution range of 11 – 34 nm (Figure 3.4.1 d), the advantage of this increase in size is that they are not susceptible to renal clearance which is known to occur with particles 8 nm and smaller in diameter.[190] However, a portion of the particles are susceptible to hepatic clearance by the liver, due to the livers ability to clear particles that are between 10 – 20 nm in diameter.[190,200] The effect of the silica coating saw the MNPs size more than double and as well as cause an increase in the size distribution of the MNPs (Figure 3.4.1e). Although the NH$_2$ Si coating resulted in the RRTCP size doubling the range of membrane thickness is relatively narrow (average thickness of 5.9 nm with a distribution range of 4.1 – 8 nm) suggesting that the thickness of coating is uniform across particles of varying sizes. The RITC labelled MNPs showed an increase in particle size with the mean MNP diameter increasing from 19.2 to 36.4 nm. This increase is likely due to the addition of the RITC coupled APTES

into the final coating step of the MNPs (Figure 3.4.1 f). The addition of the RITC APTES may have resulted in the conjugation of coated MNPS due to the additional silica interacting with multiple other MNPs resulting in an increased size. The presence of multiple MNPs in the RITC NH_2 SiRRTC MNPs may explain the increase in the coating size as if particles had agglomerated this might result in larger NPs.

The RTCP showed a larger size as well as a larger size distribution when measured via TEM this size was seen to be in excess of what was measured by XRD. A possible reason for this is the presence of amorphous iron on the surface of the particles that had not been converted into crystalline iron. This is a likely reasons as MNPs formed by co-precipitation grow as additional material is added to the particles that have already formed.[201] The mean size of particle as measured by TEM was 34.25 nm ± 11.04 nm but particles up to a size of 65 nm were measured and a minimum size of 10 nm. This shows that the RTCP produces particles with a larger size distribution than the RRTCP. Upon coating the particles increased in diameter to 42.12 ± 12.66 nm which showed a similar thickness to the RRTCP MNPs which suggests that the size of the MNPs did not affect the thickness of the silica coat.
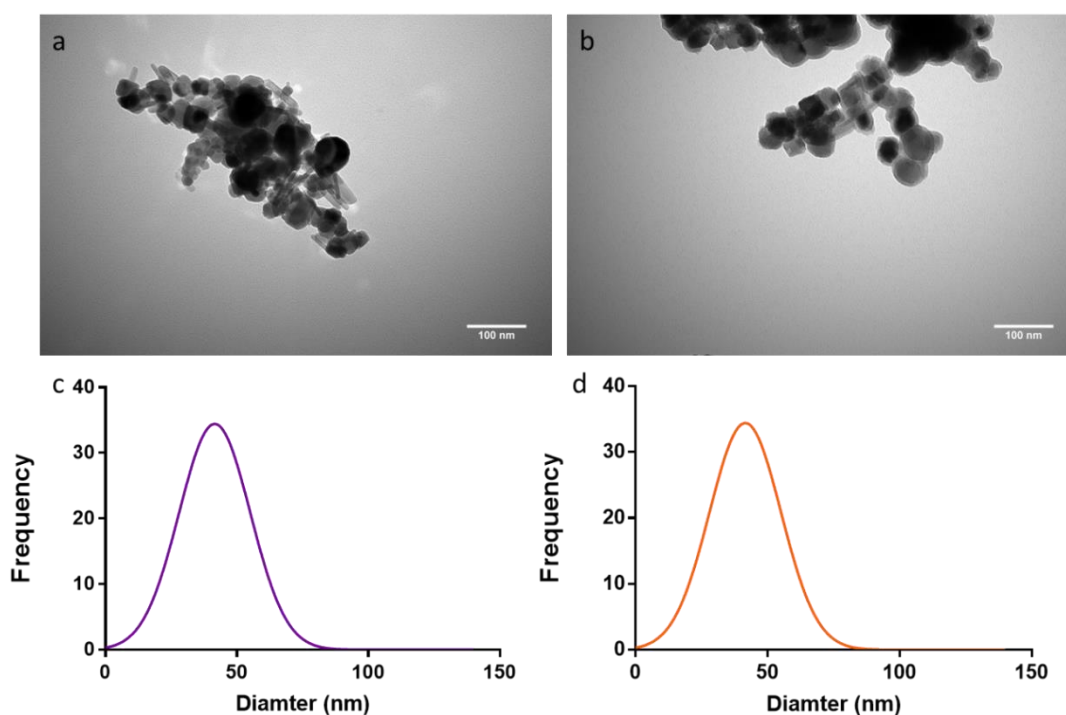
Figure 3.4.2 – TEM analysis of RTCP MNPs both uncoated (a) and amine functionalised silica coated (b) along with a gaussian distribution of their measured diameters (c) RTCP and (d) NH_2 SiRTCP.

As well as the size of the particles being important the morphology also has a large effect on the particle's ability for uptake into cells. Spherical NPs are known to be up taken at a five times higher rate than rod shaped NPs.[202] Shape determination of the synthesised MNPs

shows that sphero-octahedral magnetite particles were produced, coated within a sphere of silica, producing overall spherical particles that should help improve cellular uptake.[203–205]

3.4.3 HYDRODYNAMIC SIZING OF MNPS

Whilst direct measurement analysis of TEMs give an accurate size of the area of the particles, it does not give the size of a particle within a solution. When in solution particles can tumble and move, as well as the electric dipole layer which is dependent of the solution that the MNPs are suspended in. All of these can affect the hydrodynamic size of the particle which is not only a measurement of the particle it is a measurement of the electric dipole layer that surrounds the particle. Therefore, dynamic light scattering was used to determine the hydrodynamic size of the particle (Figure 3.4.3). In general, the average particle size for each of the MNPs was greater than the size determined by TEM. The RRTCP particles had an average particle size of 122 ± 11.64 nm when measured via DLS with a uniform size distribution. This is a large increase in particle size when compared to the TEM measurement (≈ 20 x size increase) and could be due to the effect of particle clumping due to magnetic properties or the dipole layer. The RTCP particle showed a similar increase in size as this was measured at 402.4 ± 13.1 nm which is significantly larger than the measured TEM size. This suggests that the RTCPs are more prone to agglomeration in solution which would explain why they do not remain as a suspension in solution.

The effect of surface modification on the particles produced a decrease in hydrodynamic size (81.25 ± 7.49 nm) compared to uncoated MNPs. Functionalisation of the MNPs with silica possibly improved the stability in solution by reducing the amount of agglomeration. This is beneficial for NP treatments as it reduces the likely hood of larger clusters forming as well as improving the size of the MNPs for internalisation as particles closer to 50 nm are internalised more rapidly than larger particles increasing uptake ability of the particles.[203] The RITC NH$_2$ SiRRTCP MNPs have an average particle size of 164 nm and 3 distinct populations of different sizing were observed, this may be due to the addition of the RITC that conjugates to APTES resulting in a less homogenous set of MNPs due to increased aggregation. The functionalised silica RTCP MNPs were unable to be measured via DLS as thy did not remain as a suspension long enough for accurate DLS measurements to be ran. This suggests that in the silica coating of the RTCP MNPs larger clusters of RTCP were coated together resulting in large particle formation.
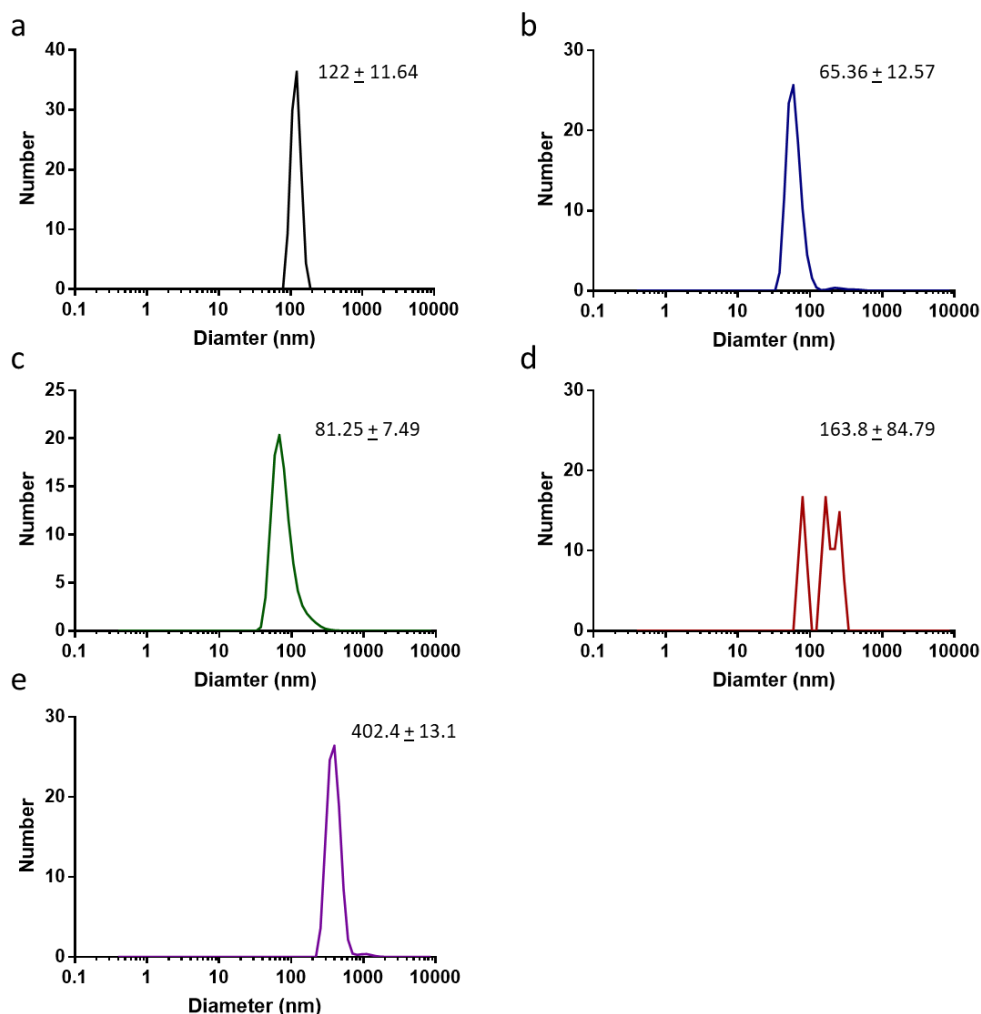
Figure 3.4.3 – DLS spectra for synthesised and coated MNPs (a) uncoated RRTCP (b TEOS coated RRTCP (SiRRTCP). (c) APTES functionalised SiRRTCP (NH$_2$ SiRRTCP) and (d) RITC coupled APTES functionalised NH$_2$ SiRRTCP (RITC NH$_2$ SiRRTCP). Data points represented are the mean $\pm$ SD (indicated in each figure).

The polydispersity index gives the heterogeneity of a sample based on its size and indicates the formation of clusters and agglomerates as well the size dispersity of the particles. Samples with values > 0.7 are known to have a broad size distribution with little heterogeneity and PDI of <0.05 indicate monodispersed particles. A polydispersity of 0.2 and below are defined as suitable for use in nanomedicine. The PDI of the particles was seen to decrease as the particles underwent coating and functionalisation. The uncoated RRTCP and the RTCP MNPs showed a similar PDI of had a PDI of 0.868 ± 0.228 and 0.738 ± 0.123 respectively (Table 3.4.2) indicating a non-polydisperse solution which decreases to 0.519 ± 0.065 in the SiRRTCP MNPs and 0.361 ± 0.052 in the NH$_2$ SiRRTCP indicating a decrease in the aggregation of particles in solution. This increases the amount of time particles will stay in solution before precipitating out as well as effecting the uptake of MNPs intracellularly. [206] The polydispersity of the RITC NH$_2$ SiRRTCP was seen to be 1 which indicates that there is

very little polydispersity in this sample this may be as a result of the further modification of the APTES layer with RITC resulting in further crosslinking.

Table 3.4.2 – Poly dispersity index (PDI) of the synthesised and coated MNPs

MNP	Poly dispersity index (PDI)
RRTCP	0.868 ± 0.228
SiRRTCP	0.519 ± 0.065
NH$_2$ SiRRTCP	0.361 ± 0.052
RITC NH$_2$ SiRRTCP	1
RTCP	0.738 ± 0.123

3.5 SURFACE PROPERTIES OF SYNTHESISED MNPs

The altering of magnetite surface properties has many benefits for biomedical applications. The presence of silica helps to improve the stability of the NPs, as well as reduce the effects of biodegradation and renal and hepatic clearance of MNPs from a biological system. The functionalisation of MNPs also effects the surface charge of the particle, this alteration can have an effect on the uptake and biocompatibility of the particles.[193,207] The charge of NPs can affect their uptake into cells, this depends on the cell type as well as the surface charge of the particles. Negatively charged plasma membrane of cells causes positively charged particles to be taken up more readily than negatively NPs but the positive surface charge also increases cell cytotoxicity possibly due to disruption of the plasma membrane of the cells.[192,193]

3.5.1 FTIR SPECTROSCOPY OF SYNTHESISED AND FUNCTIONALISED MNPs

FTIR spectroscopy was performed across all samples (Figure 3.5.1). The characteristic Fe-O Absorption band of magnetite caused by Fe-O vibration can clearly be seen at 583 cm^{-1} indicating that magnetite is present for all samples. Another indicative peak is the peak at 3422 cm^{-1} which can be attributed to water molecules on the surface of the particles. All of the spectra (Figure 3.5.1) give a representative spectra of magnetite as according to the literature.[208–210] Infra-red absorption bands seen at 1090, 950 and 800 cm^{-1} in the SiRRTCP NH$_2$ SiRRTCP and RITC NH$_2$ SiRRTCP are representative of Si-O-Si asymmetric stretching and bending, this clearly shows the presence of silica on the magnetite particles. The peak spanning from 3200 – 3650 cm^{-1} and the small peak at 1630 cm^{-1} indicate O-H stretching and H-O-H twisting. Although unclear due to the large spanning O-H peak NH stretching should be present in this region but masked by the O-H peak. Particle functionalisation has clearly taken place and the functionalisation of magnetite with silica helps to improve the stability of the MNPs in aqueous solutions. In the presence of the RITC could not be detected by FTIR

on the RITC NH$_2$ SiRRTCP MNPs and this would require further testing to identify its presence and fluorescent ability.
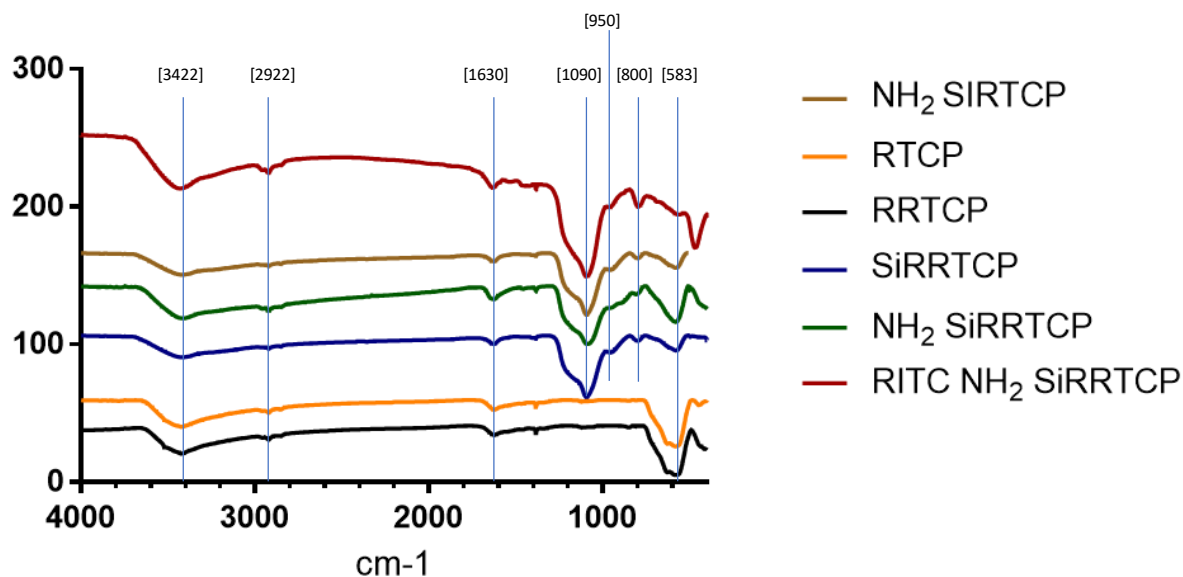
Figure 3.5.1 - FTIR Spectra of synthesised MNPs and their coatings with wave numbers from 400-4000. Major peaks and their corresponding wave numbers have been marked with a vertical line.

3.5.2 SURFACE CHARGE OF SYNTHESISED AND FUNCTIONALISED MNPS

The uncoated RTCP and RRTCP both showed negative ζ potentials when measured in MilliQ ultrapure water but these showed a large difference with -25.4 mV for the RRTCP and -49.95 for the RTCP this difference can be attributed to the size as this can influence the ζ potential as smaller particles have an increase in proton accumulation on their edge in comparison to large NPs.[211] The surface modification of the RRTCPs with silica did not alter the zeta potential of the MNPs with only a small decrease (-25.4) but when the surface was functionalised with amine functionalised silica there was a transition to a positive zeta potential which indicates that the NH$_2$ silica layer has been successfully coated on to the surface of the MNPs. The transition back to a negative surface charge in the RITC NH$_2$ SiRRTCP MNPs indicates that the RITC is bound on the surface of the MNPs or close enough to the surface to influence the charge.

Table 3.5.1 – ζ potential of the synthesised MNPs indication the charge at the slipping plane of the particles.

	RRTCP	SiRRTCP	NH$_2$ SiRRTCP	RITC NH$_2$ SiRRTCP	RTCP
Zeta Potential (mV)	-22.9 ± 1.39	-25.4 ± 2.21	38.7±0.39	-30.6 ± 1.19	-49.95

The hydrodynamic size and the zeta potential of the NH$_2$ SiRRTCP MNPs was measured again in cell culture medium supplemented with FCS and NEAA as these can alter the properties of

the MNPs due to the presence of the proteins and other large compounds within the cell culture medium. The size of the MNPs was measured as 824.87 ± 95 nm with a PDI of 0.93 showing a large increase in size in comparison to the DLS measurements in Milli Q. this increase is possibly due to the presence of the extra compounds in the media. As well as the increase in the DLS size the zeta potential of the samples changed from a positive charge of 38.7 to -10.44 mVs indicating that the compounds within the media are attracted to the surface of the MNPs creating a protein corona altering the charge of the particles when in media. [212] This Corona can alter how a host organusm repsonds to the presence of the MNPs this corona is dependent on content of the media as well as the size, shape and composition of the nanoparticles. [213]

Table 3.5.2 –Cell culture media effect on the hydrodynamic size as well as polydispersity and zeta potential of NH$_2$ SiRRTCP MNPs

DLS size (nm)	Poly dispersity index (PDI)	Zeta Potential (mV)
824.87 ± 95	0.93 ± 0.048	-10.44

3.6 FLUORESCENT COUPLING OF RITC TO APTES FUNCTIONALISED MNPS

Fluorescent coupling of RITC to MNPs allows for analysis of the internalisation and subcellular location and trafficking of MNPs within biological systems. This allows for further understanding of how MNPs behave in cellular conditions. Although the alteration of the surface properties might result in them behaving differently in a biological system. RITC was coupled to APTES prior to surface functionalisation of MNPs taking place and then added during the final surface modification step. To determine how effective this coupling was the excitation and emission spectra of the RITC was measured after synthesis with MNPs in the formation of RITC NH$_2$ SiRRTCP (Figure 3.6.1 a). The RITC NH$_2$ SiRRTCPs showed a fluorescent response from the RITC APTES coated particles with an λ max $_{ex}$ = 561 nm and λ max $_{em}$ = 587 nm excitation maximum similar to the excitation emission of other RITC conjugated nanoparticles and the known excitation/ emission of RITC (e (λex = 543 nm and λem = 580 nm). [214] The presence of the RITC on the MNPs allows for visualisation of the RITC NH$_2$ SiRRTCP MNPs under fluorescent microscopy (Figure 3.6.1 b). This fluorescent coating also allows for the measurement of MNPs via flow cytometry.
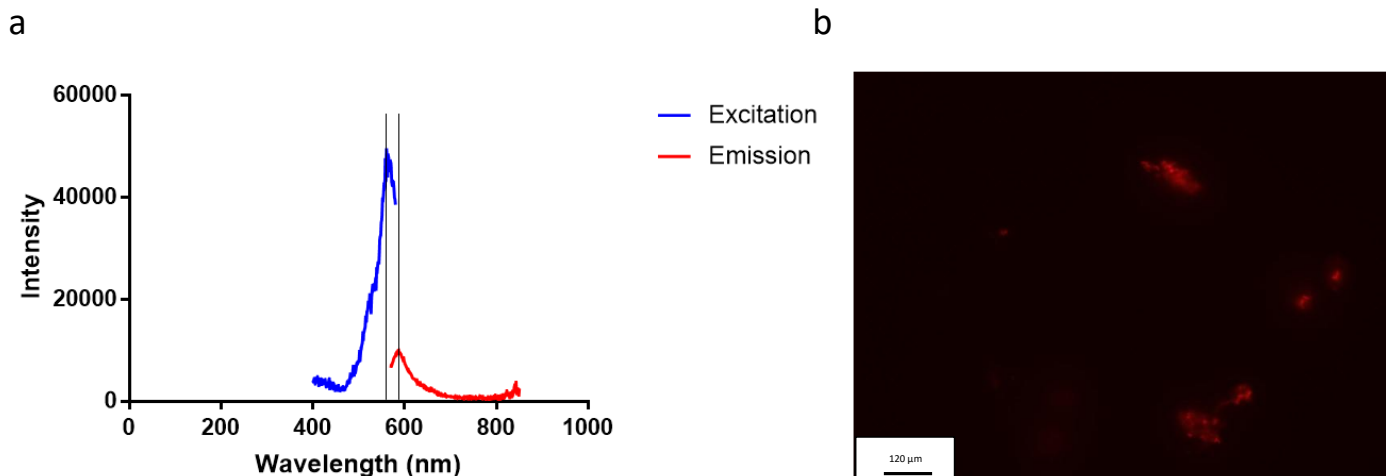
Figure 3.6.1 - Analysis of fluorescent coupling of RITC to NH2 SiRRTCP MNPs. (a) fluorimeter measurement showing the excitation and emission spectra of the MNPs. (b) Fluorescent microscopy of the particles showing a fluorescent response (red).

3.7 MAGNETIC PROPERTIES OF MNPS

The magnetic properties of NPs greatly affect how they interact with each other and how they will respond when exposed to a static or alternating magnetic field. This can affect the amount of heat generated by the particles and how the particles can generate heat for MHT as SPM NPs should only generate heat from Neéls relaxation and Brownian motion and not hysteresis loss. It is expected that the RTCP MNPs should possess a coercivity due to the majority of the MNPs being larger in diameter than the SPM range whilst the SiRRTCP MNPs should be SPM. VSM analysis was performed to determine the saturation magnetisation and coercivity of MNPs.

VSM analysis of the RRTCP and the SiRRRTCP particles showed a hysteresis loop with a coercivity of 15 Oe and 22Oe respectively which indicates that there is some bulk material present as SPM NPs should not possess any coercivity at room temperature.[148] This is idea that there is a small amount of bulk magnetite present within the sample is confirmed due to the saturation magnetisation of the MNPs being greater than the range of magnetic saturation that is describe in the literature.[215] This discrepancy between the size analysis and magnetic measurements could be due to the fact that there are larger particles that are outside the SPM range are in the sample, but these are not visible when being imaged by TEM.

The area of the hysteresis loop represents the amount of energy that can be generated via hysteresis loss, this energy is the energy that is dissipated to the surroundings when the field switches from positive to negative. The saturation magnetisation (M_s) of the MNPs was determined as 77 emu/g, this is slightly lower than expected for bulk magnetite.[216] M_s is

important in hyperthermia as the amount of heating is directly proportional to the materials M_s, which highlights the importance of correctly synthesising magnetite rather than other iron oxides, as magnetite has a much higher M_s resulting in greater heating efficiency. The loss of M_s in Figure 3.7.1 could be due to the reduced amount of magnetic material present as there is a silica coating surrounding the particles. The significant drop in M_s suggests that a large proportion of the coated particles consist of the silica coating. The presence of the coating has only produced a slight reduction in the coercivity of the Si NH_2 RRTCP compared to the RRTCP particles with 12.5 Oe in the silica coated compared to 15 Oe in the uncoated sample.
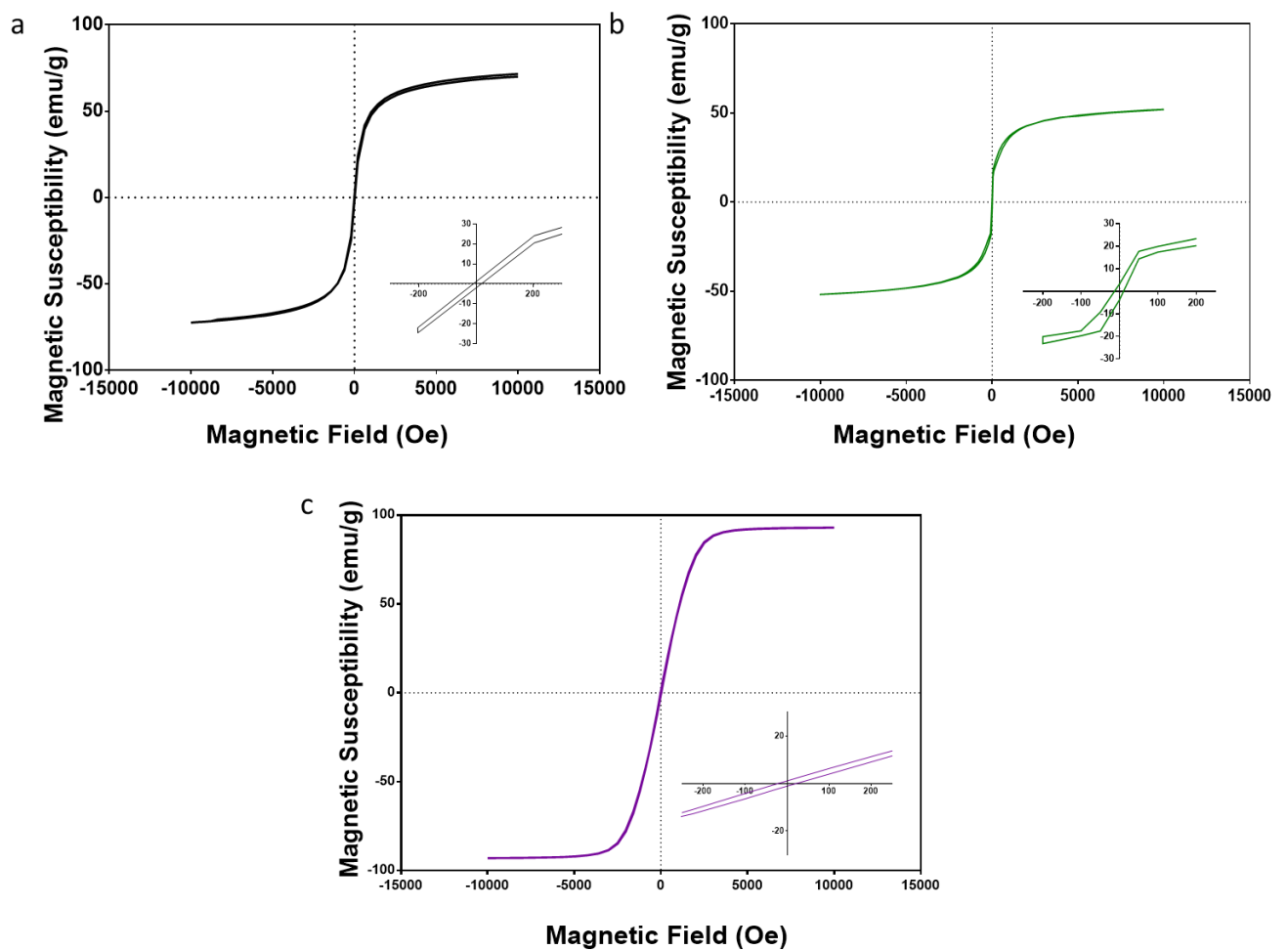
Figure 3.7.1 - VSM Data of the RRTCP (a) and the functionalised silica coated RRTCP(b) and (c) shows the uncoated RTCP. The graph shows the magnetic susceptibility and the coercivity measured in a VSM at room temperature from -10 000 to 10 000 Oe.

3.7.1 HEATING CAPACITY OF MNPS

To determine the ability of the particles to generate heat for MHT the NH_2 Si functionalised samples were suspended in Milli q ultrapure water and placed into an AMF with a frequency of 173 kHz and a field strength of 9.8 mT. Although the RTCPs had a greater coercivity they

were not able to be suspended long enough to generate any hyperthermia data, so it was decided not to take them forward as a MNP for treatments. The Si NH_2 RRTCP particles showed a significant increase in the heat generated during exposure to an AMF (Figure 3.7.2) after the background heating was removed. With a 20 °C increase in temperature to just over 45 °C (Figure 3.7.2). This showed that MNPs can heat a bulk material to temperatures in the range of a mild hyperthermia which indicates that these are suitable for MHT. Although the MNPs were dispersed in a high concentration of MNPs (8 mg/ml) the principle of nano heating would suggest that the temperature surrounding the particle are much higher than this. From the temperature trace generated by the MNPs at (8 mg/ml) the SAR of the produced particles can be calculated. The obtained SAR value of the MNPs was 49.82 ± 3.412 W/g. This value is calculated from the change in temperate over the change as well as the heat capacity and concentration of the particles. SAR values of 50W/g are known to be suitable for MHT treatment in patients as this denoted that there is sufficient energy transfer to the target material to sufficiently generate a significant temperature increase to induce cellular damage. [217] The SAR of the RRTCP MNPs of 49.82 ± 3.412 W/g indicates the ability of the NH_2 SiRRTCPs to generate SAR values that is comparable to other MNPs that have been synthesised in the literature which have successfully induced hyperthermia damage to tumour cells which indicates these MNPs would be sufficiently powerful to generate HT mediate damage and would be sufficiently powerful to generate mild hyperthermia damage within tumour cells.[218]   Although this SAR value would change dependent on the heat capacity of the material this does provide an indication that these particles are sufficiently capable of generating enough heat for HT treatment, but this would need confirmation with biological experiments and will also be dependent on other factors such as concentration of particle the cells are treated with.
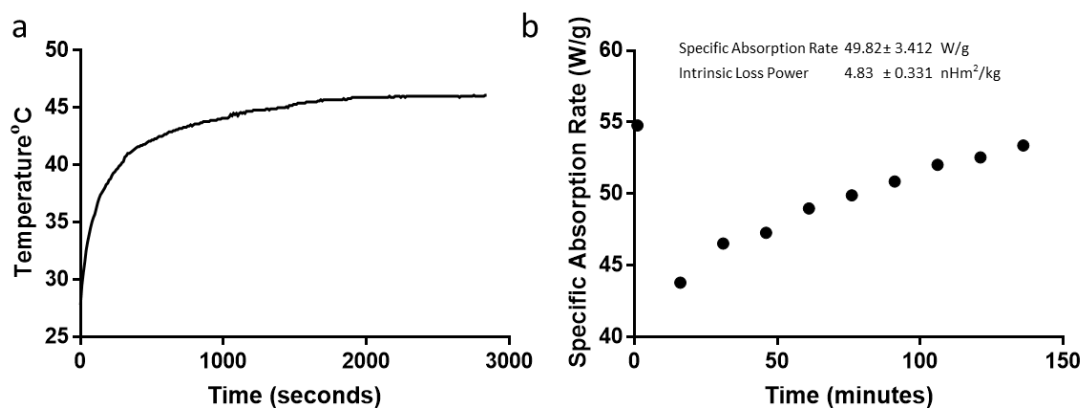
Figure 3.7.2 - Hyperthermic properties of the NH$_2$ SiRRTCP particles when exposed to an alternating magnetic field (a) shows the heating of the particles at 8 mg/ml with background subtracted. (b) shows the SAR values and the calculated ILP values determined from the heating power of the MNPs.

Although the SAR gives an indication of the power generated during exposure to an AMF this is affected by the frequency and the field strength as discussed in the introduction (1.5.2). The ILP gives an indication of the heating ability of the particles independent of external factors. This ILP of the synthesised NH$_2$ SiRRTCP MNPs shows a value of 4.83 ± 0.331 nHm^2/kg which is consistent with other values of MNPs in literatures.[219] These indicate that although the magnetic saturation and coercivity of the RTCP MNPs is higher than what is observed in the RRTCPs this does not result in an improved hyperthermia although this is most likely due to the inability of the RTCP MNPs to remain dispersed in a solution which is possibly as a result of the larger coercivity of these particles causing increased agglomeration.

3.8 SUMMARY AND CONCLUSIONS

In this chapter MNPs of two distinct sizes were synthesised using a room temperature coprecipitation reaction with alteration on the method of addition of the NaOH to a mixed valence iron solution of ferric to ferrous ions (2:1) with a silica coating present around the core shell. The synthesised RTCP and RRTCP MNPs were determined to be magnetite iron oxide from their crystalline structure and magnetic properties. Size determination of magnetite NPs by TEM analysis showed that the RRTCP MNPs had a diameter of 8.1 ± 4 nm, indicating that they were within the SPM size range of less than 20 nm.[220] This conflicted with the magnetic properties of the NPs as a coercivity of 15 Oe was observed, indicating bulk magnetic properties behaviour of the NPs. This could be caused by the presence of a small portion of larger single domain magnetic particles that were not identified on TEM. This could be due to either low numbers or clustering of the particles on the carbon coated grid as only distinct clear particles were measured by TEM. The theoretical size of the particles calculated using the Scherrer equation is consistent with TEM analysis, with a theoretical size

of 11.9 nm. The presence of the silica coating on the RRTCP MNPs can be seen to protect the particles from further oxidation as the crystalline size increased with surface modification which can be explained with phase distortion on the uncoated particles and migration of iron ions to the MNPs surface resulting in oxidation of the MNPs surface, which may explain the presence of the small maghemite peaks seen within the XRD spectra of the produced MNPs.[221,222]

The mean TEM measured size of the RTCP MNPs was 34.25 ± 11.04 nm this was 4 times larger than the RRTCP MNPs and the XRD size determination was measured at 27 nm.

Coating of the MNPs with TEOS and APTES helps to improve the particles monodispersity in solution as well as protect the particle from oxidation which is observed by the smaller crystalline size in the uncoated sample of the XRD in comparison to the costed samples. Oxidation can cause a change in the crystal structure and have a negative impact on magnetic properties. As well as providing improved monodispersity applying a coating also helps to improve retention as it reduces the elimination of MNPs via hepatic and lymphatic systems by increasing the size of the particle.[190] The presence of the amine functionalised silica coating produces a positive surface charge on the particles which should improve the uptake of MNPs.[223] Although when measured in supplemented cell culture medium the surface charge of the particles was negative.

The RRTCP particles show an SAR value of 49.82 W/g this places the particles within the range of sufficient power to supply heating at the required level for hyperthermia treatment. Whereas the larger RTCP MNPs showed an inability to heat during exposure to AMF showing that these are unsuitable for HT. Therefore, MNPs have been synthesised that display the required magnetic and size properties for use in MHT.

CHAPTER FOUR: CYTOTOXICITY AND UPTAKE OF MAGNETIC NANO PARTICLES

4 CYTOTOXICITY AND UPTAKE OF MAGNETIC NANOPARTICLES

4.1 INTRODUCTION, AIMS AND HYPOTHESIS

NPs have been developed that can provide a wide array of biomedical applications including drug delivery, magnetic hyperthermia ablation, MRI and magnetic separation.[6,95,115] The chemical and physical properties of MNPs can affect the MNPs ability for internalisation, how they interact with cellular proteins, the eventual fate of particles after treatment *in vivo* and the "nanotoxicity" of the NPs.[190,224] Most NPs are designed to produce low cellular toxicity, this is to reduce any off-target effects that might occur due to particles accumulating in sites away from the target. Although the NPs are designed to have reduced nanotoxic effects on cells at certain higher concentrations, NPs are known to be toxic in a dose dependant manner.[225,226] Due to the use of heavy metals in MNP synthesis, determining the toxicity of the developed NP is not only crucial in assessing their suitability as a therapeutic agent but also allows for insight into tolerated concentration ranges of NPs, that can be used to determine later treatment doses. This chapter will assess the nanotoxicity of the synthesised MNPs in two breast cancer derived cell lines (MCF7 an oestrogen receptor positive line and MDA-MB-231 an epithelial cell line that is estrogen, progesterone and HER-2 negative) and how the presence at increasing concentrations can affect the cells, as well as the internalisation of the MNPs. The MNPs carried forward to be tested here are the NH_2 SiRRTCP as these showed the greatest characteristics for successful MHT.

The aims of this chapter are to assess the following in both MCF7 and MDA-MB-231 cell lines *in vitro*:

1. The nanotoxicity of the MNPs at increasing concentrations and differences in how they are tolerated.
2. The effect of NP concentrations on the ability of cell proliferation.
3. The intracellular effects that the synthesised MNPs have on cells.
4. The effect of exposure time and concentration on internalisation of MNPs.

4.2 CYTOTOXIC EFFECTS OF MAGNETIC NANOPARTICLES

NP size and shape and the coating of the particles can affect how they interact with cells and how toxic they are to cells.[227,228] As well as this the type of organ can significantly affect how they respond to NPs, this is due to the differences in the cell physiology.[205,229] This is more significantly noticed in cancer cells due to their increase in cell proliferation and metabolism.[225]

4.2.1 SHORT TERM CYTOTOXICITY OF MAGNETIC NANOPARTICLES

The effect of MNPs was measured across a range of concentrations to determine a suitable concentration that shows low cytotoxicity, concentrations from 5 mg/ml to 800 mg/ml were used. An alamar blue cell viability assay was used to determine the number of viable cells after treatment with MNPs for 24, 48 and 72 hours in both MB-MDA-231 and MCF7 cells.

After 24 hours exposure both cell lines showed no effect on their viability for all concentrations of MNP (Figure 4.2.1). After 48 hours a noticeable decrease is visible in the MB-MDA-231 cells in concentrations from 200 mg/ml onwards, but there is no significant decrease in the viability. In the MCF7 cell line there is a small significant decrease in the viability of cells from a concentration of 400 mg/ml, but this decreases after 72 hours and only the 600 and 800 mg/ml concentrations show a significant drop in viability. Concentrations of 100 mg/ml upwards show a visible significant effect on the viability. MB-MDA-231 cells show a greater susceptibility to the MNPs at 72 hours indicating a concentration dependent effect. Concentrations from 50 µg/ml show a significant effect on cell viability which increases to below 50 % in concentrations from 400 µg/ml. In both cell lines it was observed that there was almost no effect on cell viability after 24 hours of incubation with MNPs, with only a small noticeable reduction in viability being visible in concentration from 100 µg/ml in the MDA-MB-231 cells and 400 µg/ml in the MCF7 cell lines.

Time as well as concentration is seen to play a major factor in the nanotoxicity of the MNPs as all concentrations tested showed high levels of tolerance after 24 hours exposure, but this decreased as the length of exposure was increased to 48 and 72 hours. With concentrations of 100 µg/ml and over showing an effect on cell viability in MCF7 cells and 5 µg/ml and over causing a decrease in cell viability in the MDA-MB-231 cells.
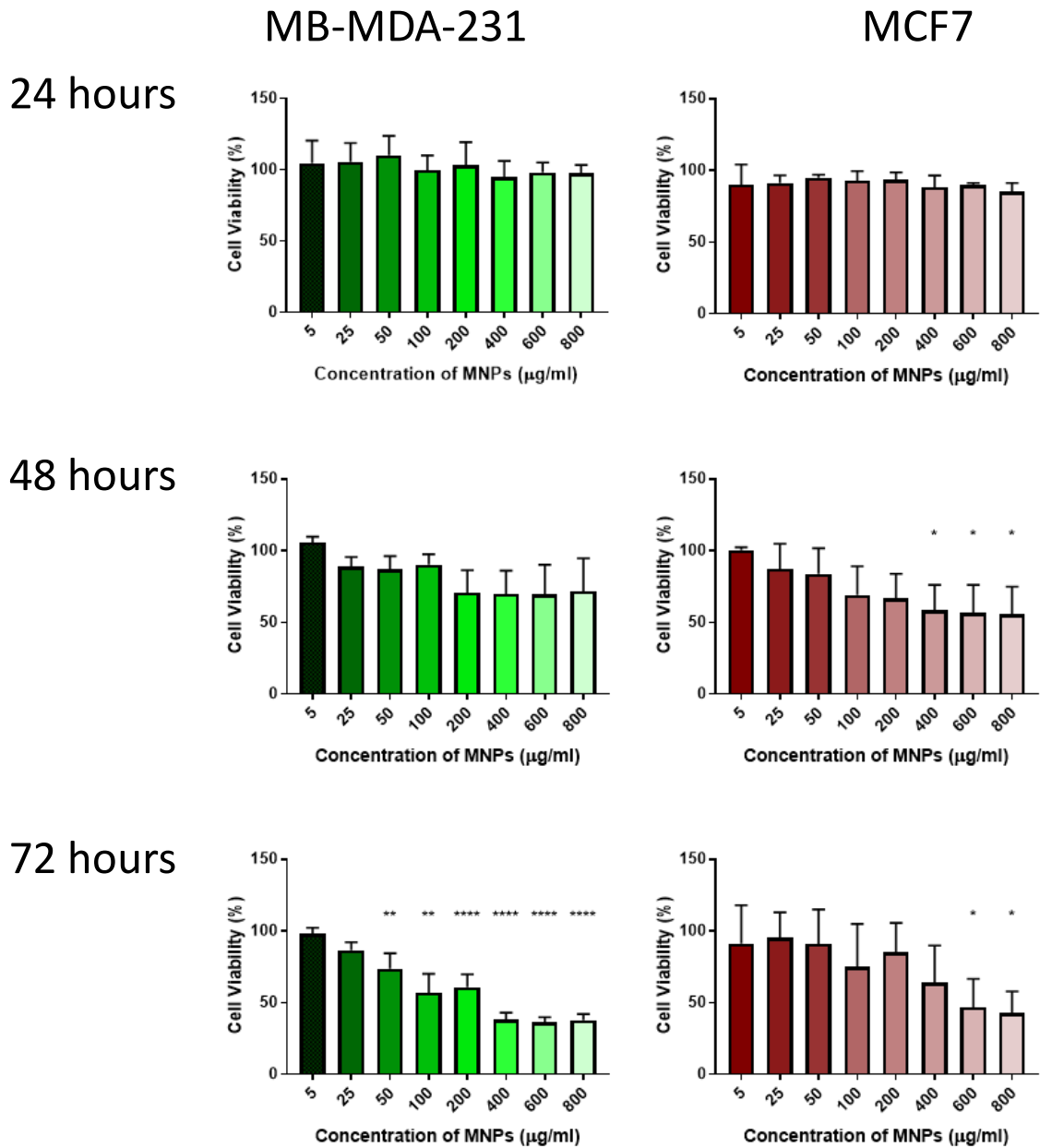
Figure 4.2.1 – Cell viability of MCF7 and MDA-MB-231 cells when treated with concentrations of MNP from 5-800 µg/ml at incubation periods of 24, 48 and 72 hours. Cell viability is shown as the average viability +/- SEM as measured by alamar blue cell viability assay normalised to the untreated control (N≥3). With the P value derived from multiple comparison ANOVA. * denotes p= ≤0.05, ** denotes p= ≤0.01, *** p= ≤0.001 denotes **** denotes p=≤0.0001 significant difference

As shown in Figure 4.2.1 concentrations over 200 µg/ml were observed to have the most effect on cell viability and because of this it was decided to not carry the concentrations higher than this forward. Although cell viability indicates the overall health of the cell giving an idea of the effects of the MNPs it does not indicate the toxicity of the MNPs. Toxicity of the MNPs was assessed via flow cytometry after 24 hours incubation (Figure 4.2.2). From these results it can be clearly seen that there is little to

no toxicity at concentrations up to 200 µg/ml, this matches the results of the cell viability assay showing the MNPs had little effect on the cells after 24-hour exposure.
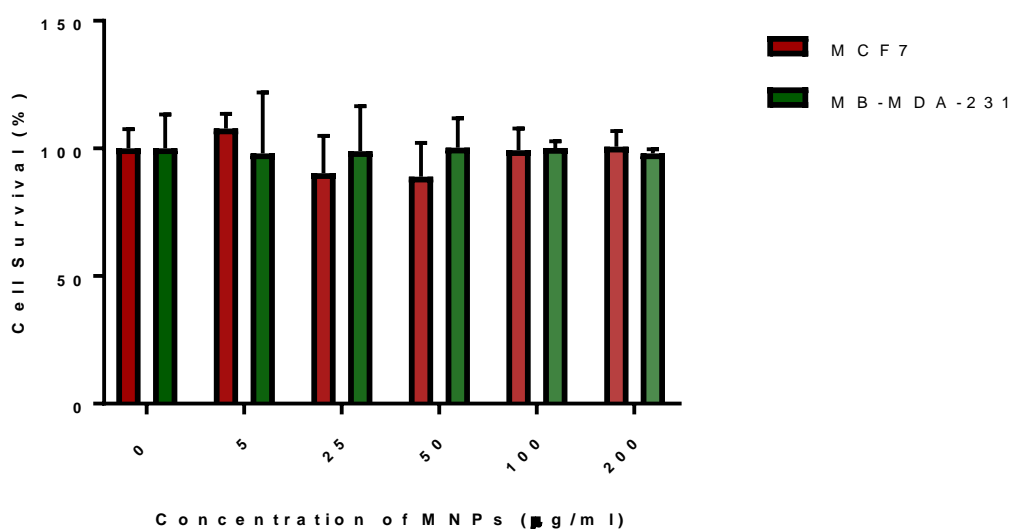
Figure 4.2.2 – Cell survival of MCF7 and MDA-MB-231 cells after 24 hours incubation with concentrations of MNPs from 5-200 µg/ml. Cell survival is shown as the average survival +/- SEM as measured by flow cytometry with P.I staining for dead cells (N=≥3). With the P value derived from multiple comparison ANOVA.

4.2.2 LONG TERM NH$_2$ SIRRTCP MNPS CYTOTOXICITY AND EXPOSURE EFFECT

The length of time that cells remain exposed to MNPs may have a dramatic effect on how cells respond, the effect of 24-hour exposure was compared to that of continuous exposure of MNPs for the duration of the experiment for both MCF7 and MB-MDA-231 cells. The clonogenic assay allows for the determination of the cell's proliferation ability as well as its ability to form colonies after exposure to MNPs. After 24 hours exposure a visible effect can be seen in concentrations of 5 µg/ml and above in both cell lines, however this did not produce a significant reduction in cell survival after 10 days in either cell line (Figure 4.2.3). Even though there was no significant reduction in the number of colonies formed the effect of the MNPs was more noticeable in this long-term assay than those seen in Figure 4.2.1 and Figure 4.2.3.

Continuous exposure of MCF7 cells to MNPs had very little effect on the cell survival with only a decrease in the 200 µg/ml concentrations (Figure 4.2.3). This contradicts the MB-MDA-231 cell line which showed a significant (p=>0.05) drop in cell survival at concentration of 25 µg/ml and above
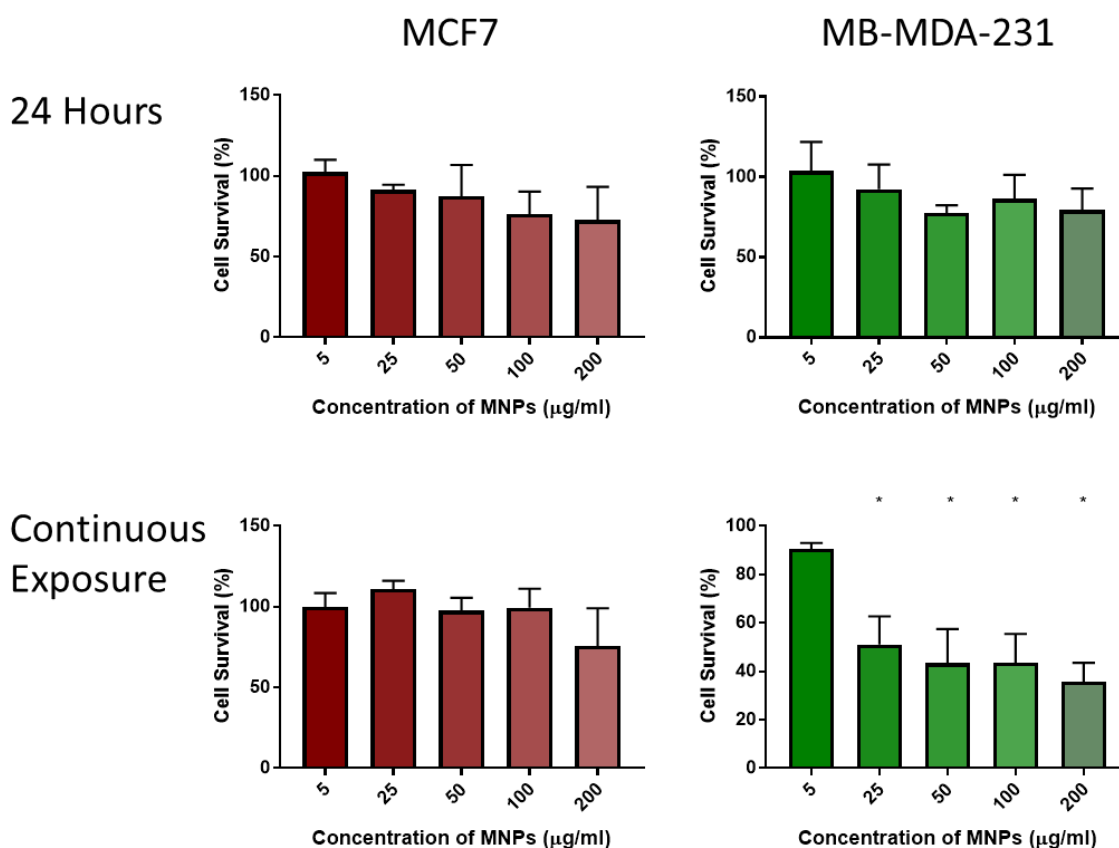
Figure 4.2.3 – Cell survival of MCF7 and MDA-MB-231 to MNP concentrations from 5 – 200 µg/ml with 24-hour exposure and continuous exposure. Clonogenic survival fraction, data points represent the mean survival fraction +/- standard error of the mean (SEM) with the p value derived from multiple comparison ANOVA. * denotes p= ≤0.05

The length of exposure has also been shown to have an effect on cell viability, with exposure times of over 24 hours shown to have a negative effect on cell survival in both MCF7 and MB-MDA-231 cells increasing as the time progressed to 72 hours (Figure 4.2.1) this was more noticeable in the MB-MDA-231 cells with concentrations of 25 µg/ml showing a decrease in viability This effect is more pronounced in the MB-MDA-231 cells which show increased sensitivity to MNPs (Figure 4.2.1, Figure 4.2.3). This suggests that the cell type may be more sensitive to MNPs. Cell uptake of MNPs may help to explain the reason behind the difference in survivability exhibited between these two cell lines.

4.2.3 CELLULAR EFFECT OF INCREASING CONCENTRATIONS OF NH₂ SIRRTCP MNPS

The effect that the presence of MNPs had on cell cycle progression was analysed to identify how concentrations of MNPs effect cells and may induce reduced cell viability at higher concentrations (Figure 4.2.4). It was hypothesised that increasing concentrations would cause a change in the cell cycle progression and this would be more apparent as the concentration of particles increased. Both MCF7 and MDA-MB-231 cells were analysed 24 hours post treatment with MNPs to maximise the amount of NPs uptake and interaction.

The percentage of cells in Sub G1 phase was seen to increase with concentrations as low as 25 µg/ml and 5 µg/ml in the MCF7 and MDA-MB-231 cell lines respectively and continued to increase as the concentration of MNPs increased which indicates an increase in cell undergoing apoptosis (Figure 4.2.4). This increase in cell presenting as apoptotic with increasing cell concentrations matches what was seen in the cell viability assays with increasing concentrations of cells showing a reduction in cell viability which suggest that the presence of high concentrations of MNPs are inducing cell apoptosis.

MCF7 cells also showed an increasing trend of cells in G1 arrest with a concomitant decrease in cells in G2/M phase of the cell cycle, this increase in G1 arrest along with the increase in the sub G1 population indicates that increasing concentrations of MNPs are inducing nanotoxicity in the cells causing apoptosis.

MDA-MB-231 cells did not show an increase in the percentage of cells in G1 phase like MCF7 but instead showed a slight increase in the percentage of cells in S phase when treated with MNPs coupled with a slight drop in the number of cells in G1. This coupled with the increase of cells in the sub G1 phase indicate an increase in apoptosis with increasing MNP concentration like that of MCF7 cells. MDA-MB-231 cells started showing an increase in Sub G1 cells down to concentrations of 5 µg ml, with significant increases in sub G1 cells at concentrations of both 100 and 200 µg ml concentrations.

In summary, both MCF7 and MDA-MB-231 cells were affected by the presence of MNPs even at concentrations as low as 5 µg/ml. Both cell lines showed increases in sub G1 fraction of cells, but this was more prominent in the MDA-MB-231 cells than the MCF7 cells, with a visible effect starting at lower concentrations and a more significant effect at MNP concentrations of 100 and 200 µg ml. These results match those seen in the cell viability and the P.I staining which showed a reduction in cell viability along with an increase in cell death. Although there is a significant increase in the number of cells in the sub G1 population this only increased to a maximum of 6% of the cells indicating that there is only a relatively small level of nanotoxicity which correlates with the low levels of toxicity observed in the P.I staining and the small loss in cell viability even at the highest concentrations of 200 µg/ml.
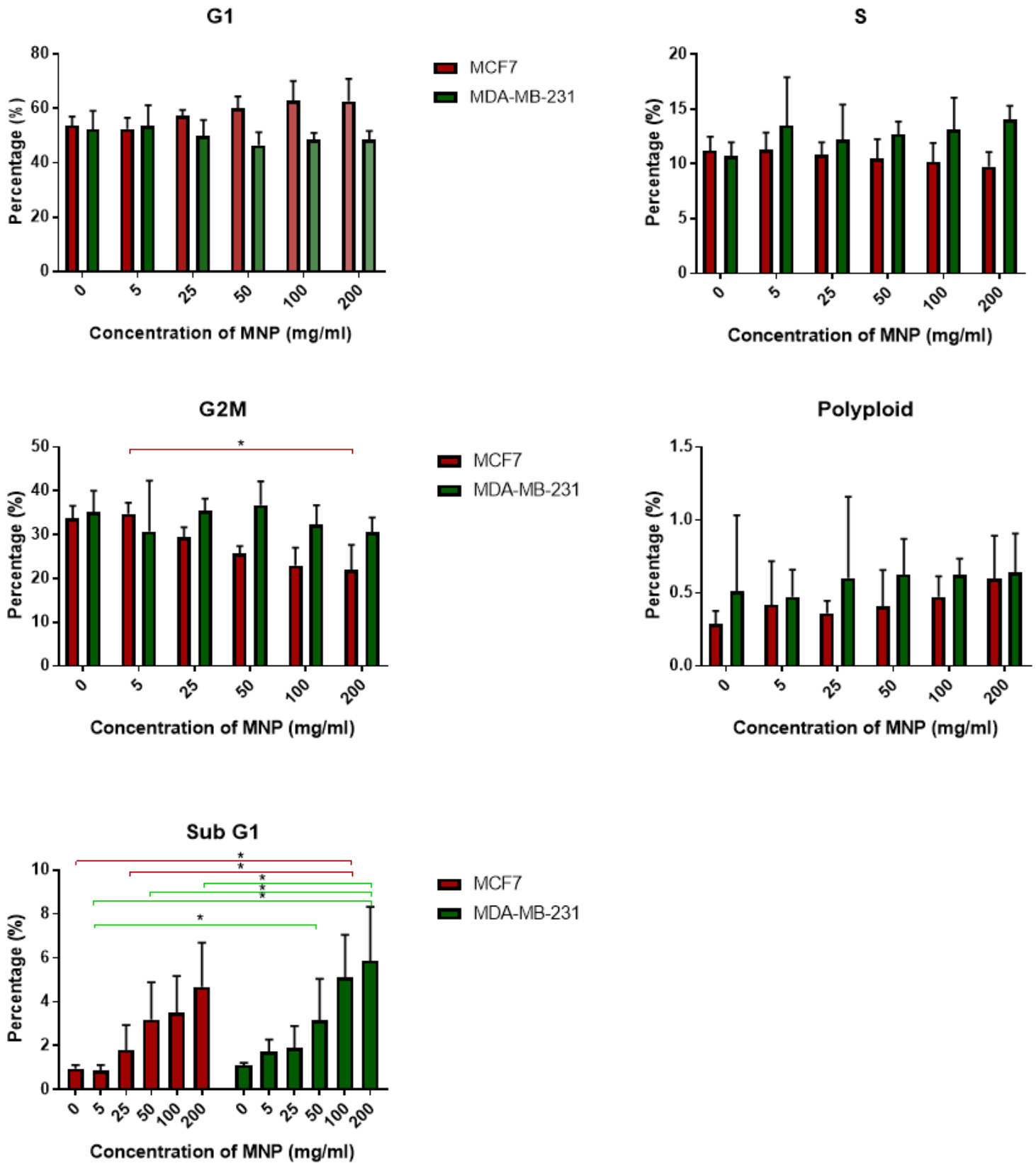
Figure 4.2.4 – MCF7 and MDA-MB-231 cell cycle distribution 24 hours post treatment with increasing concentrations of MNPs. Mean cell cycle distribution 24 hours post treatment with MNPs. Data points represent mean cell cycle distribution +/- SD (n= ≥3). * denotes p= ≤0.05, ** denotes p= ≤0.01, *** p= ≤0.001 denotes **** denotes p=≤0.0001 significant difference

The increasing presence of MNPs also resulted in an increase in γH2ax foci. These form at the site of DSBs in response to DNA damage from IR or cytotoxic agents and are the first step in recruiting DNA repair proteins to the site of a DSB. In the MDA-MB-231 cell line there was an increase in the number of γH2ax foci per cell as the concentration of MNP increased (Figure 4.2.5 a). Increasing foci formation became significant at concentrations of 100 µg/ml and above. Similarly, this was also seen in the MCF7 cell line although the MCF7 showed a significant increase in γH2ax foci at concentrations of 25 µg/ml (Figure 4.2.5 b). This indicates that MNPs induce DNA damage within the cells. This increasing number of γH2ax foci with MNP concentration may give an indication as to why there is increased observance of cytotoxicity at higher concentrations of MNPs, as well as increased population of apoptotic cells. Higher concentrations (≥100 µg/ml) may induce DNA damage within these cells that results in the greater levels of cell death that is observed.

From these results it can be said that although the 5, 25 and 50 µg/ml concentrations are observed to negatively affect cell survival and viability this is to a much smaller extent that the 100 and 200 µg/ml concentrations. This result may be as a result of a greater level of internalisation of the MNPs or possibly through other means.

a
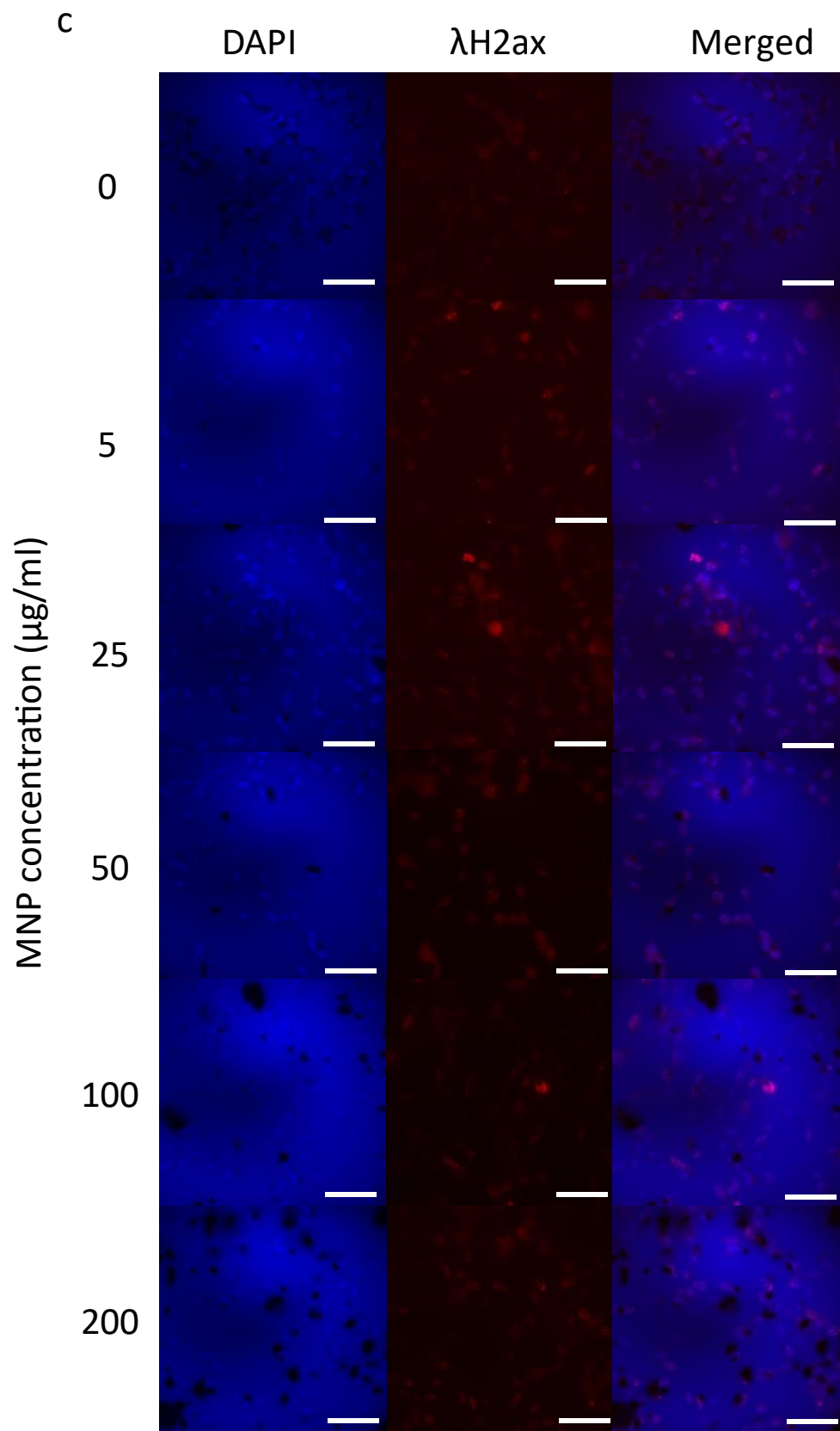
Figure legend overleaf
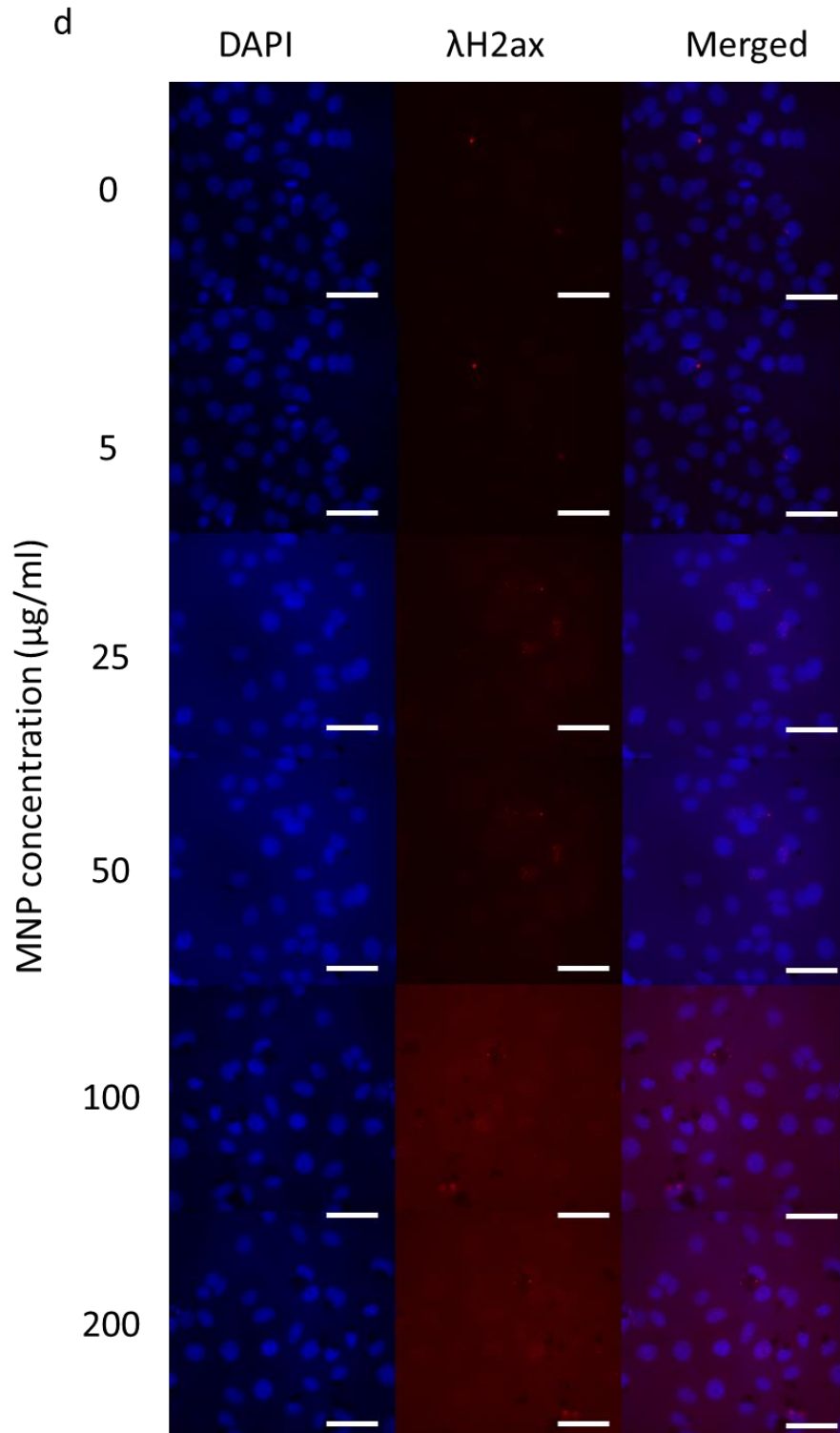
Figure 4.2.5 – λH2AX foci formation after 24-hour exposure to MNP concentrations from 0-200 μg/ml. a) measurement of foci number per cell of MNP exposure in MDA-MB-231. b) λH2AX foci formation after 24-hour exposure to MNP concentrations from 0-200 μg/ml. representative image of MDA-MB-231 and MCF7 cells with DAPI (blue) and λH2AX foci (red) and a merged image. scale bar represents 100 μm. Measurement of foci number per cell of MNP exposure in MCF7. Average λH2AX foci per cell in MDA-MB-231 n=3 (c) and MCF7 n=3 (d) after 24 hour exposure to NH_2 SiRRTCP MNPs. Significant difference represented by ** denotes p=0.01, **** denotes p=≤0.0001 significant difference.

4.3   Uptake and Localisation of MNPs in Breast Cancer Cell Lines

4.3.1   Prussian Blue staining of iron

MNP uptake into cells was qualitatively visualised by Prussian blue staining of the iron core of the MNPs (Figure 4.3.1). Staining showed increased iron content as the concentration of iron increased with an increasing presence of iron both intracellularly and extracellularly. The increase in the amount of iron seen as the concentration increases indicates that concentration plays a factor in the amount internalised. From the staining it was evident that as the concentration of MNP increased there are more cells showing iron presence which may indicate that at higher concentrations more cells internalise iron. This increase in the number of cells with iron at increasing concentrations may be linked to the increased presence of iron deposits across the sample which suggests that at the lower concentrations there is not enough MNPs to interact with all the cells present and there is more uniform covering as concentration increases, although after treatment with iron at all concentration upon visual inspection it was seen that the iron did disperse in a uniform fashion across the sample. There was no discernible difference in the amount of iron internalised by different cell types suggesting that cell line variation does not play as large a role as concentration, but this would need quantitative analysis to confirm whether there is a difference in MNP internalisation.
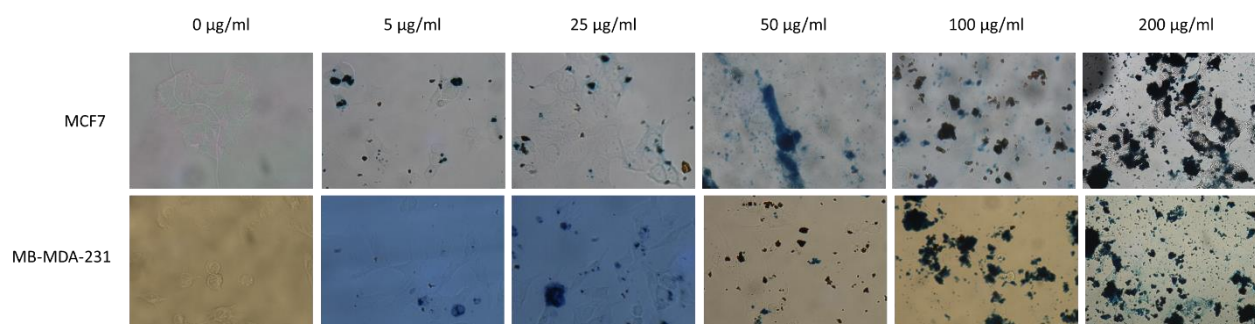
Figure 4.3.1 – Bright field microscopy of Prussian blue staining of MNPs after 24-hour incubation with increasing concentrations of MNPs from 0 – 200 µg/ml with both MCF7 and MB-MDA-231 cells (X40 magnification).

Quantification of the MNPs via Prussian blue becomes increasingly difficult with increasing concentration due to the diffusion of the iron signal on exposure to the acid solution that results in large areas of heavy staining that overpower the ability to observe the cells. Due to the difficulty in imaging the localisation of MNPs via Prussian blue other methods were adopted.

4.3.2   ICP-OES measurement of cellular uptake of MNP

ICP-OES allows for determination of the amount of iron that has been internalised by cells and was used to quantitatively measure the amount of intracellular iron after incubation with MNP. The amount of iron was measured across a concentration range of 0 – 200 µg/ml and incubation times of 1 – 24 hours post treatment. This would allow for the determination of the effect on the amount of MNP that was up taken by the cells and if one factor (concentration vs incubation time) were more

important in the internalisation of iron. Both MCF7 and MDA-MB-231 cell lines were directly compared to identify any differences in the amount of iron internalisation.

Figure 4.3.2 shows the effect of MNP concentration on the internalised iron at each time point. It is clearly visible that concentration influences the amount of internalised iron, with both cell lines showing an increase in the measured iron as the treatment concentration increases. This suggests that cells will internalise iron if it is readily available and that increasing MNP concentration increased iron concentration. This was consistent at all time points, with the highest concentration of 200 µg ml
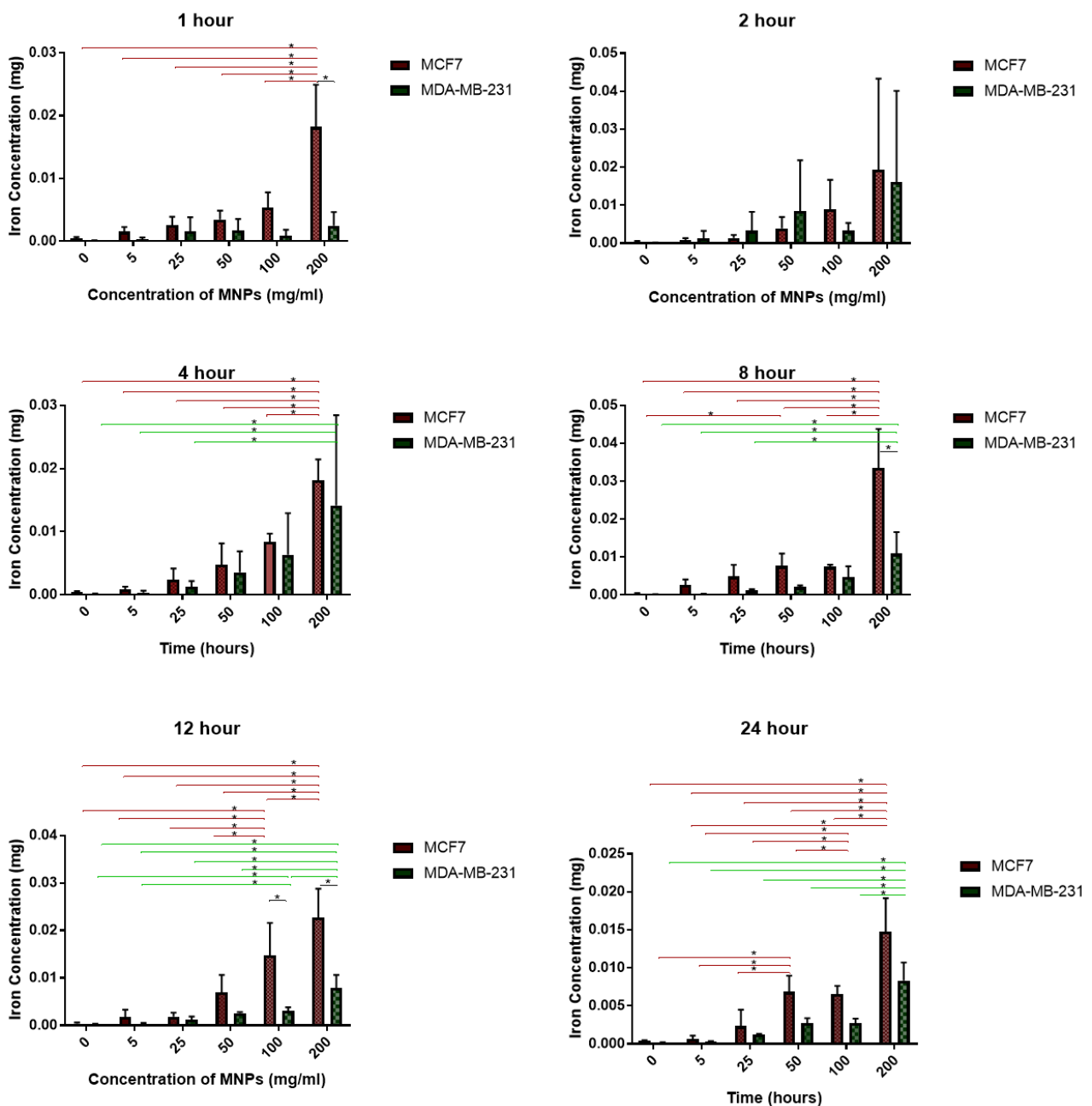
Figure 4.3.2 - Iron content measured intracellular after exposure of cells to MNPs at increasing concentration at multiple time intervals showing the effect of concentration. Intracellular iron content was measured via ICP-OES data point represent mean iron content measured (n=≥3) with SD. * denotes p= ≤0.05.

showing the highest amount of internalisation compared to all other concentrations. This may be a contributing factor as to why higher concentrations showed increased toxicity as the concentration of MNP increased due to a higher accumulation of iron within the cells leading to cytotoxic effects.

The MCF7 cell line consistently shows higher amounts of internalised iron than the MDA-MB-231 cells at all time points, this indicates that the MCF7 cells may internalise more of the MNPs or there may be a higher percentage of cells internalising MNPs in comparison. Although this is unable to be determined from ICP-OES as this averages out the entire population. As well as higher levels of internalisation the MCF7 cells showed more rapid internalisation than the MDA-MB-231 cell line as they reached a peak in iron concentration after 1 hour incubation with MNPs whereas the MDA-MB-231 were seen to increase more closely to the MCF7 levels of iron after 2 hours of incubation.

Time was seen to have only a small effect on the amount of iron the was internalised, but this was not determined to be significant (Figure 4.3.2) at any concentration. This suggests that the majority of cell uptake happens rapidly after exposure to MNPs and that there is only a small continuation of uptake as time progresses. MDA-MB-231 cells are seen to be move affected by exposure time than the MCF7 cell line as there is a noticeable but not significant trend in increasing iron concentration as the length of exposure time increases. The minimal impact of time on the amount of internalised iron may be due to cells only interacting with the MNPs that reach the cell membrane and as time progress there is no new interaction with MNPs left in solution as these have either stayed in solution of have sedimented into areas of the plate that there are no cells present, although it is seen after dosing with MNPs there is a uniform distribution of particles across the plate. The limited effect that time had on the internalisation of MNPs may be overcome if there was continued exposure of the cells to particles through agitation so it cannot be stated that the cells reach as saturation point as it is unknown where it is through a lack of cell particle interaction is the limiting factor. This can also help explain the difference in the amount of internalised iron between different concentrations as in the higher concentrations there is much more available iron and increases the amount that is internalised by the cells. Throughout this experiment there is a noticeable variation in the iron contents and this possibly due to variation brought on by differences in the amount of none internalised iron left within each well after washing and a more refined technique for uninternalized iron may be needed for improving the precision of the results.

From these results it can be assumed that internalisation is initiated very early after exposure to MNPs, and this process may be initiated as soon as the MNPs come into contact with the cell membrane and
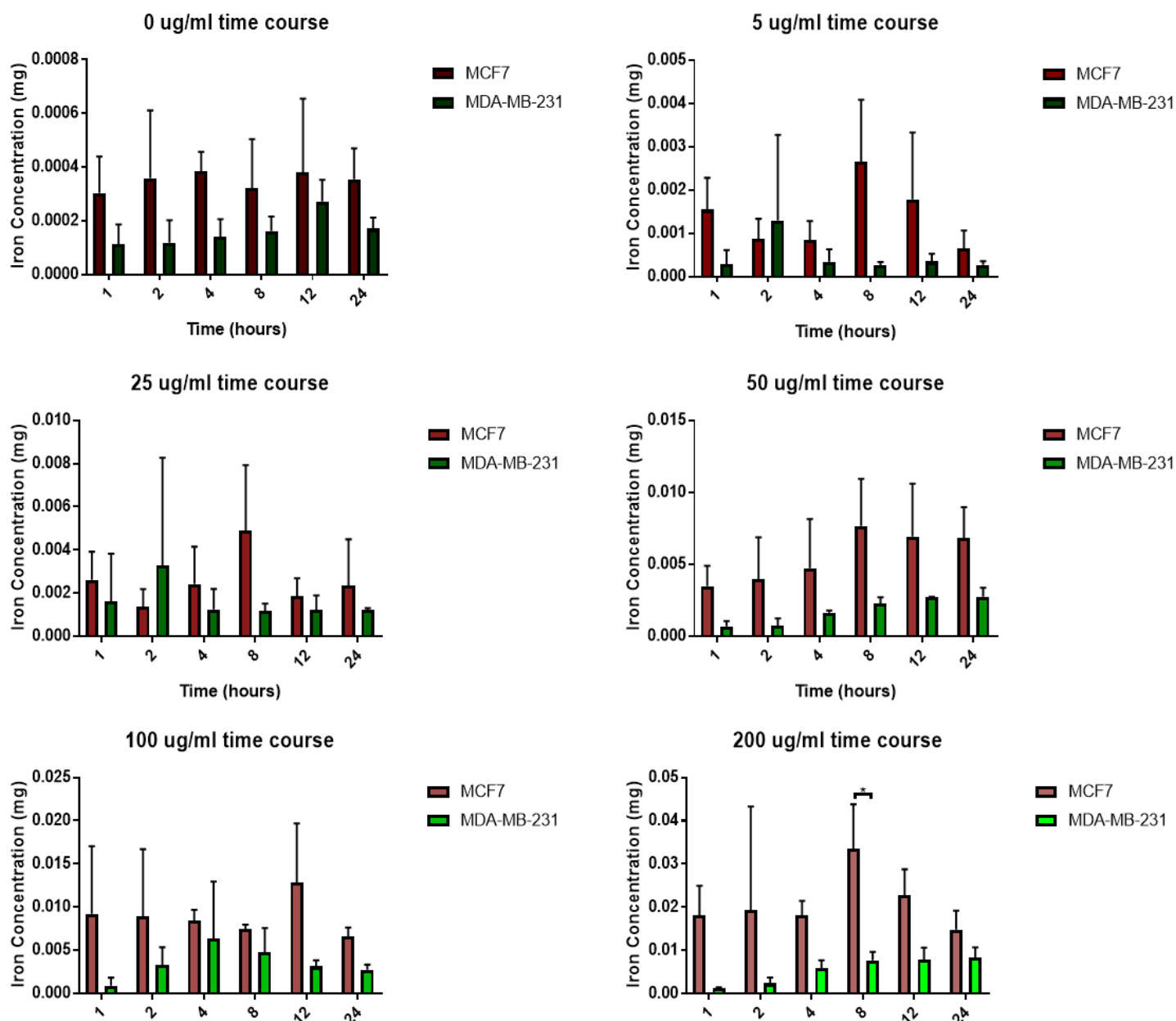
Figure 4.3.3 – Iron content measured intracellular after exposure of cells to MNPs at increasing concentration at multiple time intervals showing the effect of time on iron internalisation. Intracellular iron content was measured via ICP-OES data point represent mean iron content measured (n=≥3) with SD. * denotes p= ≤0.05.

although continued exposure does not significantly change the amount of MNPs internalised there is a small change over time indicating that treatment could be used as soon as 1 hour after treatment but allowing maximum exposure time may prove beneficial.

4.3.3 THE DETERMINATION OF MNP UPTAKE UTILISING FLUORESCENTLY DOPED MNPs.

Fluorescent doping of the APTES layer with RITC was performed to allow for imaging of NPs using fluorescent microscopy. This allowed for the determination of the number of cells that have

97

internalised the MNPs without altering the surface characteristics of the MNPs (Figure 4.3.1). If the surface characteristics of the MNPs had been altered, then they would not be visible under fluorescent microscopy due to the removal of the fluorescent Rhodamine B with the silica coating.

4.3.3.1 Uptake and localisation of RITC MNPs

Fluorescent microscopy allows for clear imaging of particles within cells and can show localisation and whether MNPs are internalised or cling to the cell membrane. Internalisation of the MNPs is crucial to how they will affect cells during hyperthermia treatment. If MNPs do not internalise then hyperthermia treatment is likely to be less effective in targeting intracellular proteins and an increased chance of inducing cell death. This is due to heating affecting the cell membrane before the nucleus, as temperature dissipates as the distance from the particles decreases.[156,230–232]

Fluorescent microscopy of MCF7 and MDA-MB-231 cells 24 hours post incubation with RITC MNPs at concentrations of 5 – 200 µg ml show internalisation of the MNPs to within the cell membrane (Figure 4.3.3) with the number of particles appearing to increase as the concentration increases. At all concentrations, and in both the MCF7 and MDA0MB-231 cell lines, the MNPs show internalisation intracellularly and they show peri nuclear localisation. This is consistent with literature that has shown that NPs, in particular silica particles of a similar size distribution are uptake as single particles and show peri nuclear localisation.[233,234] This similarity suggests that MNPs synthesised here behave in a similar manner regarding uptake and localisation. Although the particles show peri nuclear localisation, they do not appear to have entered the nucleus but remain outside of the nuclear membrane (Figure 4.3.3). This suggests that although they may be able to cross the cell membrane, they are blocked from entering the nuclear membrane. The majority of translocation of molecules from the cytoplasm to the nucleus is carried out via the nuclear pore complex, which has a pore diameter of < 39 nm. The hydrodynamic size of the MNPs is greater than this and so it could by why MNPs are unable to cross the nuclear membrane.[235] Although this inability to cross the nuclear membrane is known to reduce nanotoxic effects of the MNPs, with NPs capable of crossing the nuclear membrane showing increased mutagenic capabilities due to the interaction of the NP and intranuclear constituents.[236,237] The localisation of the MNPs to the nucleus is an increased benefit, as it localises close to BRCA2. This is a nuclear protein and close localisation can help reduce thermoablative damage to cell structure and organelles. As the concentration increases there are visibly more extracellular particles present even after extensive washing, this may affect how the cells are heated during MHT.
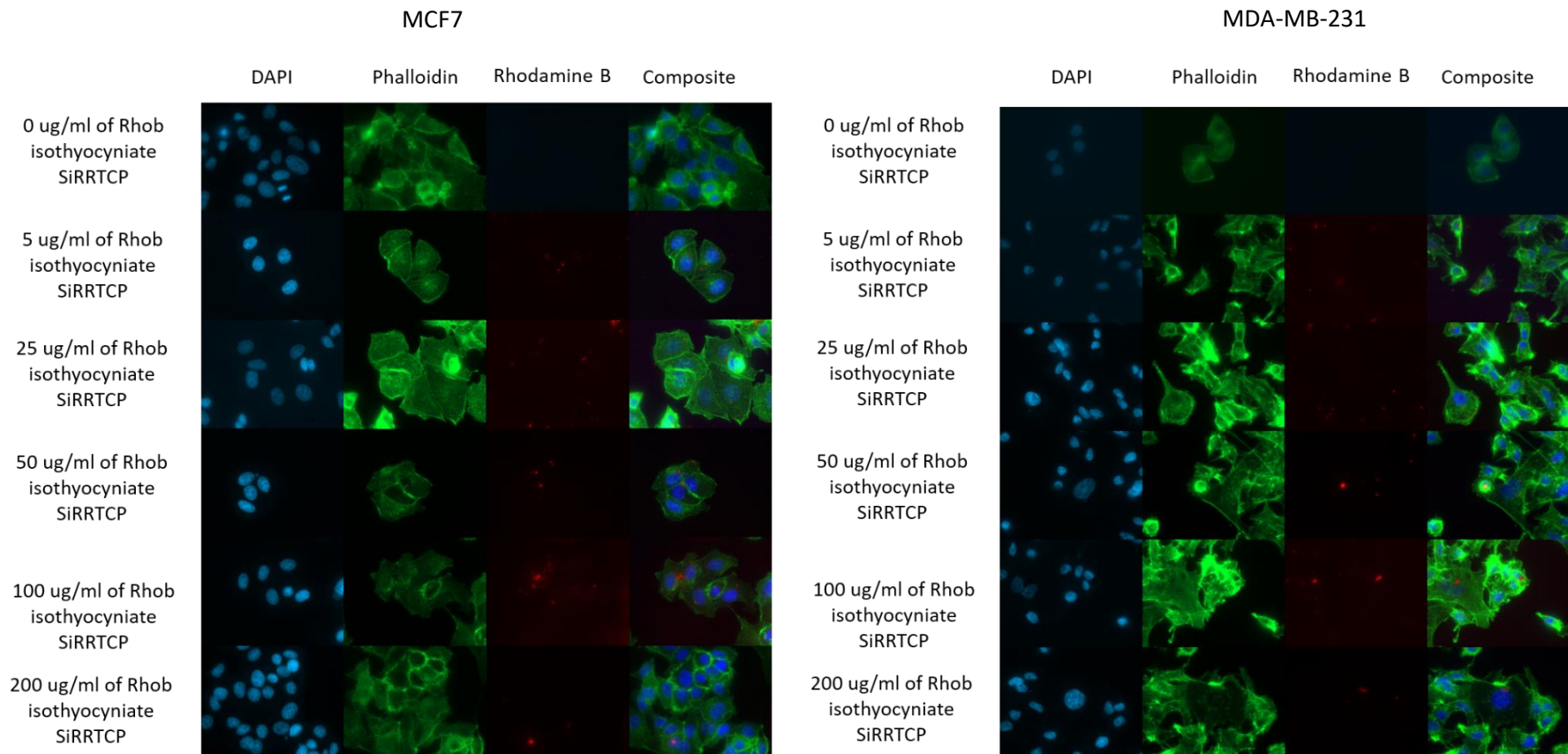
Figure 4.3.4 – Representative images showing the internalisation of RITC MNPs in both MCF7 and MDA-MB-231 cell lines image after 24-hour exposure to RITC MNPS. Immunofluorescent staining of cell structures with Dapi staining (Cyan) actin filament staining with phalloidin(green) and RITC MNP (Red). Imaged with a 40X objective on an inverted microscope.

Fluorescent tagging of the MNPs allows for the internalisation of MNPs to be quantitatively analysed via flow cytometry. This allows for the determination of the number of cells that have internalised MNPs to be assessed (Figure 4.3.5) shows the percentage of cells showing internalisation after 24 hours incubation with MNPs at increasing concentrations. As expected, there was a concentration dependent factor observed with increasing concentration of MNP causing an increase in the amount of cells that internalised MNPs. As the concentration of MNPs increased there was a rising trend in the amount of cells that showed particle internalisation, this was only significant in the 100 and 200 µg ml concentrations in both cell lines. In the MCF7 cell line concentrations of 100 and 200 µg ml showed a significant increase ($p > 0.01$) compared to all other concentrations, there was no significant difference between 100 and 200 µg/ml. A similar result is seen in the MDA-MB-231 cell line, as only 100 and 200 µg/ml showed a significant difference ($p > 0.01$) compared to lower concentrations. 200 µg/ml showed a significant increase compared to 0, 5 and 50 µg/ml. 100 µg/ml showed a significant increase compared to 0 and 5 µg/ml.

Both cell lines showed a similar percentage of internalisation at every concentration tested, this confirms what is seen from the Prussian blue staining that the type of cell does not affect how many cells are able to internalise MNPs but that this is more reliant on the MNP concentration as there is a sharp rise in the number of RITC positive cells in concentrations above 5 µg/ml and this continues to rise. The increase in the number of cells internalising MNPs may help to explain the concentration dependent result seen in the ICP-OES measurements as the higher number of cells containing MNPs would increase the amount of iron that is present in the sample as a total. These results indicate that the major limiting factor in iron uptake is the availability of iron in proximity to the cells.

From the ICP-OES analysis roughly only 10% of the iron used to treat the cells at each concentration is internalised and the rest is removed during washing. Even though it is clear from the results in the higher concentrations that they should be capable of internalising all of the particles that have been administered at the 5µg/ml as both the samples treated with 100 and 200 µg/ml internalised over 5 µg of iron (close to 20 µg) an amount greater than what is administered at the lowest concentration. This result coupled with that seen in the percentage of cells that had internalised MNPs from fluorescent microscopy a Prussian blue staining suggests that in the experiment type chosen that it is exposure to MNPs and not just concentration that is a limiting factor.

Although it is seen that there is no significant difference in the percentage of cells internalised by MNPs between both the MCF7 and MDA-MB-231 cells the difference in the amount of iron internalised by the MCF7 cell suggest that the MCF7 cells internalise more MNPs than the MDA-MB-231 cells. This shows that although there is no cell line dependant effect on the ability of the particles to internalise MNPs the amount of MNP that is uptake is determined by the cell line (Figure 4.3.5).
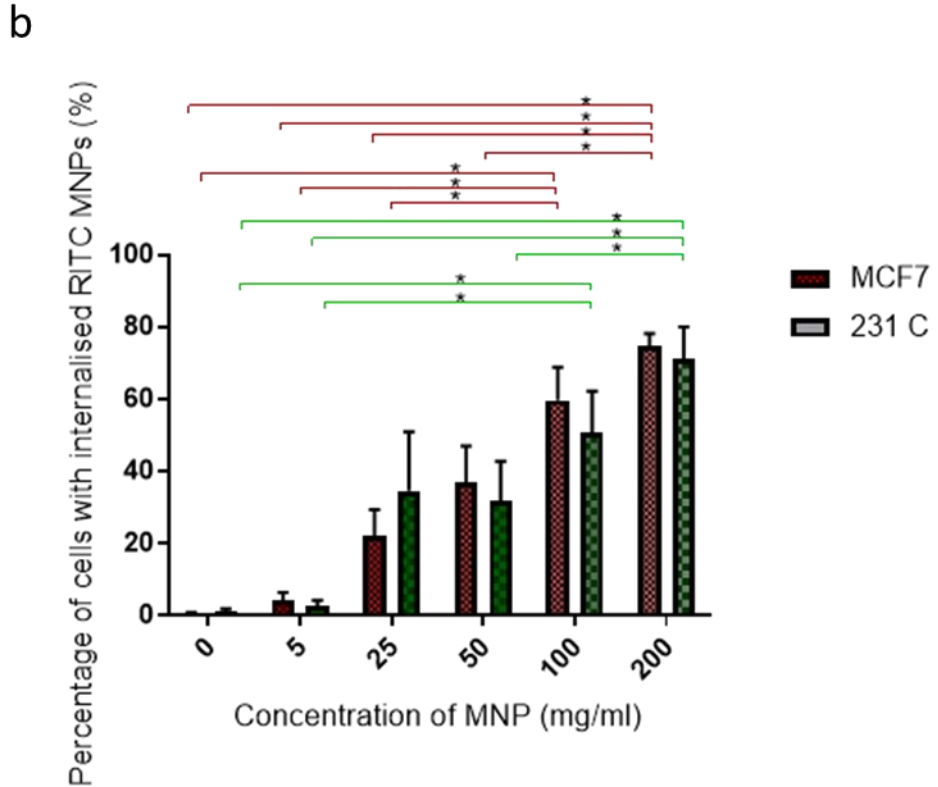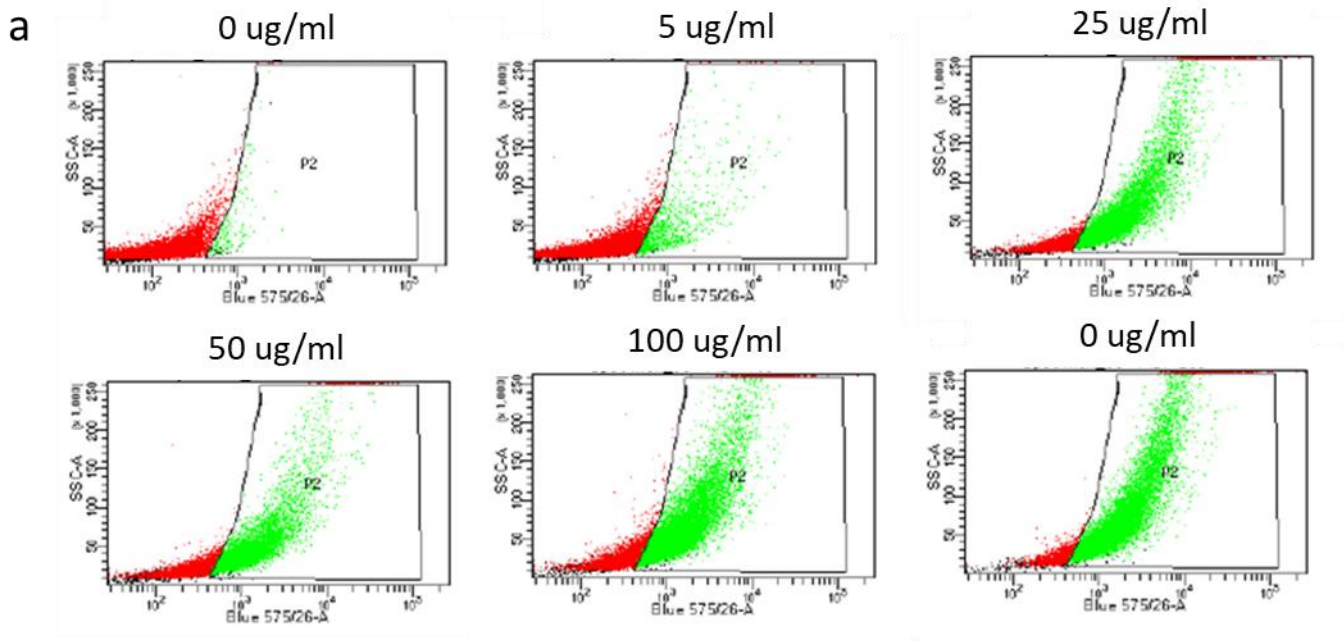
Figure 4.3.5 – Percentage of MCF7 and MDA-MB-231 cells showing internalisation of RITC MNPs after 24 hours exposure. (a) Representative MDA-MB-231 plot showing the increase in cell showing a fluorescent signal after treatment with increasing concentrations. b Percentage of cells showing a fluorescent response after treatment with RITC MNPs. Data points represent mean percentage of cells with RITC MNP uptake +/- SEM(n=≥3). * denotes P≥ 0.05

4.4 CONCLUSIONS

MNPs showed a dose dependant nanotoxicity as consistent with literature.[238] Increasing concentration showed higher levels of nanotoxicity but this was only statistically significant at higher concentrations. However, an increasing trend of toxicity was observed for all concentrations. Understanding the toxicity of MNPs is important in developing them as a treatment as MNPs (have been removed from clinical use as MRI contrasts due to safety concerns (Clariscan) as well as severe reactions (Feridex) upon administration in their use.[239,240]

Both MCF7 and MDA-MB-231 cell lines exhibited an increase in the sub G1 population of cells and as concentration of MNPs increased this indicated an increase in the number of cells undergoing apoptosis. This was concurrent with a slight drop in the number of cells in the G2M phase of the cell cycle. Increasing concentrations of MNPs led to an increased induction in the number of γH2AX foci within cell nuclei, this indicates an increase in the number of DNA DSBs. The presence of the foci indicates DNA damage within the cells, although this may indicate negative effects induced by MNPs it can also be beneficial for the treatment type (MHT) that is to be performed. As an increase in DSB would increase the likelihood of cell senescence when treated with a PARP inhibitor after degradation of BRCA2, due to the inability of the cells to perform HR to repair the DSB.

Concentration was not the only factor that was shown to influence nanotoxicity, the exposure time was also seen to increase the levels of nanotoxicity. A significant increase in nanotoxicity was observed after 48 hours, this increased further as exposure time increased. When an exposure time of 24 hours was used there was no significant effect on cell viability. The effect of continual exposure was more pronounced in the MDA-MB-231 cell lines compared to MCF7 cell line; this indicates there may be a cell line dependant component on nanotoxicity when exposure is longer than 24 hours. The effect of toxicity is especially important *in vivo. As* although the majority of MNPs are cleared from the blood stream within 24 hrs when observed *in vivo* there is accumulation of MNPs in the spleen, liver, heart and lungs after 24 and 48 hours which dissipates over the course of weeks.[241–243] With this accumulation understanding of tolerated MNP concentrations is crucial in avoiding chronic iron overload in these organs.[242]

Internalisation of MNPs was seen to be affected by the concentration of MNPs, with increasing concentrations showing increased internalisation in both cell lines. Although concentration played an effect on MNP internalisation, exposure time did not have a statistical effect on the amount of MNP internalisation. This is consistent with literature

findings that concentration plays a larger role on the internalisation of MNPs than exposure time.[224] These findings suggest that the majority of internalisation takes places as soon as MNPs interact with the cell membrane. From these finding it was decided to take forward the 5, 25 and 50 μg/ml concentrations of MNP as although there was no statistically significant drop in cell survival at the highest concentrations of 100 and 200 μg/ml there was a noticeable effect, and this would likely increase significantly when MHT. [244] The focus of mild hyperthermia is to not induce permeant cell damage but rather to induce sublethal cell damage that is then targetable with PARP inhibitors. The choice of concentration is also a factor for deciding concentration of MNPs *in vivo* as high concentrations of MNPs are more likely to cause occlusion and blockages of blood vessels due to MNP aggregation.

CHAPTER FIVE: HYPERTHERMIA OF BREAST CANCER CELL LINES

5 HYPERTHERMIA OF BREAST CANCER CELL LINES

5.1 INTRODUCTION

The use of PARP inhibition for cancer treatment relies on the idea of synthetic lethality. Synthetic lethality works on two conditions either of which would be non-lethal, but when combined they produce lethal results. In PARP inhibition this relies on a mutation in either *BRCA1 or BRCA2* within tumours which causes the loss of expression of wild type *BRCA1* or *BRCA2*. This enables the treatment with PARP inhibitors, as PARP is responsible for the repair of SSBs in the BER repair pathway and its inhibition can lead to the production of DNA lesions which are mostly DSB and stalled replication forks. These lesions are normally repaired by BRCA1 or BRCA2 and the loss of these proteins in *BRCA* mutated cancers makes them susceptible to PARP inhibition, as the accumulation of these DNA lesions which are unable to be effectively repaired by HR result in cell death.

BRCA2 has been shown to be susceptible to mild hyperthermia at temperatures that are non-lethal to the cell. However, there is little evidence of the effective use of PARP inhibitors in the treatment of cancer cell lines after mild hyperthermia (HT) has been induced.

Magnetic hyperthermia (MHT) has been shown to be more efficient in delivering heat than current methods of hyperthermia. However current MHT treatments look at the use of MNPs for thermoablation of tumours and not the application of mild hyperthermia. The application of mild hyperthermia is relatively controllable in other treatments methods, such as hot water perfusion where the temperature is controlled by the water temperature. Controlling the temperatures reached in MHT is more complicated and requires the adjustment of not only the concentration of MNPs, but the length of time spent in the magnetic field and the field strength that is applied. This is due to the how MNPs respond to an AMF and the power output of the MNPs is directly affected by a multitude of factors both intrinsic to the MNPs as well as those externally applied. So, fine tuning of these factors in applying MHT to tumours for mild hyperthermia is required. It is hypothesised that the use of controlled application of MHT can induce temperatures that are capable of inducing BRCA2 degradation without causing lethal thermal damage to cells, which would allow for cancers that are not currently able to be treated with PARP inhibitors which can produce better health related quality of life in cancer patients.[40,41]

Currently there is no work that has shown that MNPs have induce PARP sensitivity via MHT in wild type BRCA2 cell lines. This chapter will address if HT causes sensitisation of MCF7 and MB-MDA-231 cells to PARP inhibition and whether this can be replicated using MHT.

The aims of this chapter are:

- Induce BRCA2 degradation in MCF7 and MB-MDA-231 cell lines via HT.

- To treat both cell lines with a combined therapy of PARP inhibitor and HT to observe if this does induce cell death as a combination therapy.

- Identify a concentration of MNP and a length of exposure to an alternating magnetic field (AMF) that are capable of inducing BRCA2 degradation and show sublethal levels of HT based cell death.

- Use a combined therapy of MHT and PARP inhibition to induce cell death in both the MCF7 and MB-MDA-231 cell lines.

5.2 INCUBATOR INDUCED HYPERTHERMIA

5.2.1 HYPERTHERMIA INDUCED LOSS OF BRCA2

The induction of BRCA2 loss by hyperthermia would indicate that cells should become sensitised to PARP inhibition due to impaired HR. MCF7 and MB-MDA-231 cells were exposed to temperatures of 42 °C to determine if this induced loss of BRCA2 protein in these cell lines. Western blot analysis of the cells showed that exposure to hyperthermia conditions for as little as 1 hour were enough to induce loss of BRCA2 protein in both cells' lines (Figure 5.2.1). This loss of BRCA2 shows that both MCF7 and MB-MDA-231 cells are sensitive to HT treatments. This loss should infer that these cells would be sensitised to PARP inhibition after HT, if this loss of BRCA2 has resulted in impaired HR. BRCA2 is responsible for the recruitment of RAD51 to the site of ssDNA for homology search in repairing DSBs of HR. To determine if hyperthermia induced impaired HR as a result of loss of RAD51 recruitment the effect of HT on the induction of RAD51 foci in cells treated with 4 Gy of IR was observed. Incubator hyperthermia (IHT) treatment resulted in a reduction of RAD51 in both cells compared to the IR treated cells. In MCF7 cell line IHT resulted in a reduction in the number of RAD51 foci however this was reduction was not to the same level as in the untreated control which suggests that there is not complete loss of BRCA2 in the MCF7 cells. Whereas MB-MDA-231 showed a reduction in RAD51 foci to the same levels as the untreated control. This suggests that the MB-MDA-231 cell line is more sensitive to HT than the MCF7 cell line. The loss of BRCA2 and subsequent RAD51 recruitment suggest that hyperthermia should induce sensitisation to PARP inhibition.
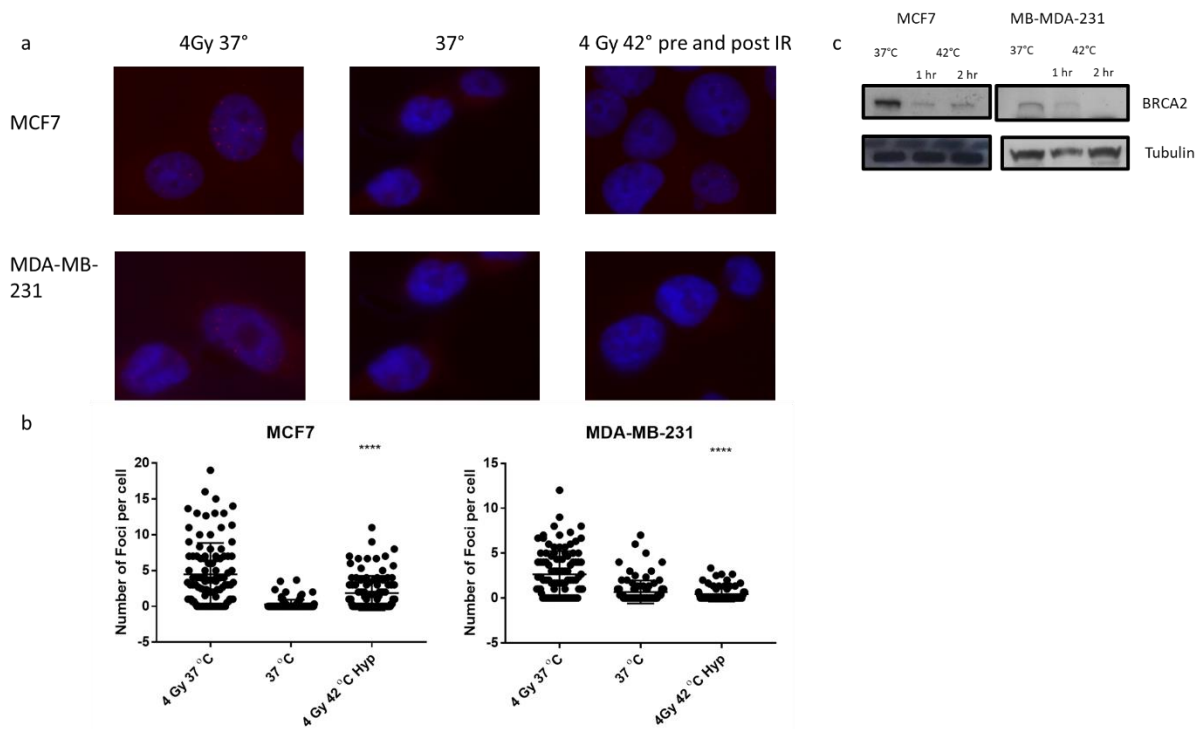
Figure 5.2.1 – Effect of sustained 2 hours hyperthermia on MCF7 and MB-MDA-231 cells. a) Rad51 foci formation after 4 Gy IR both with and without 42 °C hyperthermia viewed 4 hours after IR under 100x microscope objective. b) Average number of foci per cell after IR treatment and IR combined with hyperthermia. c) Representative western blot of BRCA2 and tubulin expression after 1- and 2-hours hyperthermia in MCF7 and MB-MDA-231 cells. **** signifies statistically significant difference (p≥0.0001) Mann Whitney U test of the significant difference between the 4gy 37 °C treated cells and the 4Gy 42 °C treated cells.

5.2.2 COMBINED OLAPARIB AND INCUBATOR HYPERTHERMIA

With the loss of BRCA2 and impaired recruitment of RAD51 after IHT treatment it is theorised that this should induce a level of cell sensitivity in these cells after treatment. To determine if a single IHT treatment would sensitise both MCF7 and MB-MDA-231 cells to PARP inhibition, both cell lines were treated for 2 hours at 37 and 42 °C with increasing concentrations of Olaparib. This single dose of IHT showed no effect on the cell's ability to form stable colonies. This is consistent with work showing that temperatures under 45 °C are sub lethal and there are only low apoptotic effects observed at temperatures of 42 °C. It was observed that the effect in both cell lines for the untreated controls at 37 °C and 42 °C and for the loading controls. This shows that hyperthermia at these temperatures is well tolerated and does not induce cell death in itself. The addition of PARP was seen to have a negative effect on the survival of the colonies in both cell lines in a similar dose dependant response. With concentrations of 2.5 µM and higher, causing a complete loss of colony formation in both cell lines (add figure reference). Although there was a dose dependant effect on the cell survival with Olaparib there was only a small not significant effect on the cell survival when treated at 42 °C instead of 37 °C at concentrations of 0.5 and 1 µM. The MDA-MB-231 cell lines showed slightly more susceptibility than the MCF7 cells as there was a significant drop at 0.5 µM but this did not continue

to the 1 µM concentration of Olaparib, although this is possibly due to the low levels of cell survival. The increased susceptibility of the MB-MDA-231 to HT matches with the observed results from the RAD51 formation after IHT which indicate a much lower foci formation after HT compared to MCF7s.
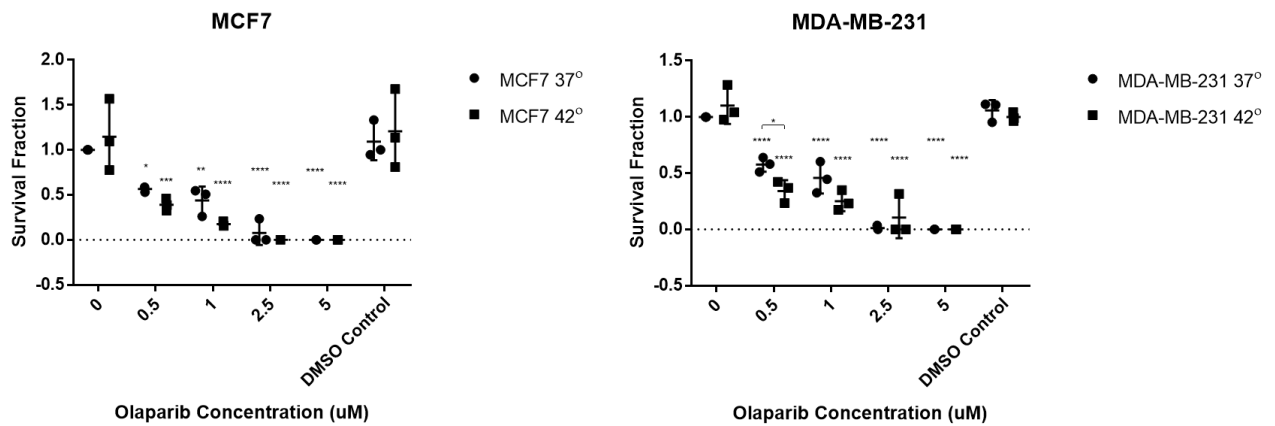
Figure 5.2.2 – Survival Fraction of MCF7 and MB-MDA-231 cells after 2 hours incubator hyperthermia (42 °C) and non-hyperthermia conditions with increasing concentration of Olaparib. Data points represent individual measurements +/- SD. * denotes p= ≤0.05, ** denotes p= ≤0.01, **** denotes p≤0.0001 significant difference (One-way ANOVA with Dunnett correction for multiple comparisons).

Although BRCA2 degradation and a reduction in RAD51 indicate a loss or reduction in effective HR via HT, this was observed in cells treated for 2 hours at 42 °C. This effect was not observed when treatment with PARP inhibitors in the MCF7 cell line and only a small effect was observed in the MB-MDA-231. Although this contradicts what was hypothesised would happen, this could be due to the fact that BRCA2 degradation via HT is not permanent. HR is only used during the S/G2 cell cycle phase and there is not a long enough degradation of hyperthermia to induce the cell death via PARP inhibition and induced synthetic lethality.

5.2.3 MULTIPLE HYPERTHERMIA TREATMENTS AND INDUCED SYNTHETIC LETHALITY

A single HT treatment was not seen to induce PARP sensitivity in the MCF7 and MB-MDA-231 cell lines, It was theorised that multiple rounds of hyperthermia treatment might increase the amount of time that BRCA2 degradation occurs for increasing the effectiveness of treatment with PARP inhibitor. HT was applied for three consecutive days along with Olaparib, with either a single or double treatment on each day. It was believed that the increased portion of time the cell was exposed to hyperthermia would increase the effect of PARP inhibition. The effect of single daily HT for 3 consecutive days showed that temperatures of 42 °C had no effect on the cell cycle. This result was promising as it showed that even with repeated treatments there was no effect in the viabilities of the cells, in both the MCF7 and the MB-MDA-231. Cell viability was measured by an alamar blue viability assay which showed that 24 hours after the final treatment there was no observed toxicity of Olaparib in either the MCF7 or MB-MDA-231 cell lines. At 48 hours the MCF7 showed a decrease in the hyperthermia treated cells at 0.5 and 1 µM, but this was not statistically significant. This decrease was observed at

72 hours but again it was not seen to be significant, but this does imply that multiple treatments may offer improved performance in HT in conjunction with PARP inhibitors. The MB-MDA-231 cell line showed no effect in the hyperthermia on cells treated at 0.5 µM in both 48 and 72 hours post final HT treatment, but there was a reduction in cell viability in the 1 µM concentration. In both the MCF7 and the MB-MDA-231 cell lines Olaparib only appeared to induce significant ($p=>0.05$) cytotoxicity at concentrations of over 1 µM at 48 and 72 hours. Because of this and the high level of toxicity that was observed in the clonogenics assay (Figure 5.2.2) it was decided to not continue with concentrations above 1µM.
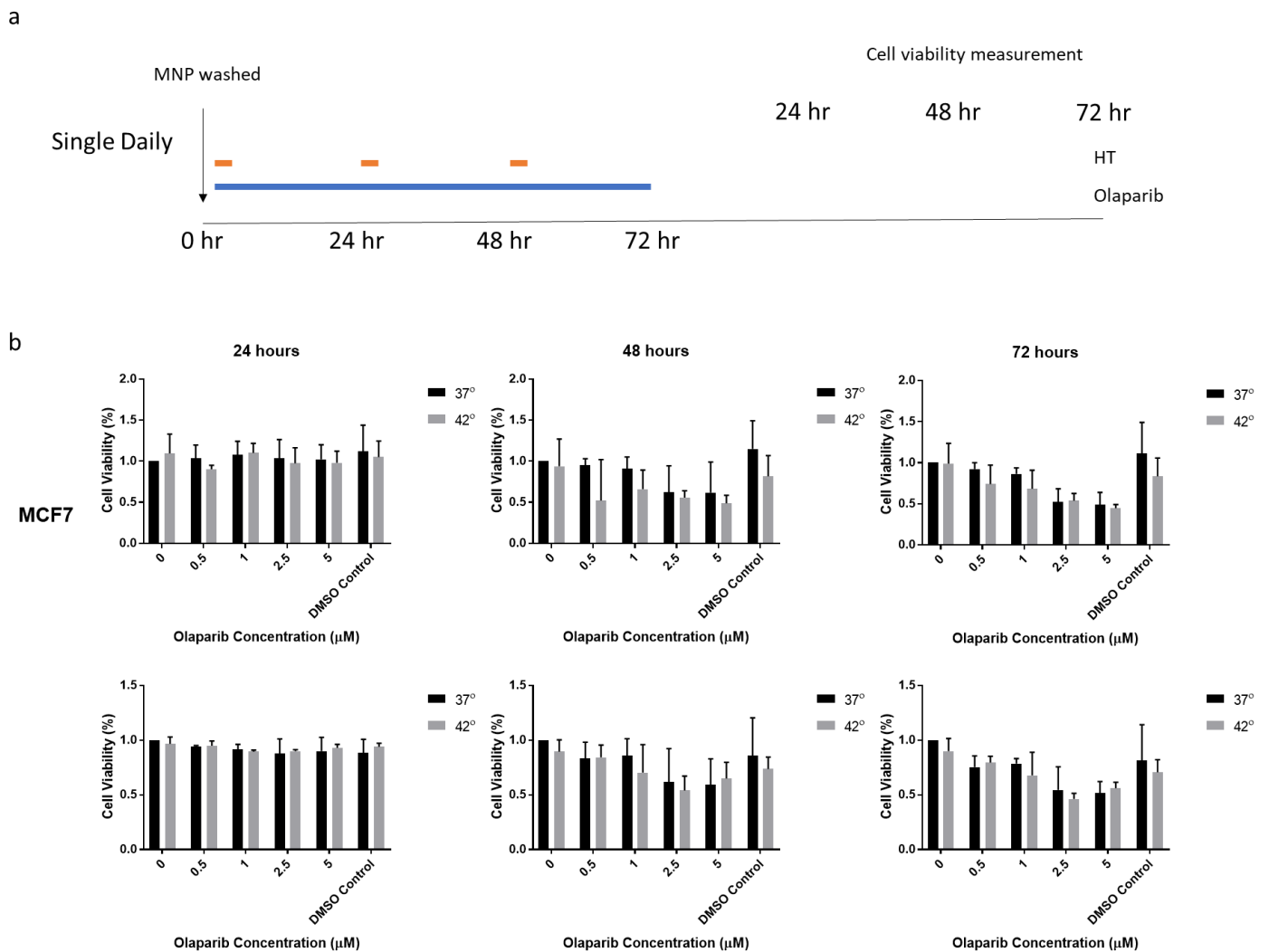
Figure 5.2.3 – Cell viability of conditions MCF7 and MB-MDA-231 cell lines with both hyperthermia conditions and 37 °C with increasing concentration of Olaparib after 3 days single daily doses of hyperthermia (2 hours). Cell viability was measured at 24, 48 and 72 hours post final hyperthermia treatment. Data points represent mean cell viability +/- the SD.

Twice daily treatment of IHT were performed with incubation at 37 °C between treatments, it was hoped that the increased exposure to HT would increase the amount of time cells were sensitised to

PARP inhibition and result in increased sensitivity. In both the MCF7 and MDA-MB-231 cell lines there was no increased sensitivity to PARP inhibition 24 hours after final treatment. After 48 hours there was an observed drop in the viability of the MCF7 cells at 1 μM but this was not observed at 72 hours. Possibly due to a further drop in cell viability after further exposure to Olaparib. In the MB-MDA-231 cells there was a small observed drop in the 0.5 and 1 μM concentrations of Olaparib but this was not statistically significant. As this progressed to 72 hours there was only a small observed decrease in viability in the 1μM concentration.
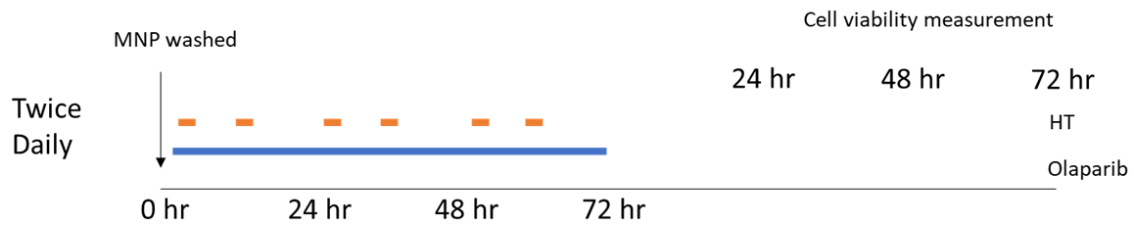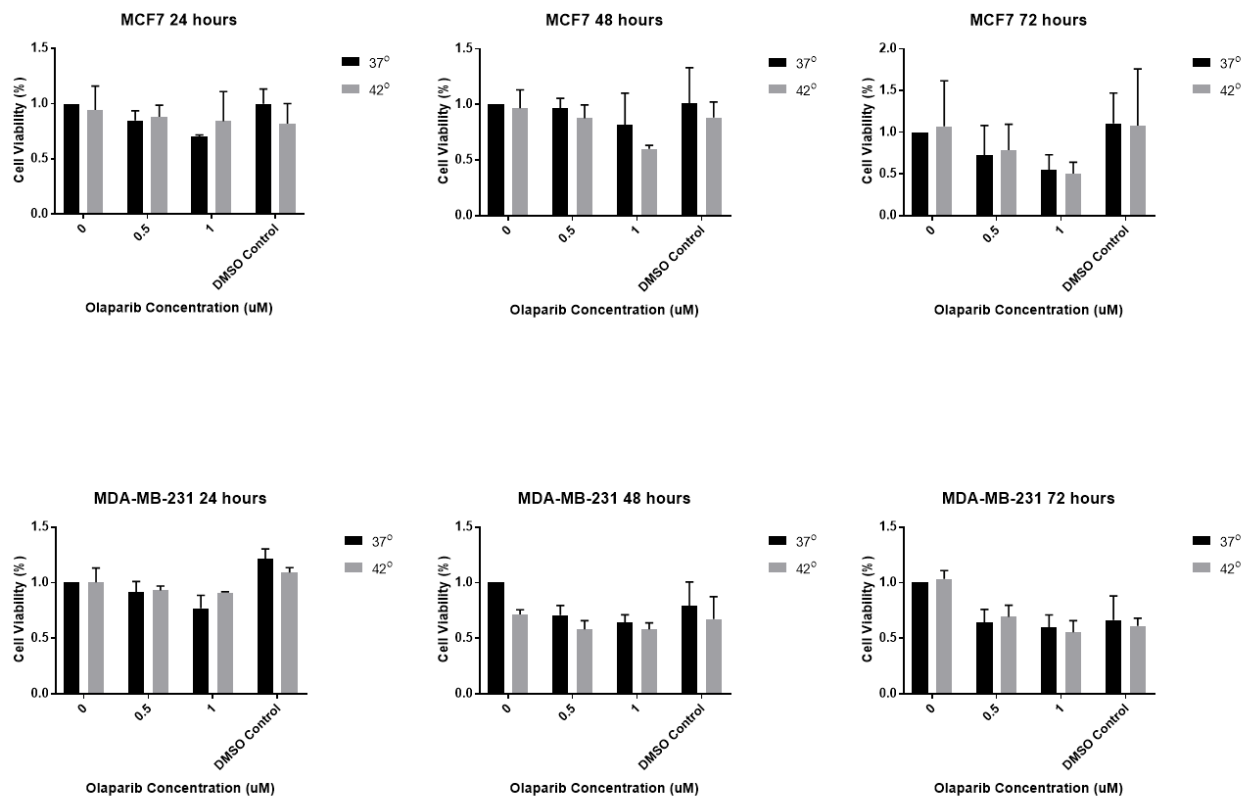
Figure 5.2.4 – Cell viability of conditions MCF7 and MB-MDA-231 cell lines with both hyperthermia conditions and 37 °C with increasing concentration of Olaparib after 3 days twice daily doses of hyperthermia (2 hours). a) Representative schematic of hyperthermia treatment regime. b) Cell viability was measured at 24, 48 and 72 hours post final hyperthermia treatment. Data points represent mean cell viability +/- the SD.

The addition of a second treatment for twice daily treatment of HT treatments did not increase sensitisation of either cell line significantly 72 hours post final treatment (Figure 5.2.4). This contradicted observed evidence of the effects of HT therapy. This lack of effect was believed to be due to the short time scale post treatment that cells were analysed for after treatment and that a more exaggerated affect may be observed with analysis at a longer time scale.

5.2.4   LONG TERM CELL SURVIVAL AFTER COMBINED HT AND PARP INHIBITION

In previous experiments exposure of MCF7 and MB-MDA-231 cell lines were exposed to 2 hours of HT for 3 consecutive days either singularly or twice daily exposures in the presence of Olaparib. This was observed to have minimal effect on cell viability 72 hours post final treatment even though HT treatment was observed to induce a degradation of BRCA2 and a reduction in recruitment of RAD51 foci indicating a loss of effective HR. To identify if HT does induce PARP sensitivity, a clonogenic assays of cell survival 10 days after initial treatment was performed to determine if this combined therapy effected the ability of the cells to form colonies and these colonies to grow. Cells were treated as shown in Figure 5.2.5a with the single and double treatments being performed at the same point daily. Both single and daily HT treatment was observed to have an effect in both cell lines. The MCF7 cell lines showed a small reduction in survival fractions when treated with a single HT dose for 3 consecutive days at both concentrations. This effect was enhanced when twice daily treatments were used and resulted in the reduction of the survival fraction to almost 1 in both the 0.5 and 1 μM concentrations. The MB-MDA-231 cell line showed similar results to the MCF7 cell line, but there was a greater noticeable effect of the single HT treatment on survival fraction than in the MCF7 cells at concentrations of 0.5 and 1 μM. When twice daily treatments were used this caused almost complete loss of colony formation in the 0.5 μM treated samples and complete loss of colony formation in the 1 μM samples. As HT treatment alone, even with multiple rounds of treatment, was shown to have no effect on the ability of the cells to form colonies this effect can be attributed to the combined treatment of the cells with both Olaparib and HT. In both cell lines it was observed that twice daily treatment of HT caused a significant reduction in cell survival compared to a single treatment alone. This confirms the hypothesis that more frequent exposure to HT conditions increases the effectiveness of PARP inhibitors, most likely through the increased length of time that BRCA2 is degraded for. The reasons for this increased effect could also lie in the fact that HR recombination only takes place during the G2/M phase of the cell cycle. By increasing the amount of HT treatment this may increase the number of cells that are susceptible to PARP inhibition as an increased population may be in this cell cycle phase whilst BRCA2 is inhibited. The MB-MDA-231 cells showed an increased sensitivity to HT with Olaparib due to complete loss of colony survival with twice daily treatment at 1 μM. The reason for this increased sensitivity requires further experimentation but it could be due to the observed

increased impairment of RAD51 formation in the MB-MDA-231 cells, although it is unclear if this is the main driving factor.

a
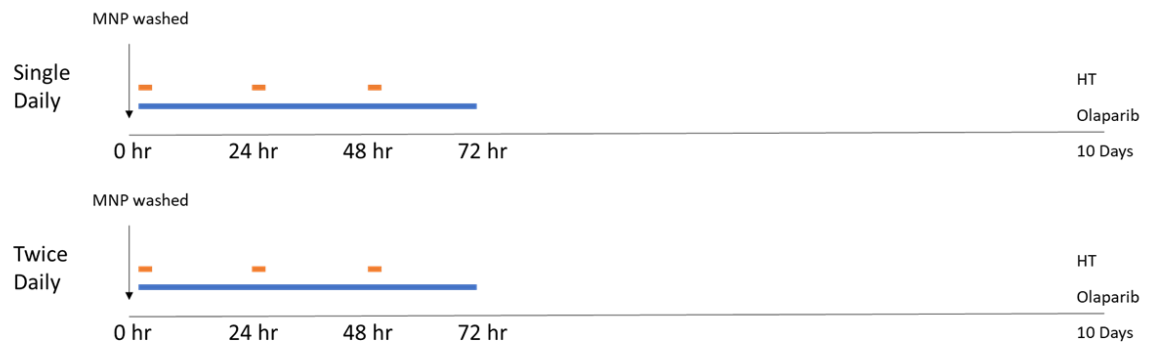
b
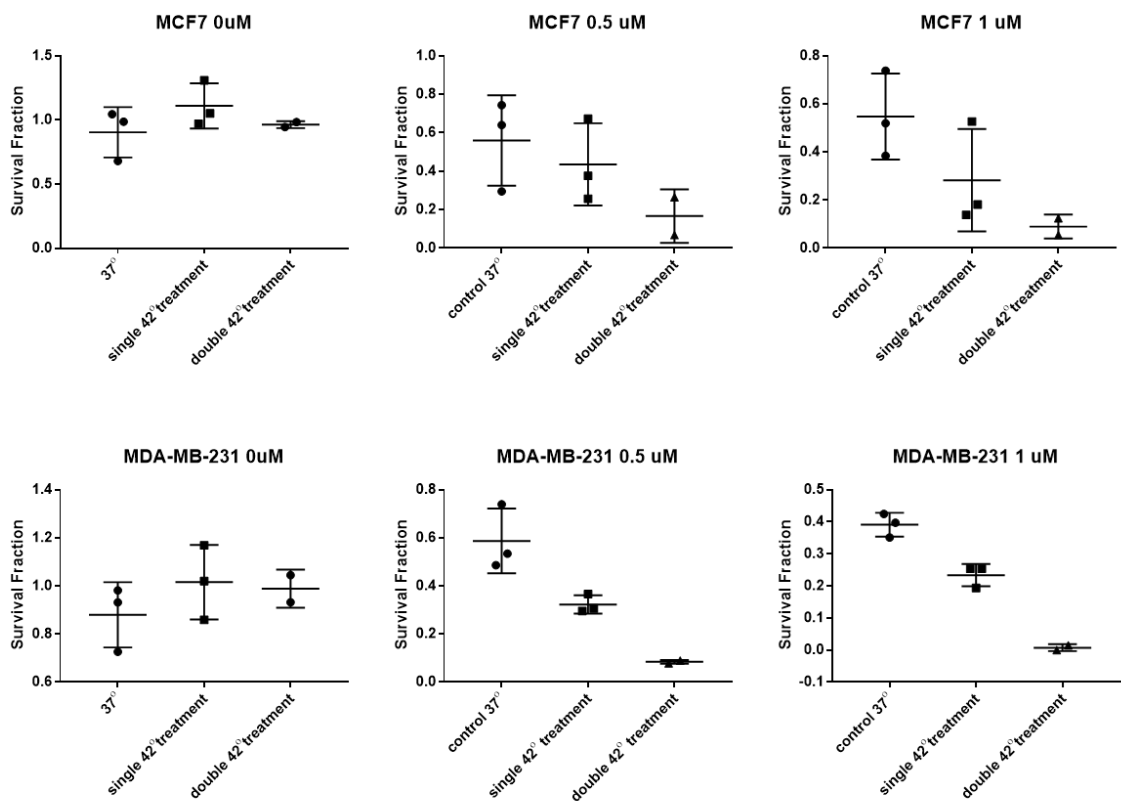
Figure 5.2.5 – Survival fraction of MCF7 and MB-MDA-231 cells treated with combined hyperthermia treatment of 42°C and increasing concentration of Olaparib with both a single and double treatment of hyperthermia for 3 consecutive days. Data points represent individual survival fractions normalised to the DMSO control +/- SD.

Previous experiments here have shown that HT is a valid method for inducing PARP sensitivity with a controlled temperature of 42 °C via an incubator (Figure 5.2.5), but it is yet unseen if this can replicate this using MHT. MHT does not allow the same controlled dose of temperature as using an incubator. Therefore, determining a safe concentration that can induce HT without causing a high level of cell death, but sufficient temperature to induce BRCA2 negativity in the cell lines tested needs to be

identified. Here MNPs were used at concentrations previously identified to be well tolerated by the cells (5, 25 and 50 µg/ml).

The effect of combined Olaparib treatment and IHT was also tested in two further cell lines TS1 and 4T1. TS1 is a MMTV-PyMT (mouse mammary tumour virus polyoma middle tumour-antigen) mouse mammary gland carcinoma model of breast cancer and 4T1 is a breast cancer cell line that resemble human triple negative breast cancer cell lines (e.g., MDA-MB-231) as it is estrogen, progesterone and HER2 negative and is used to model metastatic cancers in mouse animal models.

Both cell lines were treated with increasing concentrations of Olaparib to determine the effect of Olaparib on the cells. TS1 cell lines showed sensitivity that was consistent with both MCF7 and MDA-MB-231 with concentrations higher than 1 µM showing a significant reduction on cell survival. Whereas in the 4TI cell line there a small non-significant effect of increasing concentrations of Olaparib on cell survival. This shows that the 4T1 cell line is more tolerant of Olaparib than the other cell lines tested.

IHT treatment of the TS1 cell line showed increased susceptibility to Olaparib after both a single and twice daily treatment at both concentrations of 0.5 and 1 µM. At concentrations higher than this the survival fraction of cells treated at 37°C decreased to the same point as those treated at 42°C, which indicates that this drop was due to the concentration of Olaparib not the IHT. IHT treated samples indicating there were no further reduction that was induced by IHT. Although there was a significant decrease in the survival fraction of cells treated with IHT there was no difference noted between the single and twice daily treated samples. This lack of difference suggest that the cells are more susceptible to HT and increasing treatment of IHT does not induce further reduction in cell survival. Comparatively the 4T1 cells showed an increased resistance to IHT treatment as there single daily IHT treatments did not cause a decrease in the survival of cells and there was only a significant decrease in the survival fraction noticed in the 0.5 µM concentration but this may be as a result of at higher concentrations there is a small drop in the 37°C survival fraction.
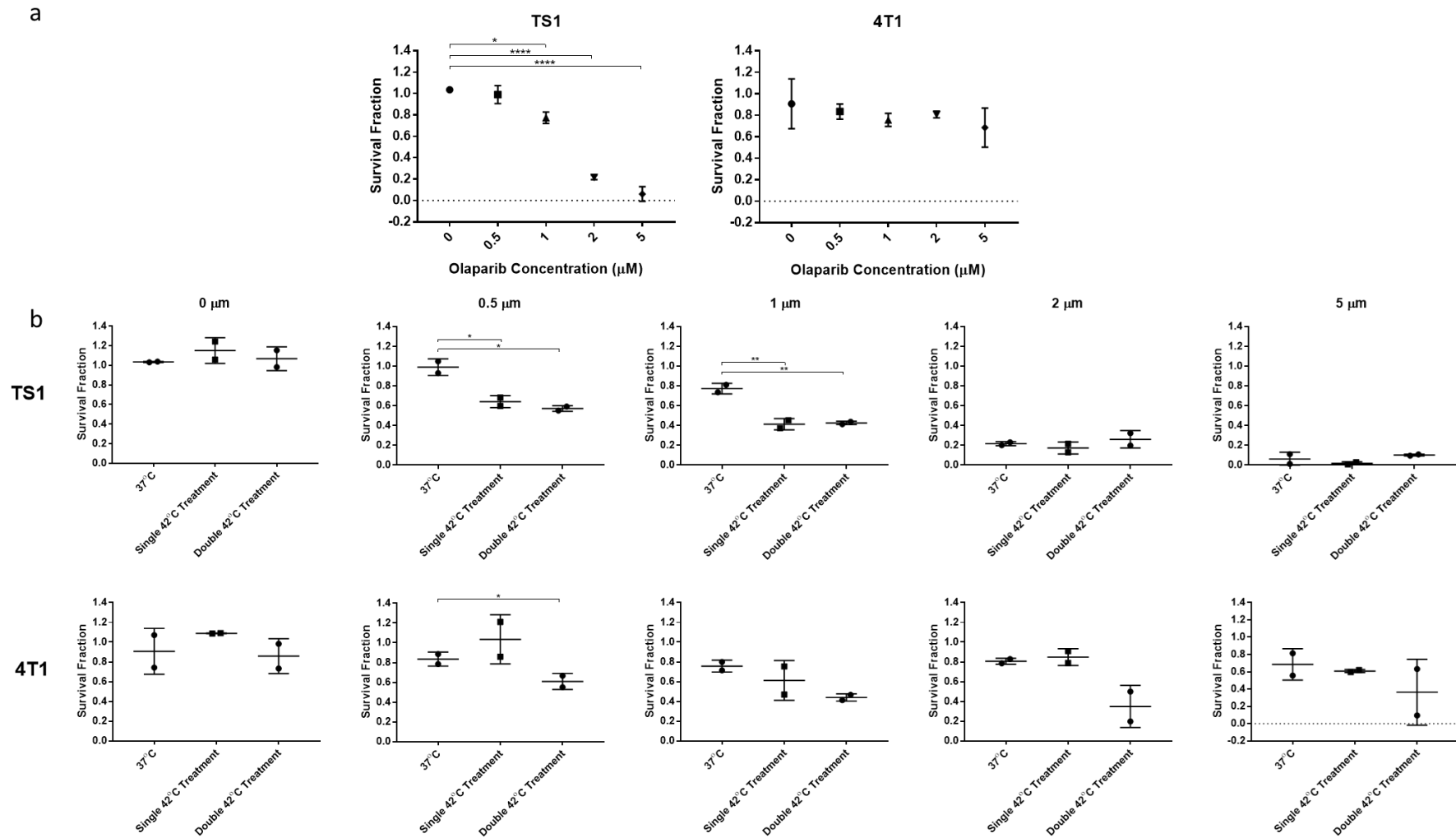
Figure 5.2.6 – Effect of combined IHT and Olaparib on the survival fraction of TS1 and 4T1 cell lines a)Survival fraction of TS1 and 4T1 cell lines after treatment with Olaparib concentrations of 0-5 µM. b) Survival fraction of TS1 and 4T1 cell line after both single and twice daily treatment with 2 hours of IHT. Data points represent individual measurements normalised to DMSO control +/- SD. * denotes p= ≤0.05, ** denotes p= ≤0.01, **** denotes p=≤0.0001 significant difference (One-way ANOVA with Dunnett correction for multiple comparisons).

These results indicate that there is a definite cell line dependant effect of HT on inducing susceptibility although the reasons for this still require further experimentation to resolve it can be speculated that this may be as a result of a difference in the effect of HT on molecular chaperones which has been previously reported.[245] This also shows that these would make a reliable *in vivo* model of combined HT Olaparib treatment.

5.3 MAGNETIC HYPERTHERMIA

5.3.1 MAGNETIC HYPERTHERMIA AND CELL SURVIVAL

MCF7 and MB-MDA-231 cells were both treated with MNPs at the previously stated concentrations and washed extensively after 24 hours to allow for MNP internalisation. A control was used for each time point to ascertain if the field or conditions influenced the cells. After incubation with MNPs cells were placed into an alternating magnetic field for 20, 25 and 30 minutes to determine a maximum safe time limit of treatment. Times of 30 minutes and above were ruled out due to being unable to produce an atmosphere of 5% CO_2 within the magnetic field. It was determined that removal from a 37 °C 5 % CO_2 environment would have a negative impact on the health of the cells. In both the MCF7 and the MB-MDA-231 cells, that were not treated with MNPs, there was no statistically observed reduction in cell viability after 20, 25 and 30 minutes within the magnetic field. Indicating that this does not affect the cells dramatically in any way. Although there was a noted temperature increase in the cell culture media when observed using an infrared camera, this did not exceed temperatures of 28.2 °C with a starting temperature of 20 °C. This closely matches the increase in temperature of the baseline control heating used to determine the SAR values of the MNPs. In the cells treated with MNPs there was a noted concentration dependant effect that was observed after hyperthermia. Higher concentrations of particles causing an increased negative effect on the survival fraction of the cells. Time was also noted to have an increasing effect on the survival fraction of the cells, with increasing time causing a larger reduction in cell survival. Concentrations of 5 µg/ml were noted to have little to no effect on the survival fraction of the cells, in both cell lines. This is not surprising as both the ICP-OES and flow cytometry showed that this concentration only induced a very small increase in the amount of iron and the percentage of cells that internalised this. As the concentration of MNPs increased to 25 µg/ml there is noticeable effect in the survival of the cells after 15 minutes in both cell lines. However, this does not induce a significant reduction in cell survival although it is noted that the MB-MDA-231 cells show an increased effect to the HT than the MCF7 cells. At 50 µg/ml there is a much more noticeable effect on cell survival after MHT, a significant drop (p=>0.05) in the survival fraction is observed after only 5 minutes of HT treatment this continues to increase as the length of time increases. MB-MDA-231 shows

the same pattern of reduced cell survival as the length of time in the AMF increases. This enhanced effect of the 50 µg/ml is expected, as although they showed similar percentage of cells internalising MNPs a much higher concentration of iron was measured, almost double. It is expected that 50 µg/ml would induce increased cell death, and this is consistent with other findings . As the length of time in the AMF increases this was also expected to increase the amount of cell death, as particles will continue to heat in an AMF.[232] The effect of MNPs on the heating of cells was observed using an infrared camera. This was performed on media containing MNPs (200 µg/ml) without washing to determine if there was an increase in temperature greater than that observed in media alone. After 30 minutes of exposure to an AMF there was a measured increase in temperatures to 32 °C (Figure 5.2.1), this is higher than that observed in media alone indicating that MNPs do induce increased hyperthermia. Although the temperature observed is not within the mild hyperthermia range this does not indicate that these temperatures have not been reached intracellularly as there is multiple accounts of supporting evidence that there is greater nanoscale heating in the immediate area surrounding the MNP (<100 nm) than in the bulk solution with temperatures dissipating further from the MNP.[230–232] These have shown that the temperature immediately surrounding the MNP differs greatly to those seen in the bulk medium with a dramatic temperature rise compared to the bulk medium up to 100 nm away.[231]
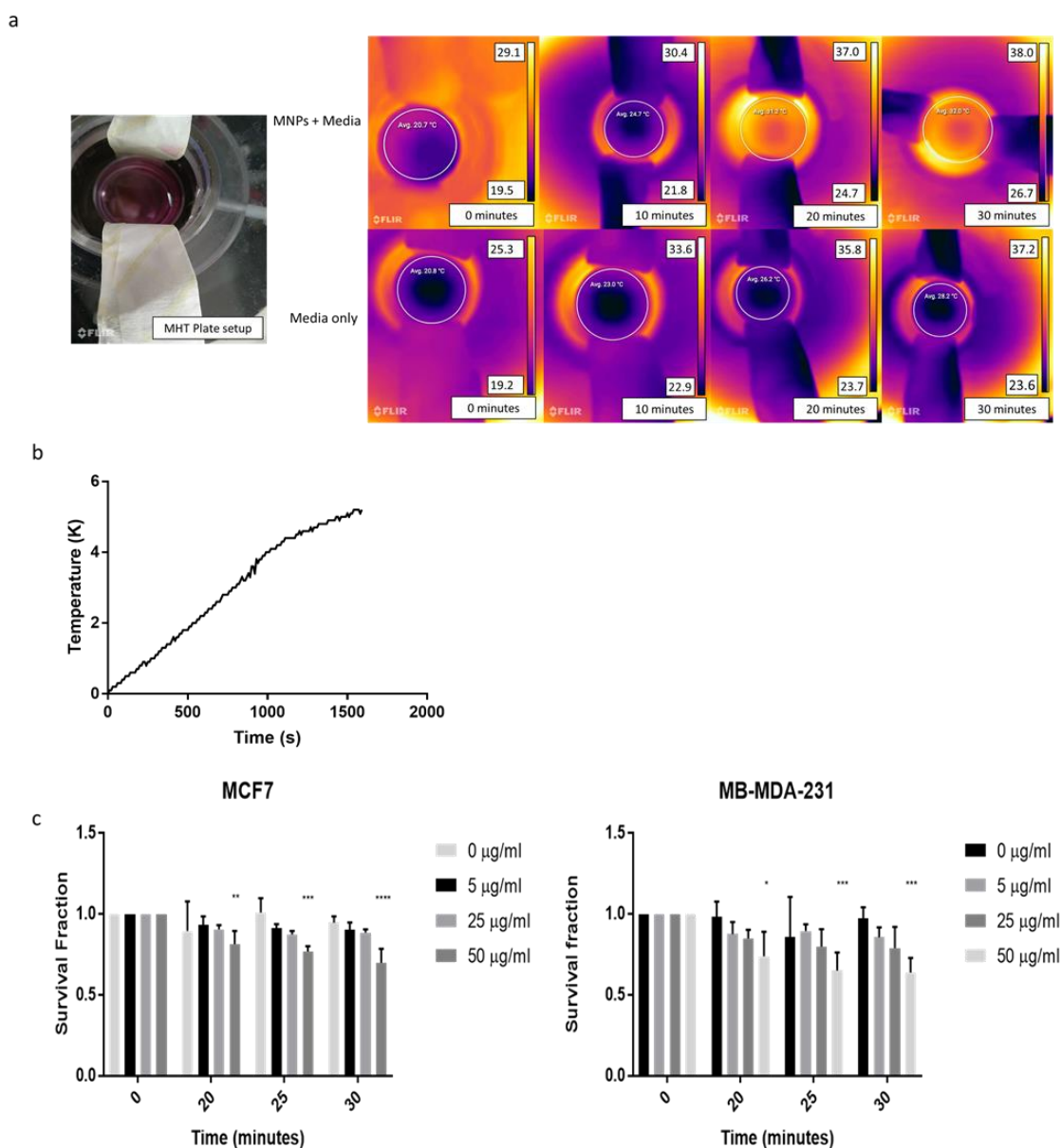
Figure 5.3.1 – Effects of hyperthermia. a) IR images of MNPs in media (500 μg/ml) and media only in an AMF. b) Base line temperature increases of water in an AMF. Survival fraction of MCF7 and MB-MDA-231 cells treated with concentrations of MNPs of 0, 5, 25 and 50 μg/ml at times of 20, 25 and 30 minutes. Data points represent mean survival fraction +/- SD. Data points represent individual measurements normalised to DMSO control +/- SD. * denotes p= ≤0.05, ** denotes p= ≤0.01, *** denotes p=≤0.001, **** denotes p=≤0.0001 significant difference (One-way ANOVA with Dunnett correction for multiple comparisons) comparing the effect of time on each individual concentration.

The 25 μg/ml concentration was chosen to identify BRCA2 sensitivity as this was seen to show the least effect on cell survival (Figure 5.3.1) with similar cell percentage uptake compared to 50 μg/ml and improved uptake compared to 5 μg/ml. This reduction on HT based cell death would also allow an improved effect of PARP inhibitors if successful in inducing BRCA2 degradation.

118

5.3.2   MAGNETIC HYPERTHERMIA AND THE EFFECT ON BRCA2

Both MCF7 and DMB-MDA-231 cells were treated with 25 µg/ml of MNPs and exposed to an AMF with a frequency of 173.1 kHz and 520.9 kHz, to determine if they were capable of inducing sufficient heat to affect the levels of BRCA2.

At frequencies of 173 kHz it was observed that HT did affect the levels of BRCA2, with a reduction after 20 minutes in the MDA-MB-231 cell line. With the higher frequency of 520.9 kHz there was an increased effect on BRCA2 levels and an increased effect with increased exposure time. The MCF7 cell line showed little effect on the level of BRCA2 at a frequency of 170 kHz, but there was a noticeable drop in the levels of BRCA2 after 15 minutes exposure to a magnetic field with this drop continuing as exposure time increased.
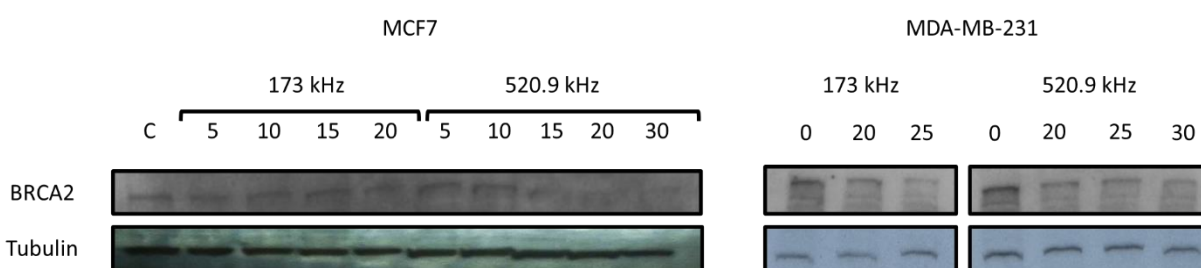
Figure 5.3.2 – Magnetic hyperthermia of MCF7 and MDA-MB-231 cells at concentration of 25 ug/ml at frequencies of 173 and 520.9 kHz for increasing time lengths showing BRCA2 and Tubulin.

The use of higher frequencies was shown to increase the effect of MHT on BRCA2 levels. This is most likely due to the increased field strength that higher frequencies produce, which would result in increased power output from the MNPs. As was previously discussed frequency and field strength effect the SAR of MNPs linearly and quadratically respectively (equation 1.2). As 30 minutes exposure to an AMF at 25 µg/ml was shown to induce very little cell death and was seen to be capable of inducing BRCA2 degradation in both cell lines, it was expected that MNPs would be able to produce the same effect that was seen when heating was applied in an incubator.

5.3.3   MNP INDUCED PARP INHIBITOR SENSITIVITY AND THE CELLULAR EFFECTS

MCF7 and MB-MDA-231 cells were treated with 25 µg/ml of MNPs and treated with Olaparib before being exposed to an AMF as detailed in (Figure 5.2.5 part a), this replicates the treatment plan that was used to induce PARP sensitivity in previous experiments.

Consistent with previous findings (Figure 5.2.5) it was found that multiple bouts of MHT induced PARP sensitivity in both the MCF7 and MB-MDA-231 cell lines (Figure 5.3.3). The MNPs under an AMF showed no effect on the cell survival which is a positive indicator that sub lethal temperatures are reached during MHT with 25 µg/ml of MNPs. Whereas Olaparib was seen to reduce cell survival when combined with MHT. This combined therapy resulted in further reduction of cell survival compared with MHT alone and Olaparib alone indicating

that MHT has induced a level of PARP sensitivity that is not seen in these cells alone. This increased PARP sensitivity can be attributed to the induction of mild hyperthermia by the MNPs, as the effect of combined MHT and PARP inhibition was seen to be greater than each treatment alone and matched the observed effect of previous work on cell survival after induction of mild hyperthermia. The effect of combined MHT and PARP inhibition was seen to be greater in both MCF7 and MB-MDA-231 cell lines than when mild HT was induced through the use of a controlled incubator, with a lower survival fraction observed in the MHT induced mild hyperthermia compared with the same Olaparib concentration. This supports the evidence that MHT is more efficient that other HT treatment types as MNPs heat the cells from an internal source rather than an external heat source. [158]
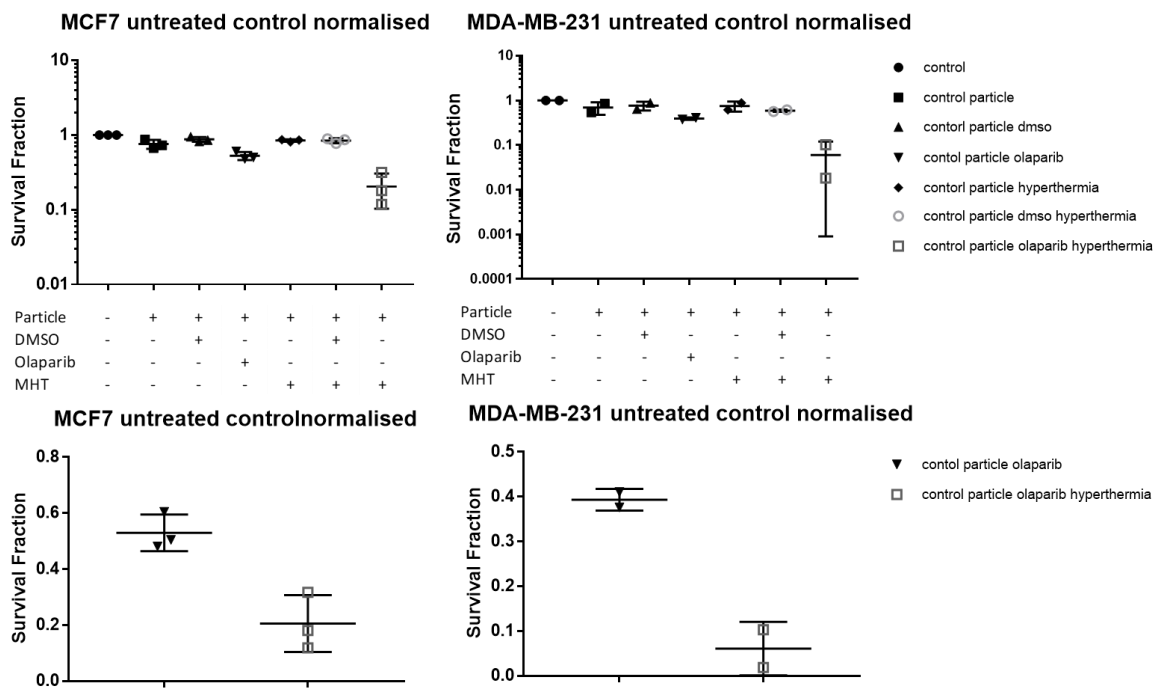
Figure 5.3.3 – Survival fraction of MCF7 and MB-MDA-231 cells treated with 25 µg/ml of MNPs and Olaparib (0.5 µM) both individually and combined therapy with MHT. Data points represent individual repeats +/- SD (Multiple comparison ANOVA comparing all the treatment conditions).

These results show that MHT can induce sublethal levels of HT via MHT, that are capable of degrading BRCA2. Combined with Olaparib treatment this has shown an increased reduction in cell survival after treatment. Here MNPs were able to induce sublethal levels of MHT to induce PARP sensitivity, but in a clinical setting a combined lethal level of MHT and PARP inhibition may prove more beneficial. Although the goal of this experiment was not to induce cell death through MHT alone but to observe an effect of the MHT on PARP sensitivity, which has been shown.

MHT was also observed to cause a reduction in RAD51 foci formation when MCF7 and MDA-MB-231 cells were treated with 30 minutes of MHT (25 µg/ml) then exposed to 4 Gy of IR() when compared to cells treated with IR alone and combined MNPs and 4 Gy IR . This matches the results observed in the IHT treated cells that also saw a reduction in RAD51 foci formation when cells were treated with 42 °C. This result supports the fact that BRCA2 has successfully been degraded in the cells treated with MHT and that sufficient temperatures have been reached to do this. The combined MNP and IR treatment was seen to cause a larger number of RAD51 foci than IR treatment alone which indicates that MNPs may enhance the effects of IR.
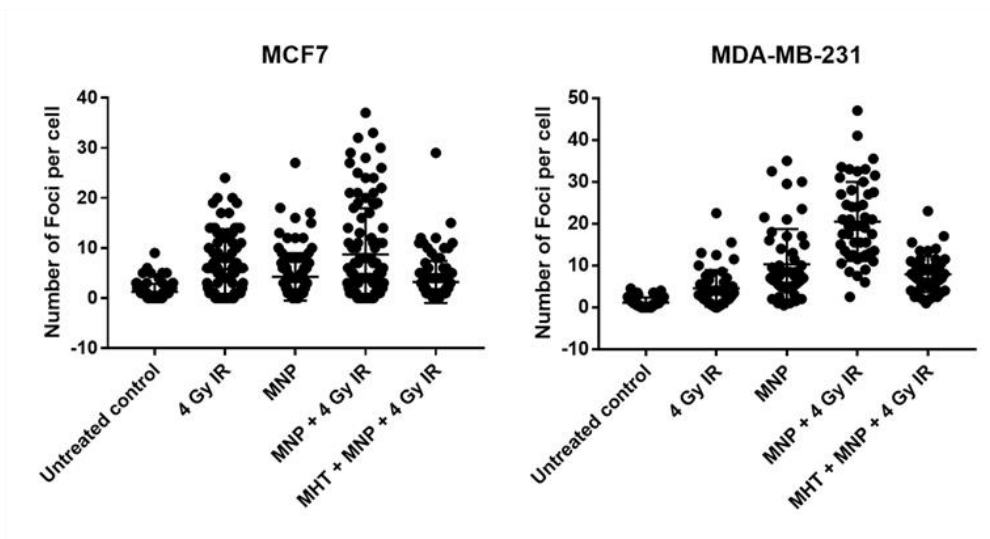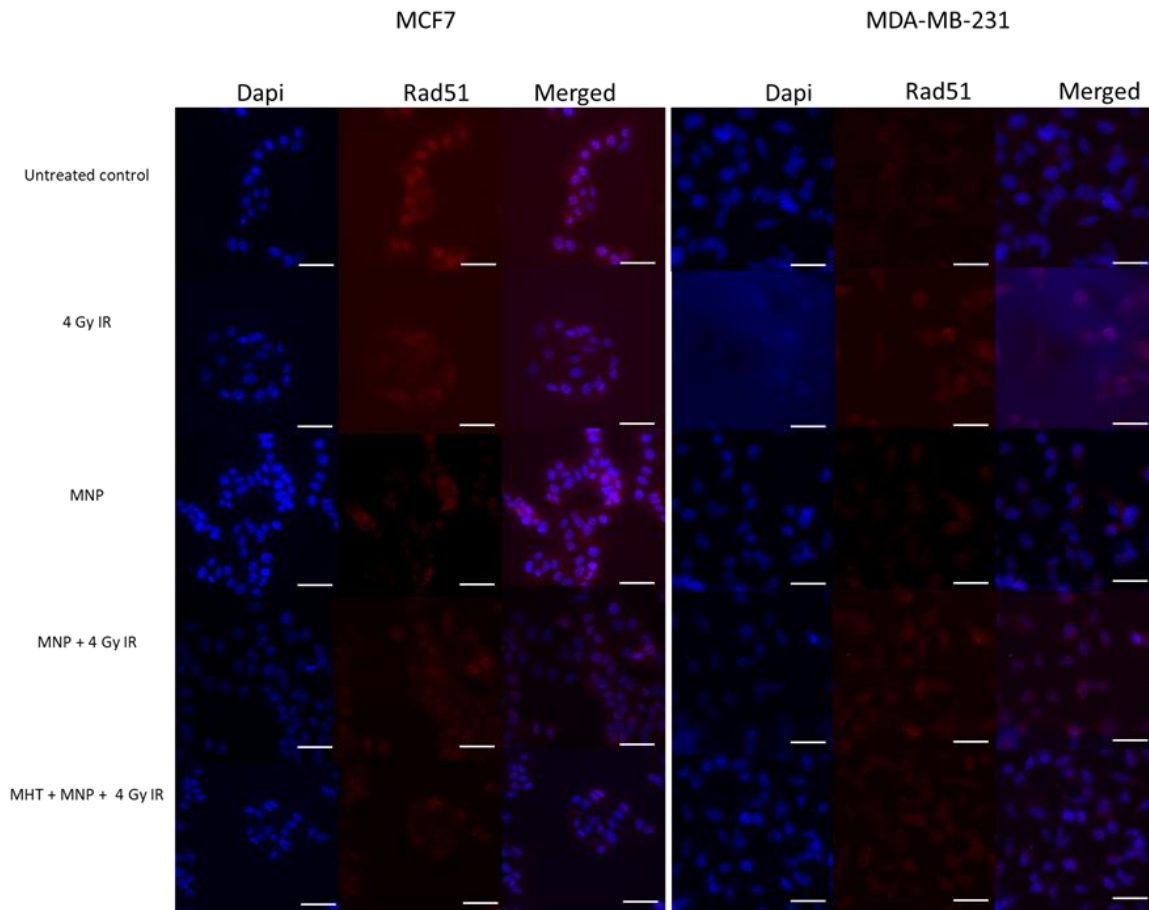
Figure 5.3.4 RAD51 foci formation in MCF7 and MDA-MB-231 cells with untreated, IR treated, MNP treated, Combined IR and MNPs and combined MHT with MNPs and IR. Cells treated with MNPs were incubated for 24 hours prior, MHT treatment to place for 30 minutes immediately before IR. a) Representative images of the treatment conditions with Dapi (blue) RAD51 (red) and a merged image. b) Mean foci formation in each of the treatment conditions. Scale bar indicates 100 μm

5.3.4 MAGNETIC HYPERTHERMIA EFFECTS ON THE CELL CYCLE

HR is only active during late S and G2 phase of the cell cycle, the effect that MHT has on the cell cycle will greatly influence how well cells respond to PARP inhibition. As only cells in in these phases will be susceptible to this kind of treatment.
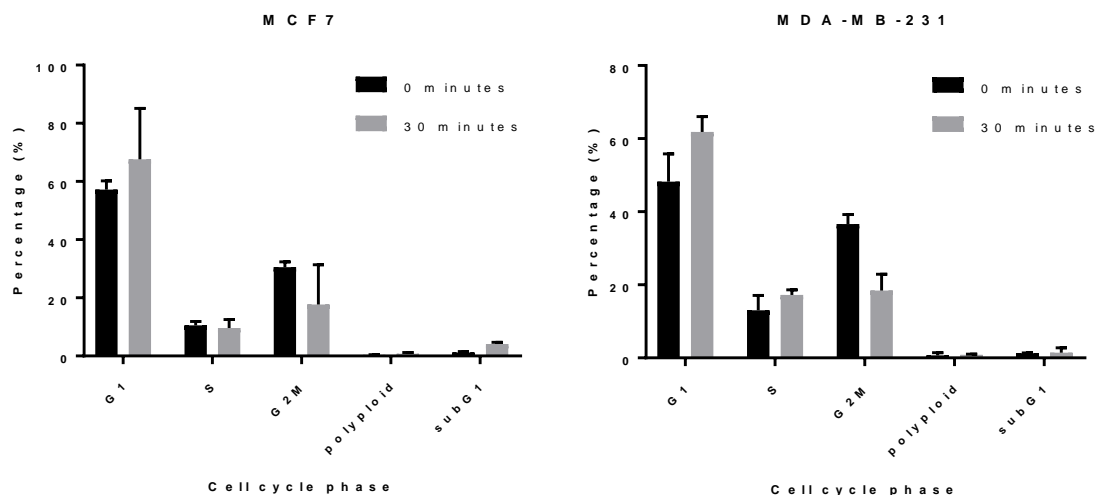
Figure 5.3.5 – Cell cycle phase of MCF7 and MDA-MB-231 cell lines treated with 25 µg/ml of MNPs and exposed to an AMF for 30 minutes. Data points represent mean cell cycle phrase +/- SD (n=2) single cell events collected in population isolated through (PI (FL-3) width vs PI (FL-3) height).

Cell cycle analysis of the MCF7 and MB-MDA-231 cells after MHT was used to determine how they responded to MHT. After exposure to MHT the cells showed a reduction in the percentage of the population that were in the G2/M phase of the cell cycle, in both cell lines. Although a significant difference is only observed in the MB-MDA-231 cell line, but a small sample was used (n=2) so this may alter for MCF7 with further repeats. Concurrently an increase is observed in the population of cells in G1 phase, which matches the loss of cells from G2/M phase. This increase in the percentage of cells in G1 phase suggest the MHT induces cell cycle arrest in these cell populations. This is consistent with literature that have noted a cell cycle arrest in cells treated with mild hyperthermia.[246,247] This cell cycle arrest observed in G1 and the reduction of cells in G2/M might explain why cell lines required multiple rounds of hyperthermia to induce PARP sensitivity. Due to the reduced portion of cells that are susceptible to PARP inhibitors and thus requiring further treatments to effect cell survival. Along with the increase in G1 arrest there was a small noted increase in the portion of cells in S phase in MB-MDA-231 cells, which has previously been attributed to HT.[246,247]

5.4 SUMMARY AND CONCLUSIONS

In this chapter it has been shown that treatment of MCF7 and MB-MDA-231 cell lines with hyperthermia at 42 °C for a minimum of 1 hour can induce a loss of BRCA2 and subsequent reduction in RAD51 foci formation in cells exposed to 4 Gy IR. Although both cell lines showed a reduction in foci formation, 4 Gy treated MCF7 cells exposed to IHT conditions only caused a reduction in the average number of foci formed compared to IR treated alone. Whereas there was an almost complete loss of foci formation in the MDA-MB-231 cells. This indicates that these cells may be more responsive to HT than MCF7 and thus more susceptible to HT treatment. It was believed that BRCA2 degradation by HT should mimic the phenotype of BRCA2 negative cell lines and that these cells should show an increased sensitivity to PARP inhibition compared with wild type cells.

It was observed that although HT does indeed induce the phenotype of *BRCA2* mutated cancers, this does not cause sensitivity to Olaparib after a single treatment with HT. Olaparib sensitivity was not observed when HT was increased to single and twice daily treatments, in both MCF7 and MDA-MB-231 cell lines, immediately after final treatment. When the effect of both HT and Olaparib treatment were combined and observed via clonogenics there was a noticeable reduction in the survival fraction of the cells. This indicated that HT was indeed inducing sensitivity to Olaparib and that this was as a direct result of the HT treatment, as there was an increased effect in the cells that were treated with twice daily treatment as compared to those treated singularly. The resulting lack of effect of a single HT treatment as compared to multiple therapies may be a result of HT causing a time dependant drop of BRCA2, for a limited period, as opposed to a permanent loss of BRCA2. This would also explain why there is an increased response in cells treated with a twice daily HT regime as opposed to a single daily treatment regime.

MDA-MB-231 cells showed an increased susceptibility to treatment with Olaparib compared to MCF7 cells, with a larger reduction in survival fraction observed at 0.5 µM and complete loss at 1 µM. This higher level of sensitivity of MDA-MB-231 cells to Olaparib may well be because of the increased effect HT seemed to have on the formation of RAD51 foci compared to MCF7 cells.

The use of MHT to cause a reduction in BRCA2 levels has not been reported, the results in this chapter show that controlled application of MHT can induce BRCA2 reductions whilst delivering sub lethal level of HT. MNP concentrations of 25 µg/ml and below showed a sub lethal level of induced HT and a concentration of 25 µg/ml was shown to reduce BRCA2 at times of 20 minutes and above, in the higher frequency of 520.3 kHz for both MCF7 and

MDA-MB-231 cell lines. Multiple treatment of MHT with MNPs were seen to be sublethal but combined with Olaparib they showed a large reduction in survival fraction successfully showing that MHT can induce PARP sensitivity thorough the use of MNPs. The treatment of both cell lines with MNPs showed a greater effect on the cell survival when HT was applied via an incubator with a reduced amount of exposure time.

It was observed that MHT treatment caused cell cycle arrest in G1 phase, in both MCF7 and MDA-MB-231 cells, and a concurrent reduction in G2/M phase. This G1 arrest and reduction in the G2/M population might also help to explain why HT does not induce higher levels of Olaparib sensitivity as would be expected. As HR is only active during G2 and late S phase so cell cycle arrest in G1 phase and a reduction of population in G2 would mean there is a smaller population that is susceptible to treatment with Olaparib.

5.4.1 LIMITATIONS

2D cell culture was used to determine both the effect of HT and Olaparib in combination in MCF7 and MDA-MB-231 cell lines. An advantage of this method is that it is inexpensive and relatively easy to use for high throughput assays, in comparison to *in vivo* methods. Although this method does have benefits it does not accurately model tumours and tumour microenvironments, so concentrations of MNP that have been observed to induce mild hyperthermia conditions in 2D cell culture would need to be reanalysed for *in vivo* models of tumours, as the uptake and localisation of MNPs would differ in these models compared to 2D culture models. Therefore, further analysis *in vivo* modelling would be required to determine if MHT is a valid treatment option for inducing PARP sensitivity.

CHAPTER SIX: BIOMIMICRY OF MAGNETOSOMES WITH POLYMER VESICLES

6 BIOMIMICRY OF MAGNETOSOMES WITH POLYMER VESICLES

6.1 INTRODUCTION

Magnetosomes perform complex biomineralisation to synthesise MNPs within their lumen. Magnetosomes show many advantages over chemically synthesised MNPs including shape control, size, and magnetic properties. These advantages coupled with their ability to be readily taken up into biological systems *in vitro* and *in viv*o makes them an ideal candidate for hyperthermia treatment of cancers as well as directable drug delivery vehicles.[248,249] While magnetosomes do possess superior physical and magnetic properties compared to chemically synthesised MNPs they also require complex growth conditions and strict control of the growth environment, with certain species of magnetosome being anaerobic and requiring low oxygen conditions at 1 %.[250] Coupled with these stringent growth conditions is the fact that magnetosome are a slow growing bacterium which results in low yields of magnetosomes, and the high cost of reagent media required for their synthesis. Due to the preformed membrane adapting and functionalising this can be a difficult and complex process compared with chemically produced MNPs. Biomimetics allows the formation of synthetic analogues of these naturally occurring bioreactors which can undergo mineralisation to produce MNPs within the vesicle. The advantage of a synthetic vesicle is that they are highly tuneable as the physical and chemical properties can be easily altered to produce vesicles that fit the required need. Physical characteristics can be altered through the controlling of the reaction or through size control techniques such as sonication and French press to produce larger or smaller in size depending on the required characteristics.[251] The chemical structure can also be adapted to produce vesicles that have longer retention as a therapeutic with the coating of so called stealth coatings which reduce the clearances of MNPs by macrophages.[252,253] The use of artificial magnetosome mimics also allows the use of conditions and temperatures that are toxic to the magnetosomes to perform reactions that are outside the range of biological systems allowing increased variation. Chemical synthesis of MNPs with tight size and shape control requires precursor materials or high temperatures to produce. The co-precipitation reaction of magnetite MNPs that are within a similar size range of magnetosome showed a high degree of agglomeration as well as a heterogenous size distribution. This highlights the level of control that is exhibited by magnetosomes. The use of artificial magnetosomes could enhance the synthesis of MNPs by mimicking the function of magnetosomes in MNP formation.

The transport and formation of MNPs within magnetosomes is strictly controlled by a large group of proteins that control the nucleation, growth, shape, and transport of iron ions across the bacterial membrane. Mimicking of these proteins' functions would be required to produce magnetosomes biomimics with similar magnetic properties. As *Mann et al* showed the presence of electron dense

material within the vesicle core in their early work on artificial magnetosomes. This material was most likely iron oxide due to the electron density the material was sparce and amorphous in nature.[106] This suggests that iron ions are not being transported across the membrane to allow formation of MNPs. Transport of iron ions across the bacterial membranes is controlled by MamM and MamB which transports iron ions from outside the MTB to within the magnetosome. This might explain the difficulty that was experienced by *Mann et al* as there was no mechanism for the transport of iron ions across the lipid membrane. Electroporation of lipid membranes results in the opening of pores within the membrane and allows the transport of material across the membrane,[254] mimicking the function of the iron transporters in magnetosomes.[255]

Polymersomes are a robust option for artificial magnetosomes as they allow for modification of the vesicle, both in polymersome design with a range of choice in the polymer hydrophobicity, the monomer length and the tuneability of the polymer to possess the desired quality for the application.[255] poly(butadiene-b-ethylene oxide) (PBD-PEO) polymersomes are one of the most commonly used polymersomes due to its ability to form multiple structures and ability to adjust the membrane thickness. These form through thin film hydration which allows the encapsulation of hydrophobic moieties within the vesicles. [256,257] Raft polymerisation is a radical polymerisation of substitute monomer by a chain transfer agent and provides a high level of control over the molecular weight, composition and structure. [258]

Mms6 is a small membrane bound protein found on the inner membrane of magnetosomes.[144] Mms6 is believed to be responsible for nucleation of magnetite within the magnetosome as well as being important in the size control of the formed MNPs. *Mms6* knock down experiments have been shown to produce MNPs that are poorly formed and smaller in size. The importance of this protein in magnetosomes makes it a vital target to mimic.

Biomimicry with PBD-PEO polymersomes has shown that MNPs can be formed within the membrane of the vesicles but these did not form in a manner that is similar to magnetosomes. [109] These produced multiple small (4 nm) MNPs within the membrane instead of the formation of a single MNP within the lumen. This suggest that the magnetosome Mms6 contains acidic residues on the C terminus which creates a negative charge for iron ion binding in magnetite nucleation.[137,144] Replication of the negatively charged acidic groups could result in the nucleation of MNPs within the core of the vesicle. Previous work in the Staniland group has shown that polymers with carboxylic acid groups can be produced which are capable of iron transport.[259] Although these did not show the formation of a single MNP within the vesicle core so further modification of the polymer vesicle may improve the MNP formation.[259]

Producing a synthetic biomimetic magnetosomes could help to reduce the cost of formation of biocompatible MNPs. MNP formation in magnetosomes is controlled by a vast array of proteins that would almost be impossible to mimic in a synthetic system.[135,142,144,260] Starting with a simpler system mimicking the structure and conditions that magnetosomes produce may help to control formation of MNP growth within polymer vesicles. Work within the Staniland group has previously shown that iron oxide nanoparticles (MNPs) can be formed within alkali filled polymersomes that are electroporated in an iron rich environment.[109,259] This showed the formation of MNPs within the membranes of the particles within a mixed valence (1:2 Fe(II):Fe(III)) solution. This shows that MNPs can form within polymersomes, but these do not completely mimic the formation of iron oxides within magnetosomes. Due to the high biocompatibility and their excellent magnetic properties compared to other synthetically produced MNPs, finding a mimic of magnetosomes would help to overcome some of the major draw backs that they have.

The aims of this chapter are to:

- Produce vesicles that are capable of the formation of MNPs when electroporated within an iron rich environment.
- Determine the effect that iron ratio and concentration have on NP formation.
- Determine how the presence of COOH motifs effect iron formation within vesicles.

6.2 SYNTHESIS OF POLYMERSOMES

The first polymer that was synthesised was the polymerization of poly butadiene (PBD) and polyethylene oxide (PEO). This forms an amphiphilic block co polymer with a PBD block (molecular weight of 2500 g mol^{-1}) and a PEO block (molecular weight of 1300 g mol^{-1}) (Figure 6.2.1). This polymer has been successfully used by Bain *et al* as a vesicle for the synthesis of MNPs. PBD-PEO polymers have both a hydrophilic (ethylene oxide) and hydrophobic (butadiene) region and when hydrated in an aqueous solution they are driven to form a vesicle structure because of the amphiphilic nature of the polymer.[109] The structure of the hydrophilic PEO and the hydrophobic PBD mimics that of phospholipid membranes with the PEO mimicking the hydrophilic head group and the PBD mimicking the hydrophobic tail as seen in bacterial magnetosomes (Figure 1.4.3). The water soluble PEO block of the polymer is known to have good biocompatibility and low toxicity both *in vitro* and *in vivo,* making them an excellent material for the formation of vesicles for biomedicines. This was tested both in a mixed valence 1:2 (Fe(II):Fe(III)) solution of iron salts and a single ferrous (Fe(II)) iron salt. To determine how iron species ratio affected the formation of MNPs within the vesicle.
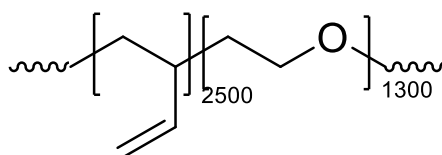
Figure 6.2.1 – Polybutadiene-b-polyethylene oxide (PBD2500-PEO1300) used that was used to form vesicles in solution.

The use of Reversible Addition-Fragmentation Chain Transfer Polymersomes (RAFT) polymerisation allows for the tuning of the polymer to better mimic the magnetosomes. Magnetosomes have a vast array of proteins for controlling the nucleation, growth and formation of MNPs within the magnetosome.[141,181] Mms6 is one of the proteins responsible for the nucleation and growth of MNPs with magnetosomes.[137,138,144] The Mms6 protein displays carboxylate acidic residues on the C terminus and aids in binding iron for nucleation of magnetite NPs, this can be mimicked by the addition of COOH to the inner membrane of the polymers.

70% PEG$_{113}$-PHPMA$_{400}$/30% PMPC$_{28}$-PHPMA$_{40}$ ([0.7 PEG$_{113}$ + 0.3 PMPC$_{28}$]) polymersomes were produced using a RAFT polymerisation technique. Polymerisation took place with the poly(ethylene glycol) macromolecular chain transfer agent (PEG macro-CTA) undergoing chain extension via a Polymerisation of a 2-hydroxypropyl methacrylate (HPMA) using a 4,4'-azobis (4-cyanopentanoic acid) (V501) initiator and a 4-cyanopentanoic acid dithiobenzanoate (CADB) chain transfer agent. The HPMA block was further polymerised by 2-(methacryloyloxy) ethylphosphorylcholine (PMPC), resulting in the chain extension of the HPMA block via the PMPC macro-CTA in a RAFT aqueous dispersion.

The molecular fraction of the PEG113-PHPMA400 block was adjusted to produce a molar ratio of 70%:30% ratio of the PEG_{113}-$PHPMA_{400}$:$PMPC_{28}$-$PHPMA_{40}$ of the amphiphilic diblock polymers. This causes the formation of nanoscale vesicles through polymer induced self-assembly (PISA) due to the variation of the hydrophilic and hydrophobic blocks with the hydrophobic in-situ (Figure 6.2.2). PISA is based on the extension of a soluble precursor block here the PEG block which acts as a steric stabiliser and a second insoluble block here the PMPC block which forms the core in-situ.[99,261] The polymerisation of drives the self-assembly once a sufficient degree of polymerisation of these blocks takes place. This process can produces vesicles worms and spheres. [99]
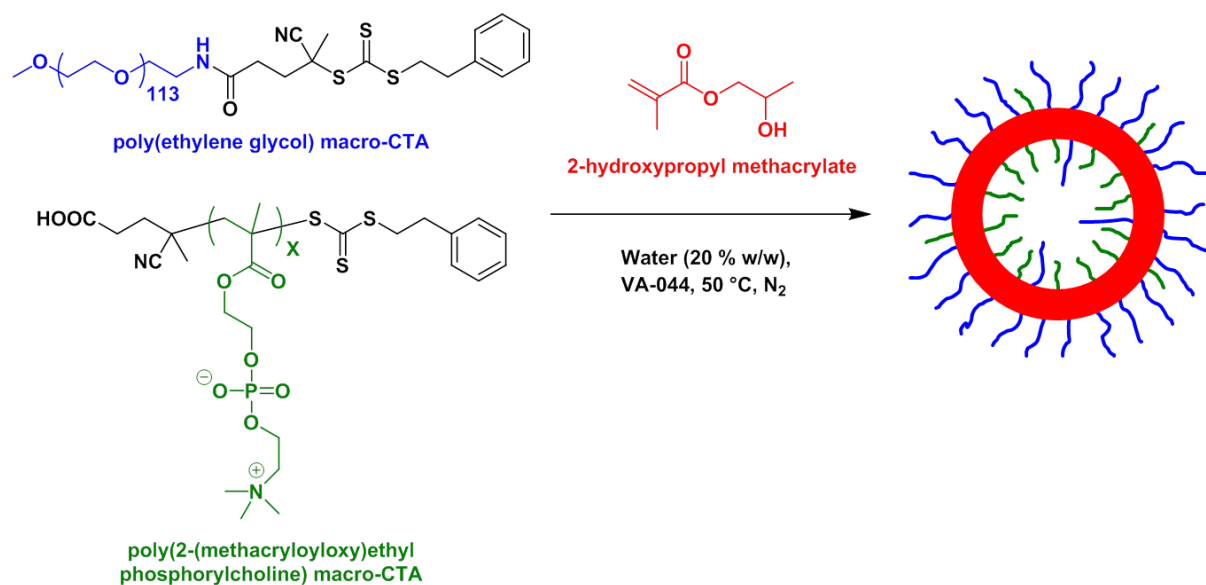
Figure 6.2.2 – Polymersome formation from PEG_{113}-$PHPMA_{400}$/$PMPC_{28}$-$PHPMA_{40}$ amphiphilic diblock copolymer via reversible addition-fragmentation chain transfer. Polymer vesicle formation is through polymer induced self-assembly (PISA).

The carboxylic acid groups of the $PMPC_{28}$-$PHPMA_{40}$ portion are hypothesised to form on the inner portion of the membrane due to the shorter chains of the $PMPC_{28}$ preferentially forming on the inner membrane compared to the longer chains of the PEG_{113} in the PEG_{113}-$PHPMA_{40}$. This orientation of the PMPC chains being preferential on the inner membrane is believed to be driven by steric effects. The formation of the polymersomes with $COOH^-$ on the inner membranes closely mimics the Mms6 protein found on the inner membrane of magnetosomes (Figure 6.2.3).
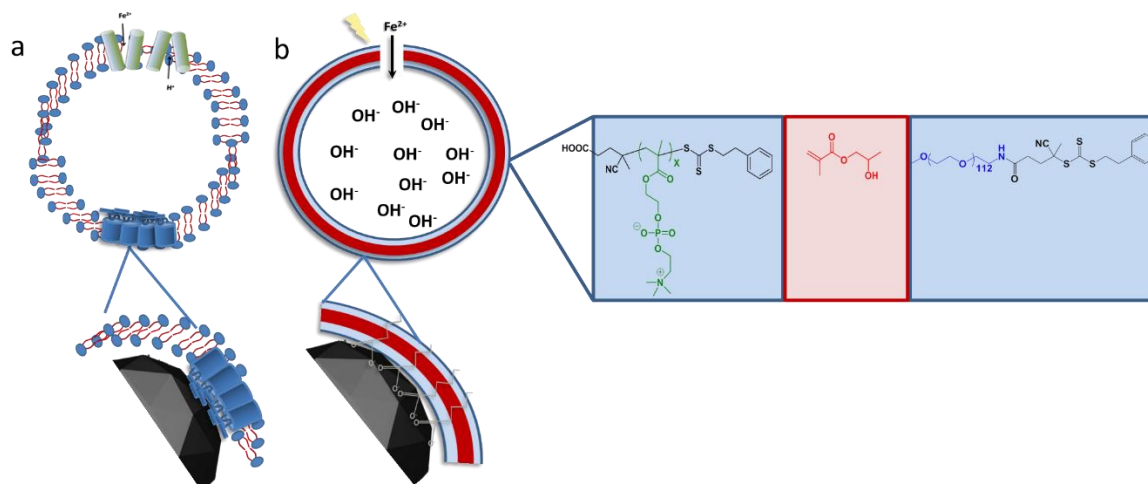
Figure 6.2.3 – a) Schematic of Mms6 binding of Fe in MNP synthesis in magnetotactic bacteria. b) The proposed method of COOH binding to iron in the formation of MNPs in the PMPC28-PHPMA40 polymersomes.

This was further expanded by altering the ratio of PEG_{113}-$PHPMA_{40}$ to $PMPC_{28}$-$PHPMA_{40}$ to determine if this effected the formation of MNPs due to altering the amount of COOH groups on the vesicles. PEG_{113}-$PHPMA_{400}$ vesicles prepared at 10% w/w from just a PEG_{113} precursor polymer (macro-CTA) were produced to form vesicles with no COOH groups present. [0.6 PEG_{113} + 0.4 $PMPC_{28}$] – $PHPMA_{400}$ vesicles prepared from a 0.6/0.4 molar ratio mixture of PEG_{113}/$PMPC_{28}$ precursor polymers chain extended with HPMA at 10% w/w solids. This should produce vesicles with a 0.6:0.4 ratio of PEG_{113}-$PHPMA_{400}$ chains/$PMPC_{28}$-$PHPMA_{400}$ chains within the vesicle. These vesicles should contain 40 mol.% COOH as a 40% PMPC stabiliser was used to form the vesicles (Figure 6.2.3). An alternative ratio of PEG_{113}-$PHPMA_{40}$ to $PMPC_{28}$-$PHPMA_{40}$ was used to form polymers with a lower COOH concentration. [0.8 PEG_{113} + 0.2 $PMPC_{28}$] – $PHPMA_{400}$ vesicles were prepared from a 0.8/0.2 molar ratio mixture of PEG_{113}/$PMPC_{28}$ precursor polymers chain extended with HPMA at 10% w/w solids. Produced vesicles should have a ratio of 0.6:0.4 of PEG_{113}-$PHPMA_{400}$ chains / $PMPC_{28}$-$PHPMA_{400}$ chains within the vesicle and should contain lower (20 mol.%) COOH. To produce vesicles at the opposite end, with all chain ends bearing the COOH motif a $PMPC_{28}$-$PHPMA_{450}$ vesicles prepared at 25% w/w (increased PHPMA DP and increased synthesis solids concentration required to favour the formation of pure vesicles) at 10% w/w and a DP_{400} in the PHPMA showed a preference for the formation of spheres instead of vesicles.
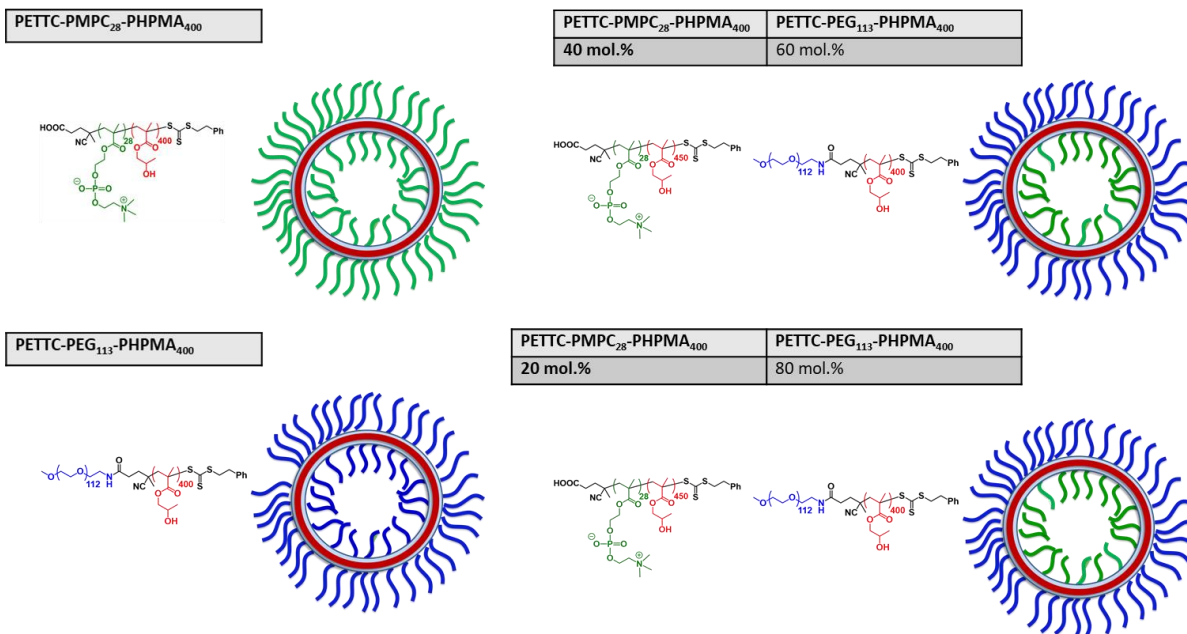
Figure 6.2.4 – Example of each of the four synthesised polymersomes and how the chains are expected to be distributed across the inner and outer membrane.

6.3 DIBLOCK PBD-PEO POLYMERSOMES AND ELECTROPORATION TO FORM BIOMIMETIC MAGNETOSOMES

PBD-PEO polymersomes were synthesised using an evaporated thin film rehydration technique. Three different methods of size control were used; stirring; sonication and extrusion through a membrane with a pore size of 100 nm. The effect of these methods on the size of the particles was measured using DLS to determine particle size (Figure 6.3.1).
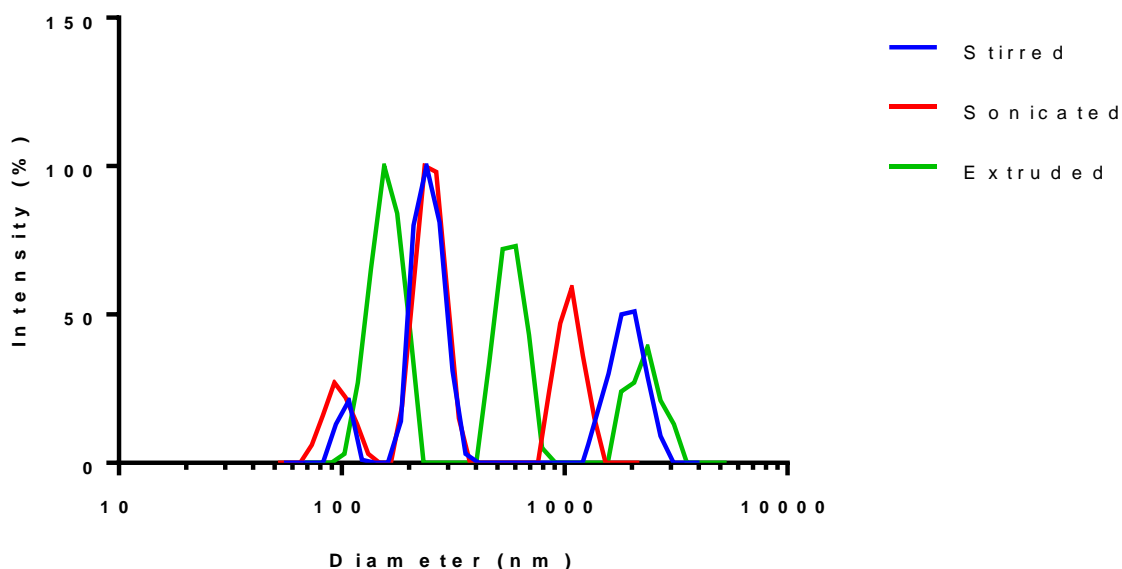
Figure 6.3.1 – Size analysis of the PBD-PEO particles after rehydration in NaOH with three different methods of size control (stirring, sonication and extrusion). Data points represent the intensity of size measured by DLS from 3 repeated measurements.

The use of these methods produced three distinct population of sizes with little difference in the average diameter of the particles. The produced polymers did not produce the size control expected

with each method producing 3 distinct size populations. Although three distinct size populations were produced extrusion of the PBD-PEO polymer showed the smallest average vesicle size. There was very little difference noted in the sonicated and stirred samples which is surprising as sonication was expected to produce a better size control over stirring due to the focused application of tip sonication.

Table 6.3.1 – Mean polymersome size of PBD-PEO polymer vesicles after formation via stirring, sonication and extrusion in a NaOH base. Size measured by DLS.

	Stirred	Sonicated	Extruded
Diameter /nm	340.53 ± 8.5	337.4 ± 55.7	328.2 ± 22.4
PDI	0.27 ± 0.046	0.27 ± 0.03	0.31 ± 0.03

The incorporation of iron ions into the polymer vesicle was initiated by electroporation of the sample in an iron rich solution. Electroporation of phospholipid membranes can increase the membrane permeability with the formation of pores within the bilayer.[254] The use of electroporation to allow iron ions to cross polymer membranes has been previously tested and this showed that the iron does enter the membrane but does not enter the inner lumen.[109,259] Polymersomes were electroporated in a 10 mM and 200 mM 1:2 Fe(II):Fe(III) solution to observe if concentration effected the formation of MNPs. Post electroporation the size of the vesicles altered from the size that was measured pre-electroporation. In the 10 mM 1:2 Fe(II):Fe(III) solution the polymersomes were seen to reduce in size across all the different size control methods. The reason for this is unclear, it may be that electroporation is affecting the polymer morphology resulting in a smaller measured diameter. In the 200 mM concentration an increase in size in the stirred and sonicated samples was observed compared to the control, whilst the extruded sample showed a size reduction. These samples showed a large variation in the spread of the measured polymers so the difference between the control and the 200 mM electroporated sample were not seen to be significant ($p => 0.01$). A possible reason for this is the formation of large amounts of iron structures surrounding the polymersome which is not removed during clean-up of the polymersome. This formation of iron structures on the outside of the polymersome could be resulting in polymersomes that appear larger which are affecting the measurement by DLS.

Table 6.3.2 – Size measurement of PBD-PEO polymersomes both pre and post electroporation in 10 mM and 200 mM mixed valence 1:2 (Fe(II):Fe(III) iron solution. $D\zeta$ is the diameter as measured by DLS.

	Pre-Electroporated	10 mm	200 mm
	$D\zeta$ average /nm	$D\zeta$ average /nm	$D\zeta$ average /nm
Stirred	340.53 ± 8.5	220.7 ± 15.1	424.8 ± 113.7
Sonicated	337.4 ± 55.7	220 ± 15.7	461.3 ± 192.8
Extruded	328.2 ± 22.4	263.4 ± 16.4	271.5 ± 73.5

Iron content was measured via ICP-OES, and this technique allows for accurate measurement of iron within the sample. Samples were measured both pre and post electroporation in a mixed 1:2 (Fe(II)/Fe(III)) solution at concentrations of 10 mM and 200 mM (Figure 6.3.2). In both the 10 mM and the 200 mM iron solution there was an increase in the Fe content of the polymersomes observed compared to the untreated control polymersomes. This increase in iron content in the polymer samples shows that iron is incorporated within the vesicle which suggests that electroporation does allow the transfer of the iron ions across the membrane. The 200 mM solution showed a higher amount of iron internalisation compared with the 10 mM, which was expected due to the higher concentration of iron the polymersomes were exposed to (Figure 6.3..) Although there was a larger increase in the 200 mM polymersomes there was also an increase in the amount of variation in the Fe content with some samples showing very little Fe. This suggests that electroporation of iron is not consistent and results in no iron ion internalisation. In the 10 mM Fe solution there was a significant increase in the extruded sample compared to the stirred and sonicated (p=>0.05), but as the Fe content was increased to 200 mM this higher level of Fe was not visible.
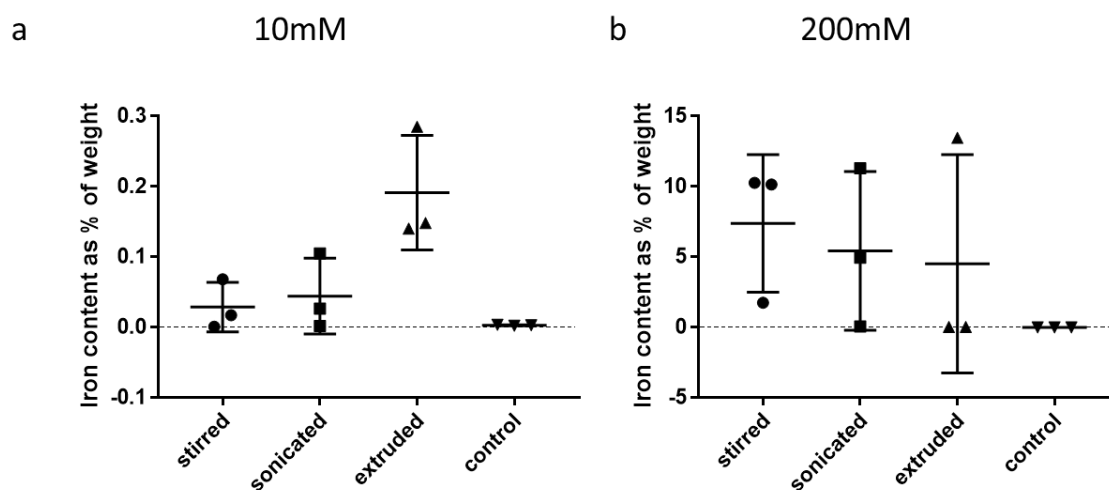
Figure 6.3.2 – Iron content of PBD-PEO vesicles at 10 mM (a) and 200 mM (b) both pre (control) and post electroporation at concentrations of 10- and 200-mM mixed valence 1:2 (Fe(II)/Fe(III)) solution. Data points represent 3 repeated samples measured for iron content via ICP-OES.
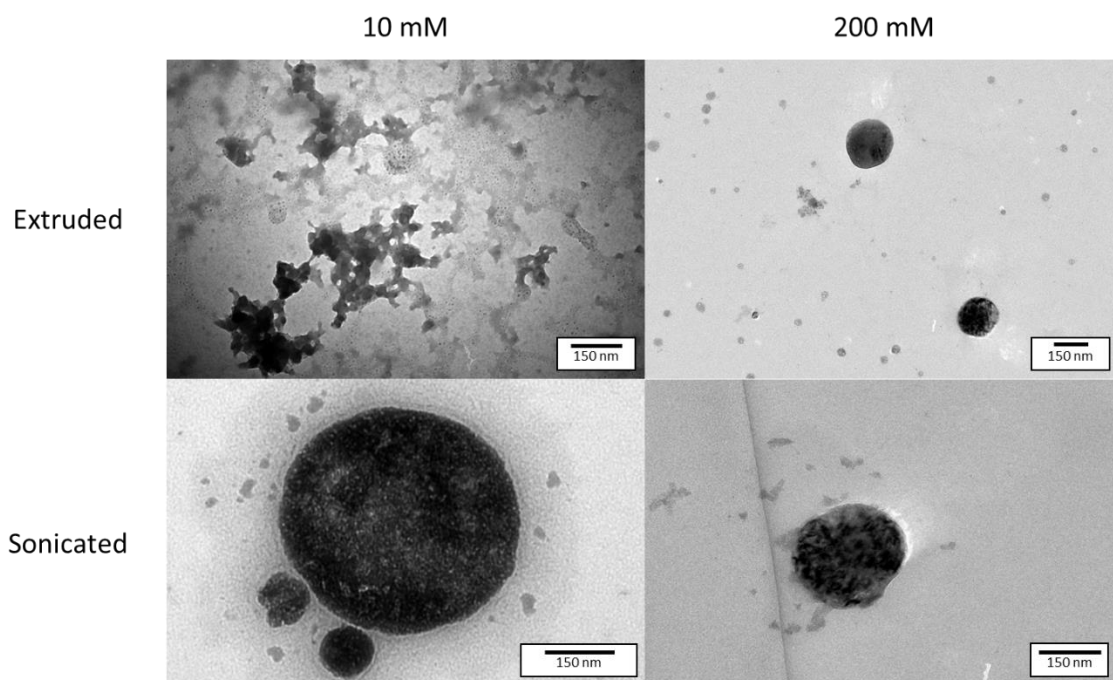
Figure 6.3.3 – TEM of PBD-PEO polymersomes both extruded and sonicated after electroporation in a mixed valence 1:2 (Fe(II):Fe(III)) salt solution at 10 and 200 mM.

TEM analysis of the extruded and sonicated polymers showed the formation of MNP within or around the polymersome with select area electron diffraction showing a diffraction pattern. However, analysis of this did not result in any known iron oxide being identified from the pattern due to only a few electron spots being present (Figure 6.3.), this may be as a result of no crystallinity in the sample or too little of the polymersome to enable this to be visible (Figure 6.3.). The stirred PBD-PEO polymersome samples showed no polymersomes when visualised by TEM in either the 10 mM or 200 mM 1:2 Fe(II):Fe(III) sample. Little polymer was visible in the sample, or the samples were obscured by large amorphous and crystalline iron structures (appendix).
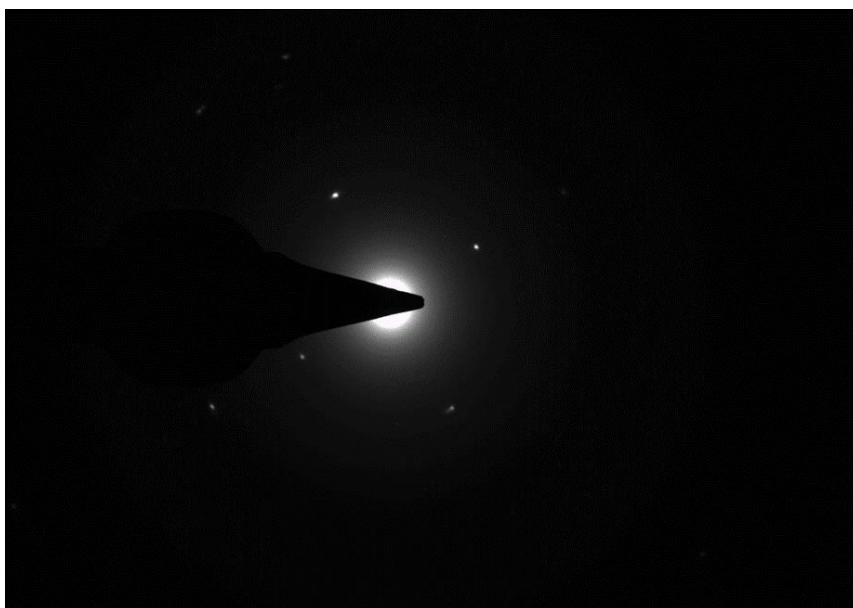
Figure 6.3.4 – Selected area electron diffraction (SAED) of 10 mM sonicated samples showing the presence of crystalline material.

These results did not match those previously identified by Bain *et al* with the PBD-PEO polymer. This may have been due to the age of the polymer, due to the high cost and amount of time available it was decided to not continue with this material and also due to the large size variability introducing to many variables to compare.

6.4   RAFT POLYMERSOMES

Raft polymers were synthesised at a variety of ratios of PEG to PMPC this alteration of the polymer ratios produces polymersomes with altered concentration of COOH groups in the polymer to produce polymersomes with different properties. Polymersomes were synthesised at ratios of 0.7 PEG 113 + 0.3 PMPC28, . [0.6 PEG$_{113}$ + 0.4 PMPC$_{28}$

6.4.1   0.7PEG113-PHPMA400/0.3PMPC28-PHPMA40

The formation of [0.7 PEG 113 + 0.3 PMPC28] polymersomes was confirmed by the loss of the HPMA vinyl proton peak at 5.68 and 6.19 ppm in the H^1 NMR spectra (appendix), this indicates that the polymers achieved >99% conversion to produce the amphiphilic diblock co polymers.

The size and morphology of the produced polymersomes were analysed using TEM and DLS (Figure 6.4.1). TEM analysis identified that polymersome vesicles had been formed, as an inner lumen was visible with in each polymersome. Vesicle formation did not produce spherical polymersomes in all cases, as there were some elongated polymersomes present indicating a heterogenous population in morphology. The size of the particles, as measured by TEM, was 154.5 ± 72 nm indicating a large heterogenous population as seen in the TEM images (Figure 6.4.1). This large spread is as a result of the presence of a small population of elongated vesicles as the histogram shows a small number of very large polymers that could influence the spread of data (Figure 6.4.1 b) as all measured samples were measured along the longest axis. DLS measurement of the RAFT polymersome showed a similar

distribution with a larger population around 200 nm and a smaller population at a higher diameter over 1000 nm (Figure 6.4.1 c), as DLS weight larger size objects more heavily than smaller objects the smaller size does suggest that this is only a minority of the whole population which matches what was observed in the TEM (Figure 6.4.1). An average diameter of 220.9 nm with a PDI of 0.264 was measured via DLS.
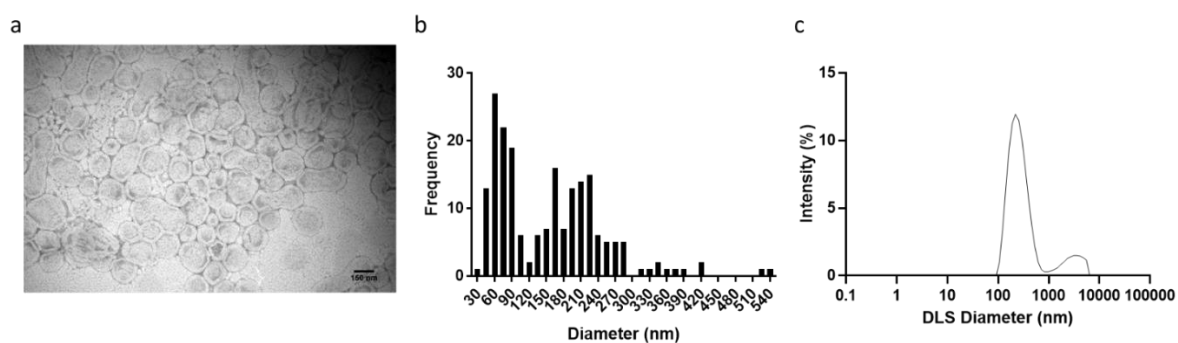
Figure 6.4.1 – Size and morphology of the PEG113-PHPMA400/PMPC28-PHPMA40 polymersomes. a) TEM analysis of the polymersome. b) Frequency distribution of polymer sizes as measured by TEM. c) hydrodynamic size measured by DLS at a pH of 7.4.

The zeta potential of the polymersomes was measured across a pH range of 3.08 – 8.38 to determine surface charge. As pH increased an increasingly negative zeta potential was observed, this plateaued out at pH 7 (Figure 6.4.2). Therefore, at pH's higher than 3.2 polymersomes have a negatively charged surface. This indicates that some of the carboxylic acid groups may have formed on the outer membrane of the polymersome instead of the optimal orientation on the inner membrane. The neutral PEG on the outer membrane should give a zeta potential that does not change with a change in pH.

One possible explanation for the PMPC chains to be on the external membrane is the larger molecular weight of the PMPC block having a shallower curvature and not preferentially orientating to the inner membrane of the polymersome. The hypothesis that some PMPC chains are displayed on the exterior membrane is supported by other work that shows $PMPC_{50}$-$PHPMA_{400}$ has a negative potential at pH values greater than 6.[262] Although there is evidence that some of the PMPC chains may be on the outer membranes, which is possibly as a result of the higher molecular weight of the PMPC block it is expected that the majority of the PMPC chains will be orientated on the inner membrane due to the PMPC block hydrophobicity. The presence of some carboxylic acid terminated PMPC groups may affect the formation of MNPs within the [0.7 PEG_{113} + 0.3 $PMPC_{28}$] polymersomes.

The DLS size was determined across the range of pH values shows that the polymersomes size is not pH dependant (Figure 6.4.1). This is important for biomedical properties as tumour microenvironments are known to be acidic, with pHs as low as 5.6 within tumours, whilst normal tissue is generally neutral pH (7.3 – 7.4).[263] The averaged z-diameter size across the pH range is 222.78 ± 3.07

nm. This is higher than measured for polymersome diameter by TEM 154.9 ± 92.95 nm. Although it is common that DLS measurements are typically higher than those measured by TEM, due to the measurement being of the polymersomes hydrodynamic size at the slipping plane (Figure 2.4.3) and the sample is hydrated rather than vacuum dried as is required for TEM which causes vesicle shrinkage. Although DLS size measurement measures at the slipping plane and results in a larger size measurement than the polymersome actually is, it is considered more accurate than TEM in polymersomes as there is no shrinkage and it removes an observer bias when measurements are made as well as measuring a larger sample population. Cryo-electron microscopy (EM) of the polymersomes allows for a more accurate EM measurements as the sample remains hydrated which maintains the polymersome size (Figure 6.4.3).[259]
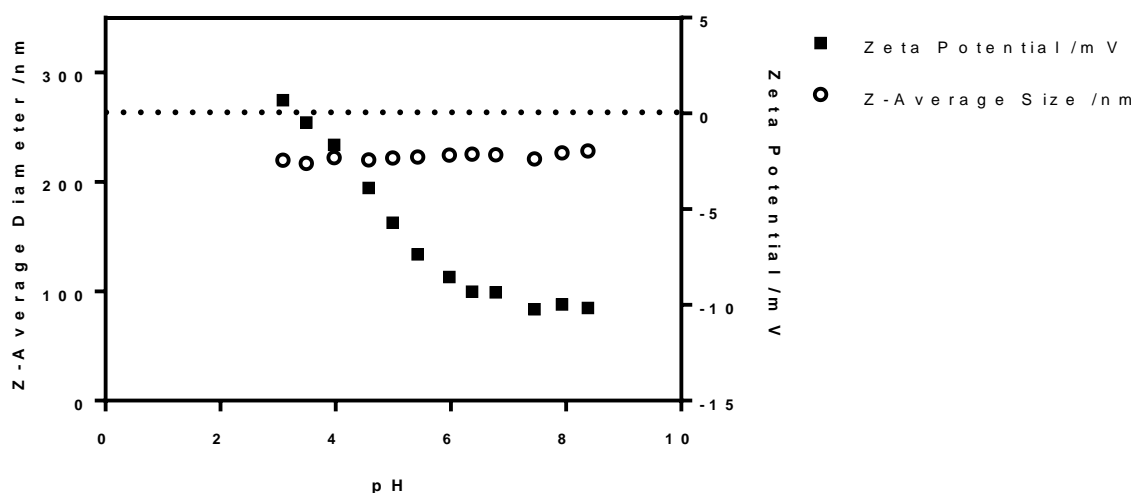
Figure 6.4.2 – Zeta potential (squares) and Z-average diameter (circles) of PEG113-PHPMA400/PMPC28-PHPMA40 across a pH range 3.08 – 8.38.
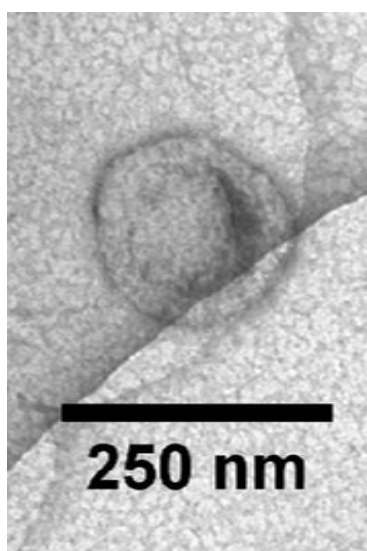
Figure 6.4.3 Cryo EM of [0.7 PEG 113 + 0.3 PMPC28] polymersomes taken from Bain et al 2019.

Earlier results showed that electroporation of base filled polymersomes in an iron rich solution leads to the influx of iron into the membrane of the polymer with the formation of MNPs taking place within the membrane.[259] NaOH soaked polymersomes were electroporated in a mixed 10 mM (Fe(II)/Fe(III)) iron solution.

After electroporation TEM analysis showed the formation of a singular MNP formation within the inner lumen of the polymer vesicles (Figure 6.4.4 e and f). This is the first time that formation of an MNPs has been shown within a vesicle. This indicates that [0.7 PEG_{113} + 0.3 $PMPC_{28}$] polymersomes are a capable biomimic of magnetosomes as it has only been previously seen that MNPs form within the membrane and not within the inner lumen. The formation of the MNP within the lumen and if a level of influence can be exerted over its physical and chemical properties may create a possible replacement for magnetosomes for biomedical purposes as polymersomes offer many advantages over magnetosomes with a much faster production rate and higher yields. The formation of the singular MNP is possibly as a result of the carboxylic acid groups present on the inner membrane of the polymersome providing nucleation points for the synthesis and growth of the MNP. These results also suggests that the carboxylic acid regions of the PHPMA are acting in a similar way to the Mms6 protein within magnetosomes providing a site for nucleation. ICP-OES analysis of the sample pre and post electroporation showed an increase in iron content within the sample indicating that the formed MNPs are iron oxide in nature. Formation of amorphous iron was observed both within the vesicle and surrounding area which may affect the ICP-OES results as this would not be the amount of iron that is just MNP. No change in the average polymersome diameter was observed pre (154.9 ± 92.95 nm) and post electroporation (148.9 ± 39.91 nm). Although the sizes are similar, a reduction in standard deviation indicates that there is a reduced spread of sizes of particles which is observed in the distribution curves.

A similar result was observed from DLS measurements with both pre (227.4 ± 3.8 nm PDI 0.110) and post (226.9 ± 85.9 nm, PDI 0.100 ± 0.029) electroporation had a similar polymersome size. This change in morphology observed via TEM can be attributed to the heat generated during electroporation. Research has shown that an increase in temperature causes the increase hydrophobicity of the PHPMA due to a loss of hydrogen bonds.[264] This increased hydrophobicity is theorised to result in the formation of more spherical vesicles to reduce the PHPMA blocks interaction with water molecules.[264]
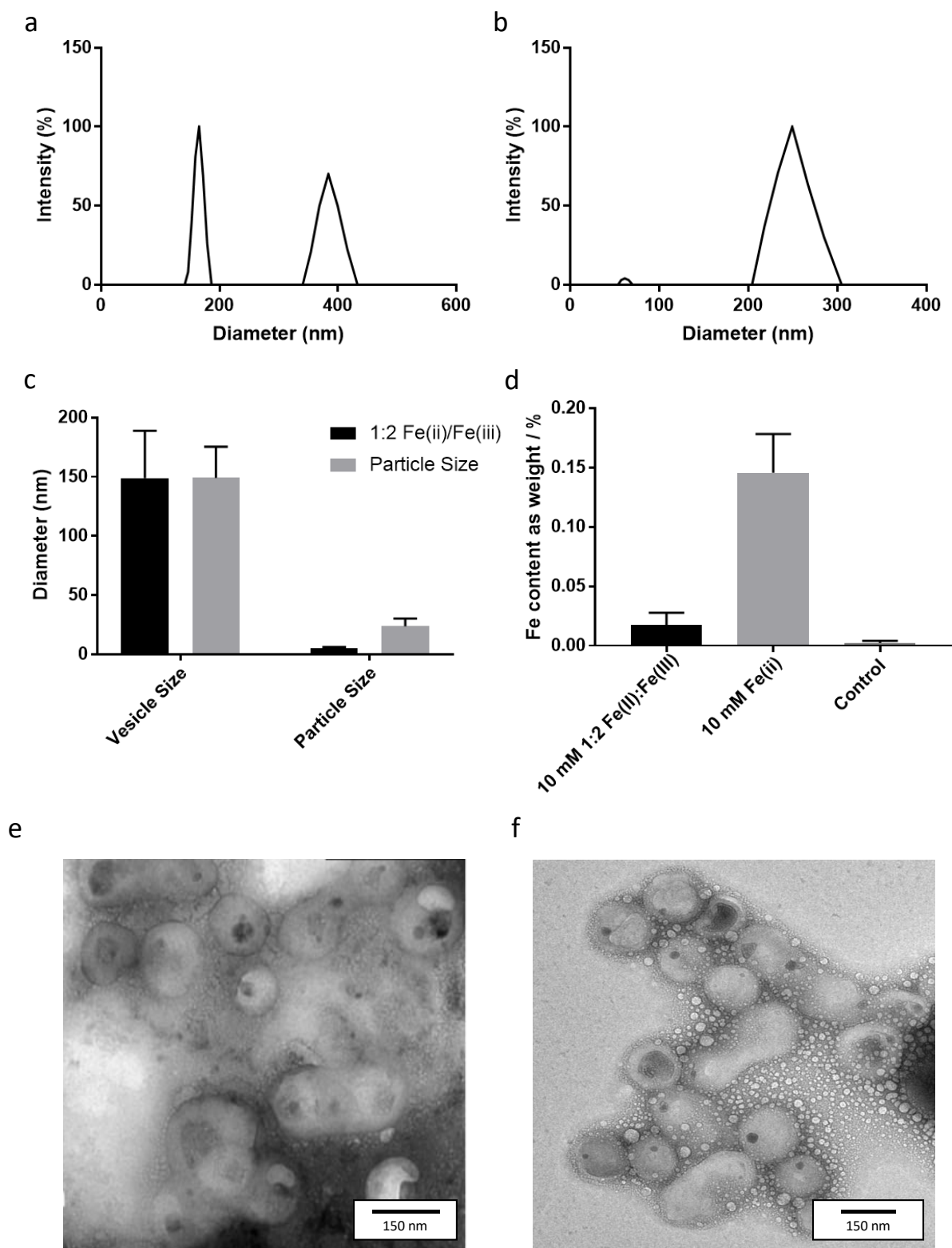
Figure 6.4.4 – Size and morphology of the PEG113-PHPMA400/PMPC28-PHPMA40 polymersomes after electroporation in a 10 mM mixed valence 1:2 (Fe(II)/Fe(III)) solution and a single (Fe(II)) iron salt solution. a-b) z-average diameter of the Fe(II)/Fe(III)and the Fe(II) solutions, respectively. c) size analysis of the polymersomes and the produced particles that were formed within the vesicle. d) Percentage of iron content within the vesicles after electroporation. TEM analysis of the polymersome after electroporation (e) Fe(II)/Fe(III) and (f) Fe(II).

TEM analysis of the MNPs within the polymer vesicle showed a diameter of 46.4 ± 18.2 nm in the mixed valence solution and a diameter of 23.71 ± 6.5 nm in the single Fe(II) solution (Figure 6.4.4).

Magnetometry data (VSM) showed a large diamagnetic response the negative gradient due to the diamagnetic polymersome (Figure 6.4.5). This diamagnetic response is because of the large amount of polymer present in the sample, as there is less than 0.1% iron content within the polymer. A magnetic response is observed between -2000 and 2000 Oe due to the presence of MNPs. Coercivity was measured as 22.8 Oe, this indicates that the particles should respond when exposed to an AMF to generate heat for hyperthermia. The measured coercivity is lower than literature values for magnetite nanoparticles of the same size, which implies that the synthesised MNP is not magnetite but maghemite or there is a large non crystalline area of iron ions around the edge.[265]
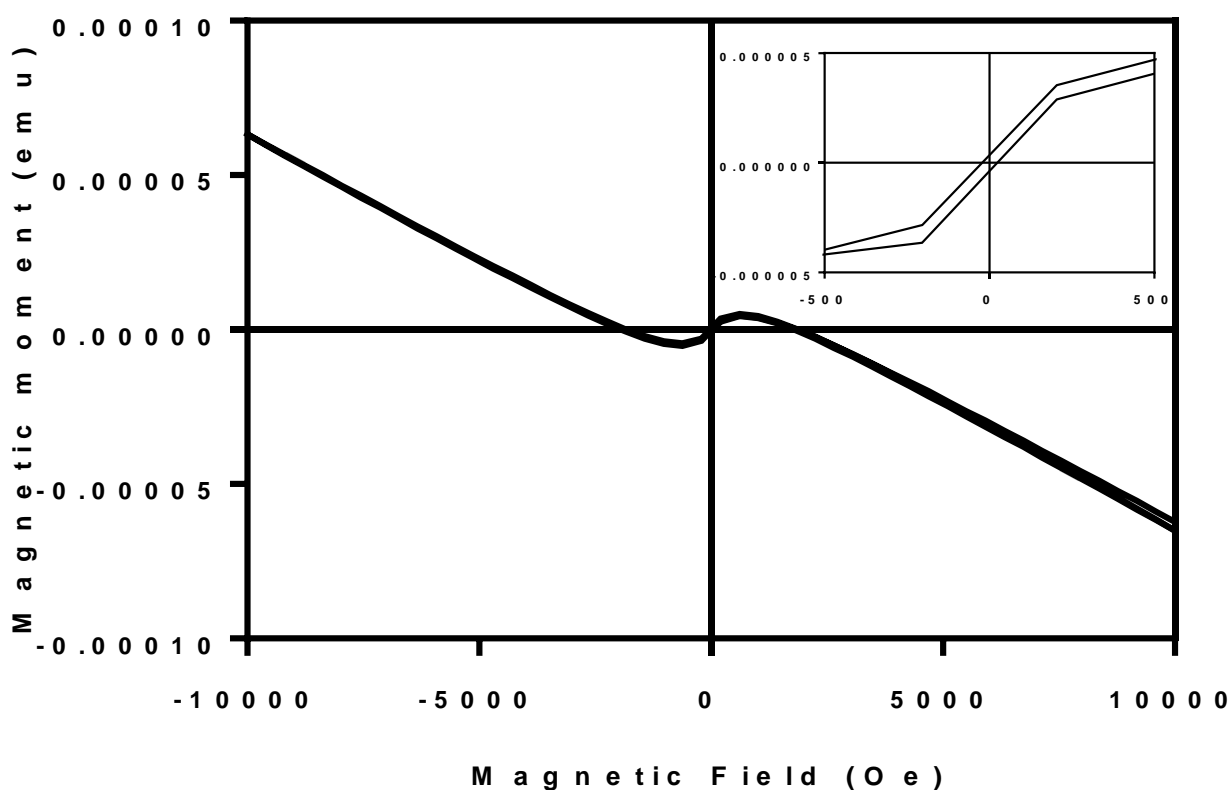
Figure 6.4.5 – Magnetic measurement of the mixed valence 1:2 (Fe(II)/Fe(III)) PEG113-PHPMA400/PMPC28-PHPMA40 polymersomes. Insert shows zoomed in portion section of the low field. Measurements were running from -10 000 – 10 000 Oe at room temperature.

The particles synthesised were measured at 46.4 ± 18.2 nm, this places them within the single domain size range and is confirmed by the small hysteresis present. Selected area electron diffraction (SAED) indicated the presence of magnetite, wüstite and haematite within the sample. This suggests the formation of multiple different iron oxide species which may explain why the Hc of the sample is lower than expected compared to literature values (Figure 6.4.6). To confirm the identity of the iron oxide, further analysis using Mossbauer spectroscopy could be used.
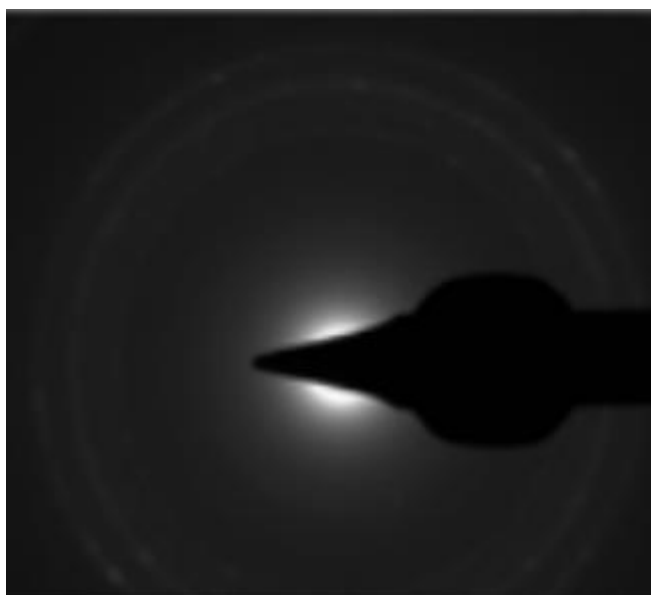
Figure 6.4.6 Selected area electron diffraction of PEG$_{113}$-PHPMA$_{400}$/PMPC$_{28}$-PHPMA$_{40}$ after electroporation in 10 mM 1:2 Fe(II):Fe(III).

6.4.3 SINGLE IRON SALT PRECIPITATION PEG$_{113}$-PHPMA$_{400}$/PMPC$_{28}$-PHPMA$_{40}$ POLYMERSOMES

In the previous section it has been shown that the use of a mixed valence solution has produced MNPs within the inner lumen in a mixed valence solution. This has also been shown to produce smaller particles within the membrane of polymers.[259] This a feat that was observed in some samples although not as commonly in our work. The use of a ferrous iron salt (Fe(II)) singularly has not previously been tested for the synthesis of MNPs within a polymersome system. The use of a ferrous iron only means that precipitation would not occur instantaneously upon exposure to basic conditions and would require the oxidation of the Fe(II) iron to Fe(III) irons. This could help to reduce the variation that was observed in the 1:2 Fe(II):Fe(III) solution with MNP formation within the membrane as the mixed valence iron solution would not react with the presence of the NaOH base. To determine if the size of the synthesised MNPs can be controlled the concentration of Fe(II) was varied from 10, 50, 100 and 200 mM. The ability to control the size of the MNP would greatly improve the use of polymersomes as a magnetosome mimic.

TEM analysis of the polymersome size of the pre and post electroporation showed that polymersome size was not greatly affected by electroporation, except in the 100 mM sample which showed an increase in polymersome size. The polymer diameter pre-electroporation was measured at 154.9 ± 92.95 nm and the measured diameter of the vesicles electroporated in the 10-, 50- and 200-mM iron solutions were 149.1 ± 26.29 nm, 146.1 ± 28.95 nm, and 142.5 ± 30.24 nm respectively (Figure 6.4.8 a). The polymer vesicle electroporated in the 100 mM solution showed an increase in size to 183.1 ± 9.45 nm. The reason for this is unknown but it may be due to a level of observer error in the measurement of the TEM results. In all electroporated samples a reduction in the standard deviation was observed indicating a reduction in the distribution of the vesicle size after electroporation. This is

consistent with polymer electroporated in the mixed valence iron solution. The excess heat generated during electroporation causes the polymersomes to rearrange into a more spherical structure.

Gradually increasing the concentration of Fe(II) resulted in a gradual increase in the size of the MNPs. Concentrations of 10, 50 100 and 200 mM produced MNPs with an average diameter of 23.71 ± 6.5nm, 44.64 ± 22.05 nm, 45.38 ± 25.13 nm, and 54.6 ± 21.43 nm respectively (Figure 6.4.8 b). The increasing size of MNP within the vesicle of the polymersome indicates that a key limiting factor in MNP size is the availability of iron. As concentration of iron solution increased there was also a marked increase in the amount of MNPs observed outside of the vesicles (Figure 6.4.8 f). Larger amorphous structures were noted also noted was the concentration of iron increased (Figure 6.4.8). Only for the 200 mM iron solution MNPs were also observed outside of the vesicles. This suggests that NaOH can leak from the vesicle into the iron solution provided, resulting in the formation of MNPs. SAED was performed and this indicated that MNPs were crystalline in nature and the spacings corresponded to the crystal structure of maghemite, goethite, hematite and wüstite (Figure 6.4.7).[266] Amorphous iron oxide was identified within the vesicle for the 200 mM iron solution, as well as MNPs. The presence of amorphous iron oxide suggests that not all of the iron ions in solution are used for the growth of MNPs, this could be due to leakage of NaOH during electroporation.
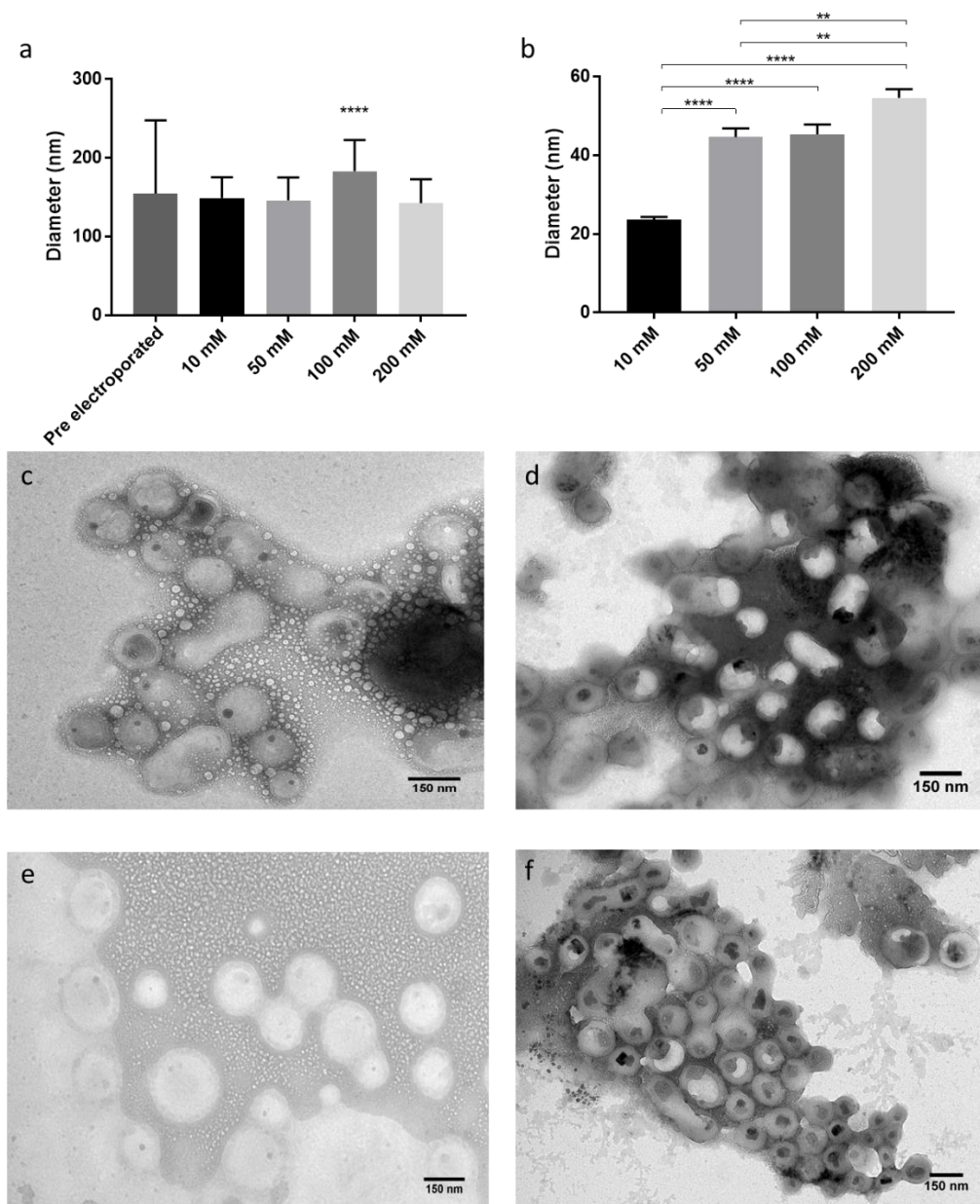
Figure 6.4.7 – Size analysis of the PEG$_{113}$-PHPMA$_{400}$/PMPC$_{28}$-PHPMA$_{40}$ polymersomes after electroporation with increasing concentration of Fe(II) salts. a) TEM size analysis of polymersome diameter. b) TEM size analysis of particles found within the vesicle. (c-f) TEM of polymersomes from concentration of 10, 50, 100 and 200 mM. . ** denotes p= ≤0.01, **** denotes p=≤0.0001 significant difference (One-way ANOVA with Dunnett correction for multiple comparisons

Particles synthesised using 10 mM Fe(II) solution were smaller than those synthesised using the mixed valence solution, the size only reached similar MNP sizes at concentrations greater than 50 mM. This suggests that more iron ions are used for synthesis of MNPs in the mixed valence solution. This is most likely due to the molar ratio of Fe(II) to Fe(III) iron ions matching the ratio for magnetite synthesis, so it is likely that more of the iron underwent precipitation forming larger particles.

These results are similar to those observed when using the mixed valence iron solution, as a single MNP was present within each of the vesicles at all concentrations. Therefore, this suggests that iron ions enter the vesicle through pores, opened by electroporation, and nucleates at a point close to or in contact with the inner membrane. Subsequent iron that enters the polymersome is believed to either be used in synthesis of MNPs or to form an amorphous iron mixture at higher concentrations. Formation of MNP at a point close to or in contact with the membrane, provides evidence that the carboxylic acid groups on the PMPC bind iron and act as a nucleation point, similar to how Mms6 binding iron for nucleation and growth of magnetite within magnetosomes.
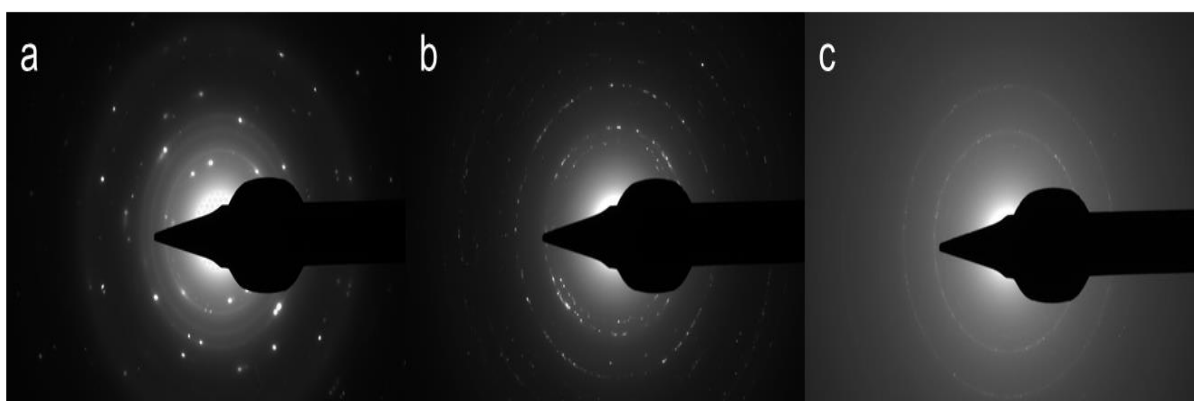
Figure 6.4.8 – Selected area electron diffraction of Fe(II) solution at concentrations of 10mM (a), 50 mM (b) 100 mM.

DLS size analysis was performed after electroporation and showed that the hydrodynamic polymersome size decreased with increasing iron concentration (Table 6.4.1). This is consistent with what was seen in the mixed valence solution. The larger decrease observed as the iron concentration increases could be put down to increasing conductivity of the sample as the concentration of iron increased. This increase in conductivity could increase the amount of heat generated when electroporated forcing the formation of smaller vesicles.

Table 6.4.1 – Hydrodynamic size of as measured by DLS at increasing concentrations of Fe(II) with Poly dispersity index (PDI).

	Iron (Fe(II)) Concentration /mM			
	10	50	100	200
DLS Size /nm	216.2 ± 96.6	200.1 ± 83.0	177.2 ± 78.4	180.8 ± 66.8
PDI	0.149 ± 0.064	0.121 ± 0.028	0.151 ± 0.027	0.146 ± 0.075

Although there is an observed difference in MNP formation within the polymer vesicle with larger MNP diameters as well as a more cubic shape and increased MNP forming outside of the polymersomes. The amount of iron determined by ICP-OES was seen to have a large variation in the amount of iron measured, although there was an increase as the Fe(II) iron concentration increased

to 100mM and then decreased in the 200 mM concentration. This decrease even though the MNP size increased shows that ICP-OES measurements are affected by the iron present outside the vesicles and are not accurate (Figure 6.4.9). However, this could indicate that ICP-OES may not be able to accurately calculate the amount of iron formed within the vesicle. Another cause of the large variation in the observed ICP-OES results could be due to the clean-up of the polymers after electroporation, this process may not be complete, and some external iron oxide may still remain. The method of performing the purification steps would need to be examined to allow thorough removal of external iron oxide without further dilution of the sample. This could be through the use of a more complex HPLC size exclusion column to improve removal of external iron ions. Even with the large amounts of iron oxide outside of the vesicles, the iron content of the samples was measured at less than 0.5% for all concentrations tested (Figure 6.4.9). However, this is higher than the iron content measured in mixed valence polymersomes (Figure 6.4.4, Figure 6.4.1) and MNPs produced by the single iron salt were smaller in diameter. The presence of higher levels of iron could indicate that there is a higher percentage of polymer vesicles that contain an MNP.
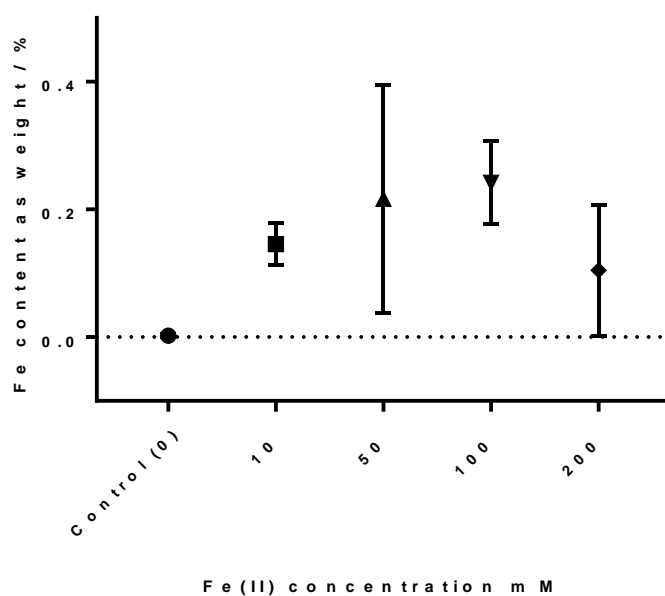
Figure 6.4.9 – Iron content of PEG_{113}-$PHPMA_{400}$/$PMPC_{28}$-$PHPMA_{40}$ polymersomes after electroporation of with concentrations of Fe(II) iron salts. Fe content measured by ICP-OES Data points represent 3 individual repeats ± SD. There is no significant difference between the points as measured by multiple comparison ANOVA.

The presence of a single MNP located within the lumen in close proximity to the inner membrane suggests that the presence of carboxylic acid groups act in a similar manner to Mms6 in MTB, but this would require further investigation to determine if this is the case. Polymers with methylated ends, instead of carboxylic acid regions, could be used and iron formation compared. If a reduction in iron formation was observed when methylated ends were used this would suggest that the presence of the carboxylic acid region is responsible.

VSM measurements of the 10- and 50-mM samples showed similar results to the mixed valence iron solution with a diamagnetic response with a negative gradient due to the presence of the polymersome. A magnetic response is observed between -2000 and 2000 Oe due to the presence of the MNPs which was similar to the mixed valence iron ion solution. Coercivity of the 10 mM and the 50 mM sample were measured at 49.5 and 55.3 Oe respectively. Even though the Fe(II) iron ion solution does not have the correct ratio of iron ions for the formation of magnetite that the mixed valence 1:2 Fe(II): Fe(III) solution has, a larger coercivity was observed in the Fe(II) concentrations even though the measured particles are smaller in diameter. This larger coercivity suggests that the Fe(II):Fe(III) mixed valence solution synthesised MNPs containing smaller crystalline MNPs surrounded by non-crystalline structure or there are more nonmagnetic iron oxides formed in this sample. This result shows that using Fe(II) iron solution only synthesises better MNPs than a mixed valence solution.
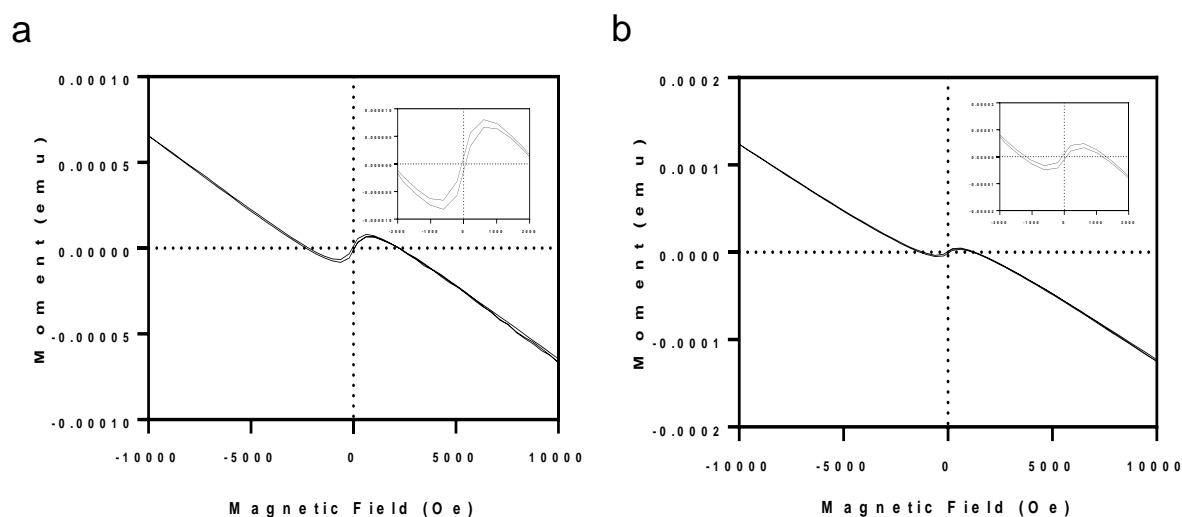
Figure 6.4.10 – VSM of between a field of -10 000 and 10 000 Oe with the insert showing the low field readings between -2000 and 2000 Fe(II) iron concentrations of 10 mM (a) and 50 mM (b).

6.5 ALTERATION OF PEG-PMPC RATIO ON IRON OXIDE FORMATION WITHIN POLYMERSOMES

To determine the effect that the carboxylic acid groups had on the synthesis of MNPs within the polymersome, polymersomes were synthesised with altering ratios of PEG-PHPMA/PMPC-PHPMA. To produce vesicles without COOH groups PEG_{113}-$PHPMA_{400}$ vesicles were prepared from just a PEG_{113} precursor polymer (macro-CTA). Vesicles with no PEG were formed from $PMPC_{28}$-$PHPMA_{450}$ vesicles, producing vesicles that would have carboxylic acid groups expressed on both the inner and outer membrane. $[0.6\ PEG_{113} + 0.4\ PMPC_{28}]$ – $PHPMA_{400}$ these vesicles should have the inner membrane populated with carboxylated $PMPC_{28}$ and the outer membrane should be populated by PEG_{113}-$PHPMA_{400}$. A $[0.8\ PEG_{113} + 0.2\ PMPC_{28}]$ – $PHPMA_{400}$ concentration was also prepared which should similarly have the carboxylated $PMPC_{28}$ populating the inner membrane albeit with a smaller

population of carboxylated $PMPC_{28}$. The variation in COOH concentration should allow the determination of the extent this plays a role in the synthesis of MNPs within the vesicle.

Table 6.5.1 – The synthesised polymersomes with the fraction of end groups with carboxylic acid groups.

Polymersome	Fraction of COOH groups
PEG_{113}-$PHPMA_{400}$	-
$[0.8\ PEG_{113} + 0.2\ PMPC_{28}] - PHPMA_{400}$	0.2
. $[0.6\ PEG_{113} + 0.4\ PMPC_{28}] - PHPMA_{400}$	0.4
$PMPC_{28}$-$PHPMA_{450}$	1

TEM sizing of the produced polymers (Figure 6.5.1) showed the that the $PMPC_{28}$-$PHPMA_{450}$ resulted in the smallest diameter vesicles (93.52 ± 15.52 nm) and the PEG_{113}-$PHPMA_{400}$ produced the largest vesicles (385.6 ± 145.6 nm). The $[0.6\ PEG_{113} + 0.4\ PMPC_{28}] - PHPMA_{400}$ and the $[0.8\ PEG_{113} + 0.2\ PMPC_{28}] - PHPMA_{400}$ polymers produced vesicles with a diameter of 201 ± 62.12 nm and 228 ± 61.89 nm, respectively. The distribution of the size of the vesicles showed that the $[0.6\ PEG_{113} + 0.4\ PMPC_{28}]$ and the $[0.8\ PEG_{113} + 0.2\ PMPC_{28}]$ both had a similar size distribution and size, with the $[0.8\ PEG_{113} + 0.2\ PMPC_{28}]$ being the larger of the two. This coupled with the large size of the PEG_{113}-$PHPMA_{400}$ vesicles suggests that the size of the vesicle is affected by the ratio of PEG-PHPMA to PMPC-PHPMA, with the higher PEG-PHPMA ratios being larger in size.
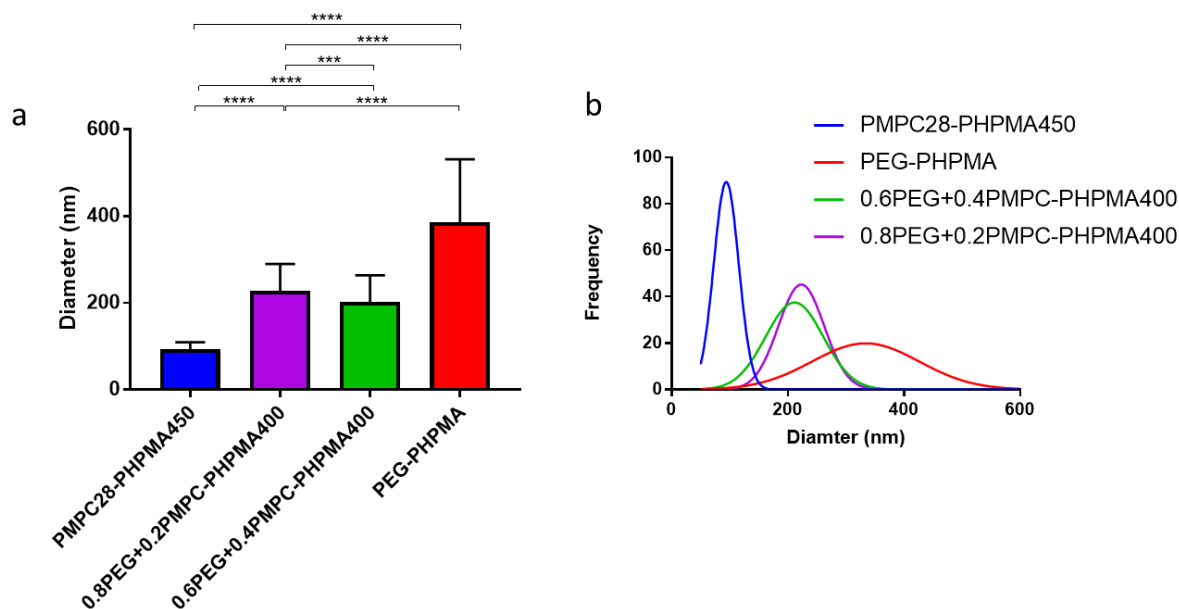
Figure 6.5.1 – Size analysis of $PMPC_{28}$-$PHPMA_{450}$ (blue), PEG_{113}-$PHPMA_{400}$ (red), $[0.6\ PEG_{113} + 0.4\ PMPC_{28}] - PHPMA_{400}$ (green) and $[0.8\ PEG_{113} + 0.2\ PMPC_{28}] - PHPMA_{400}$ (purple) polymersomes . a) TEM analysis of the polymersome diameter. b) Gaussian distribution of the TEM measured sizes of polymersomes. *** denotes p= ≤0.001, **** denotes p=≤0.0001 significant difference (One-way ANOVA with Dunnett correction for multiple comparisons

TEM analysis of all polymersomes showed vesicles with a clear lumen space, although the size of the lumen varied was dependent on the size of the vesicle and the thickness of the membrane (Figure 6.5.2). The $PMPC_{28}$-$PHPMA_{450}$ produced vesicles with what appeared to be the smallest lumen size, due to the small size of the vesicles and the thickness of the membrane itself. Inversely the PEG_{113}-$PHPMA_{400}$ appeared to have the largest lumen size due to the large overall size of the vesicles themselves. The different ratios of PEG-PHPMA/PMPC-PHPMA appeared to have vesicles with a similar lumen size, which will provide a good indicator that altering the ratio of PEG-PHPMA/PMPC-PHPMA alters the MNP size, as the amount of COOH groups within the inner membrane will change. Although not observed before it is theorised that lumen size could exert a measure of control over the size of the formed MNP after electroporation. This is different to how MNP size is controlled in magnetosomes, as this is controlled by a large number of proteins that are involved in the transport of iron ions across the membrane as well as nucleation and growth. The size of the lumen would influence the amount of NaOH that can fill the space and the amount of iron salt that can enter the vesicles. The lumen size may also affect the growth and formation of the MNP by simply producing a physical barrier to further growth.
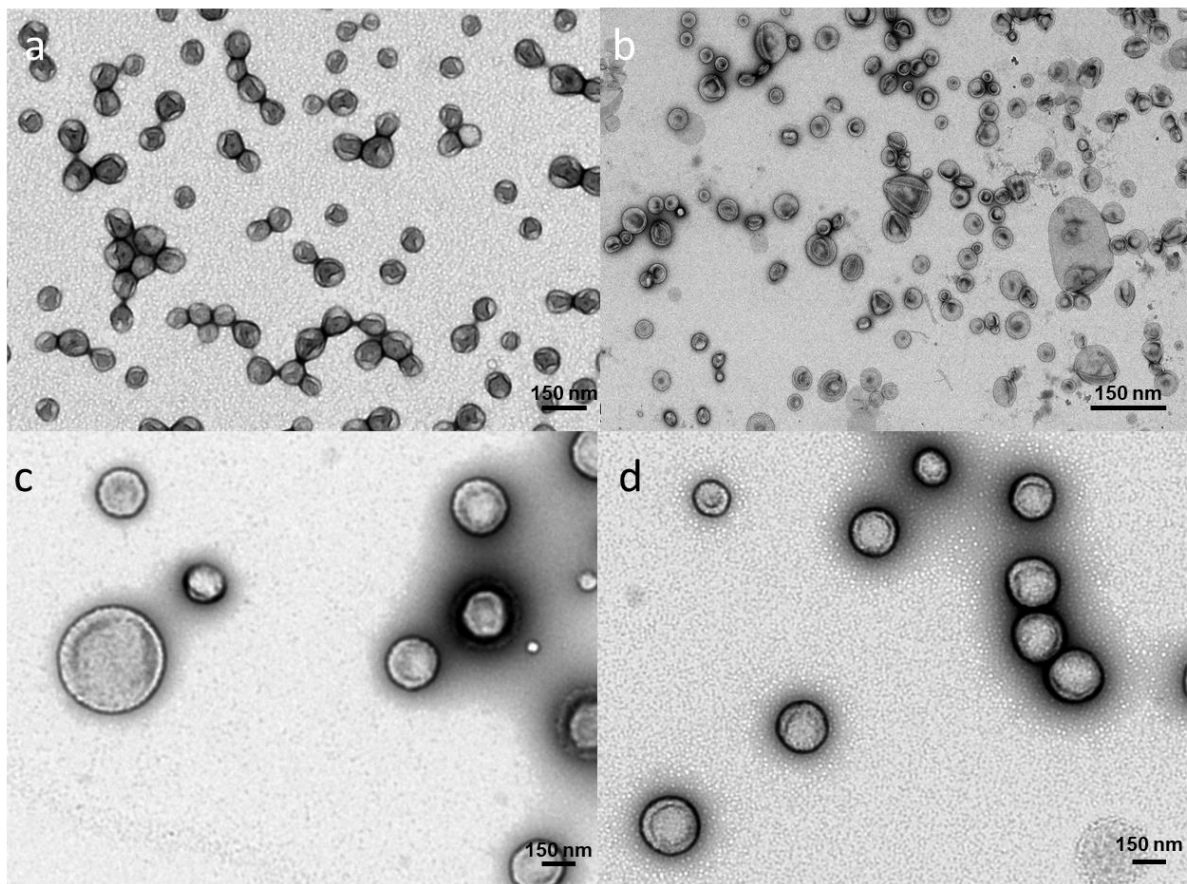
Figure 6.5.2 – TEM of produced polymers showing the size and morphology. a) $PMPC_{28}$-$PHPMA_{450}$. b) PEG_{113}-$PHPMA_{400}$. c) $[0.6\ PEG_{113} + 0.4\ PMPC_{28}] - PHPMA_{400}$ and d) $[0.8\ PEG_{113} + 0.2\ PMPC_{28}] - PHPMA_{400}$.

Further analysis of the polymersomes by DLS and small angle x-ray scattering (SAXS) showed that the DLS size were in the same range as those measured by TEM, although slightly larger due to the shrinkage of the vesicles during TEM (Table 6.5.2). This was true for all vesicles except in the 0.6 PEG_{113} + 0.4 $PMPC_{28}$ which measured the diameter of the vesicles smaller in DLS than TEM (approx. 12 nm). Whereas the 0.8 PEG_{113} + 0.2 $PMPC_{28}$ DLS size matched that of the TEM size of 228 nm. SAXS analysis of size provides a better indication of the vesicles true size, as it removes user bias measuring by sampling millions of vesicles, but it does not measure at the slipping plane as DLS does but closer to the membrane. SAXS measurements were able to be performed on all samples except the $PMPC_{28}$-$PHPMA_{450}$ due to the membrane thickness it was unable to fit this polymer to the model to produce usable data. The SAXS diameters matched more closely to the measured TEM diameter than the DLS diameter. However, in the mixed ratio PEG-PHPMA/PMPC-PHPMA the measured value was lower than what was measured by TEM, and values were much closer in size with each other. SAXS modelling of both mixed ratio of PEG-PMPC/PHPMA-PMPC show that the $PMPC_{28}$-$PHPMA_{400}$ chains populate the inner vesicle envelope (Table 6.5.2). This would mean the HOOC-$PMPC_{28}$ stabiliser chains point into the vesicles' lumen, and the PEG_{113}-$PHPMA_{400}$ chains should therefore populate the vesicles outer envelope.

All of the vesicles showed a PDI, as measured by DLS, of below 0.2 which indicates that the vesicles would be suitable for biomedical applications. Polymersomes with a PDI below 0.2 are deemed acceptable for use in biomedical applications.[267]

Table 6.5.2 – Table showing polymersome morphology as determined by TEM, DLS and SAXS. Size (D), along with the poly dispersity index (PDI) and the fraction of the PMPC on the outer membrane of the vesicles. SAXS diameter was unable to be determined for $PMPC_{28}$-$PHPMA_{450}$ due to the membrane thickness. asterisk indicates when PMPC fraction was fixed at 0.5 in the model.

Polymer	TEM D /nm	DLS D /nm	PDI	SAXS D /nm	PMPC fraction
PEG_{113}-$PHPMA_{400}$	385.6 $\pm$ 145.6	462	0.18	402	-
0.8 PEG_{113} + 0.2 $PMPC_{28}$	228 $\pm$ 61.89	228	0.13	196	0.5*~ 0
0.6 PEG_{113} + 0.4 $PMPC_{28}$	201 $\pm$ 62.12	189	0.08	192	0.5*~ 0
$PMPC_{28}$-$PHPMA_{450}$	93.52 $\pm$ 15.52	122.6	0.104	-	-

6.4.4 ELECTROPORATION IN AN FE(II) SALT AT INCREASING CONCENTRATIONS

The vesicles were electroporated in varying concentrations of Fe(II) (10, 50, 100 and 200 mM) to determine if iron concentration influenced the size of the polymersome and the size of the MNP as observed in the previous section (on page 143).

From TEM analysis of the polymersome diameter there was seen to be little effect in the $PMPC_{28}$-$PHPMA_{450}$ and PEG_{113}-$PHPMA_{400}$ with a slight variation in the measured size which can be attributed to a measuring variation due to only 100 vesicles being counted. There was a significant drop in the

measured diameter of the 10 mM [0.6PEG$_{113}$+0.4PMPC$_{28}$] polymersomes but this appears to only have affected these concentrations as the 50 and 100 mM did not show a significant difference in size to the pre-treated polymersome(Figure 6.5.3 d). It can be observed there was very little effect of electroporation in increasing concentrations when measured by TEM with the majority of the polymersomes only showing a slight variation in the measured dimeters. This was confirmed by the distribution of the measured sizes as there was no or a slight shift in the distribution of vesicle diameters (Figure 6.5.3.e-h) In the 0.8 PEG$_{113}$ + 0.2 PMPC$_{28}$ and the 0.6 PEG$_{113}$ + 0.4 PMPC$_{28}$ vesicles there was a noticed shift in the distribution curves of all of the electroporated samples to a larger size (Figure 6.5.3 g, h). Although this was not a significant shift it does suggest that electroporation is affecting the vesicle membrane in some manner, although how is still unclear.
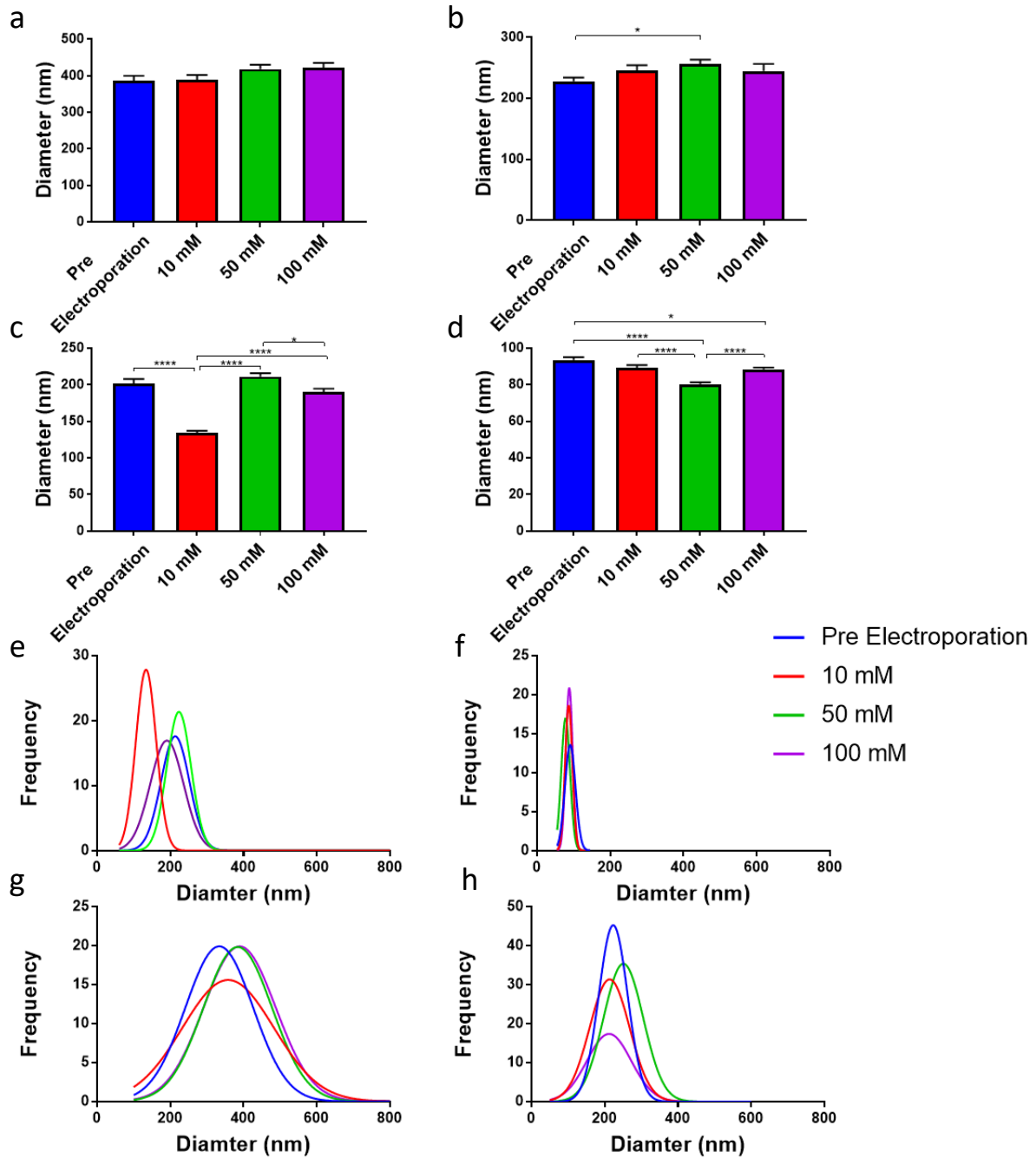
Figure 6.5.3 – Size analysis of PEG113-PHPMA400, [0.8 PEG113 + 0.2 PMPC28] – PHPMA400, [0.6 PEG113 + 0.4 PMPC28] – PHPMA400, PMPC28-PHPMA450 polymersomes size measured by TEM (a-d) and their respective size distributions (e-h). Data points represent mean size as measured by grain size analysis ± SD * represents significance (p≥0.05), **** (p≥0.0001).

DLS size analysis after electroporation showed to vary more than the effect observed in the previously discussed polymers (Figure 6.5.4). PEG_{113}-$PHPMA_{400}$, 0.6 PEG_{113} + 0.4 and 0.8 PEG_{113} + 0.2 $PMPC_{28}$ showed no effect in the size of the polymersomes after electroporation with the DLS measured size remaining consistent across all concentrations of Fe(II) and similar to the pre electroporated size (Figure 6.5.4, Table 6.5.3). This is most likely due to the w/w of these polymersomes is a more stable the 20 % w/w that the 0.7 PEG_{113} + 0.3 $PMPC_{28}$ polymersomes. From DLS spectra it can be observed

that in the PMPC$_{28}$-PHPMA$_{450}$ that multiple population sizes start to form in the 100 mM concentration of Fe(II) with a larger population starting to form. The presence of multiple populations in PMPC$_{28}$-PHPMA$_{450}$ vesicles suggest that COOH groups on the inner lumen in the mixed ratio polymers helps to improve iron nucleation within the vesicle. The large populations observed suggest that more iron oxide is forming outside of the polymersome creating agglomerates. This would be expected in PMPC$_{28}$-PHPMA$_{450}$ vesicles as they have carboxylated PMPC population on the outer and inner membranes which would promote the nucleation of iron oxides on the outer membrane. This may explain why the size of the polymers increased in the highest concentration of Fe(II) if there was the formation of large iron oxide structures nucleating on the outer membrane.
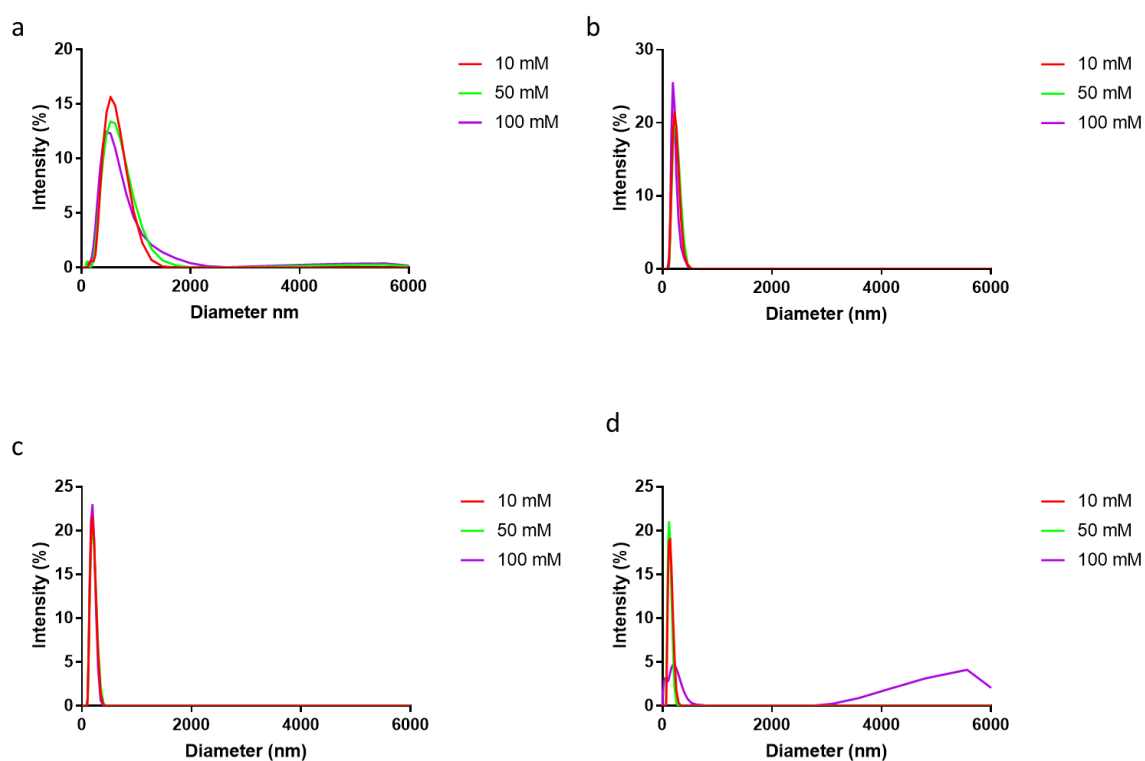
Figure 6.5.4 DLS spectra of PEG$_{113}$-PHPMA$_{400}$, [0.8 PEG$_{113}$ + 0.2 PMPC$_{28}$] − PHPMA$_{400}$, [0.6 PEG$_{113}$ + 0.4 PMPC$_{28}$] − PHPMA$_{400}$, PMPC$_{28}$-PHPMA$_{450}$ polymersomes after electroporation in increasing Fe(II) iron concentrations (a-d)

Table 6.5.3 - DLS size analysis of polymersomes after electroporation at concentrations of 10, 50 and 100 mM along with the poly dispersity index (PDI) and TEM sizes.

	Pre-electroporation			10 mM			50 mM			100 mM		
	Z-Diameter (nm)	PDI	TEM	Z-Diameter (nm)	PDI	TEM	Z-Diameter (nm)	PDI	TEM	Z-Diameter (nm)	PDI	TEM
PEG_{113}-$PHPMA_{400}$	462	0.18	385.6 ± 145.6	498.9 ± 6.6	0.193 ± 0.025	388.3 ± 140.2	492.8 ± 3.2	0.216 ± 0.025	418.6 ± 122.2	480.4 ± 4.8	0.213 ± 0.049	422.3 ± 133.4
0.8 PEG_{113} + 0.2 $PMPC_{28}$	228	0.13	228 ± 61.9	216.9 ± 5.5	0.088 ± 0.022	245.7 ± 83.6	226.8 ± 4.8	0.071 ± 0.027	256.4 ± 68.7	312.2 ± 47.3	0.344 ± 0.037	244.8 ± 90.2
0.6 PEG_{113} + 0.4 $PMPC_{28}$	189	0.08	201.7 ± 62.2	185.5 ± 4	0.046 ± 0.028	134 ± 30.9	185.9 ± 3.5	0.09 ± 0.021	211.2 ± 45.8	181.4 ± 1.4	0.055 ± 0.033	189.8 ± 49.3
$PMPC_{28}$-$PHPMA_{450}$	122.6	0.104	93.5 ± 15.5	130.3 ± 5.1	0.1 ± 0.0242	89.3 ± 13.4	121 ± 0.9	0.067 ± 0.046	80.3 ± 11.5	148.5 ± 233.4	0.781 ± 0.208	88.4 ± 9.8

TEM analysis of the polymers after electroporation indicated formation of MNPs however these varied across the polymers (Figure 6.5.5). In the $PMPC_{28}-PHPMA_{450}$ polymers it appeared that there was formation of MNPs within the lumen of the vesicles. However, MNPs did not appear in all vesicles as there where a high number that had no MNP formation, this was true for all iron concentrations tested. TEM of the $PMPC_{28}-PHPMA_{450}$ also revealed a high level of crystalline iron oxide formed outside of the vesicles and this increases as the concentration of iron increases. This amorphous iron also appeared to be in contact with the surface of the vesicles which suggests that it may be attracted to the HOOC-PMPC groups present on the outer membrane.

Even though the $PEG_{113}-PHPMA_{400}$ had no COOH groups present there was still formation of MNP, which was expected as had been seen in other polymer and liposome vesicles. However, these MNPs appeared to be present either in the lumen or on the membrane. This combined with the presence of large unstructured iron oxides in and around the vesicles suggest that iron is precipitating where it meets with base, with little control in where it is nucleating. There also appears to be the formation of multiple MNPs within the vesicle instead of the singular MNP found in the $PMPC_{28}-PHPMA_{450}$ polymers, this may be as a result of the much larger lumen size or it could be possibly related to the lack of COOH groups.

The [0.6 PEG_{113} + 0.4 $PMPC_{28}$] polymer vesicles showed the formation of a single MNP within the lumen of the vesicle at all concentrations, indicating that the COOH groups have bound the iron ions entering the lumen and nucleated at a single point. There also appears to be smaller less electron dense particles around the outer edge of the membrane. Formation could be due to NaOH leaking out of the pores created during electroporation and reacting with iron ions present around the outer membrane, this effect is observed at all concentrations.

These results are similarly matched by the [0.8 PEG_{113} + 0.2 $PMPC_{28}$] polymersomes as there appears to be a single MNP within the lumen and smaller less electron dense particles on the outer membrane. Within both polymersome samples there is pooling of iron at points where the polymersomes are in contact with one another. The reason for this is currently unclear, but it may be that a well is created trapping iron ions and is not removed during clean-up of the vesicles. Both the [0.8 PEG_{113} + 0.2 $PMPC_{28}$] and the [0.6 PEG_{113} + 0.4 $PMPC_{28}$] showed less iron structures outside of the vesicles than the $PMPC_{28}-PHPMA_{450}$ and the $PEG_{113}-PHPMA_{400}$. However, there was still some iron crystals present but at reduced levels and did not appear to be bound to the membrane. This points to the fact that the presence of COOH on the inner membrane helps to improve the synthesis of MNPs within polymersomes.

Concentration of Iron

10 mM   50 mM   100 mM

PEG113-PHPMA400

0.8 PEG113 + 0.2 PMPC28

0.6 PEG113 + 0.4 PMPC28

PMPC28-PHPMA450
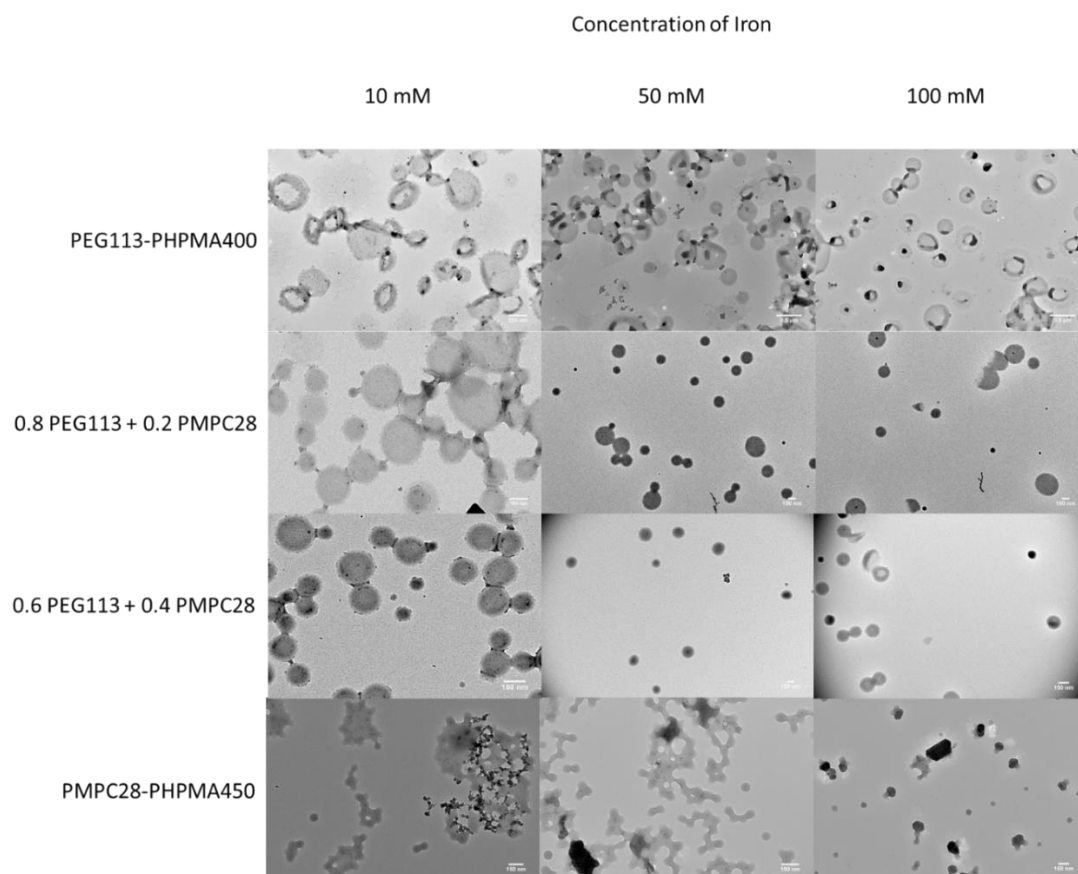
Figure 6.5.5 – TEM of polymersomes after electroporation with concentrations of 10-, 50- and 100-mM Fe(II) showing the morphology of the polymersomes as well as MNP formation and distribution.

Grain size analysis of synthesised MNPs observed that as the concentration of the iron solution increased the size of the MNP increased from $29 - 95$ nm in the PEG_{113}-$PHPMA_{400}$, $14 - 23$ nm in the $[0.8PEG_{113}+0.2PMPC_{28}]$, $11 - 17$ nm in the $[0.6PEG_{113}+0.4PMPC_{400}]$ and from $9 - 23$ nm in the $PMPC_{28}$-$PHPMA_{450}$. This increase in size in relation to increasing Fe(II) concentration matches results from 70:30 RAFT polymers in the previous section (6.4.3). This was observed across all polymers and suggests that availability of iron controls the size of the particle formed, and that the presence of carboxylic acid groups only play a role in the size control of the MNP that are formed. This is because the same effect was observed across all RAFT polymers, with and without the presence of COOH groups. Although it is seen that the availability of iron was a rate limiting factor in the size of MNP formation.
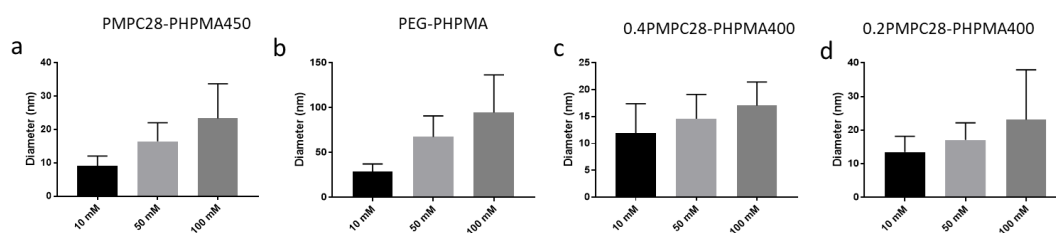
Figure 6.5.6 – TEM size analysis on the effect of increasing Fe(II) on MNPs diameter formed within the vesicles Polymersome PMPC$_{28}$-PHPMA$_{450}$, PEG$_{113}$-PHPMA$_{400}$, [0.6 PEG$_{113}$ + 0.4 PMPC$_{28}$] – PHPMA$_{400}$, [0.8 PEG113 + 0.2 PMPC$_{28}$] – PHPMA$_{400}$ (a-d) respectively.

The size of the vesicle and lumen affected the size of MNP formation, as particle size increased in line with the vesicle size at every concentration of iron tested (Figure 6.5.7). The MNPs did not completely fill the lumen at any concentrations of iron tested, it is possible that is not the physical restriction of the vesicle that was affecting particle size. It is possible that larger vesicles can encapsulate more base and so there is more available for precipitation or that larger vesicles can allow more iron to enter and so more is present in the lumen. As amorphous iron is seen within the largest vesicles (PEG$_{113}$-PHPMA$_{400}$) and is present after electroporation this indicates that it could be a larger influx of iron within these particles that causes the increase in the diameter of MNPs. To determine which factors are responsible for MNP growth, further research and modelling would be necessary.
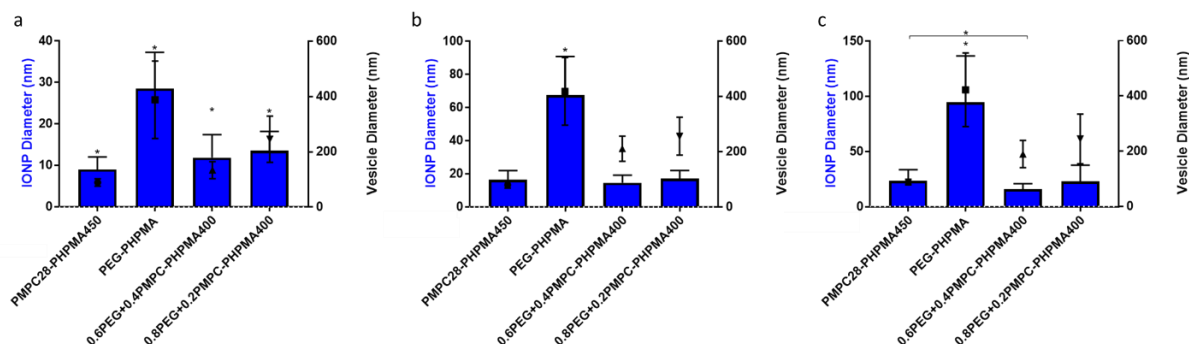
Figure 6.5.7 – Polymersome (black) and particle size (blue) analysis of Polymersome PMPC$_{28}$-PHPMA$_{450}$, PEG$_{113}$-PHPMA$_{400}$, [0.6 PEG$_{113}$ + 0.4 PMPC$_{28}$] – PHPMA$_{400}$, [0.8 PEG$_{113}$ + 0.2 PMPC$_{28}$] – PHPMA$_{400}$ after electroporation in Fe(II) concentrations of 10 mM (a), 50 mM (b) and 100 mM (c).

VSM was performed on all four polymersomes synthesised with 50 mM iron solution. As with previous work this showed a large diamagnetic response with a negative gradient (Figure 6.5.8). This is consistent with VSM of the 70:30 PEG$_{113}$-PHPMA$_{400}$/PMPC$_{28}$-PHPMA$_{40}$ polymersome used earlier (6.4.3) and previously reported work that a vast quantity of diamagnetic polymersome material overrides the weak magnetic response of the MNP themselves.[268] A small kink in the diamagnetic gradient was observed, this was also present in the previously described polymersome, and is believed to be the magnetic response of MNPs at low field indicating positive magnetic susceptibility. With a Hc of 80 Oe in the PEG$_{113}$-

PHPMA$_{400}$, 250 Oe in the [0.8 PEG$_{113}$ + 0.2 PMPC$_{28}$], 35 Oe in the [0.6 PEG$_{113}$ + 0.4 PMPC$_{28}$] and 143 in the PMPC$_{28}$-PHPMA$_{450}$.
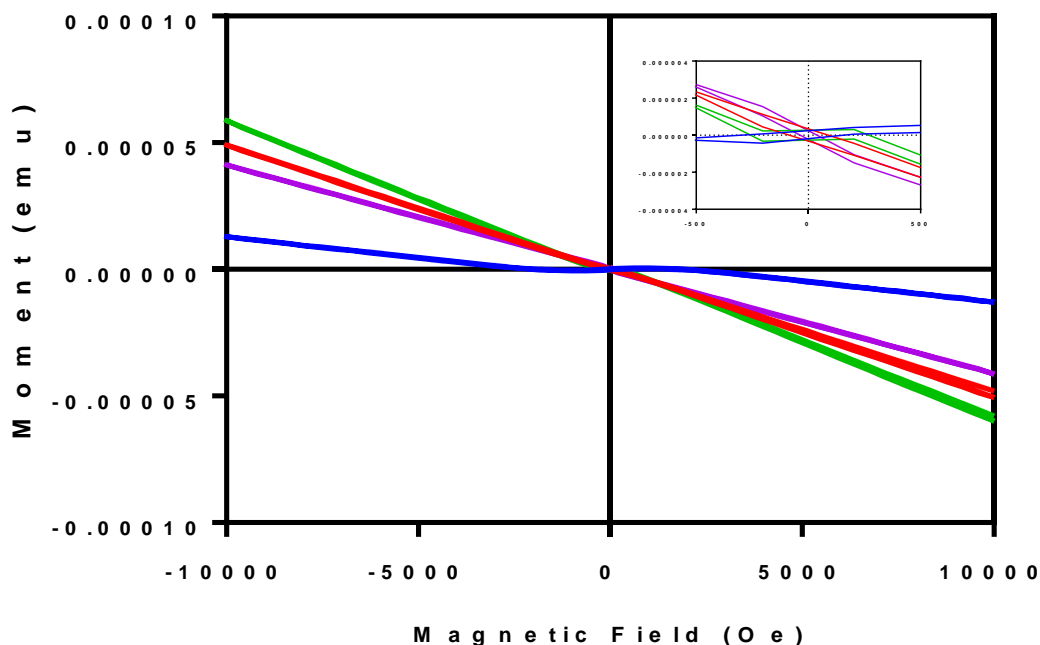
Figure 6.5.8 – Magnetic measurement of the PMPC$_{28}$-PHPMA$_{450}$ (blue), PEG$_{113}$-PHPMA$_{400}$ (red), [0.8PEG$_{113}$+0.2PMPC$_{28}$]-PHPMA$_{400}$ (green) and [0.6PEG$_{113}$+0.4PMPC$_{28}$]-PHPMA (purple) at 50mM. Insert shows zoomed in portion section of the low field. Measurements were running from -10 000 – 10 000 Oe at room temperature.

PMPC$_{28}$-PHPMA$_{400}$ polymer spheroids were used to determine if iron ions were able to enter the polymer upon electroporation even in the absence of an inner lumen. The synthesised PMPC$_{28}$-PHPMA$_{400}$ were 82 nm in diameter when measured via DLS (Table 6.5.4) to be synthesised at a 10% w/w produce spheroids where all chain ends will terminate in carboxylic acid end groups. These were electroporated at 50 and 100 mM to determine if the iron ions were able to enter the polymersome. From TEM analysis it was observed that there was no formation of MNPs within the polymersome but there was the formation of iron oxide around the outside similarly to what was seen in the other polymersomes.

Table 6.5.4 – Table of PMPC28-PHPMA400 polymersome size and polydispersity as measured by DLS.

	Pre-electroporation	10 mM	50 mM	100 mM
DLS (nm)	82	80	82	80
PDI	0.02	0.66	0.41	0.4
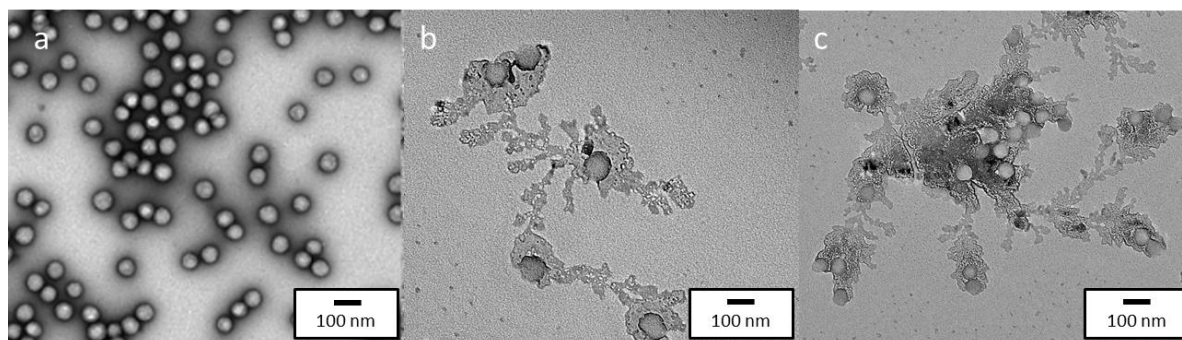
Figure 6.5.9 – TEM of PMPC$_{28}$-PHPMA$_{400}$ polymersomes pre-electroporation (a) as well as in 50 mM Fe(II) (b) and 100 mM (Fe(III).

The lack of formation of a vesicle seen in the TEM of the PMPC$_{28}$-PHPMA$_{400}$ polymersomes indicates that vesicle structures are required for the formation of MNPs within the polymersomes. This is mostly due to the iron ions not being able to enter the spheroid when electroporated. The presence of iron oxide structures on the outside of the polymersome indicate that the NaOH base was still present within the samples. Although the diameter of the polymer did not change after electroporation in increasing iron concentration when measured by DLS the PDI did increase from 0.02 in the pre electroporated to 0.66 in the 10 mM, 0.41 mM in the 50 mM and 0.4 mM in the 100 mM (Table 6.5.4). This is most likely due to the formation of iron oxide structures around a small percentage of the polymers as was observed in the TEM of the samples creating a heterogenous particle size (Figure 6.5.9).

6.6 DISCUSSION

In this chapter it has been shown that MNPs can be synthesised within the core of polymer vesicles using RAFT co-block polymers including (0.7 PEG113 + 0.3 PMPC28)-PHPMA400, PEG$_{113}$-PHPMA$_{400}$, PMPC$_{28}$-PHPMA$_{450}$, [0.6 PEG$_{113}$ + 0.4 PMPC$_{28}$] – PHPMA$_{400}$ and [0.8 PEG$_{113}$ + 0.2 PMPC$_{28}$] – PHPMA$_{400}$. The use of a PBD-PEO co block polymer was investigated, as previously used in literature,[109] but due to the polymer not responding to methods of size control resulting in the formation of 3 distinct population sizes and the inability to alter the structure this was not carried forward. It was also decided to not carry this polymer forward as formation of discrete MNPs within the polymersome was not possible.

Proteins with acidic residues are known to help control the nucleation and size formation of magnetite in MTB.[144,181] Here the presence of these acidic regions within the membrane of the polymersome is mimicked using carboxylated PMPC to determine if this alters the formation of MNPs within the vesicle. From initial work with the (0.7 PEG_{113} + 0.3 $PMPC_{28}$)-$PHPMA_{400}$ synthesised at a 20% W/W solution of PEG_{113}/$PMPC_{28}$ to HPMA, it was shown that both ratio of iron and concentration play a role in the formation of iron oxides within polymer vesicles.

Although work in mixed valence solutions did not match previously reported work where MNPs were observed to form within the membrane of the polymersome.[109,259] This is the first indication of single MNP formation within the lumen of a polymersome in a similar manner to what is observed in magnetosomes. Within the mixed valence solution there was a high sample variance when imaged by TEM, which may be due to the presence of the mixed valence solution causing precipitation rapidly after exposure to NaOH.[259] The use of only Fe(II) showed the formation of MNPs within the lumen of the vesicle in a much cleaner manner. Although analyse of the synthesised iron oxide by SAED revealed the presence of multiple iron oxide species (magnetite, maghemite and wüstite) indicating that a single iron oxide species may have been produced but a heterogenous population. In magnetosomes Mms6 is responsible for controlling the formation of magnetite within the magnetosomes although the presence of the carboxylic acid groups with in the polymersome membrane may mimic the acidic residues of Mms6 this may not be enough to control what iron oxide species is formed. This may require modification of the ratio of iron ions to allow the formation of pure magnetite MNPs within the polymersomes.

Presence of acidic regions within the polymersome was seen to help in controlling the formation of MNPs within the lumen. When polymersomes with no COOH regions were electroporated in an iron solution, MNP formation was still observed within the vesicle but this was not controlled in the same manner as observed by $PMPC_{28}$-$PHPMA_{450}$, [0.6 PEG_{113} + 0.4 $PMPC_{28}$] − $PHPMA_{400}$ and [0.8 PEG_{113} + 0.2 $PMPC_{28}$] − $PHPMA_{400}$. With these polymersomes multiple MNPs were formed on and in the polymersome and there being a much greater size distribution of the formed MNPs. Vesicles with COOH present showed single MNP formation within the lumen and showed little to no other iron oxide formation within the vesicles. The $PMPC_{28}$-$PHPMA_{450}$ had COOH present not only on the inner membrane but also the outer membrane. After electroporation with iron concentrations, it was seen that MNPs formed within the vesicles, but not all vesicles showed MNP formation. Large iron structures were also observed on the outside of the vesicle which was not as

prominent in $[0.6\,PEG_{113} + 0.4\,PMPC_{28}] - PHPMA_{400}$ and $[0.8\,PEG_{113} + 0.2\,PMPC_{28}] - PHPMA_{400}$ which showed more MNPs within vesicles than in the $PMPC_{28}$-$PHPMA_{450}$.

Iron concentration was seen to affect the size of MNPs in all RAFT polymers used, the size of the vesicle also affected the size of the MNPs formed. With larger vesicle sizes seen to directly influence particle size irrelevant of any COOH groups present. These results suggest that although COOH effects the nucleation of MNPs it is not responsible for MNP size and this is affected by other factors. Removal or methylation of COOH groups for further testing would enable further determination of the effect these acidic groups have on the nucleation of iron.

A correlation between the vesicle, or possibly lumen size, directly effecting MNPs size was also observed. Although further work would be required to determine which of these factors is responsible for MNP size would be required by altering the membrane thickness in polymersomes of the same size across a range of polymersomes sizes to determine if it is the effect of lumen or vesicle size that drives the MNP size in the synthesis of MNPs in polymersomes.

6.7 CONCLUSIONS

The formation of a single MNP within the core of the PEG_{113}/$PMPC_{28}$ showed that these polymersomes are capable of mimicking bacterial magnetosomes both in a mixed valence 1:2 Fe(II):Fe(III) and Fe(II) ion solution. Synthesised MNPs were seen to be size effected by the type of iron solution they were exposed to, with a mixed valence solution showing a larger particle size compared to the single iron solution 46.4 nm to 23.7 nm, respectively. Although the mixed valence iron solution showed a higher diameter there was a lower coercivity observed in the mixed solution, 22 Oe compared to 49 Oe in the single Fe(II) solution a t 10 mM. This reduction in Hc in the mixed valence solution was surprising due to the ratio of the ferrous to ferric ions matching that of magnetite and the larger diameter. This suggests that magnetite has not formed and that maghemite has formed instead.

CHAPTER SEVEN: CONCLUSIONS AND FUTURE WORK

7 Conclusions and future work

In this thesis it has been shown that MNPs can be synthesised and functionalised to be capable of being used within a biological system to generate mild HT to induce sensitivity to PARP inhibitors as well as this a new method of synthesis that utilises a pre synthesised polymersome membrane enables the formation of MNPs within the inner lumen.

7.1 Synthesis of Biocompatible MNPs

MNPs have been synthesised using forward and reserve co-precipitation reactions. The forward reaction involves the straightforward addition of NaOH to a mixed valence iron solution and the reverse involves addition of iron to a basic solution. NPs with two distinct sizes with 8 nm diameter in the RRTCP and 23 nm in the RTCP MNPs synthesised due to the amount of base present in the reaction. Particle size was seen to dramatically effect performance, larger particles were observed to agglomerate more rapidly than smaller particles. This resulted in them being more unstable in solution to the point that they would drop out within a few minutes of agitation. In part, increased agglomeration may be as a result of the increased coercivity measured in larger magnetite MNPs (22 Oe) compared to smaller MNPs (12.5 Oe). This is to be expected in the single domain size range (sub 100 nm) as magnetisation increases with increasing particle diameter. It was expected that increased magnetisation should improve magnetic heating however this was not the case, as there was no increase in heat generated when tested in an AMF.

Their large size and their low polydispersity results in them being unsuitable for use as a therapeutic agent, as well as their penchant for agglomeration which could result in large clusters forming within blood vessels resulting in a blockage and clot that may prove fatal within a biological system. The smaller diameter particles were shown to be well distributed in aqueous solutions, have a suitable PDI and show significant heating when exposed to an alternating magnetic field with a temperature increase of 20 °C to temperatures above 45 °C. This is at the top end of the MHT range indicating that a high concentration of MNPs could induce HT damage within cells *in vitro* and *in vivo*.

7.2 Biocompatibility of MNPs

Smaller diameter MNPs were tested in two breast cancer cell lines, MCF7 and MDA-MB-231, which is a model of triple negative breast cancers. MNPs were tested at concentrations from 5 to 800 μg/ml. The effect of MNPs concentration was measured in both the short (24 − 72 hours) and long term (10 days), an observed dose dependent toxicity of MNPs with increasing dose was noted. This caused an increasing level of nanotoxicity even at

concentrations as low as 25 µg/ml. Nanotoxicity was also observed to be cell line dependant, with MDA-MB-231 cell line being more susceptible to lower concentrations of MNPs than the MCF7 cell lines, although the reason for this is unclear. Time was also clearly seen to be a factor in nanotoxicity, with increasing times causing increased toxicity in both cell lines. At all concentrations tested, no toxicity was observed after 24 hours but as time increased the level of toxicity increased. This effect was thought to be compounded by the fact that after the 24-hour period washing steps were performed to remove any external NPs, whereas compared to cells continuously exposed for 10 days the presence of any external NPs was not removed. Therefore, it is possible that the presence of external NPs could increase toxicity. This added further consideration when utilising these NPs as a therapeutic option because if particles accumulate within other organ tissue their presence could induce toxicities. Therefore, identifying the lowest concentration of NPs that provides effective treatment is crucial.

The effect of MNP concentration on cell cycle phase also confirmed the concentration dependant effect. Increasing concentrations of MNPs resulted in both cell lines showing significant increases in the SubG1 Population, indicating increased apoptosis. G1 arrest was observed in MCF7 cells with a concurrent drop in G2/M cell population. Whereas MDA-MB-231 cells showed a slight increase in G2/M population, although this was not observed to be significant. This may indicate that different cell cycle check points may be activated in response to MNPs in different cell lines.

7.3   MNP UPTAKE AND DISTRIBUTION.

The uptake of MNPs was observed to be a dose dependant factor with higher concentrations resulting in an increase in the amount of iron uptaken. The limiting factor in this is speculated to be the amount of MNPs that make contact with the cells rather than the ability to uptake iron. The amount of iron uptaken in the highest concentration dosed (200 µg/ml) was greater than the amount uptaken when dosed with the lowest concentration (5 µg/ml). This suggests that theoretically the cell should be able to up take all of the iron dosed at the lowest concentration, but this is not observed. More complex experimentation would be required to determine whether this is a factor in MNP uptake.

Time was observed to not play a factor in the internalisation of MNPs as there was no difference in iron internalisation when the exposure time to MNPs increased. This indicates that concentration is the main driving factor in internalisation. Flow cytometry analysis supports this an increase in the percentage of the cell population that internalised MNPs was observed. An increase in iron concentration was also observed via ICP-OES this supports the

idea that the amount of exposure of cells to MNPs results in a significant increase in internalisation.

Overall, from these results it can be stated that the increased toxicity observed at higher concentration may be as a result of the MNPs that are remaining in solution suffocating the cells rather than those that have been internalised.

Visualisation of MNP internalisation and distribution identified that MNPs were readily internalised within cells and seen to localise close to the nucleus. This has been previously observed with silica coated NPs. Although MNPs localise close to the nucleus, they do not appear to permeate the nuclear membrane as from fluorescent microscopy MNPs can be seen surrounding the nuclear membrane but not within the membrane itself. This would be beneficial in targeting HT to BRCA2 as it is a nuclear protein so MNPs would localise close to the site of the nucleus. Therefore, less heating would be required to generate temperatures capable of inducing BRCA2 degradation. Lack of membrane permeation is beneficial as MNPs that are capable of crossing nuclear membranes are known to induce chromosomal damage in cells.[236,237] This is also beneficial if any MNPs were to enter off target sites as the nuclear membrane would not be permeated and so would result in lower toxicity. MNPs would not be exposed to an AMF and would not generate heat thus allowing a targeted treatment of cells only under an AMF.

7.4 HYPERTHERMIA TREATMENT OF BREAST CANCER CELL LINES

The treatment of cells with IHT resulted in the degradation of BRCA2 in MCF7 and MDA-MB-231 cells, after an exposure of only 1 hour at 42 °C. HT treatment also resulted in a reduction in the formation of RAD51 foci after 4 Gy of IR which indicates that BRCA2 has indeed been reduced as it is responsible for the recruitment of RAD51 to the site of DSBs. The effect of HT on the sensitivity of tumours cells to PARP inhibitors was measured. After a single treatment of IHT there was little effect on the viability and survival of the cells in both the 37 °C and 42 °C treated cells, with no difference or only a small difference observed. This was counter intuitive to what had been observed with the effect of hyperthermia on cells and it was believed that a single IHT dose may not degrade BRCA2 for a significantly long enough period to induce sensitivity. Further IHT was performed with treatment over 3 consecutive days, either singularly or twice daily. It was observed that this resulted in an increased sensitivity to PARP inhibitors and that twice daily treatments resulted in a higher drop in cell survival than in singular treatments. There was an increased sensitivity observed in the MDA-MB-231 cell line to combined IHT and Olaparib than the MCF7 cell line. This may be as a result of the observed decrease in RAD51 foci recruitment which along with the decreased cell survival

after treatment indicates there is a cell line dependant component in the sensitivity to HT. This was further confirmed with the TS1 and 4T1 cell lines, the 4T1 cell line showing increased resistance to the combined IHT and Olaparib treatment with only the twice daily treatment method shown to have an effect on cell survival. This indicates that there is a cell dependant factor in inducing sensitivity to Olaparib and that the cell type might drive the method of HT and the treatment regime that is required for successful therapy.

These results show that MNPs synthesised were capable of inducing BRCA2 degradation at concentrations that were non-lethal to the cell in both nanotoxicity and MHT, as increasing concentrations resulted in reduced cell survival along with increasing time. This loss of BRCA2 enabled the treatment of MCF7 and MDA-MB-231 cells with Olaparib which was shown to have a significant effect on cell survival compared with both MNP MHT treated and Olaparib treated alone. This result shows that not only are MNPs capable of inducing sensitivity to Olaparib they were able to do this with much lower exposure times than the IHT which suggests that MNPs offer a more efficient method of inducing hyperthermia.

7.5 BIOMIMICRY OF MAGNETOSOMES WITH POLYMER VESICLES

Magnetosomes have the ability to form magnetite NPs within preformed magnetosome vesicles producing well controlled MNPs in both size and morphology. The results here have shown MNP can be synthesised within a polymer vesicle through electroporation in an Iron ion rich environment. The formation of MNPs was seen to be affected by the ratio of iron salts, a 1:2 ratio of Fe(II): Fe(III) resulted in the formation of MNPs, but this produced MNPs that were not uniform in size and shape. This was observed in both PBD-PEO and PEG-PMPC/PHPMA-PMPC polymersomes. The PBD-PEO polymersomes showed very little size control with little differences observed when stirred, sonicated, or extruded as they all produced multiple distinct size populations. The initial results of MNP formation within 0.7:0.3 ratio PEG_{113}-$PHPMA_{400}$/PMPC28-$PHPMA_{400}$ with the mixed valence iron solution showed the formation of iron oxides within the polymersomes. However, similar issues to the PBD-PEO polymersomes with the mixed valence iron solution were observed, producing a large amount of variation in MNP formation as well as large amounts of extravesical iron. The single Fe(II) solution showed an improved formation of MNPs, but these are unlikely to be magnetite. XRD analysis (appendix) showed multiple peak formation although the majority of which correspond to maghemite.

Although the 70:30 PEG_{113}-$PHPMA_{400}$/$PMPC_{28}$-$PHPMA_{400}$ showed the formation of MNPs this did not produce vesicles with a uniform size and shape. As well as this it could not be confirmed that the COOH groups were present on either the internal or external membrane.

The polymersomes were further refined to reflect this by producing RAFT polymersomes $PMPC_{28}$-$PHPMA_{450}$, PEG_{113}-$PHPMA_{400}$, $[0.6\,PEG_{113} + 0.4\,PMPC_{28}] - PHPMA_{400}$, $[0.8\,PEG_{113} + 0.2\,PMPC_{28}] - PHPMA_{400}$. These polymers had membranes that expressed COOH end groups, membranes that did not contain any COOH groups and had COOH groups present in the inner membrane. This allowed determination of the role of COOH groups in the formation of MNPs to be investigated. It was observed that COOH improved the nucleation of MNPs within the membrane of the polymersomes, as PEG_{113}-$PHPMA_{400}$ showed less control in the formation of MNPs with a large amount of particle formation around the polymersomes that was observed to be low density. In contrast $PMPC_{28}$-$PHPMA_{450}$ showed the formation of a single MNP within the polymersome lumen although a large number of polymersomes without any MNP formation were also present. As well as this there was a lot of formation of large iron structures on the exterior of the membrane. The PEG_{113}-$PHPMA_{400}$, $[0.6\,PEG_{113} + 0.4\,PMPC_{28}] - PHPMA_{400}$, $[0.8\,PEG_{113} + 0.2\,PMPC_{28}] - PHPMA_{400}$ polymersomes not only showed the formation of a single MNP within the lumen of the polymersomes but also a reduction in the amount of extravesical iron present. Although COOH groups can be observed as having an effect on the nucleation of MNPs, the concentration of iron was observed to have a larger effect on the size of the MNP formed than the presence of COOH, as all the polymersomes showed an increase in MNP size with increasing iron concentrations. This was also observed previously with 0.7:0.3 ratio PEG_{113}-$PHPMA_{400}$/$PMPC_{28}$-$PHPMA_{400}$. It was also observed that lumen size was responsible for increased particle size. This is due to the fact that larger polymersomes produced larger MNPs across all iron concentrations tested. This increased size may be a result of the vesicles being able to hold higher volumes of base or that they allow a larger volume of iron to enter upon electroporation, resulting in increased of MNPs. This work has shown that it is possible to synthesise MNPs within a preformed vesicle and that by altering the vesicle properties it is possible to alter the size of the formed MNPs.

7.6 FUTURE WORK

7.6.1 HYPERTHERMIA TREATMENT OF CANCER CELLS.

The use of MNPs to induce PARP sensitivity with low levels of HT mediated cell toxicity has shown that this is a viable method for developing treatments with the ability to induce tumour death in targeted cells. Although this has only been shown in 2D cell culture models. Further work is needed in 3D and *in vivo* models where the uptake of MNPs would be markedly different, due to the ability of MNPs to reach different regions of the tumour. 3D models would allow for this to be observed and to identify if MNPs have the ability to passively move through a large region of cancer cells, or whether they would require magnetic guidance to pass through these regions. This would also create problems for

heating of tumours, especially in consideration for *in vivo,* as here in these experiments a monolayer of cells were treated which allows MNPs to spread uniformly across the entire dish, but this would not be possible in an *in vivo* model. MNPs would be more likely to be concentrated to a region in a larger mass depending on the method of delivery, this could be direct injection into the tumour or intravenous injection with magnetic targeting. A larger mass of MNPs would result in much higher temperatures being reached, so controlling temperature and ensuring consistent masses of MNPs reached the target would be vital. This is to ensure that temperature remains consistent and minimum and maximum temperatures are not exceeded.

Further development of hyperthermia is also required to ensure that there are repeatable effects in hyperthermia treatment and controlling the targeting of MNPs is crucial to this. Uptake and retention of MNPs could be improved through the use of ligands that are targeted towards specific tumour sites of interest, this would ensure more effective treatment.

7.6.2 BIOMIMICRY OF MAGNETOSOMES

Within this study it has been shown that it possible to control the formation of MNPs within the membranes of polymersomes and that formation of MNPs can be altered by adjusting chemical and physical properties of the polymersome. Although formation of an iron oxide has been demonstrated, further work is required to determine what iron oxide has been synthesised. This is due to the high concentration of polymer present that makes it difficult to obtain reliable measurements. Further work could also investigate the effect that physical size of the polymersome, and lumen has on formation of MNPs. The ultimate goal is to synthesise magnetite MNPs within the polymersomes as these have the highest magnetic properties of all MNPs. It may be possible to achieve this through alterations to the ratios of iron salts, here a 0.6 molar ratio which matches the molar ratio of ferrous to ferric irons in magnetite to produce magnetite NPs. For the final formation of magnetite, a new approach may be required this could include a reversal of the method used where iron is electroporated within the vesicle core prior to the addition of base to help improve NP formation.

8 REFERENCES

1   Y. Cheng, S. Weng, L. Yu, N. Zhu, M. Yang and Y. Yuan, *Integr. Cancer Ther.*, ,
     DOI:10.1177/1534735419876345.

2   F. Bray, J. Ferlay, I. Soerjomataram, R. L. Siegel, L. A. Torre and A. Jemal, *CA. Cancer J.
     Clin.*, 2018, **68**, 394–424.

3   K. F. Chu and D. E. Dupuy, *Nat. Rev. Cancer*, 2014, **14**, 199–208.

4   M. Payne, S. H. Bossmann and M. T. Basel, *WIREs Nanomedicine and
     Nanobiotechnology*, , DOI:10.1002/wnan.1638.

5   R. van Hillegersberg, M. T. de Witte, W. J. Kort and O. T. Terpstra, *Lasers Surg. Med.*,
     1993, **13**, 332–343.

6   C. J. Legge, H. E. Colley, M. A. Lawson and A. E. Rawlings, *J. Oral Pathol. Med.*, 2019,
     48, 803–809.

7   B. Emami and C. W. Song, *Int. J. Radiat. Oncol.*, 1984, **10**, 289–295.

8   M. Nikfarjam, V. Muralidharan and C. Christophi, *J. Surg. Res.*, 2005, **127**, 208–223.

9   L. F. Fajardo, B. Egbert, J. Marmor and G. M. Hahn, *Cancer*, 1980, **45**, 613–23.

10   L. F. Fajardo, B. Egbert, J. Marmor and G. M. Hahn, *Cancer*, 1980, **45**, 613–623.

11   K. F. Chu and D. E. Dupuy, *Nat. Rev. Cancer*, 2014, **14**, 199–208.

12   D. N. Wheatley, C. Kerr and D. W. Gregory, *Int. J. Hyperth.*, 1989, **5**, 145–162.

13   M. G. White, O. Saleh, D. Nonner, E. F. Barrett, C. T. Moraes and J. N. Barrett, *J.
     Neurophysiol.*, 2012, **108**, 2203–2214.

14   L. Qian, X. Song, H. Ren, J. Gong and S. Cheng, *Cell Stress Chaperones*, 2004, **9**, 281.

15   I. Belhadj Slimen, T. Najar, A. Ghram, H. Dabbebi, M. Ben Mrad and M. Abdrabbah,
     Int. J. Hyperth., 2014, **30**, 513–523.

16   R. L. Warters and K. J. Henle, *Cancer Res.*, 1982, **42**, 4427–4432.

17   R. S. L. Wong, J. R. Dynlacht, B. Cedervall and W. C. Dewey, *Int. J. Radiat. Biol.*, 1995,
     68, 141–152.

18   M. A. Mackey, C. R. Hunt, S. J. Suffivan, J. Blum, A. Laszlo and J. L. R. Roti, 1996, 1770–
     1775.

19   C. R. Hunt, R. K. Pandita, A. Laszlo, R. Higashikubo, M. Agarwal, T. Kitamura, A. Gupta,
     N. Rief, N. Horikoshi, R. Baskaran, J.-H. Lee, M. Löbrich, T. T. Paull, J. L. Roti Roti and
     T. K. Pandita, *Cancer Res.*, 2007, **67**, 3010–3017.

20   D. A. Dewey, Wiliam c. Saperto, Stephen A. Betten, *Radiat. Res.*, 1978, **76**, 48–59.

21   W. C. Dewey, A. Westra, H. H. Miller and H. Nagasawa, *Int. J. Radiat. Biol. Relat. Stud. Physics, Chem. Med.*, 1971, **20**, 505–520.

22   M. A. Mackey, W. F. Morgan and W. C. Dewey, 1988, 6478–6483.

23   R. P. VanderWaal, C. L. Griffith, W. D. Wright, M. J. Borrelli and J. L. R. Roti, *J. Cell. Physiol.*, 2001, **187**, 236–243.

24   A. L. Oei, L. E. M. Vriend, J. Crezee, N. A. P. Franken and P. M. Krawczyk, *Radiat. Oncol.*, 2015, **10**, 165.

25   Y. Furusawa, T. Iizumi, Y. Fujiwara, Q.-L. Zhao, Y. Tabuchi, T. Nomura and T. Kondo, *Apoptosis*, 2012, **17**, 102–112.

26   M. Jentsch, P. Snyder, C. Sheng, E. Cristiano and A. Loewer, *Sci. Rep.*, 2020, **10**, 1–14.

27   T. Turner and T. Caspari, *Open Biol.*, 2014, **4**, 140008.

28   M. L. Hegde, T. K. Hazra and S. Mitra, *Cell Res.*, 2008, **18**, 27–47.

29   M. Kusakabe, Y. Onishi, H. Tada, F. Kurihara, K. Kusao, M. Furukawa, S. Iwai, M. Yokoi, W. Sakai and K. Sugasawa, *Genes Environ.*, 2019, **41**, 2.

30   J. A. Marteijn, H. Lans, W. Vermeulen and J. H. J. Hoeijmakers, *Nat. Rev. Mol. Cell Biol.*, 2014, **15**, 465–481.

31   G.-M. Li, *Cell Res.*, 2008, **18**, 85–98.

32   R. L. Warters and J. L. R. Roti, *Radiat. Res.*, 1979, **79**, 113.

33   J. DAHM-DAPHI, I. BRAMMER and E. DIKOM, *Int. J. Radiat. Biol.*, 1997, **72**, 171–179.

34   D. Fantini, E. Moritz, F. Auvré, R. Amouroux, A. Campalans, B. Epe, A. Bravard and J. P. Radicella, *DNA Repair (Amst).*, 2013, **12**, 227–237.

35   H. H. Y. Chang, N. R. Pannunzio, N. Adachi and M. R. Lieber, *Nat. Rev. Mol. Cell Biol.*, 2017, **18**, 495–506.

36   A. Chakraborty, N. Tapryal, T. Venkova, N. Horikoshi, R. K. Pandita, A. H. Sarker, P. S. Sarkar, T. K. Pandita and T. K. Hazra, *Nat. Commun.*, 2016, **7**, 1–12.

37   J. W. J. Bergs, P. M. Krawczyk, T. Borovski, R. ten Cate, H. M. Rodermond, J. Stap, J. P. Medema, J. Haveman, J. Essers, C. van Bree, L. J. A. Stalpers, R. Kanaar, J. A. Aten and N. A. P. Franken, *DNA Repair (Amst).*, 2013, **12**, 38–45.

38   A. L. Oei, V. R. Ahire, C. M. van Leeuwen, R. ten Cate, L. J. A. Stalpers, J. Crezee, H. P. Kok and N. A. P. Franken, *Int. J. Hyperth.*, 2018, **34**, 39–48.

39   P. M. Krawczyk, B. Eppink, J. Essers, J. Stap, H. Rodermond, H. Odijk, A. Zelensky, C. van Bree, L. J. Stalpers, M. R. Buist, T. Soullié, J. Rens, H. J. M. Verhagen, M. J.

O'Connor, N. a P. Franken, T. L. M. Ten Hagen, R. Kanaar and J. a Aten, *Proc. Natl. Acad. Sci. U. S. A.*, 2011, **108**, 9851–9856.

40   C. Nalley, *Oncol. Times*, 2018, **40**, 14.

41   M. Robson, K. J. Ruddy, S.-A. IM, E. Senkus, B. Xu, S. M. Domchek, N. Masuda, W. Li, N. Tung, A. Armstrong, S. Delaloge, W. Bannister, C. Goessl, A. Degboe, R. Hettle and P. Conte, *Eur. J. Cancer*, 2019, **120**, 20–30.

42   M.-C. King, J. H. Marks and J. B. Mandell, .

43   R. Roy, J. Chun and S. N. Powell, *Nat. Rev. Cancer*, , DOI:10.1038/nrc3181.

44   N. Petrucelli, M. B. Daly and G. L. Feldman, , DOI:10.1097/GIM.0b013e3181d38f2f.

45   R. Prakash, Y. Zhang, W. Feng and M. Jasin, *Perspect. Biol.*, 2015, 1–29.

46   A. K. C. Wong, R. Pero, P. A. Ormonde, S. V. Tavtigian and P. L. Bartel, *J. Biol. Chem.*, 1997, **272**, 31941–31944.

47   J. San Filippo, P. Sung and H. Klein, *Annu. Rev. Biochem.*, 2008, **77**, 229–257.

48   X. Li and W.-D. Heyer, , DOI:10.1038/cr.2008.1.

49   L. Krejci, V. Altmannova, M. Spirek and X. Zhao, *Nucleic Acids Res.*, 2012, **40**, 5795–5818.

50   P. Sung, L. Krejci, S. Van Komen and M. G. Sehorn, *J. Biol. Chem.*, 2003, **278**, 42729–42732.

51   J. Renkawitz, C. a Lademann and S. Jentsch, *Nat. Rev. Mol. Cell Biol.*, 2014, **15**, 369–83.

52   A. A. Davies, J. Y. Masson, M. J. McIlwraith, A. Z. Stasiak, A. Stasiak, A. R. Venkitaraman and S. C. West, *Mol. Cell*, 2001, **7**, 273–282.

53   A. V. Mazin, C. J. Bornarth, J. A. Solinger, W.-D. Heyer and S. C. Kowalczykowski, *Mol. Cell*, 2000, **6**, 583–592.

54   G. Petukhova, S. Stratton and P. Sung, *Nature*, 1998, **393**, 91–4.

55   W. D. Heyer, X. Li, M. Rolfsmeier and X. P. Zhang, *Nucleic Acids Res.*, 2006, **34**, 4115–4125.

56   J. Smith, J. R. Morgan, S. J. Zottoli, P. J. Smith, J. D. Buxbaum and O. E. Bloom, *Biol. Bull.*, 2011, **221**, 18–34.

57   N. Mazloum and W. K. Holloman, *Mol. Cell*, 2009, **36**, 620–630.

58   R. Roy, J. Chun and S. N. Powell, , DOI:10.1038/nrc3181.

59   W. K. Holloman, *Nat. Struct. Mol. Biol.*, 2011, **18**, 748–54.

60   B. J. Orelli and D. K. Bishop, *Breast Cancer Res.*, 2001, **3**, 294–298.

61   A. Carreira and S. C. Kowalczykowski, *Proc. Natl. Acad. Sci. U. S. A.*, 2011, **108**, 10448–53.

62   V. E. Galkin, F. Esashi, X. Yu, S. Yang, S. C. West and E. H. Egelman, *Proc. Natl. Acad. Sci. U. S. A.*, 2005, **102**, 8537–42.

63   K. Schlacher, N. Christ, N. Siaud, A. Egashira, H. Wu and M. Jasin, *Cell*, 2011, **145**, 529–542.

64   H. Yang, P. D. Jeffrey, J. Miller, E. Kinnucan, Y. Sun, N. H. Thoma, N. Zheng, P.-L. Chen, W.-H. Lee and N. P. Pavletich, *Science*, 2002, **297**, 1837–48.

65   C. Chen, P. Chen, Z. D. Sharp, W. Lee, C. Chen, P. Chen, Q. Zhong, Z. D. Sharp and W. Lee, 1999, **274**, 32931–32935.

66   T. R. Rebbeck, N. Mitra, F. Wan, O. M. Sinilnikova, A. C. Antoniou, K. L. Nathanson and CIMBA Consortium, *J. Am. Med. Assoc.*, 2015, **313**, 1347–1361.

67   Keith W. Caldecott, *Nat. Rev. Genet.*, 2008, **9**, 619–631.

68   M. M. N. J. C. and T. H. Helen E. Bryant, Niklas Schultz, Huw D Thomas, Kayan M Parker, Dan Flower, Elena Lopez, Suzanne Kyle, *Lett. to Nat.*, 2005, **434**, 913–917.

69   M. D'Arcangelo, Y. Drew and R. Plummer, *DNA Repair Cancer Ther. Mol. Targets Clin. Appl. Second Ed.*, 2016, **105**, 115–134.

70   T. Helleday, *Mol. Oncol.*, 2011, 5, 387–393.

71   R. S. Meehan and A. P. Chen, *Gynecol. Oncol. Res. Pract.*, 2016, **3**, 3.

72   J. Murai, S. Y. N. Huang, B. B. Das, A. Renaud, Y. Zhang, J. H. Doroshow, J. Ji, S. Takeda and Y. Pommier, *Cancer Res.*, 2012, **72**, 5588–5599.

73   S. M. B. Nijman, *FEBS Lett.*, 2011, **585**, 1–6.

74   K. Overgaard and J. Overgaard, *Eur. J. Cancer*, 1972, **8**, 65–78.

75   G. Hegyi, G. P. Szigeti and A. Szász, *Evid. Based. Complement. Alternat. Med.*, 2013, **2013**, 672873.

76   H. K. Lim, *Korean J. Radiol.*, 2000, **1**, 175–184.

77   Y. Kim, B. Hyunchul Rhim, B. Hyo Keun Lim, D. Choi, B. Min Woo Lee and B. Min Jung Park, , DOI:10.1148/rg.312105056.

78   A. L. Feldman, S. K. Libutti, J. F. Pingpank, D. L. Bartlett, T. H. Beresnev, S. M. Mavroukakis, S. M. Steinberg, D. J. Liewehr, D. E. Kleiner and H. R. Alexander, *J. Clin. Oncol.*, 2003, **21**, 4560–4567.

79   P. Nasimi and M. Haidari, *Int. J. Green Nanotechnol.*, 2013, **1**, 194308921350697.

80   S. Tinkle, S. E. McNeil, S. Mühlebach, R. Bawa, G. Borchard, Y. C. Barenholz, L. Tamarkin and N. Desai, *Ann. N. Y. Acad. Sci.*, 2014, **1313**, 35–56.

81   S. Soares, J. Sousa, A. Pais and C. Vitorino, *Front. Chem.*, , DOI:10.3389/fchem.2018.00360.

82   Definition of a nanomaterial, https://ec.europa.eu/environment/chemicals/nanotech/faq/definition_en.htm.

83   S. K. Nune, P. Gunda, P. K. Thallapally, Y.-Y. Lin, M. Laird Forrest and C. J. Berkland, *Expert Opin. Drug Deliv.*, 2009, **6**, 1175–1194.

84   D. Anderson, M. Sydor, P. Fletcher and A. Holian, *J. Nanomed. Nanotechnol.*, , DOI:10.4172/2157-7439.1000e143.

85   B. Pelaz, C. Alexiou, R. A. Alvarez-Puebla, F. Alves, A. M. Andrews, S. Ashraf, L. P. Balogh, L. Ballerini, A. Bestetti, C. Brendel, S. Bosi, M. Carril, W. C. W. Chan, C. Chen, X. Chen, X. Chen, Z. Cheng, D. Cui, J. Du, C. Dullin, A. Escudero, N. Feliu, M. Gao, M. George, Y. Gogotsi, A. Grünweller, Z. Gu, N. J. Halas, N. Hampp, R. K. Hartmann, M. C. Hersam, P. Hunziker, J. Jian, X. Jiang, P. Jungebluth, P. Kadhiresan, K. Kataoka, A. Khademhosseini, J. Kopeček, N. A. Kotov, H. F. Krug, D. S. Lee, C.-M. Lehr, K. W. Leong, X.-J. Liang, M. Ling Lim, L. M. Liz-Marzán, X. Ma, P. Macchiarini, H. Meng, H. Möhwald, P. Mulvaney, A. E. Nel, S. Nie, P. Nordlander, T. Okano, J. Oliveira, T. H. Park, R. M. Penner, M. Prato, V. Puntes, V. M. Rotello, A. Samarakoon, R. E. Schaak, Y. Shen, S. Sjöqvist, A. G. Skirtach, M. G. Soliman, M. M. Stevens, H.-W. Sung, B. Z. Tang, R. Tietze, B. N. Udugama, J. S. VanEpps, T. Weil, P. S. Weiss, I. Willner, Y. Wu, L. Yang, Z. Yue, Q. Zhang, Q. Zhang, X.-E. Zhang, Y. Zhao, X. Zhou and W. J. Parak, *ACS Nano*, 2017, **11**, 2313–2381.

86   M. Hosseini, M. Haji-Fatahaliha, F. Jadidi-Niaragh, J. Majidi and M. Yousefi, *Artif. Cells, Nanomedicine, Biotechnol.*, 2015, 1–11.

87   H. Feracci, B. S. Gutierrez, W. Hempel and I. S. Gil, in *Frontiers of Nanoscience*, 4th edn., 2012, pp. 197–230.

88   F. Fang, M. Li, J. Zhang and C.-S. Lee, *ACS Mater. Lett.*, 2020, **2**, 531–549.

89   L. Sercombe, T. Veerati, F. Moheimani, S. Y. Wu, A. K. Sood and S. Hua, *Front. Pharmacol.*, , DOI:10.3389/fphar.2015.00286.

90   R. Nisini, N. Poerio, S. Mariotti, F. De Santis and M. Fraziano, *Front. Immunol.*, , DOI:10.3389/fimmu.2018.00155.

91   A. Akbarzadeh, R. Rezaei-Sadabady, S. Davaran, S. W. Joo, N. Zarghami, Y.

Hanifehpour, M. Samiei, M. Kouhi and K. Nejati-Koshki, *Nanoscale Res. Lett.*, 2013, **8**, 1.

92   V. P. Torchilin, *Nat. Rev. Drug Discov.*, 2005, **4**, 145–160.

93   D. Ag Seleci, M. Seleci, J.-G. Walter, F. Stahl and T. Scheper, *J. Nanomater.*, 2016, **2016**, 1–13.

94   K. Kuotsu, K. Karim, A. Mandal, N. Biswas, A. Guha, S. Chatterjee and M. Behera, *J. Adv. Pharm. Technol. Res.*, 2010, **1**, 374.

95   A. De, N. Venkatesh, M. Senthil, B. K. R. Sanapalli, R. Shanmugham and V. V. S. R. Karri, *Nanobiomedicine*, 2018, **5**, 184954351880535.

96   R. Rajera, K. Nagpal, S. K. Singh and D. N. Mishra, *Biol. Pharm. Bull.*, 2011, 34, 945–953.

97   M. Gharbavi, J. Amani, H. Kheiri-manjili, H. Danafar and A. Sharafi, , DOI:doi.org/10.1155/2018/6847971.

98   C. L. McCormick and A. B. Lowe, *Acc. Chem. Res.*, 2004, **37**, 312–325.

99   N. J. Warren and S. P. Armes, *J. Am. Chem. Soc.*, 2014, **136**, 10174–10185.

100   H. Zhang, 2017, pp. 17–22.

101   J. Lefley, C. Waldron and C. R. Becer, *Polym. Chem.*, 2020, **11**, 7124–7136.

102   N. J. W. Penfold, J. Yeow, C. Boyer and S. P. Armes, *ACS Macro Lett.*, 2019, **8**, 1029–1054.

103   E. Rideau, R. Dimova, P. Schwille, F. R. Wurm and K. Landfester, *Chem. Soc. Rev.*, 2018, **47**, 8572–8610.

104   J. Yang, Y. Hu, R. Wang and D. Xie, *Soft Matter*, 2017, **13**, 7840–7847.

105   P. Yang, R. Lipowsky and R. Dimova, *Small*, 2009, **5**, 2033–2037.

106   S. Mann, J. P. Hannington and R. J. P. Williams, *Nature*, 1986, **324**, 565–567.

107   M. I. Khramov and V. N. Parmon, *J. Photochem. Photobiol. A Chem.*, 1993, **71**, 279–284.

108   S. Mandal and S. De, *J. Indian Chem. Soc.*, 2021, **98**, 100061.

109   J. Bain, L. Ruiz-Pérez, A. J. Kennerley, S. P. Muench, R. Thompson, G. Battaglia and S. S. Staniland, *Sci. Rep.*, 2015, **5**, 14311.

110   Y. Liu, Y. Liu, R. L. Mernaugh and X. Zeng, *Biosens. Bioelectron.*, 2009, **24**, 2853–2857.

111   D. Chenthamara, S. Subramaniam, S. G. Ramakrishnan, S. Krishnaswamy, M. M. Essa, F.-H. Lin and M. W. Qoronfleh, *Biomater. Res.*, 2019, **23**, 20.

112 M. Jeon, M. V. Halbert, Z. R. Stephen and M. Zhang, *Adv. Mater.*, 2020, 1906539.

113 Y. Wu, M. R. K. Ali, K. Chen, N. Fang and M. A. El-Sayed, *Nano Today*, 2019, **24**, 120–140.

114 M. U. Farooq, V. Novosad, E. A. Rozhkova, H. Wali, A. Ali, A. A. Fateh, P. B. Neogi, A. Neogi and Z. Wang, *Sci. Rep.*, 2018, **8**, 2907.

115 M. Muthana, A. J. Kennerley, R. Hughes, E. Fagnano, J. Richardson, M. Paul, C. Murdoch, F. Wright, C. Payne, M. F. Lythgoe, N. Farrow, J. Dobson, J. Conner, J. M. Wild and C. Lewis, *Nat. Commun.*, 2015, **6**, 8009.

116 D. Vyas, N. Lopez-Hisijos, S. Gandhi, M. El-Dakdouki, M. D. Basson, M. F. Walsh, X. Huang, A. K. Vyas and L. S. Chaturvedi, *J. Nanosci. Nanotechnol.*, 2015, **15**, 6413–6422.

117 D. Movia, V. Gerard, C. M. Maguire, N. Jain, A. P. Bell, V. Nicolosi, T. O'Neill, D. Scholz, Y. Gun'ko, Y. Volkov and A. Prina-Mello, *Biomaterials*, 2014, **35**, 2543–2557.

118 H. Huang, J. Li, Y. Orza, A. Lu, Q. Guo, P. Wang, L. Yang, L. Mao, *Physiol. Behav.*, 2016, **176**, 139–148.

119 J. Piella, N. G. Bastús and V. Puntes, *Chem. Mater.*, 2016, **28**, 1066–1075.

120 J. Dong, P. L. Carpinone, G. Pyrgiotakis, P. Demokritou and B. M. Moudgil, *KONA Powder Part. J.*, 2020, **37**, 224–232.

121 S. C. Gad, K. L. Sharp, C. Montgomery, J. D. Payne and G. P. Goodrich, *Int. J. Toxicol.*, 2012, **31**, 584–594.

122 No Title, https://cytimmune.blog/#pipeline.

123 J. Lipka, M. Semmler-Behnke, R. A. Sperling, A. Wenk, S. Takenaka, C. Schleh, T. Kissel, W. J. Parak and W. G. Kreyling, *Biomaterials*, 2010, **31**, 6574–6581.

124 S. H. Lee, K. H. Bae, S. H. Kim, K. R. Lee and T. G. Park, *Int. J. Pharm.*, 2008, **364**, 94–101.

125 N. Wangoo, K. K. Bhasin, S. K. Mehta and C. R. Suri, *J. Colloid Interface Sci.*, 2008, **323**, 247–254.

126 L. Sun, D. Liu and Z. Wang, *Langmuir*, 2008, **24**, 10293–10297.

127 D. J. Javier, N. Nitin, M. Levy, A. Ellington and R. Richards-Kortum, *Bioconjug. Chem.*, 2008, **19**, 1309–1312.

128 D. A. Giljohann, D. S. Seferos, A. E. Prigodich, P. C. Patel and C. A. Mirkin, *J. Am. Chem. Soc.*, 2009, **131**, 2072–2073.

129 J. You, J. Zhou, M. Zhou, Y. Liu, J. Robertson, D. Liang, C. Van Pelt and C. Li, *Part. Fibre Toxicol.*, 2014, **11**, 26.

130   L. Yan, H. Da, S. Zhang, V. M. López and W. Wang, *Microbiol. Res.*, 2017, **203**, 19–28.

131   W. Lin, W. Zhang, X. Zhao, A. P. Roberts, G. A. Paterson, D. A. Bazylinski and Y. Pan, *ISME J.*, 2018, **12**, 1508–1519.

132   P. Isambert, A. Menguy, N. Larquet, E. Guyot, F. Valet, J, *Am. Mineral.*, 2007, **92**, 621–630.

133   Y. Pan, N. Petersen, M. Winklhofer, A. F. Davila, Q. Liu, T. Frederichs, M. Hanzlik and R. Zhu, *Earth Planet. Sci. Lett.*, 2005, **237**, 311–325.

134   L. Yan, H. Da, S. Zhang, V. M. López and W. Wang, *Microbiol. Res.*, 2017, **203**, 19–28.

135   M. Richter, M. Kube, D. A. Bazylinski, T. Lombardot, F. O. Glöckner, R. Reinhardt and D. Schüler, *J. Bacteriol.*, 2007, **189**, 4899–4910.

136   J. Yang, S. Li, X. Huang, J. Li, L. Li, Y. Pan and Y. Li, *BMC Microbiol.*, 2013, **13**, 203.

137   J. M. Galloway, A. Arakaki, F. Masuda, T. Tanaka, T. Matsunaga and S. S. Staniland, *J. Mater. Chem.*, 2011, **21**, 15244.

138   M. Tanaka, E. Mazuyama, A. Arakaki and T. Matsunaga, *J. Biol. Chem.*, 2011, **286**, 6386–6392.

139   Q. Wang, S. Wu, X. Li, T. Zhang, J. Yang, X. Wang, F. Li, Y. Li, Y. Peng and J. Li, *Appl. Environ. Microbiol.*, , DOI:10.1128/AEM.02394-18.

140   M. Tanaka, A. Arakaki and T. Matsunaga, *Mol. Microbiol.*, 2010, **76**, 480–488.

141   A. Lohße, S. Ullrich, E. Katzmann, S. Borg, G. Wanner, M. Richter, B. Voigt, T. Schweder and D. Schüler, *PLoS One*, , DOI:10.1371/journal.pone.0025561.

142   A. Scheffel, A. Gärdes, K. Grünberg, G. Wanner and D. Schüler, *J. Bacteriol.*, 2008, **190**, 377–386.

143   U. Heyen and D. Schüler, *Appl. Microbiol. Biotechnol.*, 2003, **61**, 536–544.

144   S. S. Staniland and A. E. Rawlings, *Biochem. Soc. Trans.*, 2016, **44**, 883–890.

145   R. Uebe, K. Junge, V. Henn, G. Poxleitner, E. Katzmann, J. M. Plitzko, R. Zarivach, T. Kasama, G. Wanner, M. Pósfai, L. Böttger, B. Matzanke and D. Schüler, *Mol. Microbiol.*, 2011, **82**, 818–835.

146   S. Barber-Zucker, N. Keren-Khadmy and R. Zarivach, *Protein Sci.*, 2016, **25**, 338–351.

147   J. M. Chem, G. Salas, C. Casado, F. J. Teran, R. Miranda and J. Serna, 2012, 21065–21075.

148   B. Issa, I. Obaidat, B. Albiss and Y. Haik, *Int. J. Mol. Sci.*, 2013, **14**, 21266–21305.

149   Y. Rabin, *Int. J. Hyperthermia*, **18**, 194–202.

150 P. Keblinski, D. G. Cahill, A. Bodapati, C. R. Sullivan and T. A. Taton, *J. Appl. Phys.*, 2006, **100**, 054305.

151 L. Polo-Corrales and C. Rinaldi, *J. Appl. Phys.*, 2012, **111**, 07B334.

152 H. Huang, S. Delikanli, H. Zeng, D. M. Ferkey and A. Pralle, *Nat. Nanotechnol.*, 2010, **5**, 602–6.

153 K. Maier-Hauff, F. Ulrich, D. Nestler, H. Niehoff, P. Wust, B. Thiesen, H. Orawa, V. Budach and A. Jordan, *J. Neurooncol.*, 2011, **103**, 317–324.

154 U. Gneveckow, A. Jordan, R. Scholz, V. Brüß, N. Waldöfner, J. Ricke, A. Feussner, B. Hildebrandt, B. Rau and P. Wust, *Med. Phys.*, 2004, **31**, 1444–1451.

155 R. R. Wildeboer, P. Southern and Q. A. Pankhurst, *J. Phys. D. Appl. Phys.*, 2014, **47**, 495003.

156 A. E. Deatsch and B. A. Evans, *J. Magn. Magn. Mater.*, 2014, **354**, 163–172.

157 J. Jose, R. Kumar, S. Harilal, G. E. Mathew, D. G. T. Parambi, A. Prabhu, M. S. Uddin, L. Aleya, H. Kim and B. Mathew, *Environ. Sci. Pollut. Res.*, 2020, **27**, 19214–19225.

158 A. Jordan, P. Wust, H. Fählin, W. John, A. Hinz and R. Felix, *Int. J. Hyperth.*, 1993, **9**, 51–68.

159 S. Majidi, F. Z. Sehrig, S. M. Farkhani, M. S. Goloujeh and A. Akbarzadeh, *Artif. Cells, Nanomedicine Biotechnol.*, 2016, **44**, 722–734.

160 G. Priyadarshana, N. Kottegoda, A. Senaratne, A. De Alwis and V. Karunaratne, *J. Nanomater.*, , DOI:10.1155/2015/317312.

161 M. C. Mascolo, Y. Pei and T. A. Ring, *Materials (Basel).*, 2013, **6**, 5549–5567.

162 T. Ahn, J. H. Kim, H.-M. Yang, J. W. Lee and J.-D. Kim, *J. Phys. Chem. C*, 2012, **116**, 6069–6076.

163 S. Aliramaji, A. Zamanian and Z. Sohrabijam, *Procedia Mater. Sci.*, 2015, **11**, 265–269.

164 T. Sugimoto and E. Matijevic, *J. Colloid Interface Sci.*, 1980, **74**, 227–243.

165 W. Wu, Q. He and C. Jiang, *Nanoscale Res. Lett.*, 2008, **3**, 397–415.

166 A. P. A. Faiyas, E. M. Vinod, J. Joseph, R. Ganesan and R. K. Pandey, *J. Magn. Magn. Mater.*, 2010, **322**, 400–404.

167 R. Dewi, H. Husain, M. Sulthonul and S. Pratapa, 2020, p. 030014.

168 P. Tartaj, M. a del P. Morales, S. Veintemillas-Verdaguer, T. Gonz lez-Carre o and C. J. Serna, *J. Phys. D. Appl. Phys.*, 2003, **36**, R182–R197.

169 A. P. Lagrow, M. O. Besenhard, A. Hodzic, A. Sergides, L. K. Bogart, A. Gavriilidis and N. T. K. Thanh, *Nanoscale*, 2019, **11**, 6620–6628.

170   S.   P.   Schwaminger,   C.   Syhr   and   S.   Berensmeier,   *Crystals*,   ,
DOI:10.3390/cryst10030214.

171   M. Unni, A. M. Uhl, S. Savliwala, B. H. Savitzky, R. Dhavalikar, N. Garraud, D. P. Arnold,
L. F. Kourkoutis, J. S. Andrew and C. Rinaldi, *ACS Nano*, 2017, **11**, 2284–2303.

172   R. Hufschmid, H. Arami, R. M. Ferguson, M. Gonzales, E. Teeman, L. N. Brush, N. D.
Browning and K. M. Krishnan, *Nanoscale*, 2015, **7**, 11142–11154.

173   M. F. Casula, Y. Jun, D. J. Zaziski, E. M. Chan, A. Corrias and A. P. Alivisatos, *J. Am.
Chem. Soc.*, 2006, **128**, 1675–1682.

174   W. Wu, Z. Wu, T. Yu, C. Jiang and W.-S. Kim, *Sci. Technol. Adv. Mater.*, 2015, **16**,
023501.

175   J. Xu, H. Yang, W. Fu, K. Du, Y. Sui, J. Chen, Y. Zeng, M. Li and G. Zou, *J. Magn. Magn.
Mater.*, 2007, **309**, 307–311.

176   N. A. Spaldin, *Magnetic Materials*, Cambridge University Press, Cambridge, 2010.

177   A. G. Kolhatkar, A. C. Jamison, D. Litvinov, R. C. Willson and T. R. Lee, *Tuning the
magnetic properties of nanoparticles*, 2013, vol. 14.

178   A. M. Mazrouaa, M. G. Mohamed and M. Fekry, *Egypt. J. Pet.*, 2019, **28**, 165–171.

179   Q. Li, C. W. Kartikowati, S. Horie, T. Ogi, T. Iwaki and K. Okuyama, *Sci. Rep.*, 2017, **7**,
9894.

180   E. Alphandéry, F. Guyot and I. Chebbi, *Int. J. Pharm.*, 2012, **434**, 444–52.

181   J. M. Galloway, A. Arakaki, F. Masuda, T. Tanaka, T. Matsunaga and S. S. Staniland, *J.
Mater. Chem.*, 2011, **21**, 15244.

182   F. Herranz, B. Salinas, H. Groult, J. Pellico, A. Lechuga-Vieco, R. Bhavesh and J. Ruiz-
Cabello, *Nanomaterials*, 2014, **4**, 408–438.

183   R. Kelsall, I. W. Hamley and M. Geoghegan, *Nanoscale Science and Technology*, Wiley-
Blackwell, 2005.

184   R. Hunter, *Zeta Potential in Colloid Science*, Elsevier, 1981.

185   V. Selvamani, in *Characterization and Biology of Nanomaterials for Drug Delivery*,
Elsevier, 2019, pp. 425–444.

186   Inductively Coupled Plasma Optical Emission Spectroscopy (ICP-OES) Information,
https://www.thermofisher.com/uk/en/home/industrial/spectroscopy-elemental-
isotope-analysis/spectroscopy-elemental-isotope-analysis-learning-center/trace-
elemental-analysis-tea-information/icp-oes-information.html.

187   S. Foner, *Rev. Sci. Instrum.*, 1959, **30**, 548–557.

188   A. O. Adeyeye and G. Shimon, 2015, pp. 1–41.

189   A. Soledad Pereyra and O. Mykhaylyk, *J. Nanomed. Nanotechnol.*, 2016, **07**, 139–148.

190   P. . Michelle Longmire, Peter L. Choyke, M.D., and Hisataka Kobayashi, M.D., 2012, **3**, 703–717.

191   D. Singh, J. M. McMillan, A. V Kabanov, M. Sokolsky-Papkov and H. E. Gendelman, *Nanomedicine (Lond).*, 2014, **9**, 501–16.

192   E. Fröhlich, *Int. J. Nanomedicine*, 2012, **7**, 5577–5591.

193   S. Behzadi, V. Serpooshan, W. Tao, M. A. Hamaly, M. Y. Alkawareek, E. C. Dreaden, D. Brown, A. M. Alkilany, O. C. Farokhzad and M. Mahmoudi, *Chem. Soc. Rev.*, 2017, **46**, 4218–4244.

194   X. Pham, E. Hahm, H. Kim, B. S. Son, A. Jo, J. An, T. A. Tran Thi, D. Q. Nguyen and B. Jun, *Nanomaterials*, 2020, **10**, 117.

195   R. von Burg, *J. Appl. Toxicol.*, 1985, **5**, 110–110.

196   M. Mahmoudi, A. Simchi, M. Imani, M. A. Shokrgozar, A. S. Milani, U. O. Häfeli and P. Stroeve, *Colloids Surfaces B Biointerfaces*, 2010, **75**, 300–309.

197   J. Lim, S. P. Yeap, H. X. Che and S. C. Low, 2013, 1–14.

198   C. R. Lin, R. K. Chiang, J. S. Wang and T. W. Sung, *J. Appl. Phys.*, 2006, **99**, 8–10.

199   V. L. C. Cafer T. Yavuz, J. T. Mayo, William W. Yu, Arjun Prakash, Joshua C. Falkner, Sujin Yean, Lili Cong, Heather J. Shipley, Amy Kan, Mason Tomson, Douglas Natelson, *Science (80-.).*, 2006, **314**, 964–967.

200   H. S. Choi, W. Liu, P. Misra, E. Tanaka, J. P. Zimmer, B. I. Ipe, M. G. Bawendi and J. V Frangioni, *Nat. Biotechnol.*, 2007, **25**, 1165–1170.

201   J. Baumgartner, A. Dey, P. H. H. Bomans, C. Le Coadou, P. Fratzl, N. A. J. M. Sommerdijk and D. Faivre, *Nat. Mater.*, 2013, **12**, 310–314.

202   C. Carnovale, G. Bryant, R. Shukla and V. Bansal, *ACS Omega*, 2019, **4**, 242–256.

203   P. Foroozandeh and A. A. Aziz, *Nanoscale Res. Lett.*, , DOI:10.1186/s11671-018-2728-6.

204   B. D. Chithrani and W. C. W. Chan, *Nano Lett.*, 2007, **7**, 1542–1550.

205   B. D. Chithrani, A. A. Ghazani and W. C. W. Chan, *Nano Lett.*, 2006, **6**, 662–668.

206   D. Eberbeck, M. Kettering, C. Bergemann, P. Zirpel, I. Hilger and L. Trahms, *J. Phys. D. Appl. Phys.*, 2010, **43**, 405002.

207   H. Markides, M. Rotherham and A. J. El Haj, *J. Nanomater.*, 2012, **2012**, 1–11.

208   D. E. Kile, D. D. Eberl, A. R. Hoch and M. M. Reddy, *Geochim. Cosmochim. Acta*, 2000, **64**, 2937–2950.

209   K. Petcharoen and A. Sirivat, *Mater. Sci. Eng. B Solid-State Mater. Adv. Technol.*, 2012, **177**, 421–427.

210   L. Han, S. Li, Y. Yang, F. Zhao, J. Huang and J. Chang, *J. Magn. Magn. Mater.*, 2007, **313**, 236–242.

211   A. S. Madden, M. F. Hochella and T. P. Luxton, *Geochim. Cosmochim. Acta*, 2006, **70**, 4095–4104.

212   T. Lima, K. Bernfur, M. Vilanova and T. Cedervall, *Sci. Rep.*, 2020, **10**, 1–9.

213   F. Barbero, L. Russo, M. Vitali, J. Piella, I. Salvo, M. L. Borrajo, M. Busquets-Fité, R. Grandori, N. G. Bastús, E. Casals and V. Puntes, *Semin. Immunol.*, 2017, **34**, 52–60.

214   Z. Vargas-Osorio, A. da Silva-Candal, Y. Piñeiro, R. Iglesias-Rey, T. Sobrino, F. Campos, J. Castillo and J. Rivas, *Nanomaterials*, 2019, **9**, 1–22.

215   J. Namanga, J. Foba, D. T. Ndinteh, D. M. Yufanyi and R. W. M. Krause, *J. Nanomater.*, 2013, **2013**, 1–8.

216   S. J. Kemp, R. M. Ferguson, A. P. Khandhar and K. M. Krishnan, *RSC Adv.*, 2016, **6**, 77452–77464.

217   M. F. Sanad, B. P. Meneses-Brassea, D. S. Blazer, S. Pourmiri, G. C. Hadjipanayis and A. A. El-Gendy, *Appl. Sci.*, 2021, **11**, 6637.

218   R. Hergt, S. Dutz and M. Robert, , DOI:10.1088/0953-8984/18/38/S26.

219   O. L. Lanier, O. I. Korotych, A. G. Monsalve, D. Wable, S. Savliwala, N. W. F. Grooms, C. Nacea, O. R. Tuitt and J. Dobson, *Int. J. Hyperth.*, 2019, **36**, 686–700.

220   J. Dulińska-Litewka, A. Łazarczyk, P. Hałubiec, O. Szafrański, K. Karnas and A. Karewicz, *Materials (Basel).*, , DOI:10.3390/ma12040617.

221   L. S. Bondarenko, E. S. Kovel, K. A. Kydralieva, G. I. Dzhardimalieva, E. Illés, E. Tombácz, A. G. Kicheeva and N. S. Kudryasheva, *Nanomaterials*, 2020, **10**, 1499.

222   S. P. Schwaminger, D. Bauer, P. Fraga-García, F. E. Wagner and S. Berensmeier, *CrystEngComm*, 2017, **19**, 246–255.

223   A. Sukhanova, S. Bozrova, P. Sokolov, M. Berestovoy, A. Karaulov and I. Nabiev, *Nanoscale Res. Lett.*, , DOI:10.1186/s11671-018-2457-x.

224   Q. Feng, Y. Liu, J. Huang, K. Chen, J. Huang and K. Xiao, *Sci. Rep.*, 2018, **8**, 2082.

225   J. S. Chang, K. L. B. Chang, D. F. Hwang and Z. L. Kong, *Environ. Sci. Technol.*, 2007, **41**, 2064–2068.

226   A. M. Alkilany and C. J. Murphy, *J. Nanoparticle Res.*, 2010, **12**, 2313–2333.

227   K. W. Powers, M. Palazuelos, B. M. Moudgil and S. M. Roberts, *Nanotoxicology*, 2007, **1**, 42–51.

228   Y. Pan, S. Neuss, A. Leifert, M. Fischler, F. Wen, U. Simon, G. Schmid, W. Brandau and W. Jahnen-Dechent, *Small*, 2007, **3**, 1941–1949.

229   A. Nan, X. Bai, S. J. Son, S. B. Lee and H. Ghandehari, *Nano Lett.*, 2008, **8**, 2150–2154.

230   U. M. Engelmann, A. A. Roeth, D. Eberbeck, E. M. Buhl, U. P. Neumann, T. Schmitz-Rode and I. Slabu, *Sci. Rep.*, 2018, **8**, 13210.

231   A. Riedinger, P. Guardia, A. Curcio, M. A. Garcia, R. Cingolani, L. Manna and T. Pellegrino, *Nano Lett.*, 2013, **13**, 2399–2406.

232   L. Yu, J. Liu, K. Wu, T. Klein, Y. Jiang and J.-P. Wang, *Sci. Rep.*, 2015, **4**, 7216.

233   S. Schübbe, C. Schumann, C. Cavelius, M. Koch, T. Müller and A. Kraegeloh, *Chem. Mater.*, 2012, **24**, 914–923.

234   Jasmin, A. L. M. Torres, L. Jelicks, A. C. C. de Carvalho, D. C. Spray and R. Mendez-Otero, 2012, pp. 239–252.

235   H. Akita, A. Kudo, A. Minoura, M. Yamaguti, I. A. Khalil, R. Moriguchi, T. Masuda, R. Danev, K. Nagayama and K. Kogure, *Biomaterials*, 2009, **30**, 2940–2949.

236   I. Papageorgiou, Z. Yin, D. Ladon, D. Baird, A. C. Lewis, A. Sood, R. Newson, I. D. Learmonth and C. P. Case, *Mutat. Res. Mol. Mech. Mutagen.*, 2007, **619**, 45–58.

237   C.-G. Liu, Y.-H. Han, R. K. Kankala, S.-B. Wang and A.-Z. Chen, *Int. J. Nanomedicine*, 2020, **Volume 15**, 675–704.

238   U. M. Graham, G. Jacobs, R. A. Yokel, B. H. Davis, A. K. Dozier, M. E. Birch, M. T. Tseng, G. Oberdörster, A. Elder and L. DeLouise, in *Physiology & behavior*, eds. L. Tran, M. A. Bañares and R. Rallo, Springer International Publishing, Cham, 2017, vol. 947, pp. 71–100.

239   A. Fymat, *Curr. trends Clin. Med. Imaging*, , DOI:10.19080/ctcmi.2017.01.555554.

240   Y.-X. J. Wang, *Quant. Imaging Med. Surg.*, 2011, **1**, 35–40.

241   T. K. Jain, M. K. Reddy, M. A. Morales, D. L. Leslie-Pelecky and V. Labhasetwar, *Mol. Pharm.*, 2008, **5**, 316–327.

242   J.-E. Kim, J.-Y. Shin and M.-H. Cho, *Arch. Toxicol.*, 2012, **86**, 685–700.

243   A. Sharma, C. Cornejo, J. Mihalic, A. Geyh, D. E. Bordelon, P. Korangath, F. Westphal, C. Gruettner and R. Ivkov, *Sci. Rep.*, 2018, **8**, 4916.

244   C. Iacovita, I. Fizeșan, A. Pop, L. Scorus, R. Dudric, G. Stiufiuc, N. Vedeanu, R. Tetean,

F. Loghin, R. Stiufiuc and C. M. Lucaciu, *Pharmaceutics*, , DOI:10.3390/pharmaceutics12050424.

245   D. Labavić, M. T. Ladjimi, E. Courtade, B. Pfeuty and Q. Thommen, *Int. J. Hyperth.*, 2020, **37**, 506–516.

246   M. Nitta, H. Okamura, S. Aizawa and M. Yamaizumi, *Oncogene*, 1997, **15**, 561–568.

247   Z. Luo, K. Zheng, Q. Fan, X. Jiang and D. Xiong, *Exp. Ther. Med.*, , DOI:10.3892/etm.2017.5257.

248   Z. Taher, C. Legge, N. Winder, P. Lysyganicz, A. Rawlings, H. Bryant, M. Muthana and S. Staniland, *Pharmaceutics*, 2021, **13**, 367.

249   J. Sun, T. Tang, J. Duan, P. X. Xu, Z. Wang, Y. Zhang, L. Wu and Y. Li, *Nanotoxicology*, 2010, **4**, 271–283.

250   C. Berny, R. Le Fèvre, F. Guyot, K. Blondeau, C. Guizonne, E. Rousseau, N. Bayan and E. Alphandéry, *Front. Bioeng. Biotechnol.*, , DOI:10.3389/fbioe.2020.00016.

251   R. Bleul, R. Thiermann and M. Maskos, *Macromolecules*, 2015, **48**, 7396–7409.

252   Z. Shen, A. Fisher, W. K. Liu and Y. Li, in *Engineering of Biomaterials for Drug Delivery Systems*, Elsevier, 2018, pp. 1–26.

253   K. P. García, K. Zarschler, L. Barbaro, J. A. Barreto, W. O'Malley, L. Spiccia, H. Stephan and B. Graham, *Small*, 2014, **10**, 2516–2529.

254   T. Kotnik, L. Rems, M. Tarek and D. Miklavčič, *Annu. Rev. Biophys.*, 2019, **48**, 63–91.

255   A. Blanazs, J. Madsen, G. Battaglia, A. J. Ryan and S. P. Armes, *J. Am. Chem. Soc.*, 2011, **133**, 16581–16587.

256   S. Matoori and J.-C. Leroux, *Mater. Horizons*, 2020, **7**, 1297–1309.

257   W. Qi, P. P. Ghoroghchian, G. Li, D. A. Hammer and M. J. Therien, *Nanoscale*, 2013, **5**, 10908.

258   G. Moad, E. Rizzardo and S. H. Thang, *Polymer (Guildf).*, 2008, **49**, 1079–1131.

259   J. Bain, C. J. Legge, D. L. Beattie, A. Sahota, C. Dirks, J. R. Lovett and S. S. Staniland, 2019, 11617–11625.

260   D. A. Bazylinski and R. B. Frankel, *Nat. Rev. Microbiol.*, 2004, **2**, 217–230.

261   E. J. Cornel, J. Jiang, S. Chen and J. Du, *CCS Chem.*, 2020, 2104–2125.

262   S. Sugihara, S. P. Armes, A. Blanazs and A. L. Lewis, *Soft Matter*, 2011, **7**, 10787.

263   E. Boedtkjer and S. F. Pedersen, *Annu. Rev. Physiol.*, 2020, **82**, 103–126.

264   J. Gaitzsch, L. Messager, E. Morecroft and W. Meier, *Polymers (Basel).*, 2017, **9**, 483.

265   K. S. Sivaranjani, G. Antilen Jacob and R. Justin Joseyphus, *J. Magn. Magn. Mater.*, 2020, **513**, 167228.

266   D. Kostyukova and Y. H. Chung, *J. Nanomater.*, 2016, **2016**, 1–9.

267   M. Danaei, M. Dehghankhold, S. Ataei, F. Hasanzadeh Davarani, R. Javanmard, A. Dokhani, S. Khorasani and M. Mozafari, *Pharmaceutics*, 2018, **10**, 57.

268   P. A. Petrov, A. Ali and D. K. Potter, *J. Mod. Phys.*, 2017, **08**, 1013–1019.
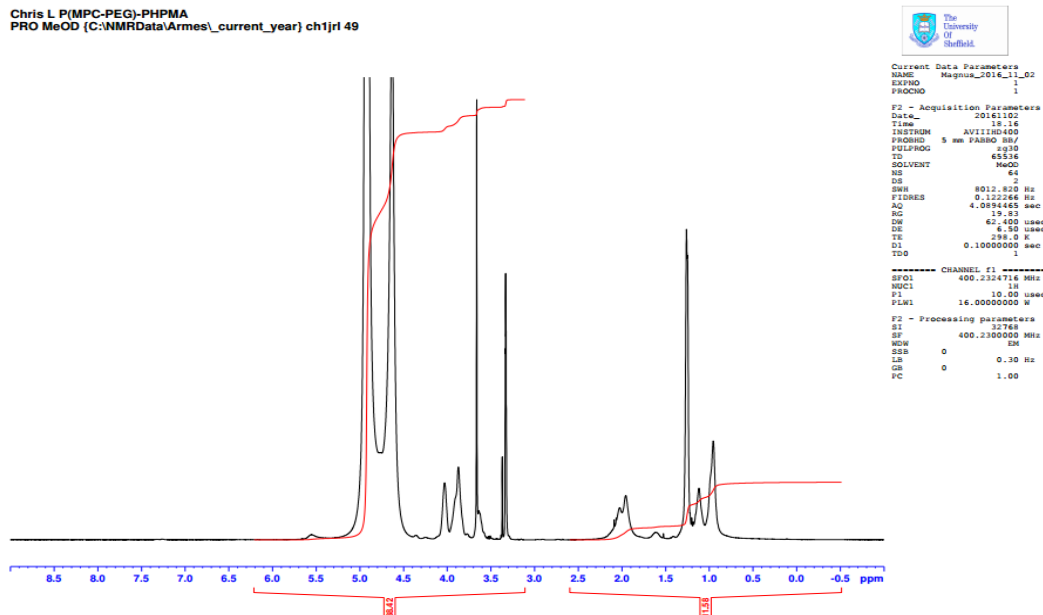
9 APPENDIX

9.1 NMR SPECTRA

Figure 9.1.1 – 1H NMR in deuterated methanol of 70/30% PEG113-PHPMA400 polymersomes.
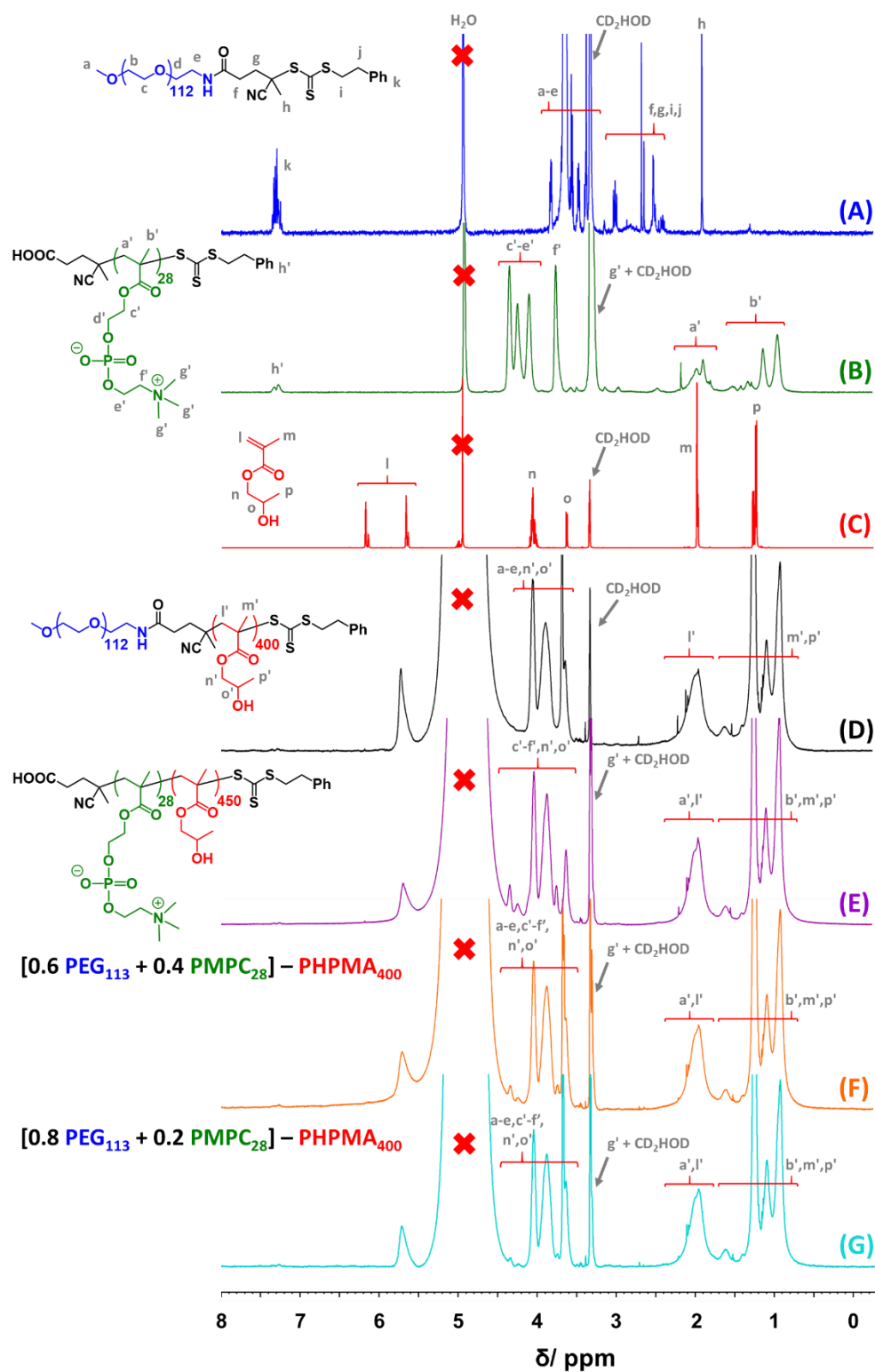
Figure 9.1.2 – ^{1}H NMR in deuterated methanol of the PETTC-PEG113 precursor (A), PETTC-PMPC28 precursor (B) HPMA monomer (C), PEG113-PHPMA400 (D), PMPC28-PHPMA450 (E), 0.6 PEG113 + 0.4 PMPC28 (F) and 0.8 PEG113 + 0.2 PMPC28 (G) Complete disappearance of vinyl protons (l) indicates >99% monomer conversion.